ABSTRACT

Title of Dissertation:	MELT EXTRACTION AND CRUSTAL THICKNESS VARIATIONS AT SEGMENTED MID-OCEAN RIDGES
	Hailong Bai, Doctor of Philosophy, 2017
Dissertation directed by:	Associate Professor Laurent G. J. Montési Department of Geology

Mid-ocean ridges are underwater volcanic mountains extending more than 55,000 km in ocean basins worldwide, accounting for nearly 80% of the Earth's volcanism. They are the birthplace of new seafloor, resurfacing two thirds of the planet over about 100 million years. At mid-ocean ridges, tectonic plates move away from each other, a phenomenon known as seafloor spreading, at rates ranging from slow (~10 cm/yr) to fast (~100 cm/yr). Plate divergence induces the underlying mantle to rise and melt. Buoyant melts segregate from the mantle and collect toward axes of mid-ocean ridges, where they are extracted and solidify into new oceanic crust. The thickness of oceanic crust, the final product of ridge magmatism, contains integrated information about plate motion, mantle flow, mantle temperature, melt generation, melt extraction and crustal accretion. In this dissertation, I investigate three types of crustal thickness variations at mid-ocean ridges to provide insights into the Earth's deep, less accessible interior.

Mid-ocean ridges are broken into segments bounded by transform faults. At fast-spreading ridges, transform faults exhibit thicker crust than adjacent ridge segments, while the crust along transform faults at slow-spreading ridges is thinner. I show that these observations are compatible with melt being extracted along fast-slipping transform faults, but not at the slow-slipping ones.

The plates on either side of a ridge axis may move away from the ridge at different rates. I reveal a discrepancy between the expected and observed topography at such asymmetrically spreading ridges, and argue that the discrepancy is best explained by asymmetric crustal thickness, with thicker crust on the slower-moving plate and thinner crust on the faster-moving plate.

Crustal thickness may differ between ridge segments separated by a transform fault, in a way that correlates with the relative motion between the ridge and the underlying mantle. I study the three-dimensional effects of background mantle flow, and demonstrate that the pattern of along-axis crustal thickness variations is controlled by the relative angle between ridge and background mantle flow.

This dissertation systematically examines the origins of crustal thickness variations at mid-ocean ridges, and provides constraints on mantle and melt dynamics.

MELT EXTRACTION AND CRUSTAL THICKNESS VARIATIONS
AT SEGMENTED MID-OCEAN RIDGES

by

Hailong Bai

Dissertation submitted to the Faculty of the Graduate School of the
University of Maryland, College Park, in partial fulfillment
of the requirements for the degree of
Doctor of Philosophy
2017

Advisory Committee:
 Associate Professor Laurent G. J. Montési, Chair
 Senior Scientist Mark D. Behn
 Assistant Professor Vedran Lekic
 Associate Professor Amir Riaz
 Assistant Professor Nicholas C. Schmerr
 Associate Professor Wenlu Zhu

Dedication

This dissertation is dedicated to my families: my parents, my grandparents, my sister, my lovely nieces Huanhuan and Lele, and my wife Yuanyuan. Your love and support always give me courage, strength, warmth and delight.

Acknowledgements

This marks the end of my PhD study. The excitement of living in US, the cultural shock, the anxiety before the first time teaching, the nights with two-hour sleep on the office floor, the depression when model did not work, the decompression when model actually worked, the sunset moonrise glorious clouds in the middle of the Atlantic Ocean, the joy of the first publication, the walks in the campus, the presentations in conferences, the stressfulness of dissertation writing. For years, you feel safe and desperate that it's never going to end, next moment, it ends. Suddenly six years feel so short. Half of me just cannot believe it and wants to go to the office tomorrow as usual, the other half is shouting and cheering: I made it!

I could not have made it without the help of my advisor Laurent Montési. He led me into the field of mid-ocean ridge research, and taught me how to be a good scientist. His support, guidance and efforts made this dissertation possible. I enjoyed working with this intelligent scientist and patient advisor. The philosophy I learned from him, to tackle a problem starting from its simplest setting, has been beneficial to both my research and everyday life.

I'm grateful to other members of my dissertation defense committee: Mark Behn, Wenlu Zhu, Vedran Lekic, Nicholas Schmerr, and Amir Riaz, for their constructive reviews of my dissertation and participations in my defense. Special thanks to Mark Behn, for traveling from Woods Hole, Massachusetts to College Park, Maryland to attend my defense.

graduate students in the Department of Geology. Thank you for making the grad

school life joyful.

Finally, so long, Maryland.

Table of Contents

List of Tables

List of Figures

Chapter 1: Introduction

1.1 Overview

Mid-ocean ridges are prominent underwater mountains extending more than 55,000 km in the global ocean basins (Figure 1.1), associated with high heat flow, seismic activity and magmatism [e.g, *Heezen*, 1960]. They have been recognized as a type of divergent plate boundaries [*Hess*, 1962], where tectonic plates move apart by the process of seafloor spreading, driven primarily by slab pull due to the weight of subducting slabs on the opposite edges of the rigid plate [e.g., *Conrad and Lithgow-Bertelloni*, 2002]. The rate of seafloor spreading varies by locality, and can be used to classify mid-ocean ridges into four categories: fast-, intermediate-, slow-, and ultraslow-spreading ridges. Plate separation induces the underlying hot mantle to upwell and melt (Figure 1.2). Melt ascends to the surface, and solidifies to form the new oceanic crust, resurfacing two thirds of the planet over a timescale of about 100 million years.

Along the axes, mid-ocean ridges are segmented by oceanic transform faults [*Wilson*, 1965], which are usually orthogonal to the ridges and parallel to the spreading directions (Figure 1.1). Plates with contrasting ages from adjacent ridge segments are juxtaposed along transform faults, affecting mantle flow and thermal structures [e.g., *Fox and Gallo*, 1984], making segmented mid-ocean ridges fundamentally three-dimensional features.
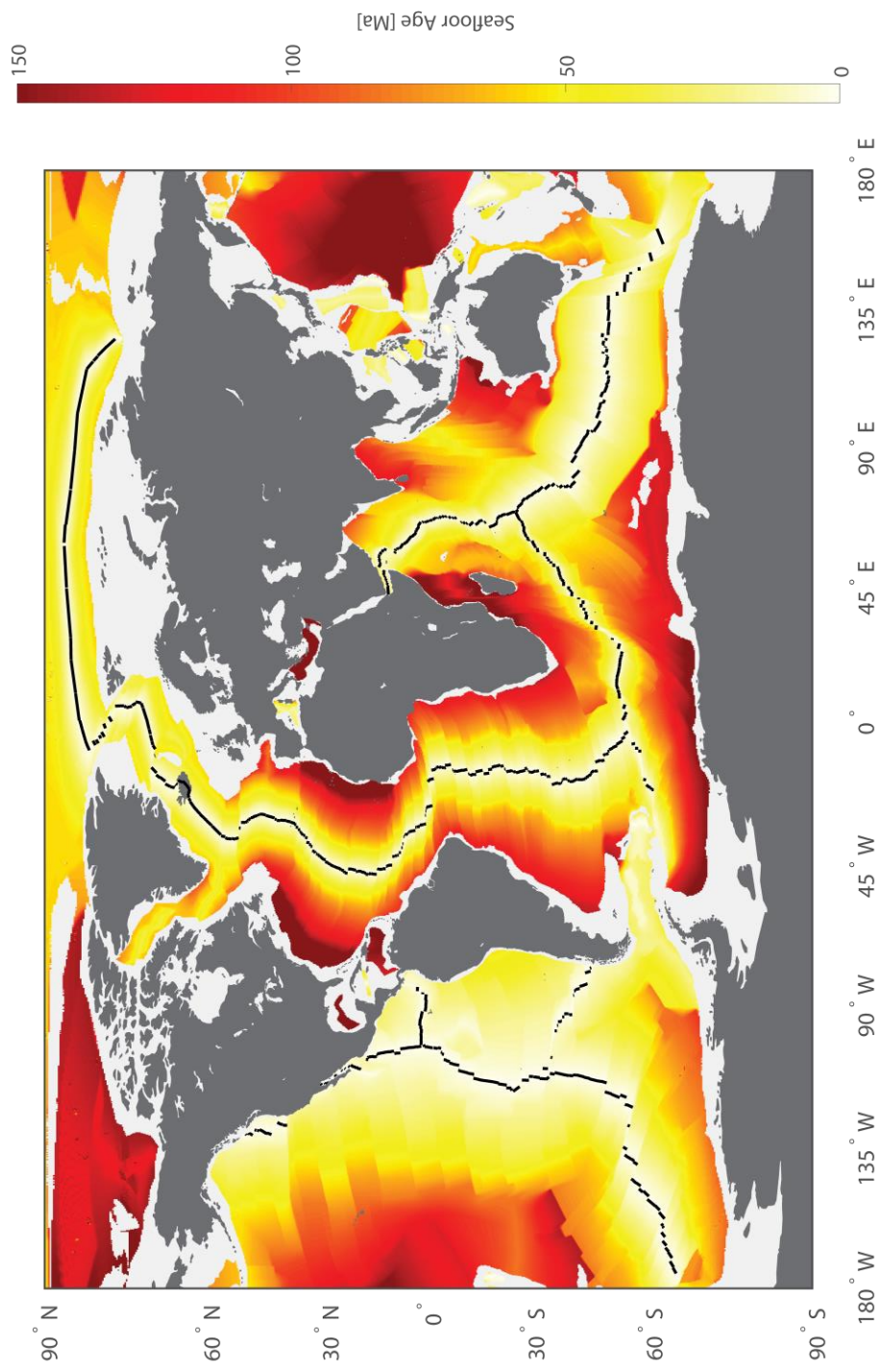
Figure 1.1 Map of seafloor age. The black line segments represent the locations of mid-ocean ridges, along which new oceanic crust is formed.

As manifestations of mantle dynamics, mid-ocean ridges provide a window into the Earth's deep, less-accessible structures and processes. Over the past decades, a wide range of geological, geophysical and geochemical studies has led to substantial progresses in understanding the linkage between mantle/melt dynamics and observed surface features such as seafloor bathymetry, crustal thickness, and basalt geochemistry [e.g., *MacDonald*, 1982; *McKenzie*, 1984; *Klein and Langmuir*, 1987; *White et al.*, 1992; *Melt Seismic Team*, 1998; *Gregg et al.*, 2012; *Gale et al.*, 2014; *Carbotte et al.*, 2015]. Among these features, crustal thickness—the final product of ridge magmatism, provides the strongest constraints on melt generation, melt extraction, and mantle flow [*Forsyth*, 1992].

However, it is often overlooked that crustal thickness represents the integrated effects of mantle and melt dynamics, and it is not well understood how various mantle and magmatic processes contribute to crustal thickness variations. This dissertation seeks to systematically investigate the origins of crustal thickness variations along-axis (Chapter 5), cross-axis (Chapter 4), and between ridge and transform fault (Chapter 3) using numerical methods (Chapter 2), and establish a quantitative link between crustal thickness variations and mantle/melt dynamics. In this chapter, I review general characteristics of mid-ocean ridges that will be helpful to understand the work presented in this dissertation.

1.2 Mantle Flow

Mantle upwelling at mid-ocean ridges can be driven either by the viscous drag of overriding spreading plates [e.g., *Spiegelman and McKenzie*, 1987; *Phipps*

3

Morgan, 1987] or by the buoyancy force from density variations primarily associated with retained melt [e.g., *Rabinowicz et al.*, 1984; *Scott and Stevenson*, 1989; *Buck and Su*, 1989; *Su and Buck*, 1993; *Katz*, 2010]. Although the buoyancy-driven flow can be used to explain some diapir-like upwelling centers [e.g., *Parmentier and Phipps Morgan*, 1990; *Wang et al.*, 2009], it is not consistent with the broad partial melting regions and the lack of deep upwelling root from geophysical observations [e.g., *MELT Seismic Team*, 1998; *Key et al.*, 2013], or geochemical signatures of mid-ocean ridge basalts [e.g., *Spiegelman and Reynolds*, 1999; *Zou et al.*, 2002]. Hence passive flow is a probably more appropriate approximation of the mantle upwelling.

Mantle driven by plate divergence follows a corner flow pattern: it first ascends vertically underneath the ridge axis, then turns a corner and moves laterally away from the ridge axis [*McKenzie*, 1969] (Figure 1.2). This flow pattern is modified by tectonic complexities, such as asymmetric spreading, ridge migration and background mantle wind.

1.3 Thermal Structure

As plates move away from the ridge axis, they age and gradually cool by conductive heat loss to the surface, the rate of which is controlled by mantle temperature, thermal diffusivity, and spreading rate. As approximated by the half-space cooling model [*Turcotte and Schubert*, 2002], the further a column of rock is from the ridge axis, the older and therefore the colder it is. The thickness of lithosphere, often approximated as depth corresponding to the 600 °C isotherm, is thus smallest at ridge axis and increases toward off-axis regions (Figure 1.2). Along
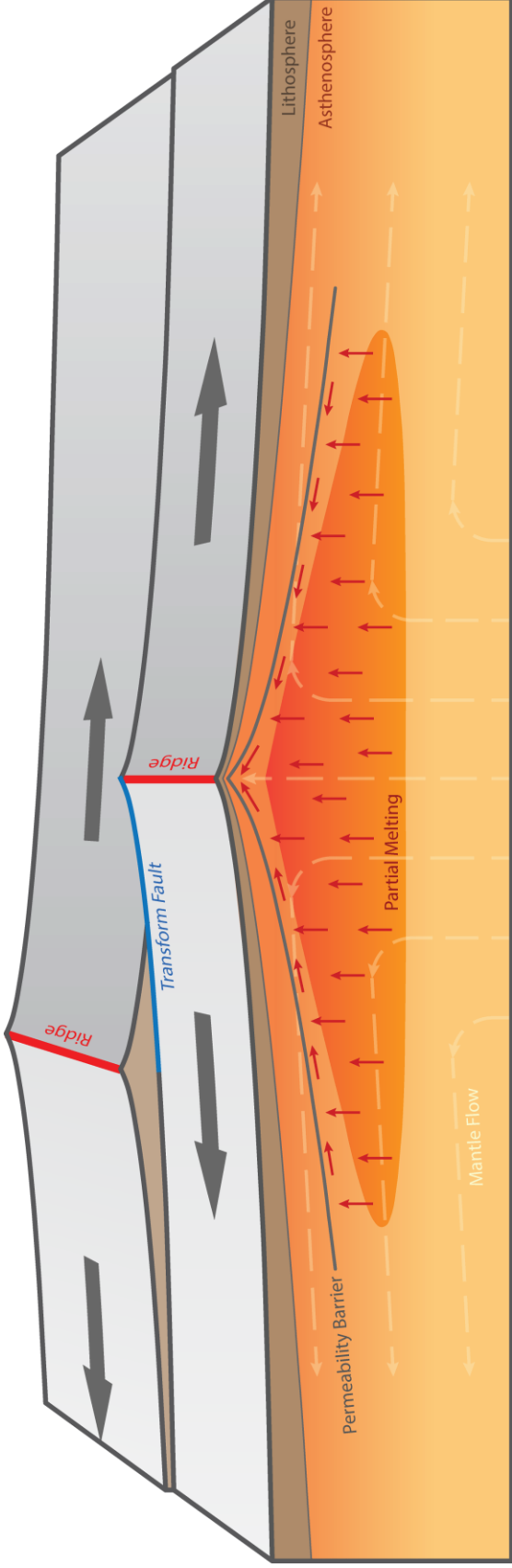
Figure 1.2 Schematic diagram of a mid-ocean ridge system in perspective view. On top, the divergence (black arrows) of tectonic plates (gray areas) occurs at mid-ocean ridges (red lines). Two ridge segments are offset by a transform fault (blue line). Plate divergence drives the underlying mantle (light orange area) to rise (white dashed streamlines) and melt (dark orange area). The buoyant melt ascends (red arrows) through the partial melting region, and collects along a low-permeability barrier (gray curve in the mantle) toward the ridge axis, where it is extracted and forms new oceanic crust.

transform faults, the temperature difference between juxtaposing plates adds a horizontal heat conduction component and cools the adjacent ridge segments, resulting in lithosphere thickening toward transform faults.

1.4 Melt Generation

Mantle melting at mid-ocean ridges is caused by adiabatic decompression during mantle upwelling. Plate divergence and/or mantle density variations [e.g., *McKenzie*, 1969; *Scott and Stevenson*, 1989] drive the already hot mantle materials to ascend, which is associated with a decrease in pressure. The melting temperature of mantle rocks decreases faster (about 0.1 °C/MPa, or 3 °C/km) with pressure release than the adiabatic cooling of mantle (about 0.01 °C/MPa, or 0.3 °C/km). When the mantle temperature equals or exceeds the melting temperature, melt is produced.

The degree and extent of mantle melting at mid-ocean ridges have been estimated from seismic tomography [e.g., *Forsyth et al.*, 1998], seafloor magnetotelluric soundings [e.g., *Evans et al.*, 1999; *Key et al.*, 2013], crustal thickness measurements [e.g., *White et al.*, 2001], laboratory experiments [e.g., *Kinzler and Grove*, 1992; *Hirschmann*, 2000; *Till et al.*, 2012], mid-ocean ridge basalts geochemistry [e.g., *Klein and Langmuir*, 1987; *Gale et al.*, 2014], and numerical models [e.g., *Reid and Jackson*, 1981; *McKenzie and Bickle*, 1988]. The melting regime is roughly triangular in cross-section and centered underneath the ridge axis, extending laterally for hundreds of kilometers (Figure 1.2). The degree of melting ranges from 0 % at onset depth of ~100 km to a maximum of more than 20 % at the shallowest melting depth. Mantle melting is a function of temperature, pressure, bulk

chemical composition, and volatile content. Higher mantle temperature, faster

spreading of seafloor (faster mantle upwelling), more fertile mantle composition, and

higher volatile content in rocks lead to a larger extent and higher degree of melting.

1.5 Melt Migration and Extraction

Despite the broad region (> 100 km) of partial melting underneath mid-ocean

ridges, neo-volcanic activity at surface is confined within a narrow zone (< 2 km

[*Macdonald*, 1982; *Vera et al.*, 1990]) at the ridge axis. This contrast indicates that

the melt must have been focused toward the ridge axis from the wide, deep region of

its generation.

The melt produced by partial melting is less dense and less viscous than the

residual mantle, and tends to rise under buoyancy (Figure 1.2). The initial melt forms

at boundaries between mineral grains of mantle rocks, producing either thin films

covering the grain boundaries, or interconnected channels along grain junctions

[*Smith*, 1948, 1964]. Scanning electron microscopy [e.g., *Waff and Bulau*, 1982; *Waff

and Faul*, 1992] and synchrotron X-ray microtomography [e.g., *Zhu et al.*, 2011] on

partially molten mantle rocks (synthesized in laboratory) demonstrate a high

connectivity in the grain boundary network of interstitial melt [e.g., *Kohlstedt*, 1992;

Zhu and Hirth, 2003; *Zhu et al.*, 2011], indicating that the melt is able to segregate

and ascend through the porous residual solid rapidly, even at low melt fractions

[*Miller et al.*, 2014].

However, how melt flow is focused toward the ridge axis is not well

understood. Several mechanisms has been proposed, as described below.

7

1.5.1 Ridge Suction

The porous flow of melt may be driven toward the ridge axis by large non-hydrostatic pressures related to mantle flow [*Spiegelman and McKenzie*, 1987; *Ribe*, 1988]. When plate-driven shear is larger than buoyancy-driven shear, flow of mantle near ridge axis is in a form similar to the corner flow [*McKenzie*, 1969], which induces a pressure gradient that focuses melt [*Spiegelman and McKenzie*, 1987]. However, the asthenospheric viscosity required for this model to focus melt over hundreds of kilometers is two orders of magnitude higher than the accepted values [e.g., *Phipps Morgan*, 1987]. Thus, this mechanism is unlikely to be significant.

1.5.2 Buoyant Upwelling

Melt focusing may be a result of buoyancy-driven mantle convection [*Rabinowicz et al.*, 1984; *Buck and Su*, 1989; *Scott and Stevenson*, 1989]. When the buoyancy-driven shear is larger than the plate-driven shear, a convection unit is superposed on the mantle corner flow, and generates a fast upwelling zone and a narrow zone of melting beneath the ridge axis [*Spiegelman*, 1993]. However, as discussed in the previous section, buoyancy-driven mantle upwelling is not consistent with the geophysical [e.g., *MELT Seismic Team*, 1998; *Key et al.*, 2013] and geochemical [e.g., *Spiegelman and Reynolds*, 1999; *Zou et al.*, 2002] observations, and it relies on higher mantle porosity than current estimates, making it an unlikely mechanism for melt focusing.

1.5.3 Hydrofracturing

Melt may be localized and extracted through conduits opened by hydrofracturing [*Sleep*, 1988; *Nicolas*, 1986, 1990]. The abundant dikes observed in mantle peridotites at ophiolites suggest that melt migration may be associated with crack propagation in the sub-lithospheric mantle. In porous mantle, when melt pressure exceeds the yield stresses of mantle rocks, hydraulic fracturing develops. The fractures will then draw melts from the surroundings. If buoyancy-driven flow dominates mantle upwelling, the maximum compressional stress is sub-horizontal at depth from 35 km to 15 km, and steepens to become subvertical at depth less than 15 km. The resulting sills and dikes tap the melt and focus it toward the ridge axis [*Nicolas*, 1990]. However, it is dubious that magma is able to fracture mantle rocks within the partial melting region where plastic deformation dominates [*Kelemen and Dick*, 1995]. Also, in order for hydrofracturing to focus melt, buoyancy-driven mantle flow has to prevail. Therefore, this mechanism may only be important for vertical melt extraction at shallow depth.

1.5.4 Shear-Induced Instability

Development of a mechanical instability related to the feedback between melt distribution and deformation can lead to melt localization [*Phipps Morgan*, 1987; *Stevenson*, 1989; *Spiegelman*, 2003; *Katz et al*., 2006]. Shear-induced petro-fabrics and pressure gradients in partially molten mantle rocks maydraw melt into high-porosity regions, where shear viscosity and fluid pressure are lower, and in turn raise the local porosity. This instability organizes melt into high-porosity melt bands that persist at low angles to the direction of maximum shear and point toward ridge axis

[*Katz et al*., 2006], providing a possible mechanism for melt focusing. However, this observation is largely based on laboratory experiments, in which the imposed strain rates are six to eight orders of magnitude higher than in the mantle [*Kohlstedt and Holtzman*, 2009]. Also, the melt bands did not occur in numerical models of mid-ocean ridges, even when the necessary conditions for its development were satisfied [*Katz*, 2010]. Thus it is unclear how significant this mechanical instability is under mantle conditions.

1.5.5 Reactive Infiltration Instability

The undersaturation of orthopyroxene in mid-ocean ridge basalts and the large fractionations between light and heavy rare earth elements in residual peridotites [e.g., *Johnson et al*., 1990] indicate chemical disequilibrium during melt transport. It is likely that melt is extracted rapidly through chemically isolated conduits [e.g., *Kelemen et al*., 1997a]. *Kelemen et al*. [1995a, 1995b] identified mantle dunites, formed by dissolution of pyroxene along melt migration pathways, as the likely conduits for focused flow. The dissolution increases the local porosity, which enhances fluid flow in the partially molten mantle and in turn leads to increased dissolution. This positive feedback, known as reactive infiltration instability, facilitates the formation of high-porosity dissolution channels [*Spiegelman et al*., 2001]. If the solubility of pyroxene in magma increases downstream, a fractal melt extraction tree may form and focus the fluid [*Hart*, 1993; *Aharonov et al*., 1995]. Based on statistical analysis of dunite channels observed in ophiolite, *Braun and Kelemen* [2002] demonstrated that a network of coalescing channels can explain the scale-invariant power-law size/frequency distribution of dunite channels, and

preserve the geochemical disequilibria between melts and residual mantle. Thus, dissolution channels is a plausible mechanism for melt migration beneath mid-ocean ridges. However, it is not clear how significant the channelized flow is, compared with diffuse porous flow, during melt transport.

1.5.6 Permeability Barrier

Rapid crystallization near the surface generates a freezing boundary that focuses the melt [*Sparks and Parmentier*, 1991; *Spiegelman*, 1993; *Ghods and Arkani-Hamed*, 2000; *Hebert and Montési*, 2010]. The flux of melt is perturbed by fast cooling at the base of the thermal boundary layer, where decompaction of the porous mantle matrix generates high-porosity channels [*Sparks and Parmentier*, 1991; *Spiegelman*, 1993]. *Hebert and Montési* [2010] studied the geochemical evolution of melts near the thermal boundary layer and predicted the existence of a permeability barrier, which corresponds to the multiple saturation point of plagioclase and pyroxene [*Kelemen and Aharonov*, 1998]. Building on the permeability barrier concept [*Sparks and Parmentier*, 1991], *Montési et al* [2011] developed a three-step scheme for melt migration and extraction: (1) Melt moves vertically in the partial melting region through pore spaces and possibly through dissolution channels (Figure 1.2); (2) Melt accumulates at the permeability barrier and moves along this barrier toward the ridge axis (Figure 1.2); (3) Melt enters an extraction zone corresponding to structural weakness (faults, dikes and shear zone) around plate boundaries, gets extracted, and forms new oceanic crust. The three-step scheme has successfully explained crustal thickness variations at ultraslow- [*Montési et al.*, 2011] and fast-spreading ridges [*Hebert and Montési*, 2011], and the spreading-rate-dependent

11

crustal thickness differences between transform faults and associated ridges [*Bai and Montési*, 2015]. These studies suggest that the low-permeability barrier may play a crucial role in focusing melt at mid-ocean ridges.

In general, there is a variety of mechanisms proposed for melt migration and extraction at mid-ocean ridges. Among them, the three-step scheme of melt extraction developed by *Montési et al.* [2011] (Section 1.5.6) captures the essential dynamics of melt extraction, and, albeit in a simplified and idealized manner, is computationally economic. Thus I adopted the three-step melt migration scheme when processing three-dimensional models of segmented mid-ocean ridges.

1.6 Crustal Thickness

Close to the surface, melts may pool and create a magma chamber underneath the ridge axis [e.g., *Cann*, 1974]. In the magma chamber, crustal accretion occurs following either "gabbro glacier" [*Nicolas et al.*, 1988; *Henstock et al.*, 1993], or "sheeted sill" [*Boudier et al.*, 1996; *Kelemen et al.*, 1997b] models, producing the layered structure of oceanic crust [e.g., *Talwani et al.*, 1965]: Right below the sea water, the first layer of oceanic crust, Layer 1, consists of mostly unconsolidated or semi-consolidated sediments, and is usually thin or not present near the ridge axis. The second layer is composed of Layer 2A, pillow basalts formed from fast cooling of erupted lava, and Layer 2B, sheeted dikes formed from magma intrusion in the fissures. The third layer is made of gabbro from slow cooling of residual magma.

The thickness of crust at mid-ocean ridges has been estimated using seismic refraction [e.g., *Canales et al.*, 2003; *Dunn et al.*, 2005], reflection [e.g., *Rohr et al.*,

1988; *Barth and Mutter*, 1996; *Carbotte et al.*, 2008] and tomography [e.g., *Toomey et al.*, 1994], gravity anomalies [e.g., *Kuo and Forsyth*, 1988; *Lin et al.*, 1990; *Wang et al.*, 1996; *Tolstoy et al.*, 1993; *Gregg et al.*, 2007; *Wang et al.*, 2015], geochemical measurements [e.g., *Klein and Langmuir*, 1987; *McKenzie and O'Nions*, 1991], and ophiolite measurements [e.g., *Nicholas et al.*, 1996]. Away from anomalous regions, the oceanic crust exhibits a uniform average thickness of about 7 ± 1 km, largely independent of spreading rates [e.g., *White et al.*, 1992]. However, crustal thickness variations exist within each ridge segments (Figure 1.3b), between adjacent ridge segments (Figure 1.3c), between conjugate plates (Figure 1.3d), and between ridge segment and adjacent transform fault (Figure 1.3b). Although variations differ by localities, some common patterns are observed. Origins of these variation patterns are investigated in this dissertation.

1.6.1 Along-Axis Crustal Thickness Variations

Away from hot spots, along the axis of each individual ridge segment, crust is typically thickest at the segment center, and thins toward the transform faults (Figure 1.3b). The range of variation depends on the spreading rates [*Chen*, 1992; *Bown and White*, 1994]. Slow-spreading ridges exhibit large crustal thickness variations from about 8 km at centers to less than 4 km near the ends [e.g., *Whitmarsh and Calvert*, 1986; *Kuo and Forsyth*, 1988; *Lin et al.*, 1990; *Blackman and Forsyth*, 1991; *Detrick et al.*, 1993; *Detrick et al.*, 1995; *Canales et al.*, 2000a; *Canales et al.*, 2000b; *Hooft et al.*, 2000; *Dunn et al.*, 2005], while crustal thickness along fast- spreading ridges
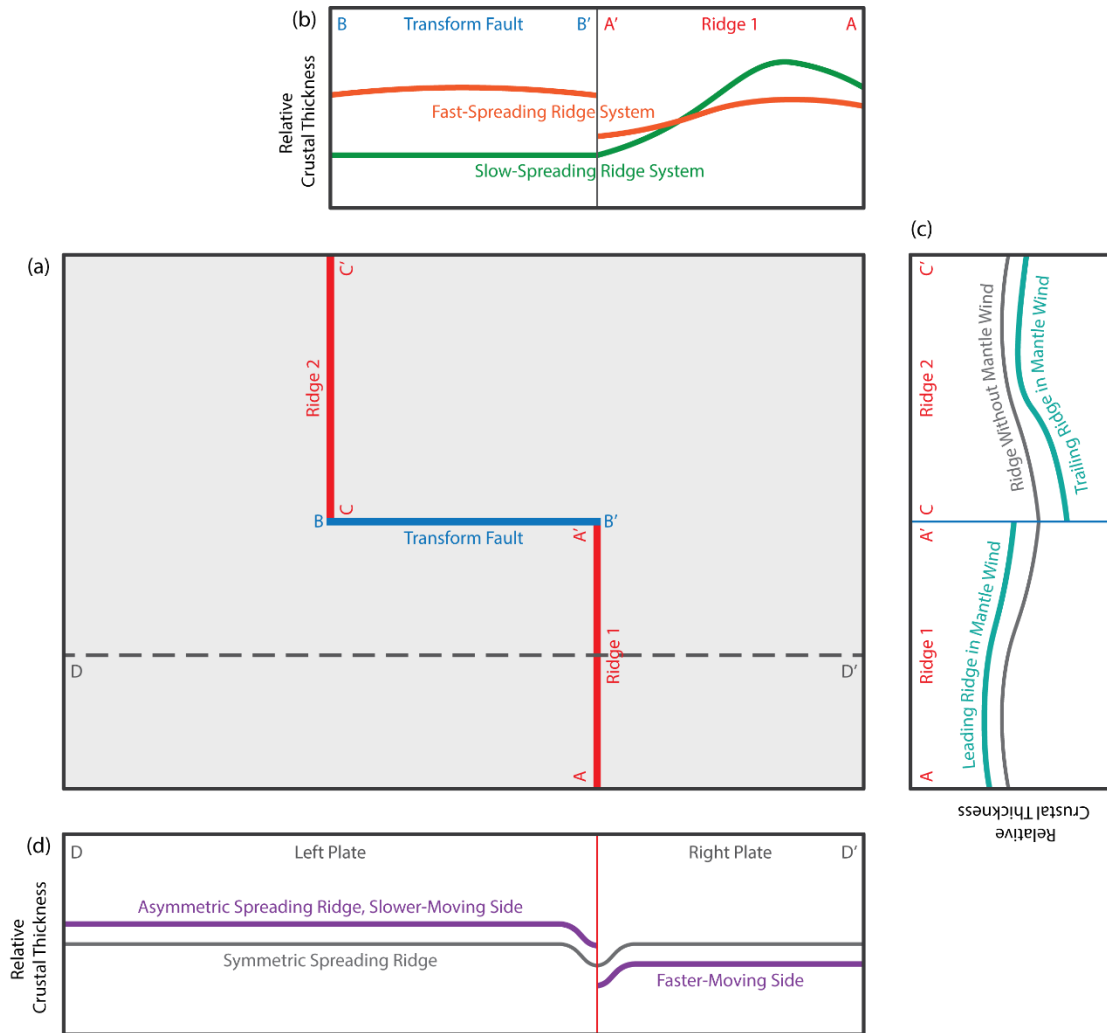
Figure 1.3 Schematic diagrams of crustal thickness variations at mid-ocean ridges. The simplified geometry of a ridge-transform-ridge system is shown in (a) in map view, where red lines represent the ridge segments and the blue line represents the transform fault. The crustal thickness difference between transform faults and adjacent ridges is shown in (b) in cross-sections representing fast- (orange) and slow- (green) spreading ridges. Within the ridge axis (the "Ridge 1" box), slow-spreading ridge has larger crustal thickness variation than the fast-spreading ridge. The difference in crustal thickness between ridge segments is shown in (c) with (teal) or without (gray) mantle wind. Profiles of crustal thickness across the axis are shown in (d) in cross-section view for symmetric (gray) and asymmetric (purple) spreading. The location of the cross-section is marked by the dash line in (a).

14

only differs by less than 2 km [e.g., *Barth and Mutter*, 1996; *Canales et al.*, 2003; *Aghaei et al.*, 2014] (Figure 1.3b). This spreading-rate-dependent variation has been attributed to different styles of mantle upwelling at fast- and slow-spreading ridges [*Lin and Phipps Morgan*, 1992], or variations in melt focusing [e.g., *Hooft et al.*, 2000]. In Chapter 3 and Chapter 5, I demonstrate that this phenomenon can also be a natural result of melt migration, controlled by the permeability barrier morphology.

Along the axes, between adjacent ridge segments, the crustal thickness variations seem to correlate with the direction of ridge migration [*Carbotte et al.*, 2004]. At fast- and intermediate-spreading ridges, the leading segments (offset in the direction of ridge migration) are consistently associated with shallower axial depth and thicker crust than the trailing segments across the discontinuities [*Carbotte et al.*, 2004; *Katz et al.*, 2004; *Supak et al.*, 2007; *Carbotte et al.*, 2008; *Weatherley and Katz*, 2010] (Figure 1.3c), though this correlation is weaker at slow-spreading ridges [*Supak et al.*, 2007]. In Chapter 5, I reproduce this observation using three-dimensional numerical models, and reveal that the pattern of crustal thickness variations is primarily controlled by the relative angle between mantle motion and ridge axes.

1.6.2 Cross-Axis Crustal Thickness Variations

Crustal accretion is usually assumed to be symmetric about the ridge axis. However, cross-axis crustal thickness differences have been reported, at slow- [e.g., *Kuo and Forsyth*, 1988; *Ballu et al.*, 1998; *Wang et al.*, 2015], intermediate- [*Rohr et al.*, 1988] and fast-spreading [*Toomey et al.*, 1994] ridges. While at slow-spreading ridges, the asymmetry has been attributed to the tectonic extension by long-lived

15

detachment faults [e.g., *Tucholke and Lin*, 1994; *Cann et al.*, 1997; *Escartin et al.*, 2008], at fast- and intermediate-spreading ridges, the origin of asymmetric crustal thickness is not well understood. In Chapter 4, I compare global ridge topography data with numerical models of different types of ridge asymmetry, and conclude that asymmetric crustal thickness across-axis is an intrinsic feature of the asymmetric spreading of ridges, with thicker crust accreted on slower-moving plates (Figure 1.3d).

1.6.3 Crustal Thickness Variations between Ridge and Transform Fault

The correlation between the gravity signatures at transform faults and the spreading rates of the associated ridges implies that the crustal thickness variations between ridges and transform faults are spreading-rate-dependent [*Gregg et al.*, 2007]. At fast-spreading ridges, the transform faults are characterized by more negative residual mantle Bouguer anomaly than the adjacent ridge segments, consistent with thicker crust along the transform faults, while at slow-spreading ridges, transform faults are associated with thinner crust (Figure 1.3b). In Chapter 3, I use numerical models to study the spatial relation between permeability barrier and melt extraction zone underneath transform faults, and argue that melt can erupt along the fast-slipping transform faults, but not at slow-slipping ones.

In general, this dissertation seeks to investigate the origins of three types of crustal thickness variations at mid-ocean ridges, and establish a quantitative link between crustal thickness variations and mantle/melt dynamics. Detailed descriptions of the numerical approach employed and study of each type of crustal thickness variations are presented in the following chapters.

16

Chapter 2: MeltMigrator: A MATLAB-based software for modeling three-dimensional melt migration and crustal thickness variations at mid-ocean ridges following a rules-based approach

Abstract

MeltMigrator is a MATLAB®-based melt migration software developed to process three-dimensional mantle temperature and velocity data from user-supplied numerical models of mid-ocean ridges, calculate melt production and melt migration trajectories in the mantle, estimate melt flux along plate boundaries, and predict crustal thickness distribution on the seafloor. MeltMigrator is also capable of calculating compositional evolution depending on the choice of petrologic melting model. Programmed in modules, MeltMigrator is highly customizable and can be expanded to a wide range of applications. We have applied it to complex mid-ocean ridge model settings, including transform faults, oblique segments, ridge migration, asymmetrical spreading, background mantle flow, and ridge-plume interaction. In this technical report, we include an example application to a segmented mid-ocean ridge. MeltMigrator is available as a supplement to this paper, and it is also available from GitHub and the University of Maryland Geodynamics Group website.

The majority of basaltic oceanic crust is formed along mid-ocean ridges, which, in the context of plate tectonics, represent a type of divergent plate boundaries [e.g., *Hess*, 1962]. As adjacent tectonic plates move apart, the underlying hot mantle rises and melts. These melts are then transported and collect beneath the ridge axis, where they are extracted, cool and accrete to form new oceanic crust.

The oceanic crustal thickness has been inferred from seismic reflection [e.g., *Carbotte et al.*, 2008] and refraction data [e.g., *Le Pichon et al.*, 1965], gravity measurement [e.g., *Kuo and Forsyth*, 1988; *Lin et al.*, 1990], ophiolite observations [e.g., *Nicolas et al.*, 1996], basalt geochemistry [e.g., *Klein and Langmuir*, 1987] and numerical models [e.g., *Reid and Jackson*, 1981]. The oceanic crust has an average thickness of 6–7 km thick [*White et al.,* 2001], but varies locally as a function of spreading rate [e.g., *Lin and Phipps Morgan*, 1992] and in more complex geological settings such as near transform faults and fracture zones [e.g., *Gregg et al.*, 2007], overlapping spreading centers [e.g., *Canales et al.*, 2003], oblique segments [e.g., *Montési et al.*, 2011], ultraslow spreading centers [*Dick et al.*, 2003], migrating ridges [e.g., *Carbotte et al.*, 2004] and plume-ridge interaction zones [e.g., *White*, 1997]. MeltMigrator makes it possible to investigate the effects of melt migration on these crustal thickness variations.

Melting takes place in a broad region (>100 km) in the mantle beneath mid-ocean ridges [e.g., *MELT Seismic Team*, 1998; *Evans et al.*, 1999; *Key et al.*, 2013]; however, crustal accretion is confined to a narrow region, <2 km from the ridge axis [*Macdonald*, 1982]. This contrast indicates that melt must be focused from the wide

generation region toward the ridge axis. Several mechanisms have been proposed to explain melt focusing, including dynamic pressure gradients in the mantle [*Spiegelman and McKenzie*, 1987], stress-induced melt bands [*Katz et al.*, 2006], hydrofracturing [*Sleep*, 1988], reactive infiltration instability [*Kelemen et al.*, 1995], and permeability barriers associated with a crystallization front [*Sparks and Parmentier*, 1991].

Here we describe a software that simulates the effect of focusing along a permeability barrier, as proposed by *Sparks and Parmentier* [1991]. The permeability barrier forms at the base of thermal boundary layer, where rapid crystallization of plagioclase and pyroxene clogs the pore space and prevents further upward migration of melts [*Kelemen and Aharonov*, 1998; *Hebert and Montési*, 2010]. A high-porosity decompaction channel is formed immediately beneath the barrier. It is then possible for melt to accumulate and travel within the decompaction channel, guided by the slope of the barrier, toward the ridge axis [*Sparks and Parmentier*, 1991].

More specifically, we follow the three-step scheme for melt focusing and extraction at mid-ocean ridges described in detail by *Montési et al.* [2011] and *Gregg et al.* [2012]. The three steps are: (1) vertical melt percolation in the asthenosphere; (2) melt collection and migration in a decompaction channel that follows a low-permeability barrier at the base of thermal boundary layer toward ridge axis; (3) melt extraction when melt enters a damage zone associated with predefined plate boundaries. MeltMigrator calculates melt migration pathways according to these three steps, estimates melt flux along mid-ocean ridges, and predicts regional crustal thickness variations.

This software is designed to study melt migration processes occurring in the mantle. Melt storage, transport and eruption at crustal level are ignored or idealized. We assume that a solution for the mantle flow field and temperature structure is available separately and simulate the melt production and migration in postprocessing. Thus, we do not attempt to rigorously include the effects of compaction pressure and the latent heat of fusion [*Wilson et al.*, 2014]. This simplification is useful when dealing with mid-ocean ridges with three-dimensional features such as transform faults, oblique segment, ridge migration, asymmetrical spreading, background mantle flow and ridge-plume interaction where a more rigorous approach may be prohibitively expensive from a computational standpoint.

2.2 Code Availability

MeltMigrator is available from GitHub with the MIT License at https://github.com/montesi/MeltMigrator. Example COMSOL input models are available at our group website http://www.geology.umd.edu/~montesi/Geodynamics/software.html#MeltMigrator.

2.3 Methods

2.3.1 Prerequisite and Model Input

MeltMigrator is programmed in MATLAB®. The main script, `meltMain`, calls a number of attendant functions, most of which are defined in stand-alone scripts, to conduct various steps of the calculation. Here we describe the calculation

procedure step by step. Scripts contained in MeltMigrator package are listed in

Appendix Table A.1 and a flowchart of the major calculation steps is included

(Appendix Figure A.1). The parameters that govern code behavior, including the

definition of the plate boundaries under consideration, are set up in the script

`setParameters`, removing the need to modify any of the attendant scripts. Each

script starts with a description of its function, definition of its internal and external

variables, and a list of dependencies (attending scripts).

      The software starts by reading a pre-existing three-dimensional

thermomechanical model of a mid-ocean ridge system. The model should be

constructed in a Cartesian coordinate system, and extend to sufficient depth to include

the bottom of the melting region. The temperature and velocity fields solved in the

model should be exportable to MATLAB®. We typically use a model of mantle flow

and thermal structure constructed using COMSOL Multiphysics® 4.3, which is

transferred into MATLAB® using LiveLink™ for MATLAB®, with the `mphinterp`

function. The software is also setup to use numerical model results saved as a text file

with x, y, z, velocity in x-direction, velocity in y-direction, velocity in z-direction,

and temperature data organized in columns. To use this capacity, users need to set the

parameter `Switch_UseCOMSOL` in `setParameters` to 0. In either mode, the

name of the file containing the model is stored as the `ModelName` variable in

`setParameters`.

      Key parameters must be entered in the `setParameters` script

independently from the external model input. They include the spreading rate and

spreading direction (in relation to the x axis) of the ridge system, the limits of model

domain, and the coordinates of waypoints that define the plate boundary. The code automatically determines the length and obliquity (defined as the angle between the plate motion direction and the normal to the ridge axis) of each plate boundary segment and stores the necessary information in the structure `Geometry`.

MeltMigrator has been applied to a variety of plate boundaries settings, including intratransform spreading centers [*Hebert and Montési*, 2011], transform faults [*Bai and Montési*, 2015], and oblique segments [*Montési et al.*, 2011]. The ridge system in the demonstration model is spreading in x axis direction at a half-spreading rate of 2 cm/yr. The plate boundary is defined by three ridge segments offset by one transform fault and one oblique segment (Figure 2.1).

2.3.2 Melting Function and Calibration

Partial melting beneath mid-ocean ridges results from adiabatic decompression of the mantle. The degree and extent of melting is a function of temperature, pressure, bulk chemical composition, and volatile content (e.g., H_2O). To simulate mantle melting in the routine, we can use either thermodynamic models such as MELTS and pMELTS [*Ghiorso*, 1994; *Ghiorso and Sack*, 1995; *Ghiorso et al.*, 2002; *Asimow and Stolper*, 1999] or a melting parameterizations [e.g., *Reid and Jackson*, 1981; *McKenzie and Bickle*, 1988; *Hirschmann*, 2000; *Katz et al.*, 2003; *Behn and Grove*, 2015]. The latter approach is typically preferred when dealing with three-dimensional calculations due to its computational efficiency. In the MeltMigrator, the melting function is implemented as a user-defined function `meltFunction` (a function of depth z and temperature T), which can be an inline function or an external function script.
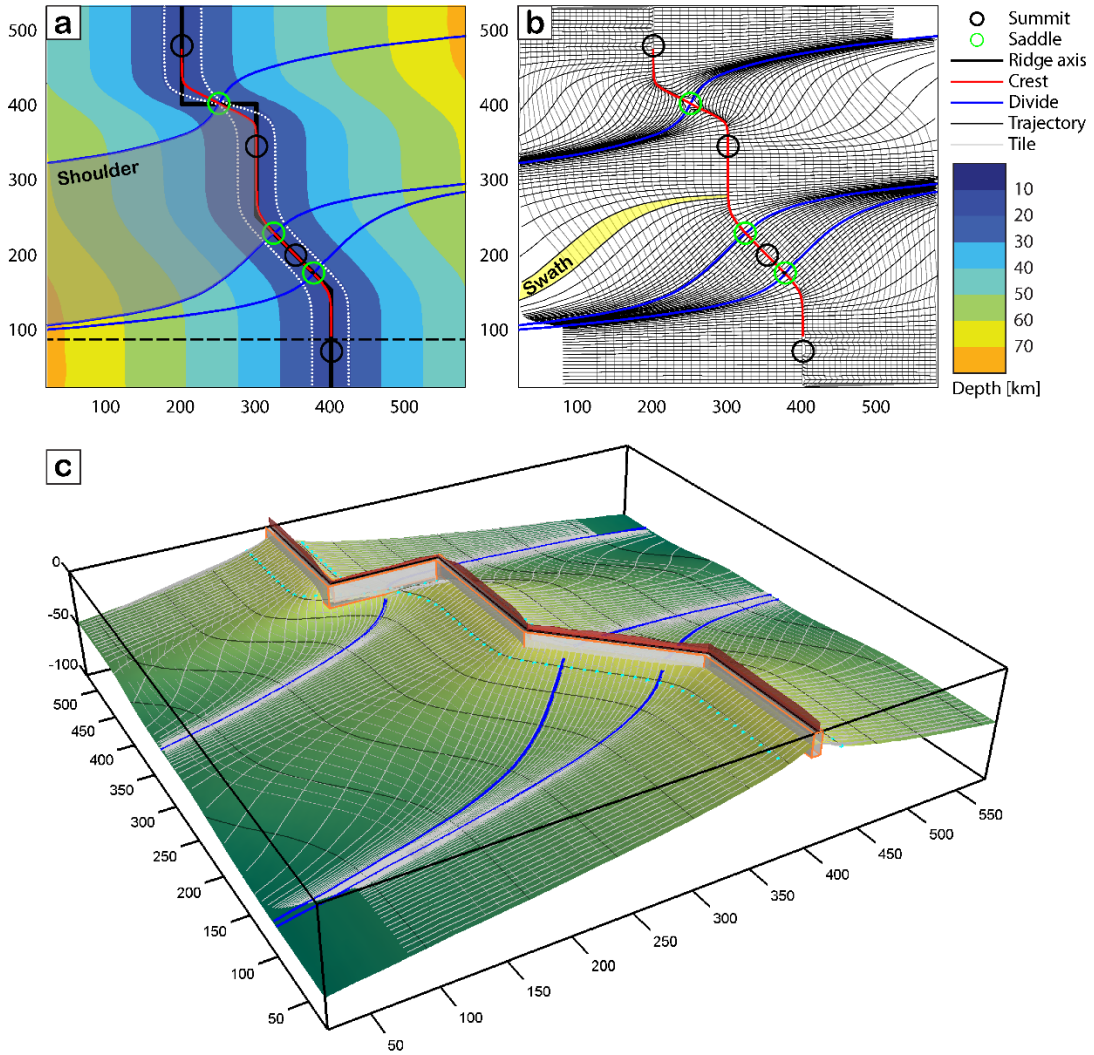
Figure 2.1 Permeability barrier and melt migration setup for a generic mid-ocean ridge model with three spreading segments offset by one transform fault and one oblique segment. a) The plate boundary is indicated by the thick black line. The colors reflect the depth of the barrier. Crest, divides, summits, and saddles are displayed as shown in the legend. A shoulder is highlighted as the shaded region. The dashed line indicates the cross section used for calibrating the melt function. The white dots serve as seeds for the melt trajectories shown in b). b) Melt trajectories and associated tessellation of the lid. A representative swath is highlighted in yellow. c) Three-dimensional rendition of the barrier (green surface with black depth contours), shoulder divides (blue), melt trajectories (white with cyan seed) and tiles. The orange box represents the melt extraction zone. The height of the red surface along the plate boundary is proportional to the accreted crustal thickness.

Multiple melting parameterizations have been developed through theoretical and experimental studies [e.g., *Langmuir et al.*, 1992; *Kinzler and Grove*, 1992; *Iwamori*, 1994; *Kinzler*, 1997; *Hirschmann*, 2000; *Katz et al.*, 2003; *Till et al.*, 2012; *Behn and Grove*, 2015]. In the simplest case, the equilibrium melt fraction for small degrees of melting (5–25%) is approximated as a linear function of temperature in relation to the solidus and liquidus—i.e., the difference between temperature and solidus, scaled by the difference between solidus and liquidus [*Bottinga et al.*, 1978; *Reid and Jackson*, 1981]. The linear melting formula by *Reid and Jackson* [1981], which is adopted in the demonstration example, is provided in the `meltFunctionRJ1981` script. Alternatively, the script `meltFunctionMELTS` uses a look-up table of results from the alphaMELTS thermodynamics software [*Smith and Asimow*, 2005].

It is possible to automatically adjust the melting function so that a reference crustal thickness, specified by the variable named `CrustalThickness_Reference`, is produced at a certain point along the mid-ocean ridge axis. The calibration is conducted along a two-dimensional vertical cross section, perpendicular to a selected ridge segment, ideally away from transform faults, oblique segments, and/or borders of the computational domain. In the example model, the script places the cross section at the center of the longest ridge segment. The temperature and vertical velocity data from the external model are interpolated on a grid of sampling points on the cross section from the input model result. The crustal thickness obtained by collecting all the melt produced in the selected cross section, H_a, is given by:

$$H_a = \int_0^{L_m} \int_{z_b}^0 \frac{\partial F}{\partial z} \frac{v_z}{2V_p} dz \, dx \qquad (2.1)$$

where F is the melt fraction calculated using `meltFunction`, v_z is the vertical

velocity of the mantle, V_p is the half-spreading rate, L_m is the length of the cross

section, and z_b is the depth to the base of the melting column [e.g., *Reid and Jackson*,

1981]. The calculated value of H_a is then divided by the user-defined reference crustal

thickness to produce a scaling factor, with which `meltFunction` is updated, so that

desired level of crustal thickness can be generated along the target portion of ridge

segments. This scaling factor can be interpreted as a measure of the efficiency of melt

extract, or a correction on the melting function parameters. The calibration operation

is optional and can be switched on/off using the variable named

`Switch_MeltCalibration` in `setParameters`.

As noted above, it is also possible to use MeltMigrator with thermodynamic

models in mantle melting calculation (e.g., alphaMELTS) [*Smith and Asimow*, 2005]

by calling `meltFunctionMELTS` as `meltFunction` for melt fraction

calculation, although this tends to be computationally expensive. alphaMELTS is a

versatile program that utilizes the MELTS [*Ghiorso and Sack*, 1995] and pMELTS

[*Ghiorso et al*., 2002] algorithms to calculate the equilibrium assemblages of

multicomponent systems, such as the mantle, along a user-defined thermodynamic

path. It may perform batch, fractional or continuous melting, and crystallization

calculations in anhydrous, water-undersaturated, or water-saturated settings. It also

features a batch mode, making the large-scale automatic processing possible.

To use alphaMELTS in our calculations, we constructed a look-up table of

melt fraction and temperature as a function of depth and mantle temperature. In the

example provided in the Appendix, we use the isentropic mode of alphaMELTS, which assumes continuous melting with a retained melt fraction of 1%. We start with the chemical composition of depleted MORB mantle (DMM) derived by *Workman and Hart* [2005]. For each mantle potential temperature, we increase depth until the mantle is solid and initiate isentropic decompression, recording the melt fraction and temperature at each depth. For each sampling point of the numerical model, we take the temperature and pressure into the look-up table to find the corresponding melt fraction. Besides melt fraction, alphaMELTS outputs a rich collection of results, including the major and trace element composition of the solid and the liquid, abundance and composition of mineral phases, and the physical properties of all phases present, which can also be stored in the look-up table and used to evaluate the chemical properties of the magma (the function of tracking chemical species is not included in the current version of MeltMigrator).

2.3.3 Permeability Barrier Sampling and Characterization

A critical aspect of the three-step melt migration procedure adopted here is the involvement of a permeability barrier at the base of thermal boundary layer [*Sparks and Parmentier*, 1991; *Montési et al*., 2011]. The barrier forms a lid to the upward melt migration zone and will be referred interchangeably as the permeability barrier or the lid. The permeability barrier appears where the melt crystallizes rapidly [*Korenaga and Kelemen*, 1997] and is often associated with the multiple saturation point of pyroxene and plagioclase [*Kelemen and Aharonov*, 1998; *Hebert and Montési*, 2010].

The permeability barrier forms a two-dimensional surface embedded in the three-dimensional temperature field. The determination of the barrier is done by a stand-alone function `lidSample`. First, a sampling grid is overlain on the computational domain (sampling resolution information is stored in structure `Res`). A depth-sampling vector is devised with a finer sampling spacing at shallower depth, where the permeability barrier is most likely located. For each grid point, the temperature in the sampling column is obtained by interpolating the temperature data imported from the numerical model (e.g., using `mphinterp` for COMSOL Multiphysics® models or MATLAB® function `scatteredInterpolant` for models constructed with other software). The temperature at which the lid is formed is defined as the solution to a user-defined function `lidTemperature`, which is set by default to

$$T_{lid} = 1240 + 1.9z \qquad (2.2)$$

where T_{lid} is expressed in °C and z in km, following *Montési and Behn* [2007] and *Hebert and Montési* [2010]. This equation represents approximately the locus of plagioclase/pyroxene multiple saturation during basalt crystallization [*Kelemen and Aharonov*, 1998], with the effects of pressure [*Yang et al.*, 1996] incorporated. The depth of permeability barrier in each sampling column is then solved using `lidDepth` (by default, `lidDepth` uses the MATLAB® equation solver `fzero`). The *x*, *y*, and *z* coordinates, the temperature at the permeability barrier, barrier slope, and the horizontal gradients of the slope are calculated and stored in the MATLAB® structure `Lid`. The `Lid` structure is then saved in .mat format and called again later by several additional routines.

2.3.4 Melt Trajectory Tracking and Melt Swath Discretization

Melt is assumed to travel upward along the slope of the lid until it either (1) enters a melt extraction zone or (2) the slope of the lid drops below a critical value. Details on the definition of the melt extraction zone and its relation to the critical slope are given by *Montési et al.* [2011] and *Bai and Montési* [2015].

To simulate melt transport along the lid, we discretize the permeability barrier into contiguous swaths separated by melt transport lines that follow the local direction of maximum slope [*Magde and Sparks*, 1997]. Melt cannot cross these lines and all the melt produced beneath a given swath collects within a restricted portion of the melt extraction zone. To define these swaths more easily, we first analyze the morphology of the lid and define coherent regions, or shoulders, where the melt would collect at a single point if there were no melt extraction zone.

The permeability barrier is a curved surface (Figure 2.1), which by analogy to land topography can be described in terms of summits and depressions. Summits are connected by crests that roughly follow mid-ocean ridge segments and separate mantle domains corresponding to the two divergent plates at the mid-ocean ridge axis [*Montési et al.*, 2011]. Each local elevation minimum along the crest defines a saddle. Starting at each saddle, divides are formed by tracking lines of maximum downhill slope along the lid. The boundary of each shoulder is set by the divides and the portion of the crest between two saddles (Figure 2.1a). All the melt generated underneath the shoulder would collect at the associated summit if left to propagate without limit along the lid.

The function `saddlePreparation` is used to locate saddles, crests, and divides. The user should specify the coordinate of target points near each saddle, preferentially at the center of the offset (transform fault or oblique segments). Alternatively, the user could select target points directly on the lid depth map using MATLAB® function `ginput` (use variable named `Switch_SaddleSelectionByMouse` to switch on). Because discontinuities along the mid-ocean ridge cause the isotherms to deepen, at least one saddle should be defined at each offset. In more complicated settings, more than one saddle may be needed. For example, Figure 2.1a shows that there are two saddles underneath the oblique segment of our demonstration model.

Saddles are defined as flat areas (0 slope) found by integrating a system of partial differential equations that describe how lid slope S_l changes with the horizontal coordinates x, y

$$
\begin{cases}
\dfrac{\partial x}{\partial L} = \dfrac{\frac{\partial S_l}{\partial x}}{\sqrt{\left(\frac{\partial S_l}{\partial x}\right)^2 + \left(\frac{\partial S_l}{\partial y}\right)^2}} \\[4ex]
\dfrac{\partial y}{\partial L} = \dfrac{\frac{\partial S_l}{\partial y}}{\sqrt{\left(\frac{\partial S_l}{\partial x}\right)^2 + \left(\frac{\partial S_l}{\partial y}\right)^2}}
\end{cases}
\tag{2.3}
$$

$$
S_l = \sqrt{\left(\frac{\partial z_l}{\partial x}\right)^2 + \left(\frac{\partial z_l}{\partial y}\right)^2}
\tag{2.4}
$$

where L represents the traveled distance. We use MATLAB®'s `ode45` to solve for this system of equations.

Crests and divides are found by solving similar equations, only focused on depth z_l instead of slope

$$\begin{cases} \dfrac{\partial x}{\partial L} = \dfrac{1}{S_l} \dfrac{\partial z_l}{\partial x} \\ \dfrac{\partial y}{\partial L} = \dfrac{1}{S_l} \dfrac{\partial z_l}{\partial y} \end{cases} \qquad (2.5)$$

To initiate the search, we first define a series of points along a circle centered at the saddle. The deepest point along that circle and the point on the circle directly opposite to it are selected as the starting point for the divides. Similarly, the highest point and the point on the opposite side of the circle are selected as the starting points for the crests. Equation 2.5 is then solved using MATLAB®'s `ode23`.

The resolution of saddle lines is controlled by the integration interval set by the parameter `Res.Saddle` in `setParameters`. To achieve higher accuracy, some options may be added to set up the acceptable error, either relative or absolute. Information describing the saddle points, crests, and divides are stored in structure `Saddle`.

Next, the `meltTrajectorySeed` function defines seeds from which melt trajectories are calculated. Although other strategies may be devised, we find it convenient to take equally spaced seeds along a contour of fixed temperature difference between the maximum temperature and the solidus temperature of the sampling columns (defined as `T_MeltSeed` in `setParameters`). Generally, two sets of seeds, one for each plate, are sufficient for generating melt trajectories (Figure 2.1a, white dots). Seeds are found from starting points identified on the two sides of the model parallel to the spreading direction by integrating a trajectory perpendicular to the temperature gradient using the `ode113` solver. Additional treatment may be needed if dealing with complex geometry.

30

Melt trajectories are generated using function `meltTrajectory`. First, the seeds are separated according to the shoulder that they span using a customized function `lineSegmentIntersect` [*Erdem*, 2010]. Then, trajectories are followed along directions of maximum slope upward and downward from each seed using Equation 2.5 and MATLAB®'s `ode23` solver. To ensure that the full trajectory is covered, a long integration time span is selected, and a fixed number of time steps is used for all the integration. This may result in repeated points at the end of the segment where the gradient is zero. The line segments are truncated to where the coordinates begin to change, by deleting the repeated points. Truncated upslope portion and downslope portions are then combined to form a complete melt trajectory line segment. The resolution of the melt trajectories is controlled by the integration interval set by the user in `setParameters`. The density of melt trajectories is controlled by the spacing of melt seeds, although additional trajectories are automatically generated if none of the seeded trajectories passes close to the saddles that form the corner of the shoulder.

Near the crests of the permeability barrier, where the slope approaches zero, numerical noise may result in unrealistic melt trajectories with abrupt turns over short distances. Some of the lines terminate before reaching the edge of the shoulder, while others extend along the crests for tens of kilometers. This pattern does not reflect the anticipated idealized behavior of the migrating melt (although mantle heterogeneities may perturb the smooth, idealized permeability barrier, and lead to irregular paths for melt migration [e.g., *Katz and Weatherley*, 2012]), but is controlled by the model discretization. This situation may be improved by adjusting the integration properties

31

and reducing the error tolerance at the cost of prolonging the calculation process. Ultimately discretization errors are limited by the input numerical model resolution.

Melt trajectory information, including the coordinates of points on the line and the distance along the line, is stored in structure `Shoulder.Trajectory`. The depth, slope, and temperature along each melt trajectory are interpolated from the corresponding data of the permeability barrier (`Lid` structure), and saved along with the trajectory information. The melt trajectories for the example model are plotted in Figures 2.1b and 2.1c.

The portion of the lid that is defined by two adjacent melt trajectories forms a swath. Melt generated underneath a swath travels upslope along the swath and collects along a segment of the plate boundary associated with the swath. The associated plate boundary segment is identified by connecting the termination of melt trajectories to the nearest points on plate boundaries. Because our interest is in melt migration, we only consider the portion of melt trajectories beneath which melt is generated. Additionally, any portion of melt trajectories deeper than a critical depth (`LidDepthLimit`, default 60 km) is discarded, because the permeability barrier may not develop if crystallization occurs at a great depth [*Hebert and Montési*, 2010].

The function `meltSwath` assembles melt swaths and divides each swath into a predefined number of quadrilaterals. At this point, each melt trajectories may contain a different number of points and is resampled into a fixed number of points so that the quadrilaterals spanning one melt trajectory to the next conform between adjacent swaths. The areas and the center coordinates of quadrilaterals are calculated. The depth and slope of permeability barrier at the center of the quadrilateral are

interpolated from the `Lid` structure. A melting column is defined from the center

point at the surface of each quadrilateral down to the bottom of the model, and

sampled according to a predefined depth sampling vector. At each sampling depth,

the temperature and vertical velocity of the mantle are interpolated from the imported

model data. Melt fraction is calculated using `meltFunction` and integrated over

the entire column. We compute

$$p = \begin{cases} 0 & , \ F < F_c \\ \max\left(v_z \frac{\partial F}{\partial z}, 0\right), & F \geq F_c \end{cases} \tag{2.6}$$

$$f = \int_{z_b}^{z_t} p \, dz \tag{2.7}$$

where p is the melt production rate, F_c is the critical melt fraction representing the

retained melt fraction in the mantle, which is set by the parameter

`MeltFractionCutoff` in `setParameters`, f is the melt flux, and z_t is the

minimum depth of the melting column [*McKenzie*, 1985]. This calculation assumes

that melt generated in the melting columns rises vertically, as expected from the latest

estimates of mantle permeability [*Miller et al.*, 2014]. Migration along the

permeability barrier is simulated by summing the melt flux in all quadrilaterals along

each swath in the direction of melt migration toward the plate boundary. The swath

and quadrilateral information are stored in structure `Shoulder.Swath` for later

use.

2.3.5 Melt Extraction and Crustal Thickness Calculation

Crustal thickness calculation is conducted in the `crustCalculation`

script. First, the thickness of crust accreted along the plate boundary (Figure 2.2a) is

calculated by the `meltExtraction` function. As described in *Montési et al.*

[2011], we defined a Melt Extraction Zone (MEZ) along plate boundaries and assume that all melt that enters the MEZ is extracted to the nearest plate boundary. The MEZ may be associated with structural damages such as diking and fracturing in the brittle lithosphere and the ductile shear zones at greater depth [*Nicolas*, 1986, 1990; *Kelemen et al.*, 1992; *Kelemen and Dick*, 1995; *Macdonald et al.*, 1996; *Perfit et al.*, 1996; *Hebert and Montési*, 2011; *Kaczmarek and Tommasi*, 2011; *Bai and Montési*, 2015]. We simplify the MEZ as a box extending from the plate boundaries to an extraction width of d_e and an extraction depth of z_e (Figure 2.1c). Second, in the `crustalHistory` function, crustal thickness is advected following plate motion to generate a map of crustal thickness (Figure 2.2b) over the entire computational domain [*Bai and Montési*, 2015].

Melt extraction in the model is controlled by three parameters: s_e (`ExtractionSlope`), d_e (`ExtractionWidth`), and z_e (`ExtractionDepth`). Starting with the deepest quadrilateral in a swath, the function `extractionDetermination` determines if the current quadrilateral is located in the MEZ. If it is, the melt contained in that quadrilateral is assigned to the nearest plate boundary segment. If not, the melt moves onto next quadrilateral in the swath, but only if slope of the lid is larger than s_e. Otherwise the melt in that quadrilateral is trapped and refertilizes the ambient mantle, forming what we term cryptic crust. Following *Bai and Montési* [2015], we recommend using 4 km, 20 km and 0.1 for `ExtractionWidth`, `ExtractionDepth`, and `ExtractionSlope`, respectively. The MEZ can be switched off by setting the value of
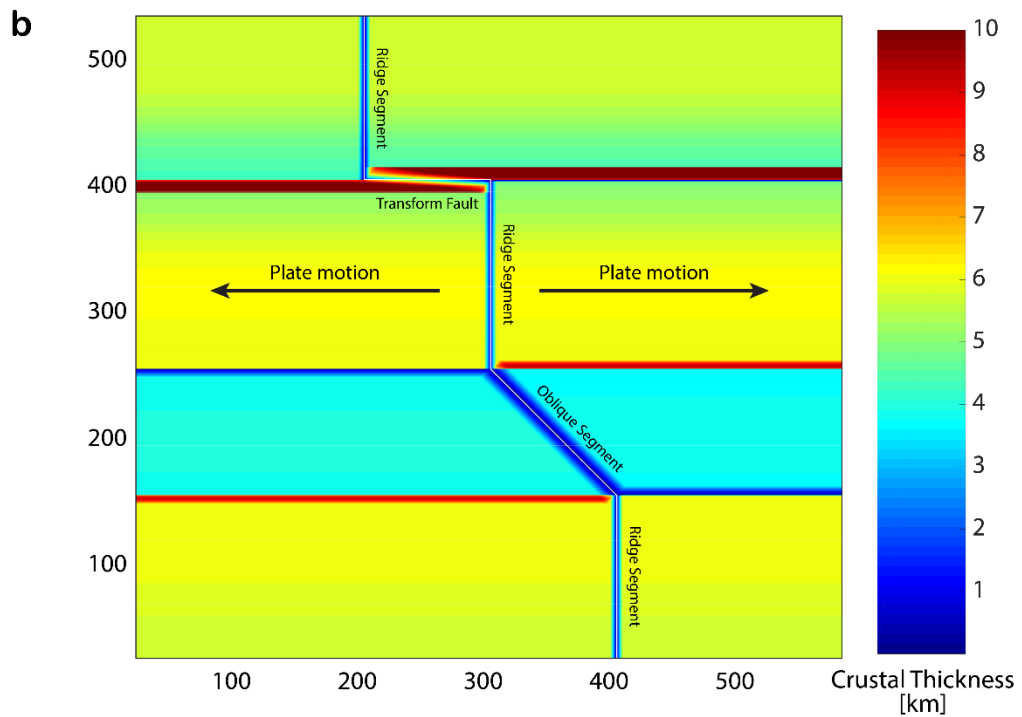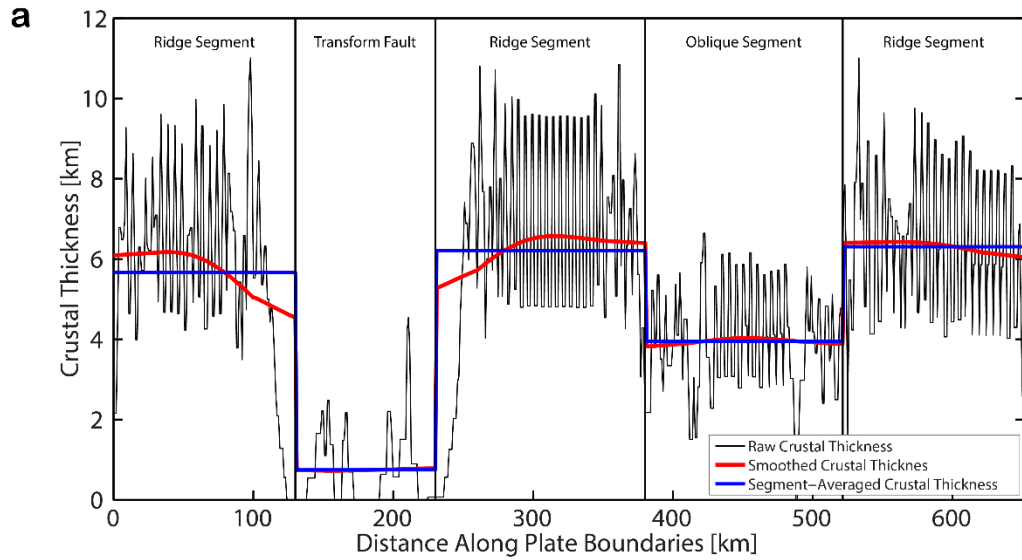
Figure 2.2 a) Crustal thickness profile along plate boundary segments (labeled) for the example model. Thin black line shows unfiltered crustal thickness. The red line shows smoothed crustal thickness with a smoothing width of 60 km. The blue line shows the average crustal thickness within each plate boundary segment. b) Map view of crustal thickness distribution over seafloor in the example model. Spreading directions and plate boundary segments are labeled.

`ExtractionWidth` to `NaN`, in which case melt can only get to the surface when it reaches a ridge segment.

The quadrilaterals within the MEZ are projected onto the nearest plate boundary segment. That projection spans a length L_d of the plate boundary and serves as the destination of the melt collected in that quadrilateral. We predefine points along the plate boundary and track the thickness of melt accumulated at each point. If a point is within the receiving segment of a quadrilateral, its crustal thickness increases by

$$dH = \frac{f_t A}{2 V_p L_d} \qquad (2.8)$$

where A is the area of the quadrilateral and f_t is the total melt flux at the quadrilateral, due to melting directly below the quadrilateral and transport from deeper quadrilaterals along the swath. We also track the average and maximum melt fraction, the average melting depth, and the thickness of cryptic crust along the swath. After iterating over all the quadrilaterals and all the swaths, we obtain a profile of melt delivery, expressed as a crustal thickness, along the plate boundary (Figure 2.2a).

Model discretization often results in short-wavelength noise in the crustal thickness profile (Figure 2.2a). To reduce this numerical artifact, we smooth the profile using the function `fastSmooth`, [*O'Haver*, 2008]. It filters the data (e.g., crustal thickness, average melt fraction, etc.) in each plate boundary segment separately, with three passes of a sliding boxcar average over a smoothing width L_f (`SmoothingWidth`). The smoothing width decreases progressively close to the edges of the segment, but gets no smaller than $L_f/2$. The treatment removes short-wavelength noise but preserves larger-scale anomalies associated with the changes in

plate boundary type and geometry (Figure 2.2a). The smoothing step can also be interpreted as representing redistribution of melt at crustal level and is therefore conducted segment by segment. The smoothing width L_f can be regarded as the distance of lateral dike propagation in the crust. A value of ~50 km is geologically plausible [*Fialko and Rubin*, 1998].

The distribution of crustal thickness throughout the computational domain can be inferred from the crustal accretion profile along plate boundaries, assuming the newly formed crust is advected in the direction of spreading. For convenience, we reorient the plate boundaries such that the spreading direction is parallel to the x axis. After reorientation, we set up a new model boundary around the plate boundaries, leaving sufficient space to cover the original model. The new model geometry is then gridded into rectangular tiles.

Initially, the crustal thickness in each tile is set to 0. If a tile is within an accretion width d_a of a plate boundary, we add to its crustal thickness the thickness of crust accreted to the axis, scaled by the ratio between the tile width and the accretion width. The accretion width is typically different from the width of the MEZ, as the extracted (erupted) melt is mobile and may travel for some distance on the seafloor, in surface lava flows, lava tubes, or otherwise [*Chadwick and Embley*, 1994; *Sinton et al.*, 2002; *Smith and Cann*, 1999]. The width of the accretion zone can be set to different values at spreading centers and transform faults using the `AccretWidth_Ridge` and `AccretWidth_Transform` parameters. Each tile may collect melt accreted at several plate boundary segments.

Finally, starting from the tiles at the plate boundaries, the crustal thickness in each tile is carried onto the next tile in the spreading direction. A map of seafloor crustal thickness is produced as the output (Figure 2.2b). The script further calculates and reports the average crustal thickness within the ridge domain, the transform fault domain, the oblique segment domain, and the whole domain as diagnostics.

2.4 User Workflow

The user interacts with the software principally by adjusting parameters in the `setParameter` script. In principle, it is possible to specify all the required parameters and let the code run. However, it is often useful to check outputs at intermediate steps and adjust the necessary parameters.

In our experience, the following user workflow leads to the best results. First, edit `setParameter`. The user should specify the name of the pre-existing model, the geometry of the model bounding box and the plate boundary, then run `meltMain` through the cell labeled "Lid Sampling." This step extracts the lid information and produces plots of lid topography. Based on the graphical output, the user should specify the starting points for the saddle (variable `SaddleInitialPoint` in `setParameter`). If desired, adjust the remaining parameters in `setParameter`, which control the choice of melting function, the type of calibration, and the resolution of the lid tessellation and crustal thickness calculation. The user can then run `meltMain` to completion.

2.5 Conclusions

The MeltMigrator software processes three-dimensional mantle temperature and velocity data imported from external numerical models and returns melt migration trajectories, melt flux along plate boundaries, and crustal thickness distribution of the seafloor, with options of calculating mantle melting using thermodynamic models. It treats melt generation and migration as processes independent of mantle convection, and therefore is capable to handle three-dimensional mid-ocean ridge models with complex settings such as oblique segment, asymmetrical spreading, background mantle flow, and ridge-plume interaction, although compaction is represented only approximately. The software provides results that can be compared with gravity, seismic, and topographical data sets collected at mid-ocean ridges and may help users to gain insight into the melt migration and crustal accretion processes in their target regions.

The code is flexible and can be applied to mid-ocean ridge models constructed in various codes or software environments. Programmed in a modular manner, the routine can be easily tweaked or replaced based on users' need. With proper modification, it may be extended to other divergent systems such as rift zone and back-arc spreading center, and subsurface fluid migration in nondivergent settings.

Chapter 3: Slip-rate dependent melt extraction at oceanic transform faults

Abstract

Crustal thickness differences between oceanic transform faults and associated mid-ocean ridges may be explained by melt migration and extraction processes. Slow-slipping transform faults exhibit more positive gravity anomalies than the adjacent spreading centers, indicating relative thin crust in the transform domain, whereas at intermediate-spreading and fast-spreading ridges transform faults are characterized by more negative gravity anomalies than the adjacent spreading centers, indicating thick crust in the transform domain. We present numerical models reproducing these observations and infer that melt can be extracted at fast-slipping transforms, but not at slow-slipping ones. Melt extraction is modeled as a three-step process. (1) Melt moves vertically through buoyancy-driven porous flow enhanced by subvertical dissolution channels. (2) Melt accumulates in and travels along a decompaction channel lining a low-permeability barrier at the base of the thermal boundary layer. (3) Melt is extracted to the surface when it enters a melt extraction zone. A melt extraction width of 2–4 km and a melt extraction depth of 15–20 km are needed to fit the tectonic damages associated with oceanic plate boundaries that reach into the upper mantle. Our conclusions are supported by the different degrees of magmatic activities exhibited at fast-slipping and slow-slipping transforms as reflected in geological features, geochemical signals and seismic behaviors. We also

constrain that the maximum lateral distance of crust-level dike propagation is about 50–70 km.

3.1 Introduction

Oceanic transform faults commonly offset mid-ocean ridges, and influence the thermal structure of spreading centers and the associated melt generation [*Parmentier and Forsyth*, 1985; *Langmuir and Bender*, 1984; *Phipps Morgan and Forsyth*, 1988; *Gregg et al*., 2009; *Roland et al*., 2010; *Hebert and Montési*, 2011]. Transform faults are generally assumed to be magma-poor, as conductive cooling from the adjacent old, cold lithosphere across the transforms may efficiently reduce mantle temperature and melt production beneath the transforms [*Fox and Gallo*, 1984; *Shen and Forsyth*, 1992]. However, evidence of volcanism has been discovered at several transform faults. Ophiolite complexes in Cyprus reveal diking activities in a transform fault setting [*Murton and Gass*, 1986]. Basaltic lavas were recovered from basins in the Blanco transform at the intermediate-spreading Juan de Fuca Ridge [*Gaetani et al*., 1995], and the Garrett and Siqueiros transforms at the fast-spreading East Pacific Rise [*Hékinian et al*., 1992; *Perfit et al*., 1996]. We explore here the conditions under which melt may be extracted at oceanic transform faults and how this is related to the crustal thickness inferred from Residual Mantle Bouguer Anomalies (RMBA)

A recent compilation of RMBA from 19 oceanic ridge-transform systems [*Gregg et al*., 2007] suggests that crustal accretion is taking place along transforms but only at fast-spreading and intermediate-spreading mid-ocean ridges. At slow-spreading mid-ocean ridges, transform faults exhibit more positive gravity anomalies

41

than the associated spreading centers. By contrast, at intermediate-spreading and fast-spreading ridges, transform faults are characterized by more negative gravity anomalies than the adjacent spreading centers [*Gregg et al.*, 2007]. Gravity anomalies reflect density variations that may result from variations in rock porosity, alteration, crustal thickness, or mantle diapirism and melting. Since the most negative anomalies are not located in the transform troughs, where porosity and alteration are expected to be the highest, the RMBA differences between transforms and ridges are interpreted as consequences of crustal thickness variations: the crust at intermediate-slipping and fast-slipping transforms is thicker than at the adjacent ridge, implying active magmatism at these transforms. By contrast, no thickening is observed at slow-slipping transforms, consistent with focused mantle upwelling at slow-spreading ridges [*Lin et al.*, 1990; *Gregg et al.*, 2007; *Gregg et al.*, 2009].

Several mechanisms have been proposed to explain volcanic activity at transform faults, including: (1) "leaky" transform faults [*Menard and Atwater*, 1969]; (2) intratransform spreading centers (ITSCs) [*Fornari et al.*, 1989; *Gregg et al.*, 2009]; and (3) three-dimensional migration of melt toward the transform faults [*Karson et al.*, 2002; *Hebert and Montési*, 2011]. "Leaky" magmatism is induced by transtensional forces from plate reorientation on a transform fault [*Menard and Atwater*, 1969]. It has been invoked to account for magma extrusion and intrusion in the transform troughs [e.g., *Thompson and Melson*, 1972; *Murton and Gass*, 1986; *Hékinian et al.*, 1992], but it does not explain the excess crust at the Clipperton transform [*Gregg et al.*, 2007], which is under transpression [*Pockalny*, 1997]. Several ITSCs have been sampled and contain young volcanic rocks [e.g., *Fornari et*

al., 1989]. Related crustal accretion is likely to contribute to thickened crust in the fast-slipping transform domains [*Gregg et al*., 2009], but basaltic lavas are also recovered from transform valleys away from ITSCs [*Perfit et al*., 1996; *Tepley et al*., 2004], suggesting that ITSCs alone cannot explain all of the volcanism in transforms. Recent numerical models incorporating a temperature-dependent mantle viscosity with a viscous-plastic approximation for brittle failure generate enhanced mantle upwelling beneath areas with high strain rate, like transforms [*Behn et al*., 2007; *Roland et al*., 2010]. This enhanced upwelling induces elevated temperature and thin lithosphere, which may promote melt transport toward the transform faults.

While the mechanisms mentioned above are not mutually exclusive, we focus here on the effects of three-dimensional melt migration beneath ridge-transform systems. At mid-ocean ridges, melt is generated by decompression of the mantle that rises in response to the divergence of plates. Subsequent extraction of melt can be modeled as a three-step process [*Sparks and Parmentier*, 1991; *Montési et al*., 2011; *Gregg et al*., 2012]: (1) Melt moves vertically through buoyancy-driven porous flow enhanced by subvertical dissolution channels [e.g., *Kelemen et al*., 1997]. (2) Melt accumulates in and travels along decompaction channels associated with a permeability barrier at the base of thermal boundary layer [*Sparks and Parmentier*, 1991; *Spiegelman*, 1993; *Hebert and Montési*, 2010] generally sloping toward the ridge axes. (3) Melt is extracted to the surface when it enters a melt extraction zone [*Ghods and Arkani-Hamed*, 2000]. The melt extraction zone probably reflects structural damage related to the tectonic activities at the plate boundary [*Montési et al*., 2011]. It may be present at both ridge and transform segments of oceanic

spreading centers [*Hebert and Montési*, 2011]. However, the width and depth of melt extraction zone remain poorly constrained.

To explain the thickened crust and active magmatism at fast-slipping transforms, and the absence of magmatism at slow-slipping transforms, we hypothesize that, at fast-spreading ridges, the melt extraction zone intersects the permeability barrier beneath the transform fault and magma erupts along the transform, resulting in thickened crust in the transform domain; at slow-spreading ridges, the permeability barrier is too deep to intersect the melt extraction zone beneath the transform domain, resulting in little magmatic activity and thin crust along the transform fault. This hypothesis is evaluated using numerical models of the three-dimensional mantle flow and thermal structure of segmented ridges and the associated pattern of melt migration, focusing, and crustal accretion.

3.2 Model Setup

The oceanic crustal thickness is regarded as a direct indicator of melt delivery along mid-ocean ridges and transform faults. We predict crustal thickness variations at ridge-transform-ridge systems using three-dimensional numerical models of melt migration, and provide new constrains on the melt extraction processes at segmented mid-ocean ridges.

Mantle flow and the thermal structure beneath each ridge-transform system are solved using the commercial finite element software COMSOL Multiphysics® 4.3, which has been benchmarked for nonlinear temperature-dependent flow in geological systems [*van Keken et al.*, 2008]. For a transform with length *L*, the

44

computation domain is 3×L long, 2×L wide and 100 km deep, with orthogonal

segments of length L representing the simplified geometry of the ridge-transform-

ridge system (Figure 3.1). Half-spreading rates are imposed on the two plates on top

of the domain. Temperature on top is assumed to be 0°C, and a mantle temperature of

1375°C is imposed on the bottom. The bottom and side boundaries are set to be

stress-free and open to mantle upwelling and convective flux.

A triangular mesh is defined on the top surface of the model. The element size

is variable, with a maximum size of 10.5 km, and refined at the plate boundaries

where the minimum element size is less than 6 km. The mesh is extruded vertically

with layer spacing varying from 2.5 km near the surface to ~6 km at the bottom. This

mesh resolution has been tested to be sufficiently fine as not to affect the model

solutions, while keeping the computational cost at acceptable level.

Using the configuration described above, we tested nine transform fault

systems (Table 3.1), with transform length ranging from 70 to 160 km, and half-slip

rate ranging from 1.1 to 7.45 cm/yr. The difference in RMBA data between the

transform faults and adjacent ridge segment (ΔRMBA$_{T-R}$) are given by *Gregg et al.*,

[2007], and will be used to constrain the model input parameters.

Conservation of mass, momentum and energy are expressed by:

$$\nabla \cdot \mathbf{V} = 0 \tag{3.1}$$

$$\nabla P = \nabla \cdot [\eta(\nabla \mathbf{V} + (\nabla \mathbf{V})^{\mathrm{T}})] \tag{3.2}$$

$$\rho c_p (\mathbf{V} \cdot \nabla)T = \nabla \cdot (k\nabla T) \tag{3.3}$$

where $\mathbf{V}$ is the mantle velocity field, ρ is the density of mantle, η is the mantle

viscosity, c_p is the heat capacity, k is the thermal conductivity, P is the pressure, and
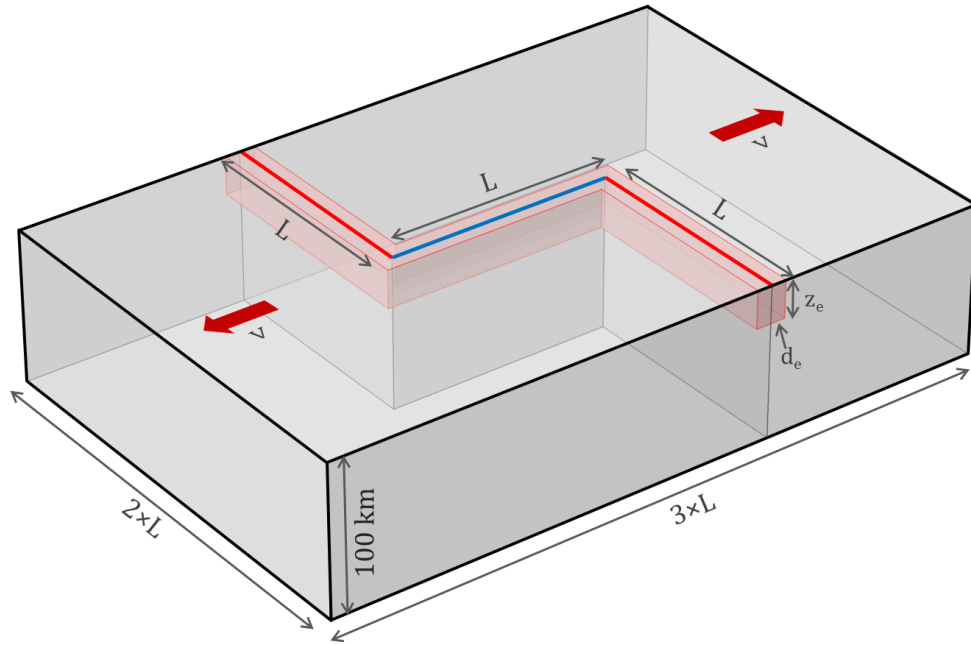
Figure 3.1 Model geometry of a generic ridge-transform-ridge system. The orthogonal segments on top represent ridge axes (red), and the transform fault (blue). The length of each segment is L. The computation domain is $3 \times L$ long, $2 \times L$ wide and 100 km deep. Half-spreading rates are imposed on top of the two plates separated by the segments (dark red arrows). The red box denotes the melt extraction zone around the plate boundaries, with a width of d_e and a depth of z_e.

Table 3.1 Characteristics of the transform faults modeled in this study. Expected crustal thickness differences ΔH are calculated from the difference of residual mantle Bouguer anomaly between the transform and the ridge ($\Delta RMBA_{T-R}$) assuming an oceanic crust density of 2700 kg/m^3 and a mantle density of 3300 kg/m^3 [*Wang et al.*, 2011].

Transform Fault	Ridge System[1]	Approximate Latitude	Half-Slip Rate [cm/yr]	Length [km]	$\Delta RMBA_{T-R}$ [mGals] [2]	ΔH [km]
Garrett	EPR	12°S	7.45	130	-6.0	0.24
Wilkes	EPR	8°S	7.25	100	-7.7	0.31
Siqueiros	EPR	8°N	5.9	150	-13.6	0.54
Clipperton	EPR	10°N	5.75	90	-3.6	0.14
SEIR 1	SEIR	48°S	3.77	135	-8.2	0.33
SEIR 2	SEIR	50°S	3.72	80	-13.2	0.53
Kane	MAR	24°N	1.25	160	6.6	-0.26
Atlantis	MAR	30°N	1.2	70	35.4	-1.41
Hayes	MAR	34°N	1.1	90	13.7	-0.55

[1] EPR: East Pacific Rise; SEIR: South-East Indian Ridge; MAR: Mid Atlantic Ridge
[2] from *Gregg et al.* [2007]

T is the temperature. The variables and parameters used in this study are compiled

with units and values in Table 3.2. This set of equations describes the mantle as an

incompressible material, and neglects the thermal and mechanical effects of melting

and related mantle porosity. Density is constant throughout the model. Therefore, we

ignore the possibility of buoyancy-driven upwellings and focus on plate-driven flow.

Although upwellings may play an important role at the slower ridges, we will see that

this approach is sufficient to explain the global pattern of crustal thickness differences

between spreading centers and transform faults.

Mantle viscosity has a significant impact on mantle flow and the temperature

field. We adopt the temperature-dependent viscosity with a viscoplastic

approximation for brittle weakening following *Behn et al*. [2007] and *Roland et al*.

[2010]:

$$\eta = \min(\eta_T, \eta_Y) \tag{3.4}$$

$$\eta_T = \eta_0 \exp\left[\frac{Q}{R}\left(\frac{1}{T} - \frac{1}{T_m}\right)\right] \tag{3.5}$$

$$\eta_Y = \frac{C_0 - \mu\rho g z}{\sqrt{2}\dot{\varepsilon}_{II}} \tag{3.6}$$

where η_T is the temperature-dependent viscosity, η_Y is the effective viscosity

associated with brittle failure [*Chen and Morgan*, 1990], η_0 is the reference viscosity,

Q is the activation energy, R is the gas constant, T_m is the mantle temperature, C_0 is

the cohesion, μ is the friction coefficient, g is the gravity acceleration, z is the depth,

and $\dot{\varepsilon}_{II}$ is the second invariant of the strain rate tensor. Incorporating this viscoplastic

rheology reduces the effective viscosity and induces mantle upwellings in areas with

high strain rate such as the transform domain, leading to elevated temperature and

Table 3.2 Parameters and variables used in the study.

Name	Symbol	Value	Unit	Equation
Coordinates	x, y, z		km	
Transform length	L	50 – 350	km	
Mantle velocity	$\mathbf{V}$		cm·yr^{-1}	(3.1) (3.2) (3.3)
Pressure	P		Pa	(3.2)
Temperature	T		°C	(3.3) (3.5) (3.7) (3.10)
Gravity	g	9.8	m·s^{-2}	(3.6)
Mantle density	ρ	3300	kg·m^{-3}	(3.2) (3.3) (3.6)
Effective viscosity	η		Pa·s	(3.2) (3.4)
Viscosity (ductile process)	η_T		Pa·s	(3.4) (3.5)
Viscosity (brittle process)	η_Y		Pa·s	(3.4) (3.6)
Reference viscosity	η_0	10^{19}	Pa·s	(3.5)
Activation energy	Q	250	kJ·mol^{-1}	(3.5)
Gas constant	R	8.314	J·mol^{-1}·K^{-1}	(3.5)
Mantle potential temperature	T_m	1375	°C	(3.5)
Cohesion	C_0	10	MPa	(3.6)
Friction coefficient	μ	0.6	No dimension	(3.6)
Second invariant of the strain rate tensor	$\dot{\varepsilon}_{II}$		s^{-1}	(3.6)
Specific heat capacity	c_p	1250	J·kg^{-1}·K^{-1}	(3.3)
Effective thermal conductivity	k		W·m^{-1}·K^{-1}	(3.3) (3.7)
Reference thermal conductivity	k_0	3	W·m^{-1}·K^{-1}	(3.7)
Nusselt number	Nu	8	No dimension	(3.7)
Smoothing factor	A	0.75	No dimension	(3.7)
Maximum temperature of hydrothermal circulation	T_{cut}	600	°C	(3.7)
Maximum depth of hydrothermal circulation	z_{cut}	6	km	(3.7)
Temperature of permeability barrier	$T_{barrier}$		°C	(3.8)
Width of melt extraction zone	d_e	2 – 8	km	
Depth of melt extraction zone	z_e	10 – 40	km	
Crustal redistribution length	L_f	10 – 70	km	
Crustal thickness	H		km	(3.9)
Crustal thickness difference	ΔH		km	(3.12) (3.13)
Half-spreading rate	V_p	1.0 – 7.5	cm·yr^{-1}	(3.9)
Distance along melt trajectories	x_m		km	(3.9)
Length of a melt trajectory	x_{ml}		km	(3.9)
Melt flux	f		km·yr^{-1}	(3.9) (3.10)
Bottom of the melting column	z_b		km	(3.10)
Top of the melting column	z_t		km	(3.10)
Melt production rate	p		yr^{-1}	(3.10) (3.11)
Melt fraction	F		%	(3.11)
Critical melt fraction	F_c	1	%	(3.11)
Relative standard deviation	σ		km	(3.12)
Degree of constrains	ν	15	No dimension	(3.13)

increased melt supply beneath the transform domain [*Behn et al*, 2007].

The thermal structure of mid-ocean ridges is influenced by the hydrothermal circulation of seawater in the cold brittle crust [*Sinha and Evans*, 2004]. As the properties and dynamics of the circulating seawater are poorly constrained [e.g., *Fontaine and Wilcock*, 2007], we adopted the simplified model, originally proposed by *Phipps Morgan et al.* [1987] and *Phipps Morgan and Chen* [1993], that captures the effect of hydrothermal circulation as an enhanced thermal conductivity. Here we used the parameterization of *Phipps Morgan and Chen* [1993] where hydrothermal circulation is limited to temperatures less than $T_{cut} = 600°C$ and depth less than $z_{cut} =$ 6 km and where thermal conductivity decreases exponentially with increasing depth and temperature:

$$k = k_0 + k_0(\text{Nu} - 1) \exp\left[A\left(1 - \frac{T}{T_{cut}}\right)\right] \exp\left[A\left(1 - \frac{z}{z_{cut}}\right)\right] \Big/ \exp(2A) \quad (3.7)$$

where k_0 is the reference thermal conductivity, Nu is the Nusselt number, and A is a smoothing factor.

After the mantle flow and thermal structure of the model are solved using COMSOL Multiphysics®, data are exported to MATLAB® to investigate melt trajectory. The extent of melting is a function of temperature, pressure, and the chemical composition of mantle [*Grove et al.*, 1992; *Langmuir et al.*, 1992]. Here we assume equilibrium batch melting and use the nonlinear anhydrous melting functions proposed by *Katz et al.* [2003], which includes the change of melting rate due to the exhaustion of pyroxene.

After melt is generated, it segregates from the residual solids through porous flow and/or channelized flow [e.g., *Kelemen et al.*, 1997]. The rate of melt migration

depends on the permeability of the upper mantle [e.g., *Zhu and Hirth*, 2003; *Zhu et al.*, 2011]. A recent experimental quantification of mantle permeability using three-dimensional X-ray microtomography leads to an estimation of melt transport velocity in the order of 1 m/yr [*Miller et al.*, 2014]. Since the crustal thickness is not directly affected by the melt transport velocity, we ignored the variations in rate of melt migration, and assume melt moves vertically uniformly through mantle before getting to the base of thermal boundary layer, where rapid crystallization of melt facilitates the formation of a permeability barrier [*Sparks and Parmentier*, 1991]. The permeability barrier develops when the decompaction time scale of mantle exceeds the crystallization time scale of melt [*Korenaga and Kelemen*, 1997]. It is associated to the multiple saturation point of plagioclase and pyroxene [*Kelemen and Aharonov*, 1998; *Hebert and Montési*, 2010]. The temperature of the permeability barrier is given approximately by *Montési and Behn* [2007]:

$$T_{\text{barrier}} = 1240°\text{C} + 1.9z \qquad (3.8)$$

where T_{barrier} is the temperature of permeability barrier and z is depth below seafloor in kilometers. Subcrustal reflectors possibly corresponding to the permeability barrier have been recently seismically detected along East Pacific Rise (EPR) at the predicted depth [*Arnoux and Toomey*, 2013].

As the pore space above the permeability barrier is closed, melt accumulates in a decompaction channel that develops at the base of the barrier [*Sparks and Parmentier*, 1991; *Spiegelman*, 1993]. Melt then moves along the barrier toward the ridge axis, where the barrier is shallowest. Fertile heterogeneities in the mantle may perturb the decompaction channel and lead to melt pooling at the base of the

lithosphere away from ridge axis [*Katz and Weatherley*, 2012]. We neglect this effect

as the amplitude and spatial distribution of mantle heterogeneities is poorly

constrained. Since we assume that melt is driven by its buoyancy, melt migration

along the permeability barrier will follow the direction of maximum slope [*Magde*

and Sparks, 1997], which, in our models focus melt to the ridge axes. Some melt

travels laterally to a different ridge segments other than the one closest to where melt

was generated. Along the way, it may travel underneath the transform fault, as

illustrated in Figure 3.2 [*Weatherley and Katz*, 2010; *Hebert and Montési*, 2011].

A melt extraction zone (MEZ), where melt is able to penetrate the

permeability barrier and get extracted to the surface [*Montési et al*., 2011] is defined

around the plate boundaries near the surface. Physically, the MEZ may be associated

with the structural damages in the cold, brittle lithosphere, but as we will see, it needs

to extend to greater depths. Field observations indicate that diking and fracturing

present at mid-ocean ridges and transform faults are possible mechanisms for the melt

extraction [*Nicolas*, 1986, 1990; *Kelemen and Dick*, 1995; *Macdonald et al*., 1996;

Perfit et al., 1996]. Transport along melt-impregnated ductile shear zones [*Kelemen et*

al., 1992; *Kaczmarek and Tommasi*, 2011] may play a role at greater depth. We

assume here that the MEZ extends from the plate boundaries to an extraction width of

d_e, and an extraction depth of z_e (Figure 3.1). Both parameters are poorly constrained

and have been varied systematically in this study. Melt entering MEZ is directly

extracted to the surface and accretes to the nearest plate boundary, contributing to the

crustal thickness. We assume the MEZ is present along the entire plate boundary

system, including transform faults.
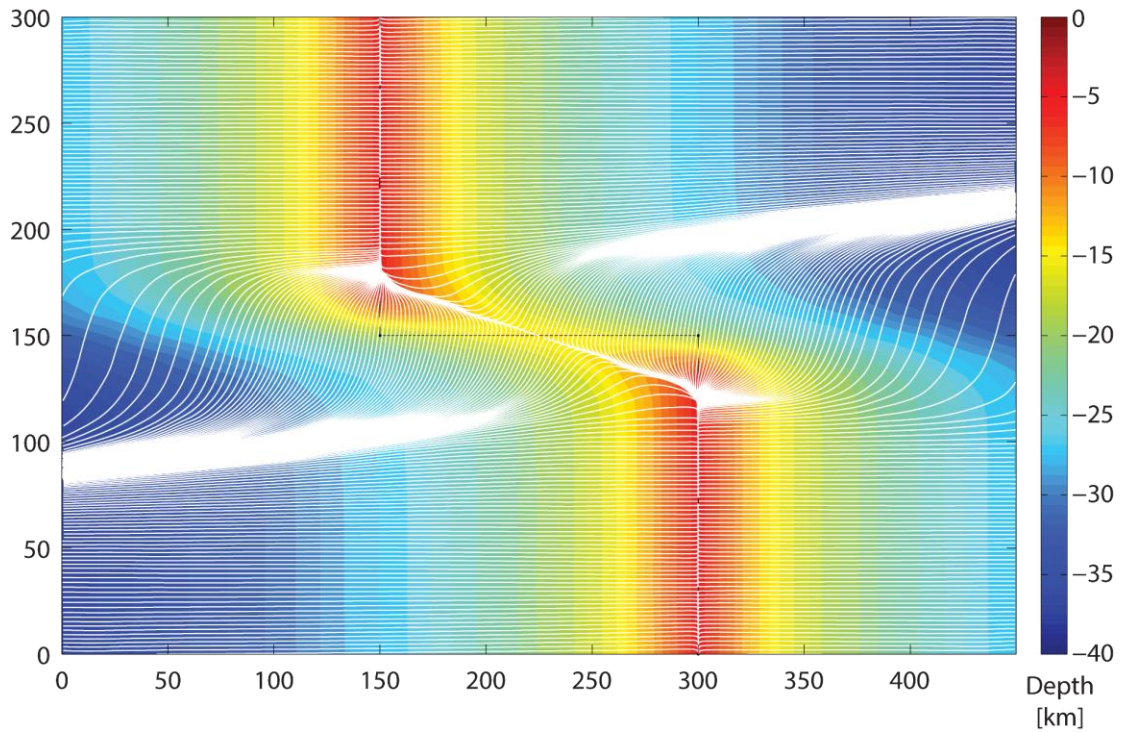
Figure 3.2 Map of the depth of permeability barrier in the computation domain for the fast-slipping Siqueiros transform (half-slip rate: 5.9 cm/yr, transform length: 150 km). White lines are the trajectories of melt along the barrier. If melt extraction is ignored, some of the melt travels laterally underneath the transform fault to a different ridge segment.

Crustal accretion along the plate boundaries is calculated using the following

equations [*Montési et al.*, 2011]:

$$H = \frac{1}{2V_{\text{half}}} \int_0^{x_{ml}} f \, dx_m \tag{3.9}$$

$$f = \int_{z_b}^{z_t} p \, dz \tag{3.10}$$

$$p = \begin{cases} 0 & , \ F < F_c \\ \max(v_z \frac{\partial F}{\partial z}, 0) , & F \geq F_c \end{cases} \tag{3.11}$$

where H is the crust accretion, defined as the thickness of crust accreted at each

instant along the ridge axis (Figure 3.3), V_{half} is the half-spreading rate, f is the melt

flux, x_m is the distance along melt trajectories, x_{ml} is the length of each melt

trajectory, z_b and z_t are the depth of the bottom and the top of the melting column, p

is the melt production rate, F_c is the critical melt fraction representing the retained

melt fraction in the mantle [*Kelemen et al.*, 1997; *The MELT Seismic Team*, 1998],

and v_z is the velocity of mantle upwelling. Here, we assume $F_c = 1\%$, consistent with

estimates of residual melt fractions in the mantle [*McKenzie*, 1985; *The MELT

Seismic Team*, 1998]. Changing this parameter has only a minor effect on our

calculations.

We applied a smoothing function along the calculated crust accretion profile

to represent horizontal redistribution of melt at crustal level along each segment of

the plate boundary [*Montési et al.*, 2011]. The smoothing is implemented using the

script `fastsmooth` contributed to MatlabCentral. It processes the data with three

passes of a sliding average (boxcar), with a smooth width L_f. We modified the script

so that it handles the edges of the signal (the first $L_f/2$ points and the last $L_f/2$ points)
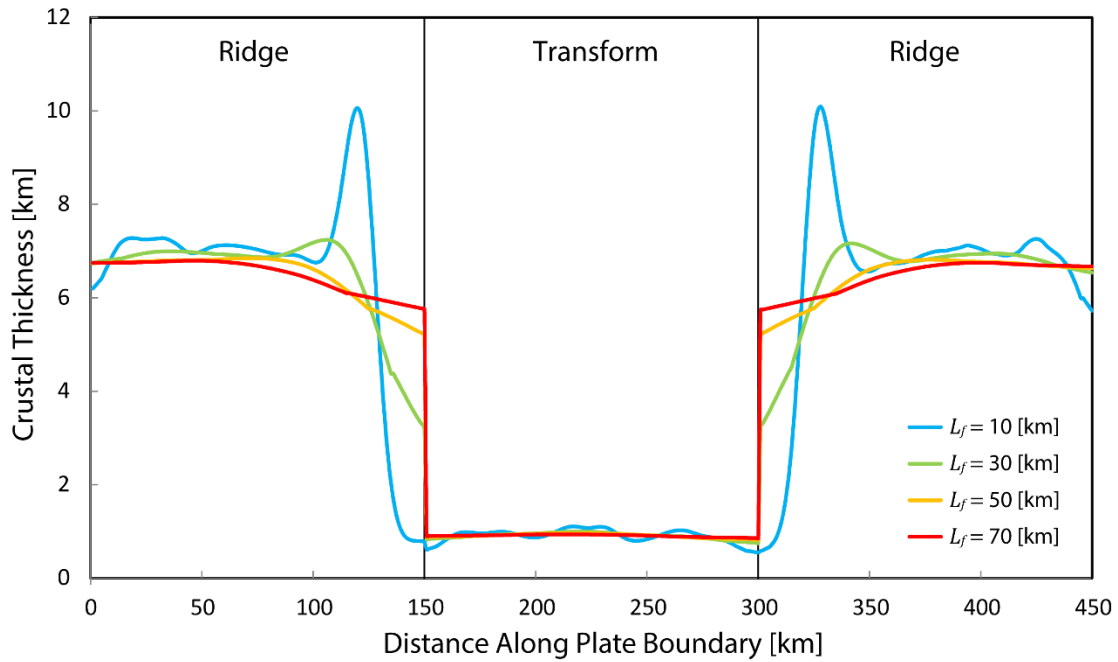
Figure 3.3 Crustal accretion profile for the fast-slipping Siqueiros transform (half-slip rate: 5.9 cm/yr, transform length: 150 km), with an extraction width of 2 km and an extraction depth of 15 km. The three boxes indicate crust accretion along ridge, transform and ridge, respectively. Profiles in different colors correspond to different crustal redistribution length L_f. As L_f increases, the crust is more uniform along the ridge segment, and crustal accretion close to the transform increases.

with progressively smaller smooth width closer to the end, but no smaller than $L_f/2$.

Each segment of the plate boundaries is smoothed separately.

The width of smoothing L_f can be regarded as the distance of lateral dike propagation. We varied this melt redistribution length scale L_f from 10 to 70 km, consistent with geological constrains (see Discussion section 3.4.2 for detail). With increasing L_f, the crust is averaged along the segment, and the crust accretion close to the transform increases (Figure 3.3). As will be discussed to a greater extent later, the degree of magmatism within the transform segment is not sensitive to the variation of L_f. The parameter L_f controls the ridge contribution of crust at transforms. Crustal accretion along the plate boundaries is integrated over time, considering the predefined trajectory of plates away from the ridge axis, to generate maps of crustal thickness over the computation domain (Figure 3.4).

3.3 Results

We modeled nine transform fault systems (Table 3.1), and tested different extraction width d_e, extraction depth z_e, and crustal redistribution length L_f with an idealized ridge-transform-ridge geometry. Each model outputs mantle flow, temperature field, extent of melting, and trajectories of melt along the permeability barrier, and generates maps of crustal thickness over the computation domain. We compiled the model results and studied the influences of spreading rate on the crustal thickness variations.

Two examples of crustal thickness maps are shown in Figure 3.4. The upper
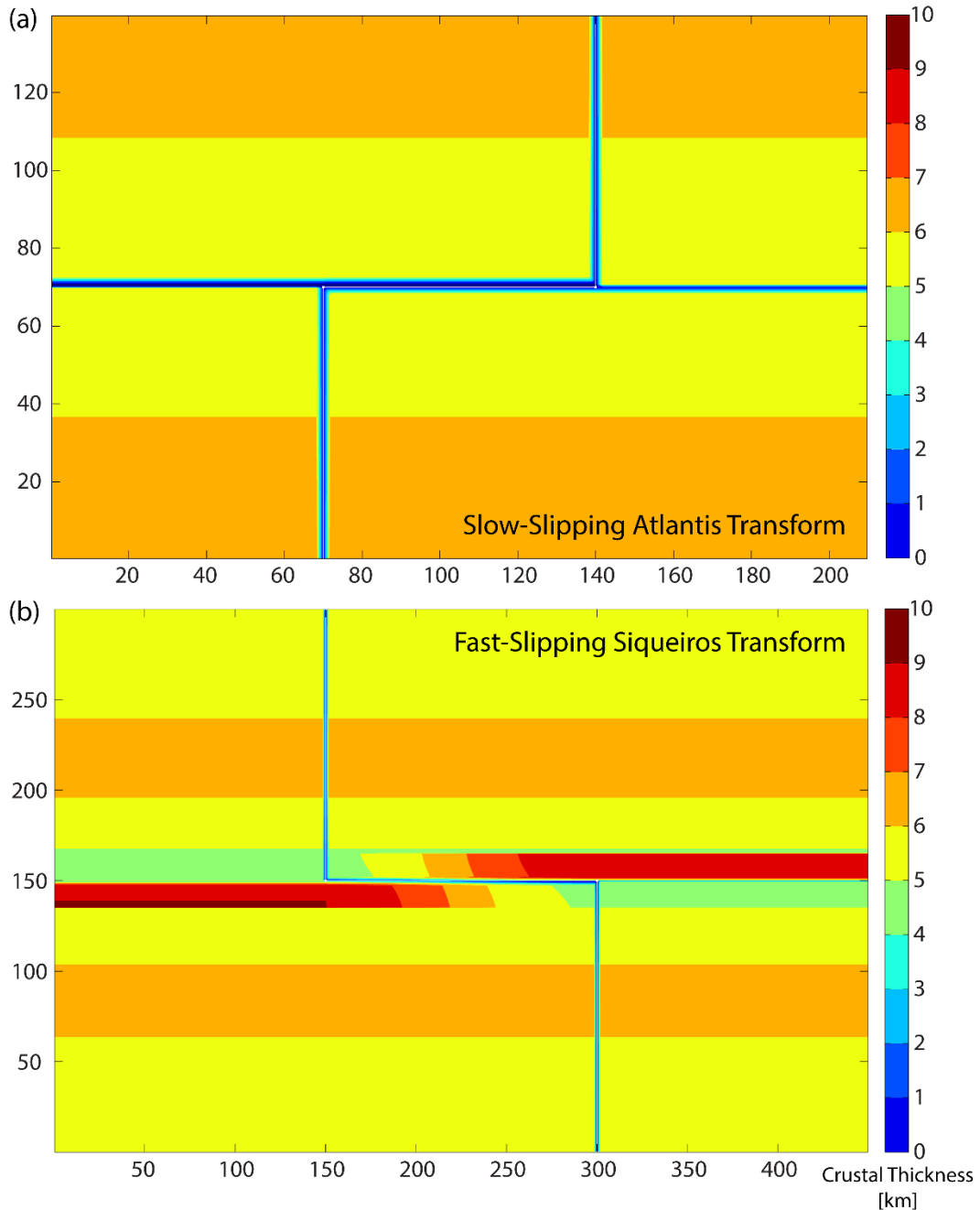
Figure 3.4 Maps of crustal thickness for the slow-slipping Atlantis transform (half-slip rate: 1.2 cm/yr, transform length: 70 km) and the fast-slipping Siqueiros transform (half-slip rate: 5.9 cm/yr, transform length: 150 km). A crustal redistribution length of 50 km, an extraction width of 2 km and an extraction depth of 15 km are used. In both cases, the average crustal thickness for most area of the seafloor is about 6–7 km. Thickened crust develops along the fast-slipping transform with crustal thickness increases from the inner corner of ridge-transform intersection to the tips of the fracture zone, whereas no thickening occurs at the slow-slipping transform.

one is for the slow-slipping Atlantis transform (half-slip rate: 1.2 cm/yr, transform length: 70 km), and the lower one is for the fast-slipping Siqueiros transform (half-slip rate: 5.9 cm/yr, transform length: 150 km). The results shown here are for an extraction width d_e of 2 km, an extraction depth z_e of 15 km, and a crustal redistribution length L_f of 60 km.

In both cases, the average crustal thickness for most of the seafloor is about 6–7 km, in agreement with the global trend of oceanic crust [*Chen*, 1992; *White et al.*, 1992; *Wang et al.*, 2011]. Along the ridge segments, crustal accretion decreases close to the transform fault (Figure 3.3) due to the cooling effect of the transform offset, sometimes called the "transform fault effect" [*Phipps Morgan and Forsyth*, 1988]. At the slow-slipping transform (Figure 3.4a), the "transform fault effect" results in a minimum of crustal thickness along the transform fault and associated fracture zones.

Thickened crust is generated along the fast-slipping transform (Figure 3.4b). Although the "transform fault effect" results in a minimum in the crustal thickness along the ridge as it meets the transform fault, crustal thickness increases in the spreading direction from the inner corner of ridge-transform intersection to the tips of the fracture zone. The thickened crust is due to crustal accretion along the transform (Figure 3.3), which accumulates on the plate as it is rafted away from the spreading center. By contrast, no crust is accreted along the slow-slipping transform fault (Figure 3.4a).

To quantitatively evaluate the model results, we define two ridge domains and one transform domain as 20 km wide swaths along plate boundaries centered at ridge axes and transform faults. The width of the swaths is set to account for the resolution

of RMBA inversions, which is about 20–25 km [*Sandwell and Smith*, 1997]. We average the crustal thickness in the transform and ridge domains of our model and define the crustal thickness difference ΔH as the difference between averaged crustal thickness in the transform domain, H_T, and in the ridge domain, H_R. A similar measure can be evaluated from the RMBA reported by *Gregg et al.*, [2007].

A chi-square (χ^2) analysis [*Press et al.*, 2007] is used to estimate the goodness of fit between the model results and the observation for the nine transform fault systems investigated:

$$\chi^2 = \sum_{i=1}^{9} \left(\frac{\Delta H_i^{\text{model}} - \Delta H_i^{\text{observation}}}{\sigma} \right)^2 + \sum_{i=1}^{9} \left(\frac{H_{R_i}^{\text{model}} - H_{R_i}^{\text{observation}}}{\sigma} \right)^2 \qquad (3.12)$$

Ideally, σ would be the standard error on the observations. However, this quantity is not reported by *Gregg et al.* [2007]. Therefore, we use instead a relative standard error, estimated from the best fit [*Press et al.*, 2007]:

$$\sigma^2 = \frac{1}{\upsilon} \min \left[\sum_{i=1}^{9} \left(\Delta H_i^{\text{model}} - \Delta H_i^{\text{observation}} \right)^2 + \sum_{i=1}^{9} \left(H_{R_i}^{\text{model}} - H_{R_i}^{\text{observation}} \right)^2 \right] \ (3.13)$$

where υ is the degree of freedom. As we have two observations, H_R and ΔH for each of nine study areas, and we vary three parameters (d_e, z_e, and L_f), $\upsilon = 9 \times 2 - 3 = 15$. Two sets of constraints are used: the ΔRMBA-converted crustal thickness difference $\Delta H^{\text{observation}}$ (assuming an average oceanic crust density of 2700 kg/m^3 and a mantle density of 3300 kg/m^3 [*Wang et al.*, 2011]) and the reference thickness of oceanic crust $H_R^{\text{observation}}$ (7.1 km [*White et al.*, 1992]).

A range of values for the extraction width d_e (2–8 km), extraction depth z_e (10–40 km), and crustal redistribution length L_f (10–70 km) have been tested in the

models. The resulting χ^2 values are plotted over the parameter space, as shown in Figure 3.5. Models with the minimum χ^2 values fit the observation best.

For models with small values of extraction depth and extraction width, χ^2 decreases with increasing crustal redistribution length. However, for larger extraction depth and width, χ^2 increases for the longest crustal redistribution length.

Several combinations of parameters produce acceptable models, using a χ^2 significance level of 0.5% (corresponding to a χ^2 value of 30.578). Acceptable models can be categorized into two groups. The first group has smaller values for extraction width and depth (d_e: 2–4 km, z_e: 15–20 km), and larger crustal redistribution length (L_f: 50–70 km). The second group has larger values for extraction width and depth ($d_e > 4$ km, $z_e > 35$ km), but smaller crustal redistribution length (L_f: 15–45 km). Neither group can be favored from purely statistical arguments. However, the first group is most consistent with geological observations, as discussed in the next section.

To better understand the physical difference between the two groups of parameter combinations, we examined the crustal accretion profiles for models in each group (Figure 3.6). For models with fast slip rate, both groups feature melt extraction along the transform faults (Figure 3.6b). However, for slow-slipping models with the first group of parameters, no melt is extracted along the transforms, whereas for models with the second group of parameters, melt extraction occurs along the slow-slipping transform (Figure 3.6a). Both groups of parameters satisfy equally well the observed slip-rate-dependent RMBA variations between ridge and

60
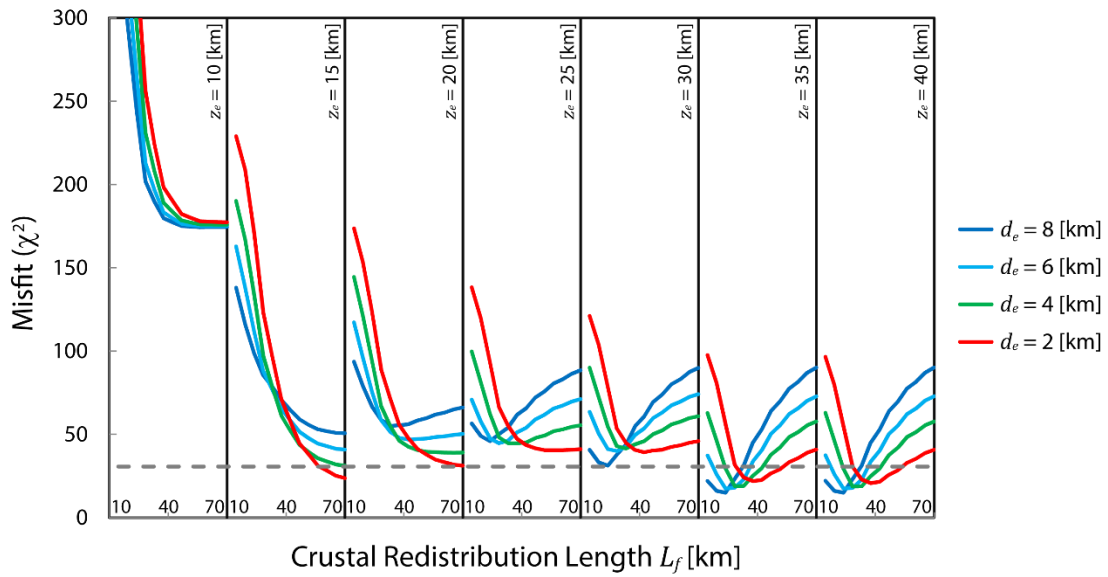
Figure 3.5 Misfit (χ^2) for models with varying melt extraction width d_e, melt extraction depth z_e and crustal redistribution length L_f. Different colors represent model result with different melt extraction width. Each box contains results for a different melt extraction depth. Crustal redistribution length increases in each box. The dashed grey line shows the χ^2 corresponding to a significance level of 0.5%.
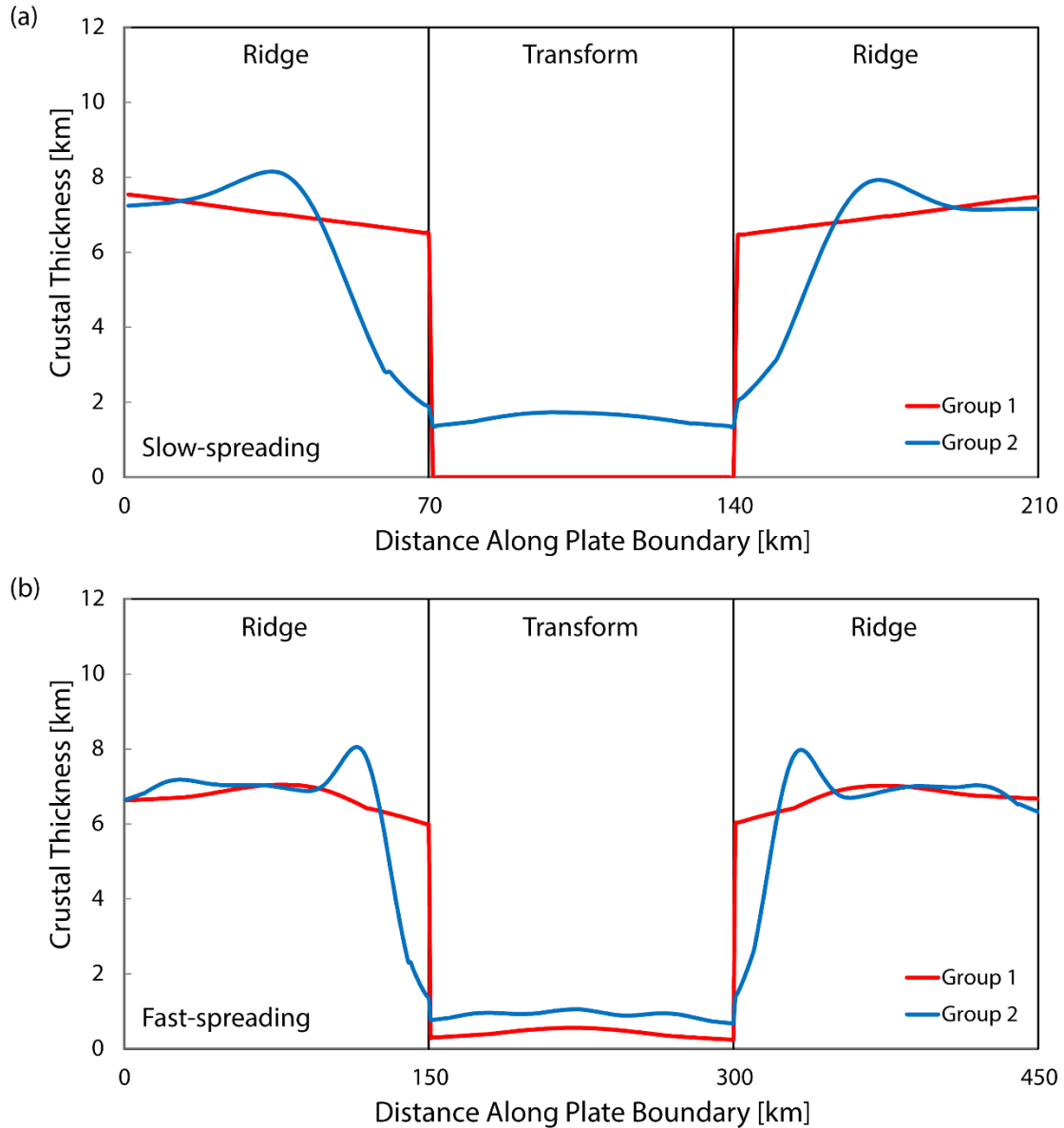
Figure 3.6 Crustal accretion profiles for models with the first group of parameters (in red, d_e: 2–4 km, z_e: 15–20 km, L_f: 50–70 km) and the second group of parameters (in blue, d_e: > 4 km, z_e > 35 km, L_f: 15–45 km), for a) slow- (half-slip rate: 1.2 cm/yr) and b) fast-slipping transforms (half-slip rate: 5.9 cm/yr). Both groups have melt extraction along the fast-slipping transform faults. However, for the first group of parameters, no melt is extracted along the slow-slipping transforms, while for the second group of parameters, melt extraction occurs along the slow-slipping transform.

transform domains and produce realistic crustal thicknesses. The major difference lies in, whether melt extraction is possible along the slow-slipping transforms.

3.4 Discussions

3.4.1 Melt Extraction at Slow-Slipping Transform Faults?

To find out if melt extraction at slow-slipping transform faults is possible, we looked into the geological, geochemical and seismic observations at oceanic transform faults. Little evidence can be found supporting magmatism at slow-slipping transforms. Therefore, the first group of acceptable models appears more geologically realistic than the second group.

Magmatism at fast-slipping to intermediate-slipping transforms has been discussed in a number of geological studies. For example, at the fast-spreading East Pacific Rise, bathymetric surveys, dredging and submersible dives have discovered constructional volcanic mounds and fresh lavas in the troughs of the Clipperton transform [*Kastens et al*., 1986], the Siqueiros transform [*Perfit et al*., 1996], the Garrett transform [*Hékinian et al*., 1992], the Terevaka transform [*Constantin et al*., 1996], and the Raitt transform [*Castillo et al*., 1998]. Fresh basalts have also been found along the intermediate-slipping Blanco transform [*Gaetani et al*., 1995]. By contrast, magmatic activity is sparsely reported at slow-slipping transforms, which are instead dominated by exposures of serpentinized peridotite [*Thompson and Melson*, 1972] or thin and weathered basalt layer on top of transform valley flanks [*Auzende et al.*, 1989; *Bonatti et al.*, 2003], implying that melt extraction seldom occurs there.

Besides, lavas erupted along fast-slipping transform faults are generally more primitive and more porphyritic than lavas from the nearby ridge axes [*Perfit et al.*, 1996; *Castillo et al.*, 1998; *Wendt et al.*, 1999]. This suggests that magma in the transform is extracted directly and rapidly to the surface, and no crustal processes in magma chambers are involved [*Fornari et al.*, 1989; *Hékinian et al.*, 1995]. They underwent a different cooling history from lava erupted along the spreading center. By contrast, basalts collected at slow-slipping transform faults have MgO content at the same level as the samples recovered from the adjacent ridge axes [*Lawson et al.*, 1996; *Bryan et al.*, 1981], implying the crust at slow-slipping transforms is created at the associated ridge segment, without evidence for a different crystallization history that would represent magmatism along the transforms.

Melt extraction processes at oceanic transform faults can also be reflected in seismic activity. Teleseismic data indicate different kinds of earthquakes at fast-slipping and slow-slipping transforms. Studies of earthquake scaling relations for oceanic transform faults demonstrate that the seismic coupling coefficient, defined as the ratio between the observed and expected seismic moment [*Pacheco et al.*, 1993] is about 0.15, implying that nearly 85% of the fault slip is aseismic [*Boettcher and Jordan*, 2004]. Aseismic phenomenon can be accounted for by creep events [*Wesson*, 1988], slow and silent earthquakes [*Beroza and Jordan*, 1990; *Miller et al.*, 2002], all of which are typically attributed to fault weakening resulted from changes of fluid pressure [*Obara*, 2004; *Kodaira et al.*, 2004; *Becken et al.*, 2011]. Magma injection and eruption along transform faults may lead to elevated fluid pressures that weaken the faults [*Vidale and Shearer*, 2006; *Becken et al.*, 2011]. If melt is extracted along

64

fast-slipping transforms, but not at slow-slipping transforms, we should expect fast-slipping transforms to be more aseismic than the slow-slipping ones. Previous studies suggest that the seismic coupling coefficient decreases with increasing slip rate, with more aseismic slip at fast-slipping transforms than at slow-slipping transforms [*Kawaski et al.*, 1985; *Rundquist and Sobolev*, 2002]. This trend is in agreement with our prediction.

However, *Boettcher and Jordan* [2004] argue that seismic coupling coefficient does not decrease significantly with increasing slip rate. They do not identify a systematic relation between seismic coupling coefficient and slip rate. These conflicting conclusions may result from the large spatial variability of seismicity within the transforms, which is ignored in some studies [e.g., *Rundquist and Sobolev*, 2002], but kept in the recent one [*Boettcher and Jordan*, 2004]. Earlier studies may have underestimated the seismic coupling coefficient for two reasons: (1) they use data from the Harvard Centroid Moment Tensor (CMT) catalog and the International Seismological Center (ISC) online bulletin, which have short catalog duration (~36 years) that may not be sufficient to span the long earthquake cycles at slow-slipping transforms (> 60 years, assuming a stress drop > 10 MPa [*Boettcher and McGuire*, 2009]); (2) they use a half-space cooling model to calculate the temperature limit of seismicity. More realistic thermal models incorporating a viscoplastic rheology, non-Newtonian viscous flow and the effects of shear heating and hydrothermal cooling lead to a smaller seismogenic area [*Liu et al.*, 2012]. These effects are more pronounced for the slow-slipping transforms. Taking these effects into account, it is possible that the seismic coupling coefficient is actually higher at

slow-slipping transform than at fast-slipping transforms, implying that slow-slipping transforms are at least less magmatic than the fast-slipping ones.

The differences in seismic behavior between fast-slipping and slow-slipping transform faults are better illuminated through microearthquake experiments conducted at different mid-ocean ridge systems. At the fast-spreading East Pacific Rise, an array of autonomous underwater hydrophones in the vicinity of the Clipperton transform fault recorded a cluster of earthquakes associated with dike intrusion and propagation [*Dziak et al.*, 2009]. At the Blanco transform, Juan de Fuca Ridge, low-frequency, periodic tremor-like signals, and earthquake swarms are also documented, and interpreted to be of volcanic origin, which has been confirmed by ocean-bottom photographs and water column data [*Dziak et al.*, 1996]. By contrast, at the slow-spreading Mid-Atlantic Ridge, earthquakes along the Kane transform [*Wilcock et al.*, 1990] and Oceanographer transform [*Cessaro and Hussong*, 1986] detected by ocean bottom seismometers show focal mechanisms of normal faulting, indicating differential lithospheric extension across the transform faults, caused by a deficit of magmatism [*Cessaro and Hussong*, 1986]. Besides, a recent 4 year hydroacoustic monitoring of seismicity at northern Mid-Atlantic Ridge between ~15°N and ~35°N [*Smith et al.*, 2002; *Smith et al.*, 2003] did not record microearthquakes with the characteristics of magmatic activities along the transforms (Deborah K. Smith, personal communication, 2013). Although seismic behavior is complicated by the stress state and material property of each individual transform faults, generally speaking, most seismic events at slow-slipping transforms have a tectonic origin, while seismicity at fast-slipping transforms mainly reflects magmatic

66

processes [*Rundquist and Sobolev*, 2002]. The distinct patterns of earthquakes at transform faults with varying slip rate indicate that melt extraction occurs along the fast-slipping transforms, but not at slow-slipping ones.

3.4.2 Preferred Parameters for Melt Extraction

As melt extraction along slow-slipping transform is unlikely to take place, we consider that the first group of acceptable models, i.e., those with melt extraction width d_e between 2 and 4 km, melt extraction depth z_e between 15 and 20 km, and crustal redistribution length L_f between 50 and 70 km, are the most realistic. The dimensions of MEZ and crustal redistribution implied by these models are supported by several observations.

At mid-ocean ridges, neovolcanic activity is typically confined within about 2 km of the ridge axis [*Macdonald*, 1982], in agreement with our preferred value for melt extraction width between 2 and 4 km. Broader melt extraction zones may be appropriate at ultraslow-spreading center [*Standish and Sims*, 2010], which, as they lack transform offsets [*Dick et al.*, 2003], are not considered in this study.

Our preferred extraction depth between 15 and 20 km implies that extraction of melts in the ridge and transform domains mainly occurs through fractures and shear zones in the lithosphere. The depth of fracturing can be assessed from the maximum depth of earthquakes at transform faults. Ocean bottom seismometer studies [e.g., *Wilcock et al.*, 1990], teleseismic inversions [e.g., *Abercrombie and Ekström*, 2001] and laboratory extrapolation [e.g., *Boettcher et al.*, 2007] suggest that the seismicity at transform faults is limited by the location of 600°C isotherm, and

67

extends to a depth of ~20 km [*Bergman and Solomon*, 1988; *Abercrombie and Ekström*, 2001; *Schlindwein et al.*, 2013].

Thus fractures provide a plausible way for melt to penetrate the lithosphere, and our preferred values for melt extraction depth are supported. On the one hand, since in the model we neglected the latent heat of crystallization of melt, which impacts the thermal structure [*Katz*, 2008] and thins the thermal boundary layer, the actual extraction zone could be shallower than inferred here; On the other hand, the buoyancy-driven mantle flow neglected in this study may have an effect for ridges spreading slower than 1 cm/yr, thin the lithosphere underneath the ridges, focus melt away from the transforms and deepen the melt extraction zone. If the melt extraction occurs through fractures, the extraction depth probably depends on the thickness of the brittle layer and varies with spreading rate and lateral locality. Slow-slipping transforms may have deeper MEZs, and the extraction depth for fast-slipping transforms may be relatively shallower (see Discussion section 3.4.3 for detail). Our models are not sensitive to these variations as long as the permeability barrier and the MEZ intersect and we use one uniform extraction depth for simplicity. Furthermore, mantle exposures at ophiolites show that melt is typically associated with shear zones [*Kelemen et al.*, 1992; *Kaczmarek and Müntener*, 2008; *Kaczmarek and Tomasi*, 2011]. Therefore, melt extraction enhanced by deformation processes can continue throughout the lithosphere.

The crustal redistribution length can be constrained by the observations of lateral dike propagation, which has been documented in Iceland [*Einarsson and Brandsdottir*, 1978], in Hawaii [*Klein et al.*, 1987], on the Juan de Fuca Ridge [*Fox et*

al., 1995; *Dziak et al*., 1995], and on the East Pacific Rise [*Dziak et al*., 2009]. The

observed lateral dike propagation distances vary, but most of them exceeds 30 km.

Along the CoAxial segment, Juan de Fuca Ridge, a swarm of earthquakes migrated

more than 60 km along the axis [*Dziak et al*., 1995]. At the East Pacific Rise, 9°50'N,

regional seismicity reflected a lateral dike intrusion event with a propagation distance

of 25–40 km [*Dziak et al*., 2009]. The length scale of crustal redistribution is

controlled by the width, thermal state, and pressure gradient of propagating dikes.

Thermodynamic models of lateral dike propagation show that, with a width of 1.5 m,

a constant pressure drop of 5 MPa and a temperature of 1200°C, magma can travel in

cold host rocks (temperature: 0–500°C) for more than 50 km before freezing [*Fialko*

and Rubin, 1998]. Thus, our preferred crustal redistribution length between 50 and 70

km is geologically plausible. Besides, even with such large melt redistribution length

scale, along-axis variations of crustal thickness are preserved in our models, as is

observed at both fast-spreading and slow-spreading ridges [*Lin et al*., 1990; *Canales*

et al., 2003].

3.4.3 Expectations for Global Systematics

With the preferred values for melt extraction width and crustal redistribution

length, we systematically vary slip rate, transform length, and melt extraction depth to

understand the systematic variation in crustal thickness between transform domain

and ridge domain that may be expected at locations other than the nine examples

analyzed by *Gregg et al*. [2007].

The relationship between crustal thickness difference and spreading rate for

models with a transform length of 150 km, a crustal redistribution length of 50 km, an

extraction width of 2 km and varying extraction depths is shown in Figure 3.7a. The crustal thickness difference varies with spreading rate, and changes from negative at slow-spreading ridges, to positive at fast-spreading ridges (except for $z_e = 10$ km, with which the transform faults cannot accumulate thicker crust than the adjacent ridges, even the fast-slipping ones). In other words, intermediate-slipping and fast-slipping transforms accumulate thicker crust than the associated ridges, while no thickening is present at slow-slipping transforms. The extraction depth controls the spreading rate at which crustal thickness changes from negative to positive. The variations of crustal thickness difference at half-spreading rate between 1 and 4 cm/yr reflect the spatial relationship between permeability barrier and MEZ (Figure 3.7b). The transition from nonintersection to intersection between MEZ and permeability barrier beneath a transform fault occurs between half-slip rate of 1 and 4 cm/yr. At extraction depth less than 10 km, magma cannot be fully extracted, resulting in oceanic crust thinner than the general estimation. Depending on the transform length, at extraction depth between 15 and 20 km, the MEZ cuts the permeability barrier at fast-slipping transforms, but not at slow-slipping ones. And at extraction depth larger than 35 km, the MEZ penetrates the permeability barrier everywhere in the domain despite the slip-rate. To satisfy the RMBA observation, at slow-slipping transforms, the melt extraction depth can be as deep as 30 km, while at fast-slipping transforms, the extraction depth may vary from 15 to 20 km. Once the MEZ fully intersects the permeability barrier, crustal thickness differences become stable and are no longer affected by the spreading rate.
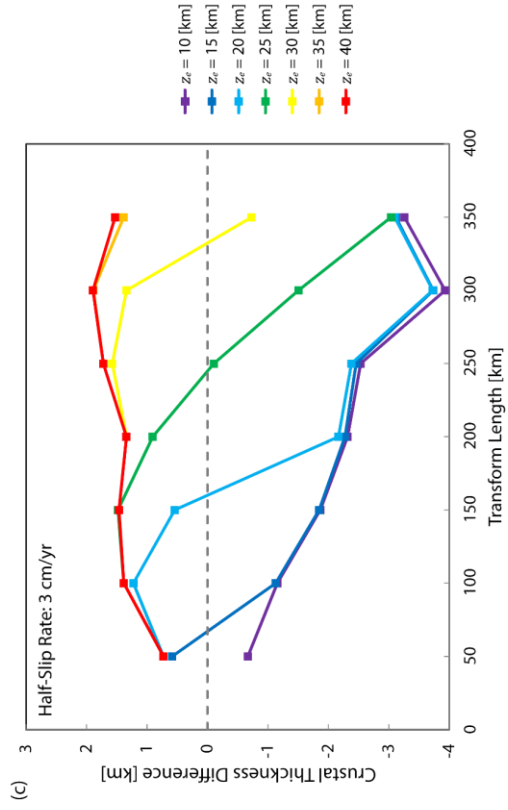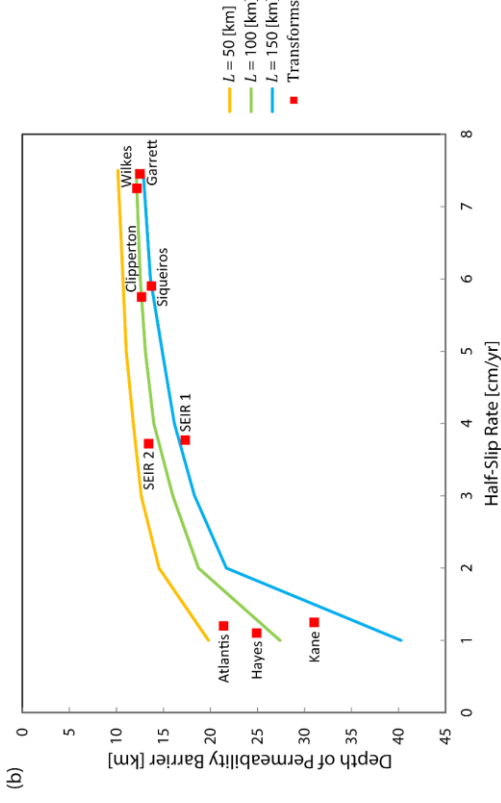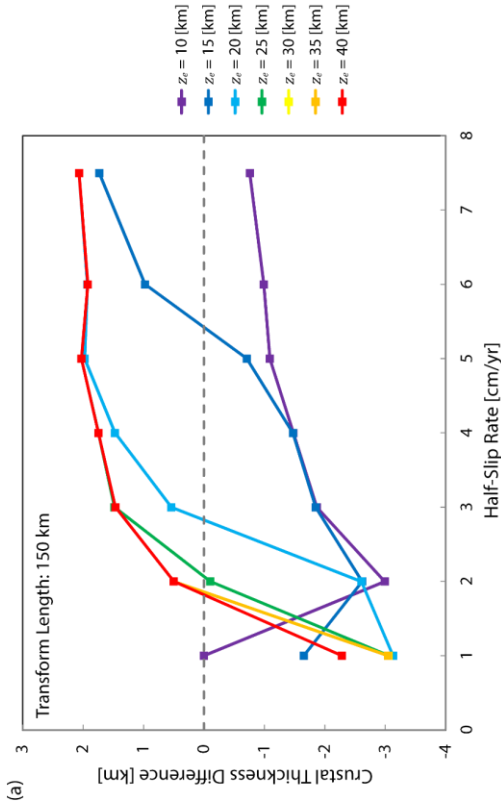
Figure 3.7 (a) Relationship between crustal thickness difference and spreading rate for a transform length of 150 km. (b) Relationship between depth of permeability barrier at the center of the transform and half-slip rate. Lines in yellow, green and blue are results from models with transform length of 50, 100 and 150 km respectively. Red squares are results from models with specific geometry of the indicated transforms. (c) Relationship between crustal thickness difference and the length of transform for a half-slip rate of 3 cm/yr. Different colors represent results with different melt extraction depth. An extraction width of 2 km and a crustal redistribution length of 50 km are used throughout.

71

Figure 3.7c shows the relationship between crustal thickness difference and transform length for models with half-spreading rate of 3 cm/yr, a crustal redistribution length of 50 km, an extraction width of 2 km, and different extraction depths. For melt extraction depth smaller than 20 km, the crustal thickness difference decreases with increasing length of transform. For melt extraction depth larger than 15 km, the crustal thickness difference increases with increasing length of transform at short transforms, and may decrease for the longest transforms. Increasing the extraction depth increases the transform length for which the maximum crustal difference is obtained. The small value of crustal thickness difference at short offset is a combination of the small temperature anomaly associated with the transform and a lack of time for crust to accumulate along the transform fault. The reduced crustal thickness difference at long offset is due to the decreased melt production and greater depth of the permeability barrier beneath the transform as conductive cooling becomes dominant. The width of the partial melting region in the upper mantle could be as wide as 200 km at fast-spreading ridges and as narrow as 50 km at slow-spreading ridges [*Chen*, 2000]. Therefore, when the transform fault is long enough, the partial melting regions beneath two adjacent ridge segments may be isolated, and no cross-segment melt transport may occur, resulting in an absence of magmatic activities in the transform domain.

3.4.4 Mechanisms for Magmatism at Fast-Slipping Transform Faults

Magmatic activity at fast-slipping transform faults has been attributed to both "leaky" transforms [*Menard and Atwater*, 1969] and ITSCs [*Fornari et al.*, 1989]. In most cases, magmatic transforms are transtensional due to the plate reorientation

[e.g., *Thompson and Melson*, 1972; *Hékinian et al*., 1992; *Perfit et al*., 1996; *Dziak et al*., 1996] and feature ITSCs [e.g., *Fornari et al*., 1989; *Hékinian et al*., 1992]. Young lava flows are found in the pull-apart basins and in the vicinity of the ITSCs. However, along some transforms such as Siqueiros and Garrett, fresh basaltic rocks are also present on the transform floor and intratransform wall away from ITSCs [*Perfit et al*., 1996; *Tepley et al*., 2004]. In addition, crustal thickening and volcanism at the transpressional Clipperton transform [*Pockalny*, 1996] cannot be easily explained by the "leaky" transform concept or ITSCs. Melt extraction at transforms is more universal than transtension or ITSCs. Our models assume melt extraction occurs regardless of tectonic environment, although it is likely that transtension makes melt extraction easier.

While three-dimensional melt migration and extraction is the focus of our study, this mechanism is not incompatible with leaky transforms and ITSCs. Plate reorientation not only induces transtensional forces that create leaky transforms and ITSCs, it may also enhance structural damages at transforms [*Menard and Atwater*, 1969], which may facilitate the formation of the melt extraction zone. This damage is expected at both transpressional and transtensional faults, although more so in the latter case. Additionally, migration of ridge may lead to asymmetric melt production beneath the leading and trailing plates, contributing to the crustal thickness variation at segmented mid-ocean ridges [*Carbotte et al.*, 2004].

In general, melt extraction at ridge-transform systems can be complicated by changes of plate motions, and magmatic activity at fast-slipping transform faults may

result from the combined effects of "leaky" transform, ITSCs, and three-dimensional melt migration and extraction processes.

3.4.5 Geochemical Segmentation at Fast-Spreading Ridges

Melt extraction at transform faults may provide a new explanation for geochemical segmentation (or, "transform discontinuities"). Geochemical segmentation refers to different ridge segments offset by transforms or nontransform discontinuities having distinct signatures in major elements, trace elements and isotopic chemistry [*Schilling et al*., 1982; *Machado et al*., 1982; *Langmuir and Bender*, 1984; *Thompson et al*., 1985; *Langmuir et al*., 1986]. This phenomenon is most prominent at fast-spreading ridges, where even non-transform discontinuities impart geochemical segmentation [*Langmuir et al*., 1986], whereas at slow-spreading ridges, geochemical segmentation is more ambiguous [e.g., *Batiza et al*., 1988; *Langmuir et al*., 1992; *Reynolds and Langmuir*, 1997].

According to our models, fast-slipping transform faults act as an easy pathway for magma to erupt. Therefore, they prevent cross-segment transportation of melt. Only a limited amount of melt can travel beneath the inactive fracture zone outside the transform domain (Figure 3.2). On this basis, at fast-spreading ridges, low degree of mixing is expected for melts from different ridge segments with different source composition, and any original heterogeneity can be preserved and reflected at each segment. By contrast, at slow-spreading ridges, melt travels along the permeability barrier across the transform fault without being extracted in the transform domain, extensive mixing of melts between segments is possible. Melts with different compositions are homogenized, resulting in less obvious geochemical segmentation.
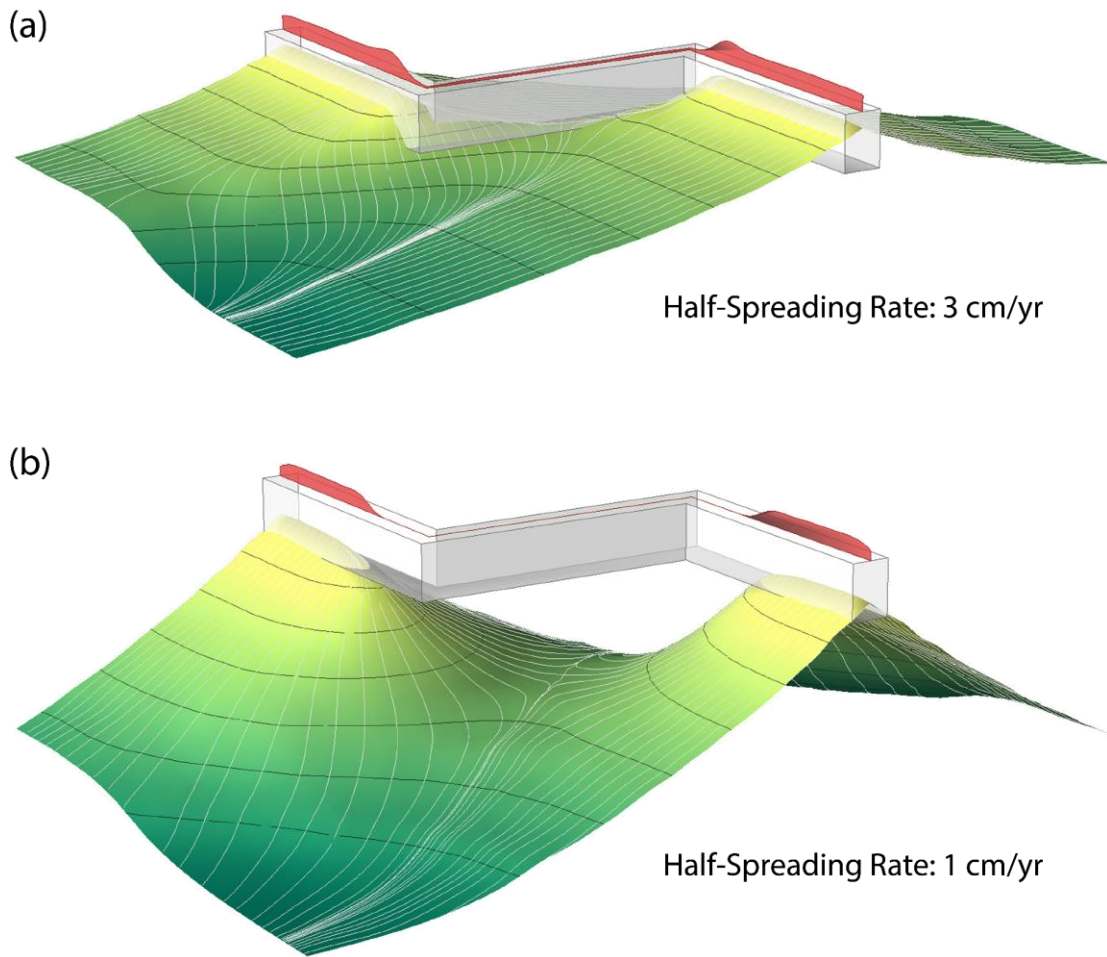
Figure 3.8 Spatial relationship between permeability barrier and melt extraction zone for a) a fast-spreading ridge (half-spreading rate: 3 cm/yr) and b) a slow-spreading ridge (half-spreading rate: 1 cm/yr) with a transform length of 150 km. The curved surface represents the permeability barrier with 5 km depth contours (black) and color-coded with depth (yellow to green from shallow to deep). White lines on the permeability barrier surface are melt trajectories. White boxes are the melt extraction zones. The red areas on top of melt extraction zones indicate melt flux at surface. At fast-slipping transform (a), the permeability barrier intersects with the melt extraction zone and melt can be extracted along the transform. At slow-slipping transform (b), the permeability barrier does not intersect with the melt extraction zone and no melt is extracted along the transform fault.

In summary, whether melt is extracted along oceanic transform faults depends on the slip rate of the transforms. At fast-spreading and intermediate-spreading ridges, the MEZ intersects the permeability barrier underneath transform faults. Melt extraction occurs along the transforms, resulting in thickened crust in the transform domain. By contrast, beneath slow-slipping transforms, the MEZ does not intersect the permeability barrier, no melt is extracted in the transform domain, so the crust there is thin (Figure 3.8). The melt extraction zone is estimated to be about 2–4 km wide, 15–20 km deep. Crustal thickness is smoothed over a length scale of 50–70 km reflecting along-axis dike propagation at crustal level.

Melt extraction occurs mainly through fracturing in the lithosphere near plate boundaries, with possible extensions in ductile shear zones, and may be complicated by changes in plate motions. Magmatism at fast-slipping transform faults may be a result of "leaky" transform, ITSCs, three-dimensional transport of melt toward transforms, or the combination of the three. Fast-slipping and slow-slipping transform faults exhibit different degree of magmatic activities, and the difference can be reflected in geological features, geochemical signals and seismic behavior at transform faults. Melt extraction along transforms may also provide a possible explanation for geochemical segmentation observed at fast-spreading ridges.

Chapter 4: Asymmetric spreading, asymmetric topography, and asymmetric crustal thickness at mid-ocean ridges

Abstract

Despite the classic view that mid-ocean ridges are symmetric systems, maps of seafloor age show that asymmetric seafloor spreading is ubiquitous. When spreading is asymmetric, the faster-moving plate is younger and hotter than the slower-moving plate at a given distance from the ridge axis, and therefore should have more elevated topography. We compile the age, spreading asymmetry and topography data of about 600 ridge segments, and calculate the topography differences between the faster-moving plates and conjugate slower-moving plates. We also solve for the thermal structure underneath an asymmetric spreading ridge and calculate the associated topography asymmetry. Comparison between the observed and predicted topography asymmetry shows that observed asymmetries are consistently lower, and they may even have opposite signs to the predicted asymmetry. These discrepancies indicate that the topographic effect of asymmetric spreading is counterbalanced by other processes or phenomenon. Candidates include background mantle flow, mantle thermal anomalies, ridge migration, flexure, off-axis volcanism, and asymmetric crustal thickness. We review each of these candidates and argue that the topography asymmetry is best explained by asymmetric crustal thickness associated with asymmetric spreading, wherein the crust is thinner on the faster-moving plate than that on the slower-moving side, while background mantle

flow and mantle thermal anomalies can produce regional perturbations. Asymmetric crustal thickness may originate from the longer time the slower-moving plate spends in the crustal accretion zone.

4.1 Introduction

At mid-ocean ridges, plate divergence affects mantle flow and its thermal structure, induces decompressional melting, forms new oceanic crust, and shapes the seafloor topography. In the classic view [e.g., *Morgan*, 1971], mid-ocean ridges are symmetric systems, where symmetric seafloor spreading drives symmetric mantle upwelling, induces symmetric mantle melting, and results in symmetric topography. More detailed studies, however, have revealed that asymmetry is common at mid-ocean ridges, whether evident in seafloor bathymetry [e.g., *Calcagno and Cazenave*, 1994; *Scheirer et al.*, 1998; *Fujiwara et al.*, 2003; *Carbotte et al.*, 2004], marine magnetic anomaly [e.g., *Weissel and Hayes*, 1971; *Allerton et al.*, 2000], seismic and electrical tomography [e.g., *Toomey et al.*, 1998; *Evans et al.*, 1999; *Bodmer et al.*, 2015], seamount and hydrothermal vent distribution [e.g., *Davis and Karsten*, 1986; *Scheirer et al.*, 1998; *McCaig et al.*, 2007], or basalt geochemistry [e.g., *Escartín et al.*, 2008; *Langmuir et al.*, 2013]. The observed asymmetries have been attributed to several processes, including asymmetric spreading [e.g., *Müller et al.*, 1998], background mantle flow [e.g., *Phipps Morgan and Smith*, 1992], ridge migration [e.g., *Shouten et al.*, 1987], and heterogeneous mantle temperature/composition [e.g., *Cochran*, 1986].

Among all the symmetry breakers at mid-ocean ridges, asymmetric spreading, also known as asymmetric accretion, is most commonly and directly observed. With asymmetric spreading, plate accretion occurs at different rates on conjugate ridge flanks, dynamically equivalent to one plate moving faster than the other relative to the ridge axis. It can be caused by asymmetric cooling [*Hayes*, 1976], ridge migration with respect to the mantle [*Stein et al.*, 1977], ridge-plume interaction [*Müller et al.*, 1998], or, especially in the case of slow-spreading, sustained motion along a detachment fault [e.g., *Smith et al.*, 2006; *Escartín et al.*, 2008; *Smith et al.*, 2014; *Parnell-Turner et al.*, 2016].

Asymmetric spreading was first noted in the South Atlantic Ocean using magnetic surveys [*Dickson et al.*, 1968]. Later, more asymmetric spreading regions were identified, such as East Pacific Rise [*Rea*, 1976; *Cormier and MacDonald*, 1994], Southeast Indian Ridge [*Weissel and Hayes*, 1971], Juan de Fuca Ridge [*Elvers et al.*, 1973], Galapagos Ridge [*Hey et al.*, 1977], and Reykjanes Ridge [*Talwani et al.*, 1971].

Recently, based on a set of self-consistent digital isochrons of global ocean basins [*Müller et al.*, 1997] constructed from a compilation of magnetic anomalies and plate motions [*Royer et al.*, 1992], *Müller et al.* [2008] quantified the degree of spreading asymmetry at global mid-ocean ridges, and found that asymmetric spreading is ubiquitous in all ocean basins. The East Pacific Rise as a whole shows excess crustal accretion of 10.4% on the Nazca Plate. At the Southwest and the Western Southeast Indian Ridge, excess accretion of 3.1% and 1.7% occurs on the Antarctic Plate. At the Eastern Southeast Indian Ridge, more crust is accreted to the

Australian flank. In the South Atlantic Ocean, the South American Plate gets excess

crustal accretion between 2.4% and 4.1%. In the North Atlantic Ocean, the degree of

excess accretion is smaller, at about 0.6% [*Müller et al.*, 1998]. Beyond these regional

values, spreading asymmetry varies segment-to-segment and over time.

In theory, asymmetric seafloor spreading should lead to prominent

asymmetric topography. The seafloor topography, to first order, is controlled by plate

age, as approximated by the half-space cooling model or plate cooling model

[*Turcotte and Oxburgh*, 1967, *Parsons and Sclater*, 1977]: an older plate is colder

and denser than a younger plate, and therefore should be less elevated. With

asymmetric spreading, at equal distance from the ridge axis, the faster-moving plate is

younger than the slower-moving plate. Therefore, we expect higher topography on

the faster-moving side than on the slower-moving side.

Although asymmetric topography has been observed at several mid-ocean

ridges [e.g., *Calcagno and Cazenave*, 1994; *Scheirer et al.*, 1998; *Fujiwara et al.*,

2003], no correlation between spreading asymmetry and topography asymmetry has

been reported. To systematically investigate the missing link between asymmetric

spreading and asymmetric topography, we compile the topography and spreading

asymmetry data of mid-ocean ridge segments worldwide, and construct numerical

models to predict the topography asymmetry associated with various degrees of

spreading asymmetry. The comparison between the observed and predicted

topography asymmetries provides new insights and constraints on some mantle and

crustal processes at mid-ocean ridges, and in particular suggests that crustal thickness

across ridge axis may be asymmetric.

4.2 Observed Spreading and Topography Asymmetries at Mid-Ocean Ridges

If the theoretically predicted relationship between asymmetric spreading and asymmetric topography holds, we should expect to observe: (1) globally widespread asymmetric mid-ocean ridge topography, (2) higher topography on the faster-moving plate than that on the conjugate slower-moving plate, and (3) increasing amplitude of topography asymmetry with increasing degree of spreading asymmetry. To test if these conditions are true, we first compile the available observational data from global mid-ocean ridges.

4.2.1 Data Compilation

We include data from about 600 mid-ocean ridge segments selected from the global catalog of *Gale et al.* [2013] based on data availability (Figure 4.1). The selected segments span a total of about 47,000 km, with individual segment lengths ranging from 6.6 km to 375 km and full spreading rates (denoted here as V_{full}) ranging from 0.7 cm/yr to 17 cm/yr. The segments cover 10 ridge systems and are grouped into 23 regions for ease of processing.

Within each region, we compile the age [*Müller et al.*, 2008], spreading rate [*Müller et al.*, 2008], ETOPO1 topography [*Amante and Eakins*, 2009], sediment thickness [*Whittaker et al.*, 2013], and degree of spreading asymmetry [*Müller et al.*, 2008] using MATLAB® with Mapping Toolbox™. The effect of sediment loading on topography is removed following a standard correction procedure described by *Crough* [1983]. An example of sediment-unloaded topography map, covering the East
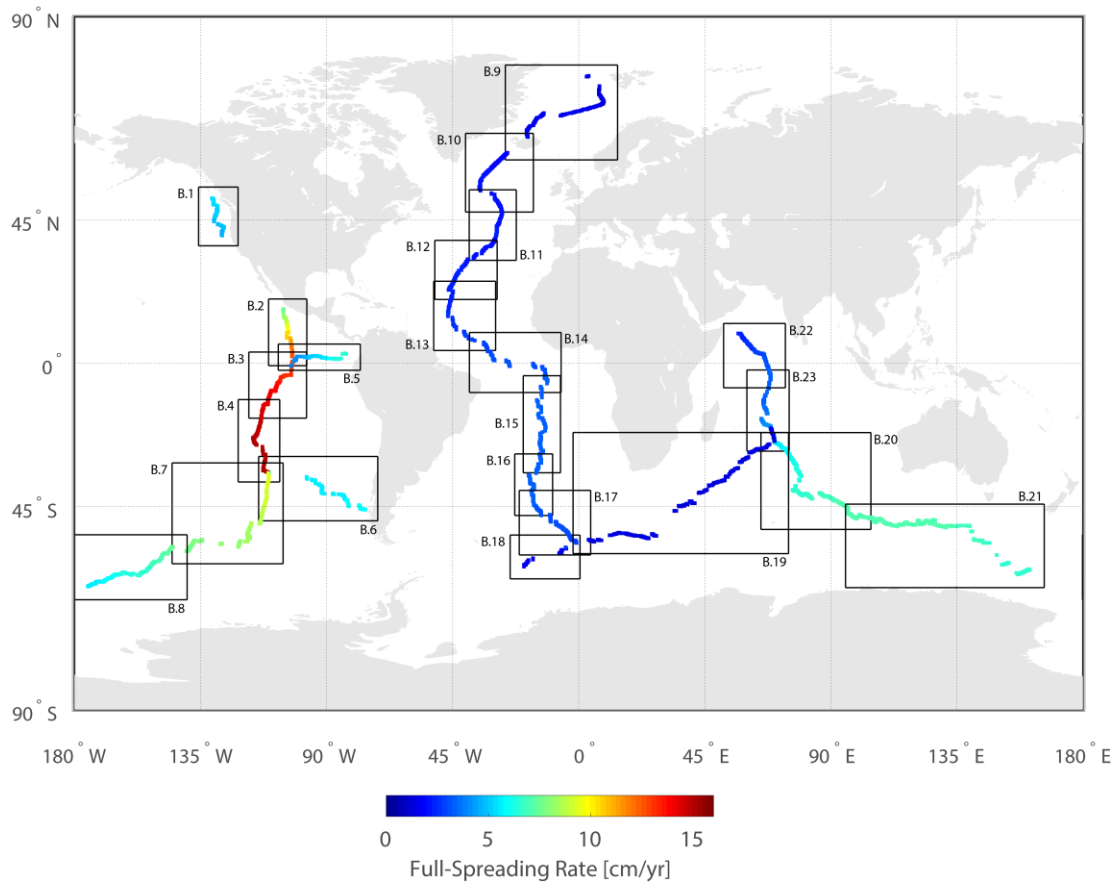
Figure 4.1 Locations of the ridge segments included in the data compilation. Color represents the full-spreading rate. Black boxes outline the sub-regions we use in our analysis. Maps of each sub-regions are included in the Appendix, with figure numbers labeled in this figure.

Pacific Rise from the Equator to ~15°S is shown in Figure 4.2. Similar maps for all the studied regions are provided as Appendix Figures B.1 to B.23.

The ridge segment coordinates and spreading directions from the global spreading center catalog [*Gale et al.*, 2013] do not always agree with the topography and seafloor age data. For consistency, we correct the spreading direction by making it conform to the local seafloor spreading fabrics [*Matthews et al.*, 2011; *Wessel et al.*, 2015]. The actual location of the ridge axis is determined by the age of the seafloor. Using the ridge segment coordinates from the global catalog as an initial guess, we create a search path parallel to the spreading direction every 5 km along the segment. The ridge axis is set at the point with the minimum seafloor age (no older than 0.5 Ma) on the search path.

To characterize the asymmetry in topography across the ridge axis, we define a sampling profile starting at each ridge axis point determined from the previous step, and extending 200 km on each plate following the spreading direction (Figure 4.2). Age, degree of spreading asymmetry, and sediment-unloaded topography on the sampling profiles are interpolated from the regional data, with a fixed sampling resolution of 1 km. For each sampling profile, we compare the data on two plates, and calculate the mean data difference between two sides.

4.2.2 General Characteristics

4.2.2.1 Topography Difference

We define "topography difference" as the average difference in topography between plates on the right-hand-side and the left-hand-side (in orientations shown in Appendix Figures B.1 to B.23) of the ridge, denoted here as Δh_{R-L}.

83
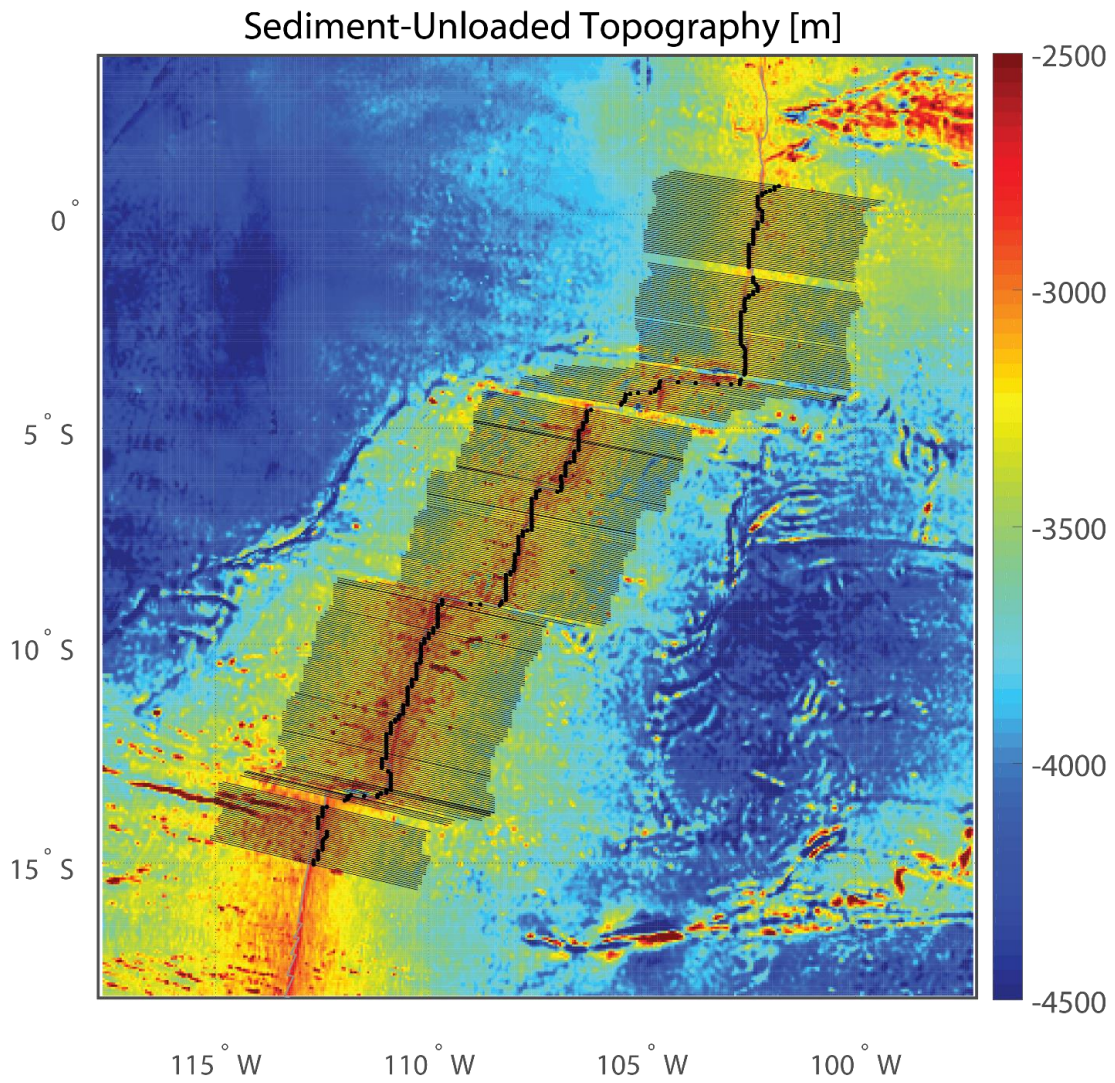
Figure 4.2 Sediment-unloaded topography of the Southern East Pacific Rise. The black dots mark the ridge axis determined from the seafloor age. The thin black lines indicate the sampling profiles. Data are interpolated on the sampling profiles and compared between two sides.

The sign of Δh_{R-L} varies along the ridge axis (Figure 4.3). How often the sign of Δh_{R-L} switches appears to depend on the spreading rate of the ridge: ultraslow- and slow-spreading ridges like Southwest Indian Ridge, Northern Mid-Atlantic Ridge and Central Indian Ridge tend to have more frequent along-axis changes of Δh_{R-L} polarity, with a wavelength smaller than 100 km, while intermediate- and fast-spreading ridges like Juan de Fuca Ridge and East Pacific Rise show along-axis alternation of Δh_{R-L} polarity over larger wavelengths of hundreds of kilometers. At slow-spreading Southern Mid-Atlantic Ridge, although the sign of Δh_{R-L} does not switch frequently, its values change abruptly over a length scale of about 100 km.

The wavelength of Δh_{R-L} variation mimics the spreading-rate-dependence of ridge segmentation: the typical ridge segment length is smaller than 100 km for slow-spreading ridges, and increases to 100–1000 km at intermediate- and fast-spreading ridges [*Sandwell and Smith*, 2009]. This similarity suggests that the processes responsible for the observed asymmetric topography occur at segment-scale.

The amplitude of topography difference, $|\Delta h|$, has a global average of about 200 m, but varies from ridge to ridge (Figure 4.4a, Appendix Tables B.1, B.2). $|\Delta h|$ is smaller at Pacific-Antarctic Ridge, Galapagos Ridge and East Pacific Rise, with regionally averaged values of about 150 m. At Juan de Fuca Ridge and Southwest Indian Ridge, large topography differences are present, with segment-averaged $|\Delta h|$ values often in excess of 300 m.

Ignoring the Juan de Fuca Ridge, the data averaged over each ridge system hints at a possible correlation between V_{full} and $|\Delta h|$ (Figure 4.4a). Although the trend is subtle, it remains that the East Pacific Rise, by far the fastest-spreading ridge on the

85
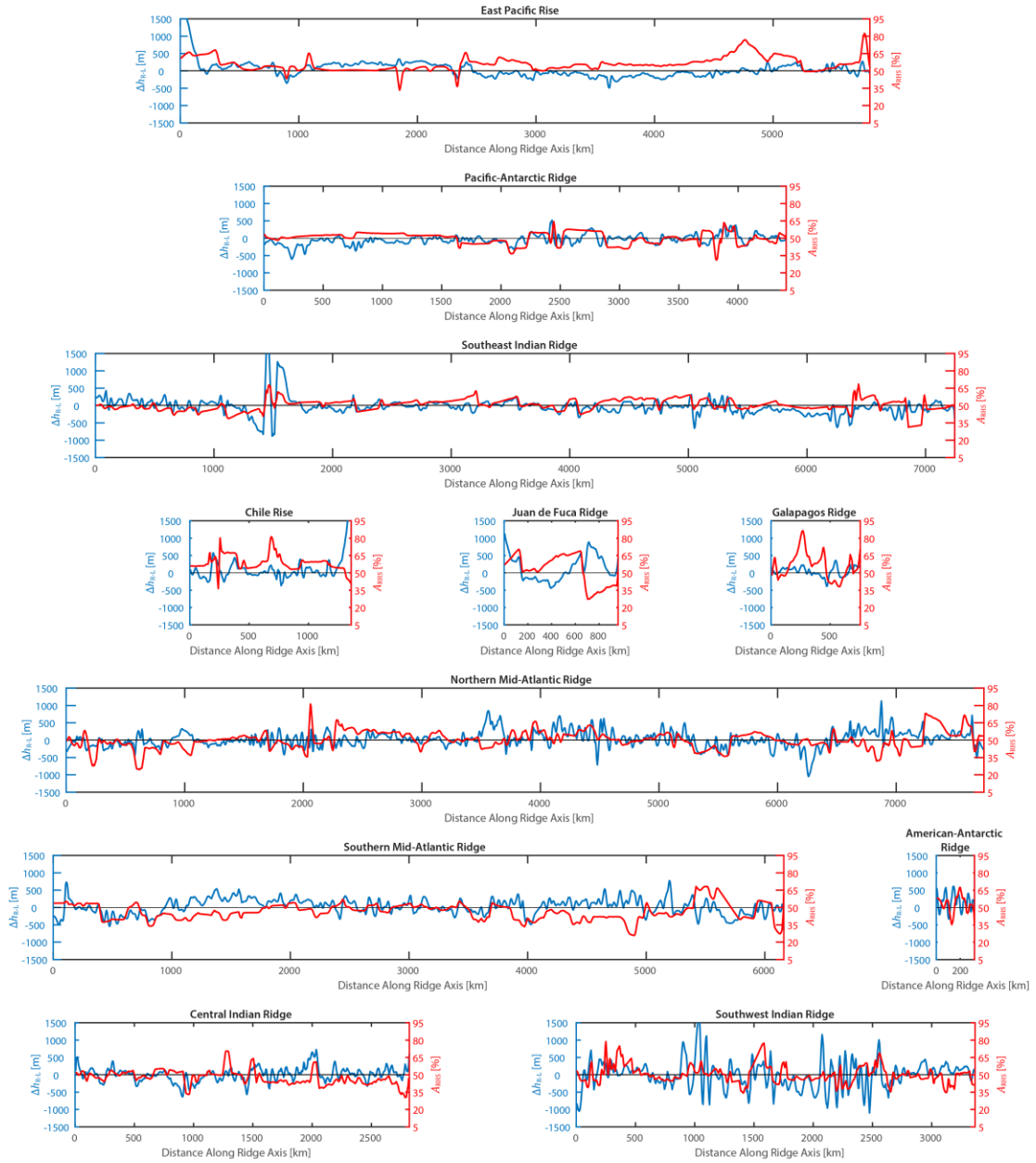
Figure 4.3 Along-axis variations of $\Delta h_{\mathrm{R-L}}$ (blue profile) and A_{RHS}, defined as the spreading asymmetry of the right-hand-side plate (red profile). The right-hand-side plate (refer to Appendix Figures B.1 to B.23) moves faster if A_{RHS} is larger than 50%, and moves slower if A_{RHS} is below 50%. Present here are profiles for East Pacific Rise, Pacific-Antarctic Ridge, Southeast Indian Ridge, Chile Rise, Juan de Fuca Ridge, Galapagos Ridge, Northern Mid-Atlantic Ridge, Southern Mid-Atlantic Ridge, American-Antarctic Ridge, Central Indian Ridge, and Southwest Indian Ridge.

86
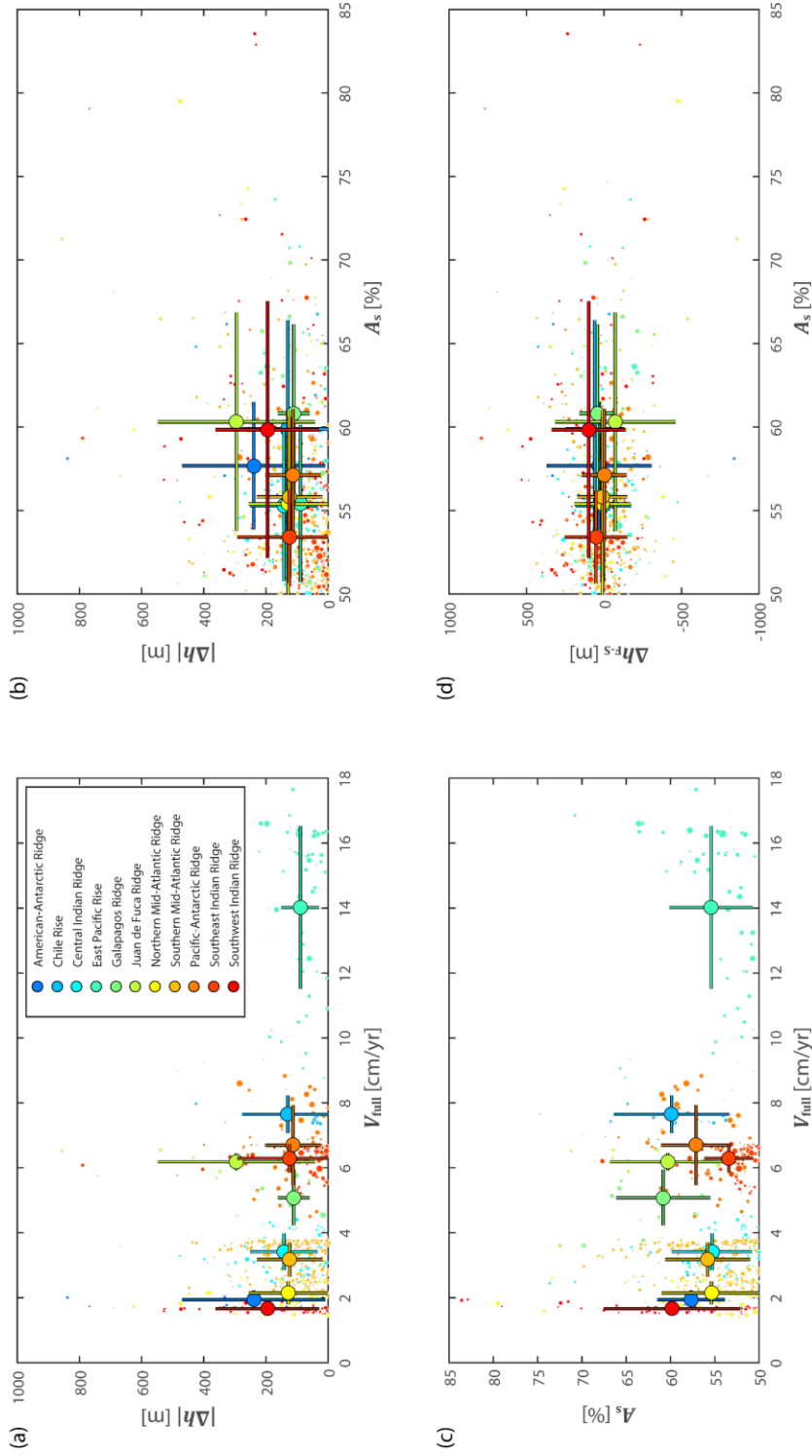
Figure 4.4 Relations between (a) V_{full} (full spreading rate) and $|\Delta h|$ (amplitude of topography difference), (b) A_s (spreading asymmetry) and $|\Delta h|$, (c) V_{full} and A_s, and (d) A_s and Δh_{F-S} (topography difference between faster-moving and slower-moving plates). Larger symbols are ridge-wide averages with error bars of one standard deviation (Appendix Table B.1). Smaller symbols are segment-wide averages (Appendix Table B.2). The symbols are color-coded according to the ridge systems (see panel a).

Earth, has limited $|\Delta h|$, and the two slowest ridges in the dataset, the Southwest Indian Ridge and the American-Antarctic Ridge, both display large $|\Delta h|$. The Juan de Fuca Ridge constitutes an exception to the proposed trend, possibly because it is influenced by the small sizes of the Juan de Fuca Plate and Explorer Plate, and the proximity of the Cascadia subduction zone.

4.2.2.2 Spreading Asymmetry

We define "spreading asymmetry" as the percentage of the total spreading taken by the faster-moving plate, denoted here as A_s. In principle, A_s may vary from 50% (symmetric spreading) to 100% (one plate moves at the full-spreading rate, the other is stationary, relative to the ridge axis). We also denote the percentage of the total spreading taken by the right-hand-side plate as A_{RHS}.

Asymmetric spreading is present at all mid-ocean ridge systems we surveyed (Figures 4.3, 4.4c). The global average A_s is about 55%. Ridge segments with A_s between 50% and 55% are the most abundant, and the number of ridge segments decreases progressively with increasing A_s. Although most asymmetric segments are associated with slow-spreading ridges, there is no evidence of a systematic relation between A_s and V_{full} (Figure 4.4c). Intermediate-spreading ridges show both high and low A_s: the Juan de Fuca Ridge, Galápagos Ridge, and Chile Rise are all relatively asymmetric, whereas the Southeast Indian Ridge has the lowest A_s.

Similar to the variations of Δh_{R-L}, the faster-moving side alternates along the ridge axis (Figure 4.3) at a wavelength that appears to depend on V_{full}: smaller wavelength of polarity change at slow-spreading ridges, and larger wavelength at intermediate- and fast-spreading ridges. A_s can change dramatically and the fast-

moving side may switch between adjacent segments. Thus, asymmetric spreading is more likely controlled by lithospheric-scale processes, rather than the deeper mantle circulation [*Gerya*, 2010; *Püthe et al.*, 2014].

4.2.2.3 Relation between Topography Difference and Spreading Asymmetry

Although both A_S and $\Delta h_\mathrm{R-L}$ vary at segment-scale, there is no direct correlation between the two. To study their relations, we define "topography asymmetry" as the average difference in topography between the faster- and slower-moving plates, denoted here as $\Delta h_\mathrm{F-S}$. Considerations of seafloor age-depth relation imply that topography should always be higher on the faster-moving plate and lower on the slower-moving plate, and $\Delta h_\mathrm{F-S}$ should always be positive, but this is not always the case (Figure 4.4d). Higher topography correlates with faster-moving plate at a few segments, most conspicuously at the Central Indian Ridge and portions of the Northern Mid-Atlantic ridge (Figure 4.3). However, negative $\Delta h_\mathrm{F-S}$ is observed at the Southern East Pacific Rise, Juan de Fuca Ridge, Northern Pacific-Antarctic Ridge and Eastern Southeast Indian Ridge.

Interestingly, $|\Delta h|$ shows a slight correlation with A_S, especially when ridge-averaged values are considered (Figure 4.4b). The trend is dominated, however, by the contrast between, on the one hand, the Juan de Fuca Ridge and the American-Antarctic ridge, which are highly asymmetric in both spreading rate and topography, and, on the other hand, the Southeast Indian Ridge, which is asymmetric in neither. Clear exceptions to this trend are the Chile Rise and the Galápagos Ridge, both of which have strong spreading asymmetry but little topography asymmetry. Although

the correlation may not be robust, it is intriguing that no ridge consistently shows large topography asymmetry without spreading asymmetry.

4.3 Expected Topography Asymmetry from Asymmetric Spreading

The lack of correlation between Δh_{F-S} and A_s indicates that plate age is not the sole control on topography asymmetry. In order to investigate the other sources of topography asymmetry, we develop numerical models of mid-ocean ridges with various types of asymmetry. Specifically, we correct the data for the expected effects of asymmetric spreading, and discuss which other processes would be able to generate the residual signal.

4.3.1 Numerical Setup

The numerical models are built in a two-dimensional plane perpendicular to the ridge axis (Figure 4.5). Mantle flow field and thermal structure of mid-ocean ridges are solved using the commercial finite element software COMSOL Multiphysics® 4.3, assuming incompressible mantle with a constant density. The governing equations are provided in the Appendix. The computational domain is 2000 km wide and 400 km deep, with the ridge axis located at the center of the top boundary, separating it into two plates. We use a triangular mesh for the models, with refinement toward the top boundary and ridge axis. The size of the smallest element at the ridge axis is about 5 km. The mantle temperature at the bottom is set at 1375 °C and the temperature on top is assumed to be 0 °C. The bottom and side boundaries are stress-free and open to mantle flow. A temperature-dependent viscosity with a

$V_x = (1 - A_s)V_{\text{full}}$ $V_x = A_s\, V_{\text{full}}$

$T = 0\,°\text{C}$

$\sigma_n = 0,$
$\partial T/\partial x = 0$

$T = 1375\,°\text{C},\ \sigma_n = 0$

$\sigma_n = 0,$
$\partial T/\partial x = 0$

400 km

2000 km
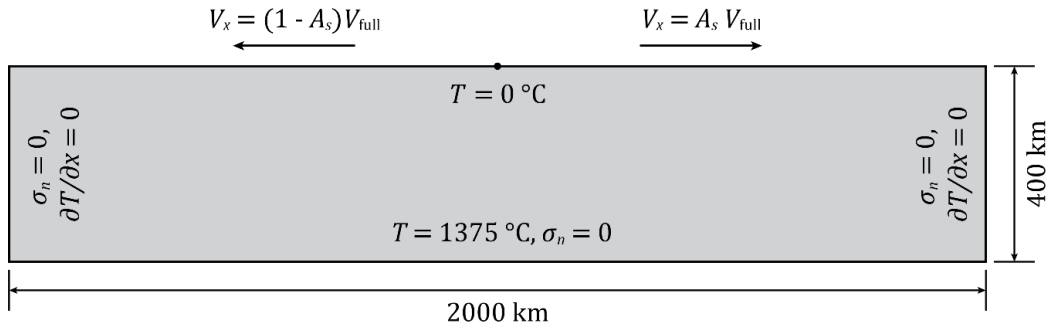
Figure 4.5 Geometry and boundary conditions of the asymmetric spreading model. The point at the center of the top boundary represents the ridge axis. V_x is the spreading rate imposed on the top boundary, V_{full} is the full-spreading rate of the ridge, and A_s is the degree of spreading asymmetry. For symmetric models, A_s is 50%; for asymmetric spreading models, A_s ranges from 55% to 85%. A range of V_{full} from 2 cm/yr to 18 cm/yr is tested. T is the temperature and $\partial T/\partial x$ is the temperature gradient in x-direction. σ_n is the normal stress.

viscoplastic approximation for brittle weakening is adopted following *Behn et al.*

[2007], and the effect of hydrothermal cooling is approximated as an enhanced

thermal conductivity [*Phipps Morgan and Chen*, 1993; *Roland et al.,* 2010] (a

detailed description is available in Appendix).

We apply a velocity of A_sV_{full} to the right-hand-side plate, and a velocity of

$-(1 - A_s)V_{full}$ to the left-hand-side plate. We vary V_{full} from 2 to 18 cm/yr and

A_s between 50% and 85% (A_s larger than 85% is not observed). Our strategy is to

solve first for a symmetric mid-ocean ridge models ($A_s = 50\%$) to serve as a reference

and template for asymmetric models, and progressively increase the spreading

asymmetry A_s.

After solving for the mantle flow field and thermal structure in COMSOL

Multiphysics®, we export each model into MATLAB® and calculate the degree and

extent of mantle melting and seafloor topography. Melt fraction is estimated using a

linear melting parameterization, as a function of temperature [*Reid and Jackson*,

1981]. We predict the seafloor topography based on mantle density, which varies as a

function of mantle temperature, pressure, and degree of depletion. Assuming isostasy

and a constant crustal thickness, the topography is calculated by:

$$h = \frac{\int_0^{y_c}(\rho - \rho_m)dy}{\rho_m - \rho_w} \tag{4.1}$$

$$\rho = \rho_m[1 - \alpha(T - T_{ref}) - \gamma F][1 + \beta(P - P_{ref})] \tag{4.2}$$

where h is the relative topography, y is the depth, y_c is the compensation depth, ρ is

the mantle density, ρ_m is the reference mantle density, ρ_w is the water density, α is

the thermal expansion, β is the compressibility, γ is the depletion coefficient

[*Oxburgh and Parmentier*, 1977; *Su and Buck*, 1993], F is the melt fraction

approximating the degree of mantle depletion, T is temperature, P is pressure, T_{ref} is the reference temperature, and P_{ref} is the reference pressure. The parameters used in this study and their values are listed in Appendix Table B.3.

To better illustrate the effects of the asymmetric spreading, we present the velocity, temperature, and melt fraction fields, and their perturbations from the symmetric case. We also compare the topography on the two plates and calculate the mean topography difference over 200 km distance from the ridge axis for a direct comparison with observations ($\Delta h_{\text{F}-\text{S}}$).

4.3.2 Numerical Results

The results from an asymmetric spreading model are shown in Figure 4.6 and Appendix Figure B.24. The faster-moving plate drives the mantle beneath it to move faster, and draws the mantle from beneath the slower-moving plate, creating a skewed mantle upwelling tilting towards the faster-moving side (Figure 4.6a). The temperature field is asymmetric, with a larger vertical temperature gradient on the faster-moving side than that on the slower-moving side (Figure 4.6a, Appendix Figure B.24).

The temperature reduction on the slower-moving side is always larger than the temperature increase on the faster-moving side, resulting in a cooler mantle overall. This effect is more pronounced for slow-spreading ridges. Part of the temperature anomaly is simply the result of plate ages being different on two sides of the ridge. However, the numerical model includes additional processes such as dynamic pressure and the nonlinear effects of mantle temperature and strain rates. These
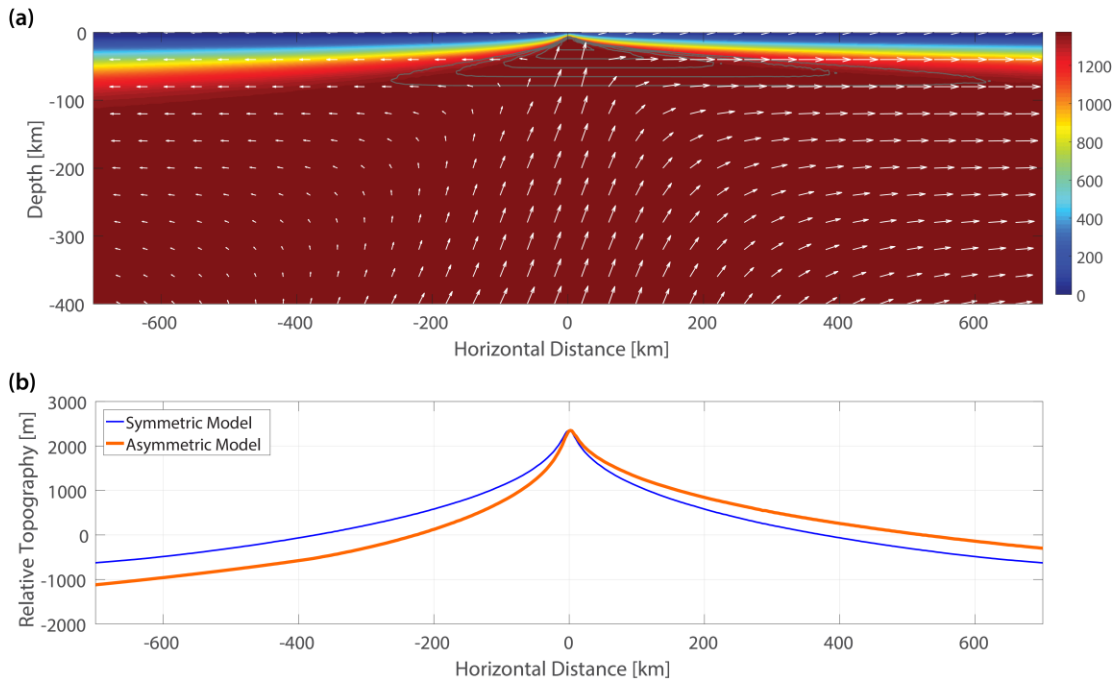
Figure 4.6 Example asymmetric spreading model with a full-spreading rate of 6 cm/yr and a spreading asymmetry of 70% (right-hand-side plate is faster). (a) Mantle temperature (color surface), velocity (white arrows) and melt fraction (gray contours). Mantle on the faster-moving side is hotter with larger extent of partial melting. (b) Seafloor topography profile predicted in the asymmetric (orange) and symmetric (blue) models. Topography is more elevated on the faster-moving side, as expected from considerations of seafloor age-depth relation.

effects weaken the higher-temperature/faster-moving side of the model, facilitating upwelling there (Appendix Figure B.24). Melt fraction is increased beneath the faster-moving plate, and decreased beneath the slower-moving one. The perturbation in melt fraction can be as high as 5%, as a result of the shifting of the melting region towards the faster-moving side (Figure 4.6a, Appendix Figure B.24).

With hotter, more depleted and more buoyant mantle, the faster-moving side shows higher topography than the slower-moving side (Figure 4.6b). The topography difference averaged over 200 km on either side of the ridge axis increases with increasing spreading asymmetry and decreasing spreading rate (Figure 4.7a). Topography asymmetry can reach more than 1000 m for highly asymmetric slow-spreading ridge models. This is because the higher spreading asymmetry introduces a larger contrast in thermal structure between the two plates, but this effect is less significant with higher spreading rate, as the age contrast is inversely proportional to the spreading rate.

4.4 Discussions

Although the predicted and observed topography asymmetries have similar amplitude, it is clear that the model is in other ways a poor predictor to the observations (Figure 4.7a). The systematic increase of topography asymmetry with increasing spreading asymmetry and decreasing spreading rate is not nearly as prevalent in nature as in the models (Figure 4.4c, d). This implies that topography asymmetry is controlled by not only asymmetric spreading, but also other
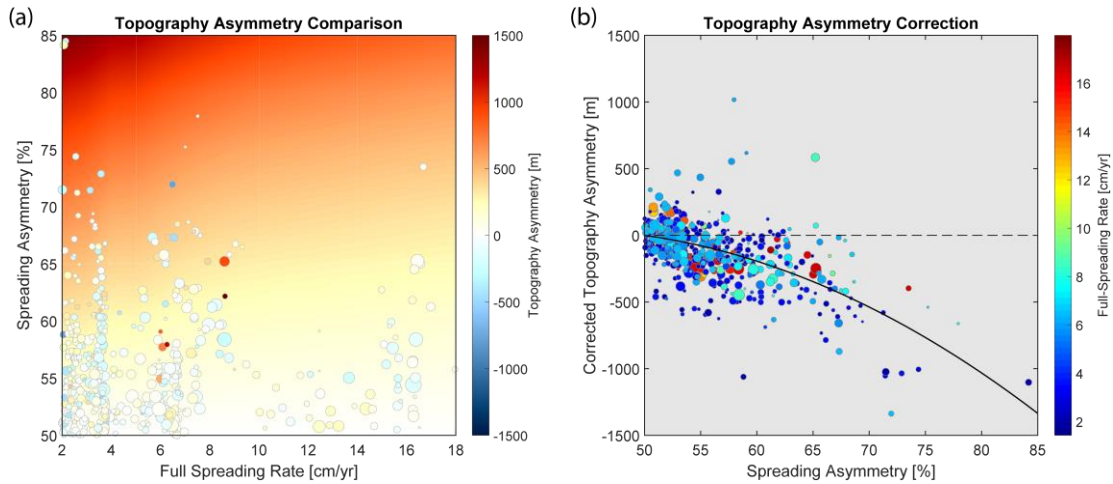
Figure 4.7 (a) Topography asymmetry (Δh_{F-S}, dots) and prediction from the asymmetric spreading model (colored background surface) as a function of spreading rate and spreading asymmetry. The color of each dot represents the observed topography asymmetry. Dot size is proportional to the length of the corresponding ridge segment. (b) Topography asymmetry corrected for the prediction from the asymmetric spreading model (Δh_C). Zero deviation is marked by the dashed black line. Each dot is colored according to spreading rate and its size is proportional to the length of the corresponding ridge segment. The solid black line illustrates $\Delta h_C = -0.75 A_s^2 + 63 A_s - 1275$, which represents the trend between corrected topography asymmetry and spreading asymmetry A_s.

phenomena. Candidates include background mantle flow, mantle thermal anomalies, ridge migration, flexure, off-axis volcanism, and crustal thickness asymmetry. We examine each of these candidates and argue that asymmetric crustal thickness is the most likely origin of the observed signal.

4.4.1 Topography Asymmetry Correction

As asymmetric spreading is observed over most of the studied segments, we need to remove its contribution to the observed dataset. To do this, we calculate the corrected topography asymmetry Δh_C by subtracting the predicted topography asymmetry (Figure 4.7a) from the observed values. In more than 75% of the cases, Δh_C is negative, reflecting the observation that the faster-moving plate is not as elevated compared with the slower-moving plate as expected from the models. Interestingly, Δh_C decreases with increasing degree of spreading asymmetry (Figure 4.7b). The trend can be roughly captured by a second-degree polynomial:

$$\Delta h_\mathrm{C} = -0.75 A_\mathrm{s}^2 + 63 A_\mathrm{s} - 1275 \tag{4.3}$$

where Δh_C is in meter and A_s is in percent. Although there is considerable scatter around this trend, the processes proposed to influence topography asymmetry are likely correlated with spreading asymmetry and should be able to generate a trend similar to Equation 4.3.

4.4.2 Background Mantle Flow

Background mantle flow, or mantle wind, is driven by mantle density variations, relative plate motion and/or lithosphere rotation, and may introduce a deviation of mantle flow from the passive upwelling induced by plate divergence at

97

mid-ocean ridges. It has been used to explain the flattening of seafloor older than 70 Ma [*Cazenave and Lago*, 1991; *Phipps Morgan and Smith*, 1992], anomalous seafloor topography occurring south of Australia [e.g., *Hayes*, 1976; *Buck* et al., 2009], asymmetries at the Southern East Pacific Rise [e.g., *Toomey et al.*, 2002; *Conder et al.*, 2002], basin-wide slope asymmetry [e.g., *Conrad and Husson,* 2009; *Watkins*, 2016], and, in a different context, sub-slab seismic anisotropy [*Paczkowski et al.,* 2014]. Mantle wind can be inferred from gravity data [e.g., *Hager and Richards*, 1989], seismic anisotropy [e.g., *Long and Becker*, 2010], and residual topography [e.g., *Crosby and McKenzie*, 2009].

A global viscous mantle flow model [*Conrad and Behn*, 2010] reveals that mantle wind is present at most of the mid-ocean ridges. Using the stress field from that mantle flow model, we calculate the ridge-perpendicular horizontal mantle pressure gradient and averaged it over depth between 100 km and 400 km. Results show that at most ridges, the magnitude of ridge-perpendicular pressure gradient is less than 1 Pa/m. Exceptions are the Southern Central Indian Ridge, Galapagos Ridge and Equatorial Mid-Atlantic Ridge, where the ridge-perpendicular mantle pressure gradient exceeds 2 Pa/m.

To investigate its topographic effects, we simulate the mantle wind by imposing a pressure field that varies linearly with horizontal distance on the side and the bottom boundaries. If there was no plate divergence, these boundaries would result in a mantle wind similar to Poiseuille flow [*Richards et al*., 2001; *Höink and Lenardic*, 2010; *Conrad et al*., 2011; *Natarov and Conrad*, 2012; *Shiels and Butler*, 2015]. We ignore the possibility of vertical pressure gradients and small-scale mantle

flow anomalies. The plate moving in the mantle wind direction is identified as the trailing plate while the plate moving against the mantle wind is identified as the leading plate. To avoid the incoming mantle having unrealistic temperature, we impose on the side boundaries the temperature solution from half-space cooling model. We test the magnitude of pressure gradient from 0.5 Pa/m to 2.5 Pa/m with A_s fixed at 50%.

Model results (Figure 4.8, Appendix Figure B.25) show that the imposed pressure gradient drives a horizontal mantle flow in the asthenosphere, sufficient to overcome the original passive mantle upwelling pattern [*Conder et al.*, 2002; *Katz et al.*, 2004; *Weatherley and Katz*, 2010]. The asthenospheric flow rises underneath the leading plate toward the axis, and descends underneath the trailing plate away from the axis. The temperature of the leading plate is decreased compared with the symmetric models, while the trailing plate has a higher temperature than the corresponding part in the symmetric models (Appendix Figure B.25). Accordingly, the melt fraction decreases under the leading plate, and slightly increases under the trailing plate. The topography is higher on the hotter and more depleted trailing side than on the leading side (Figure 4.8).

The topography asymmetry predicted by mantle wind model increases with increasing mantle pressure gradient and decreasing spreading rate, and can reach about 200 m (Figure 4.9a). Considering the mantle pressure gradient is less than 1 Pa/m at most ridges, its effects are likely to be negligible. In addition, background mantle flow is unlikely to vary from segment to segment, as the topography asymmetry does. Therefore, we rule out background mantle flow as a major
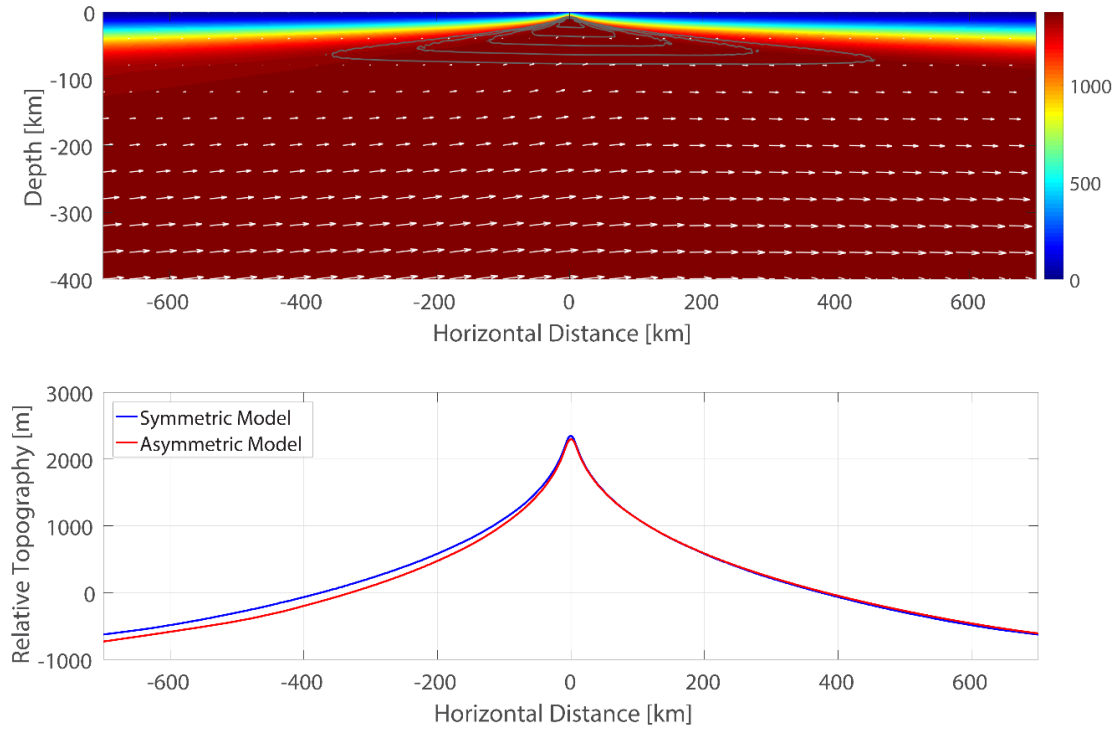
Figure 4.8 Results from an example mantle wind model with a full-spreading rate of 6 cm/yr and a mantle pressure gradient of 2 Pa/m. Upper figure shows the mantle temperature (color surface), velocity (white arrows) and melt fraction (gray contours). Lower figure shows the model-predicted seafloor topography (red profile), with topography from a symmetric model for reference (blue profile).
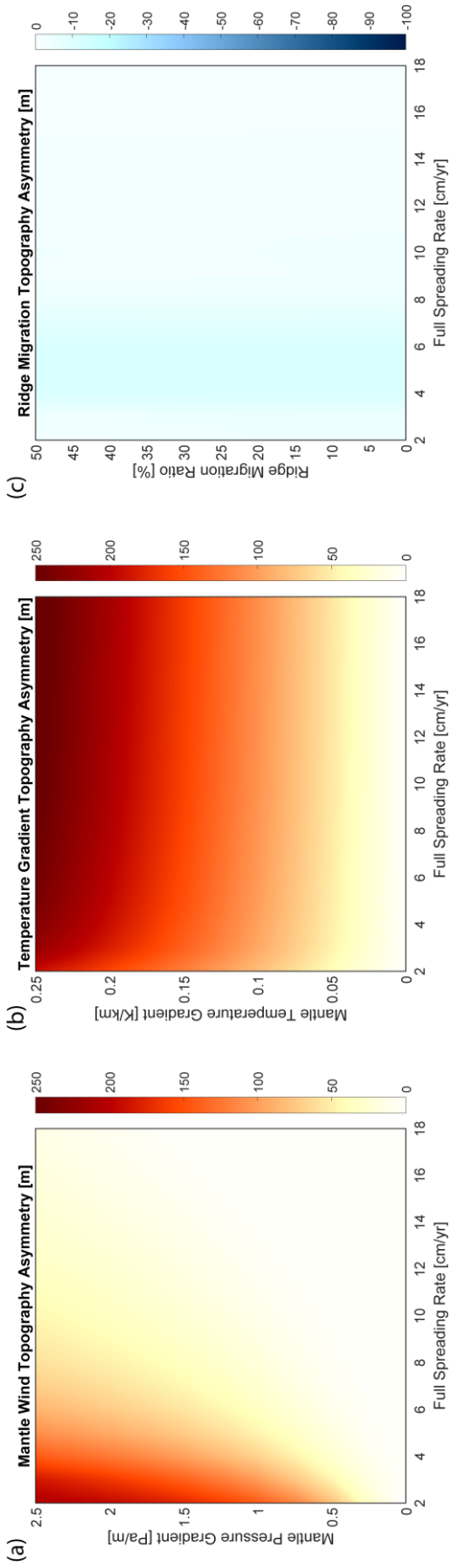
Figure 4.9 Topography asymmetry predicted by the (a) background mantle flow, (b) horizontal mantle temperature gradient, and (c) ridge migration models. The horizontal axis is spreading rate in all cases and the vertical axis the variable causing asymmetry, limited to a realistic range. Note that the color scale is different in each panel and also in Figure 4.7a.

contributor to the topography asymmetry, although it may contribute to the scatter in Δh_C (Figure 4.7).

4.4.3 Mantle Thermal Anomalies

If a mantle thermal anomaly or heterogeneity is present, the associated density variations will likely influence mantle dynamics and seafloor topography. Both an anomalously high temperature on one side of the ridge originating from a mantle plume [*Tommey et al.*, 2002; *Conder et al.*, 2002] and gradients in mantle potential temperature and/or composition [*Cochran*, 1986] have been proposed as origins of the asymmetric seismic velocity structure in the MELT region of the East Pacific Rise [*MELT Seismic Team*, 1998]. Global shear velocity models [e.g., *Kustowski et al.*, 2008; *Moulik and Ekström*, 2014] show that shear velocity anomalies are often not symmetric about ridge axes, indicating that, assuming temperature exerts a dominant control on shear wave velocity, mantle temperature is also asymmetric about the ridge. Regions with hotter and more buoyant mantle will likely have more elevated topography.

To quantify the effects of mantle temperature anomalies using numerical models, we impose a linearly-varying temperature on the bottom boundary of the computational domain, following *Katz* [2010]. The base temperature beneath the ridge axis is fixed at 1375 °C, and linearly increases from the right-hand-side to the left-hand side of the model. A range of thermal gradient from 0.05 K/km to 0.25 K/km are tested.

The applied thermal gradient directly impacts the mantle thermal structure. The side where higher mantle temperature is imposed is hotter, the side with lower

imposed bottom temperature is colder, as expected (Figure 4.10, Appendix Figure

B.26). The temperature perturbation is smaller near the surface due to the high

thermal conductivity in the lithosphere and the imposed uniform surface temperature.

The temperature perturbation leads to a noticeable perturbation in melt fraction, with

the hotter side showing deeper and larger degree of melting, and less melting on the

colder side. The imposed thermal gradient causes density variations in the

asthenosphere, which elevate topography on the hotter side and lower the topography

on the colder side (Figure 4.10). The compilation of model results in the parameter

space shows that while not significantly influenced by the full-spreading rate, the

topography difference increases linearly with increasing magnitude of thermal

gradient and reaches a maximum of about 250 m at a temperature gradient of 0.25

K/km (Figure 4.9b). Although we do not have models with thermal gradient larger

than 0.25 K/km, we expect the topography difference to continue growing beyond the

modeled parameter range.

The mantle thermal gradient impacts the seafloor topography by changing the

mantle density, but there are three reasons why it is probably not the main control on

topography asymmetry. (1) To produce negative values of Δh_C, the mantle thermal

gradient has to be consistently opposite to the spreading asymmetry, i.e., with hotter

mantle underlying the slower-moving plate and *vice versa*. This feature is not

reflected in the global shear velocity models [e.g., *Kustowski et al.*, 2008; *Moulik and

Ekström*, 2014]. (2) The variations of topography asymmetry and spreading

asymmetry both occur at smaller length-scale than over which we expect the mantle

temperature to vary [e.g., *Dalton et al.*, 2014]. (3) The magnitude of mantle thermal

103
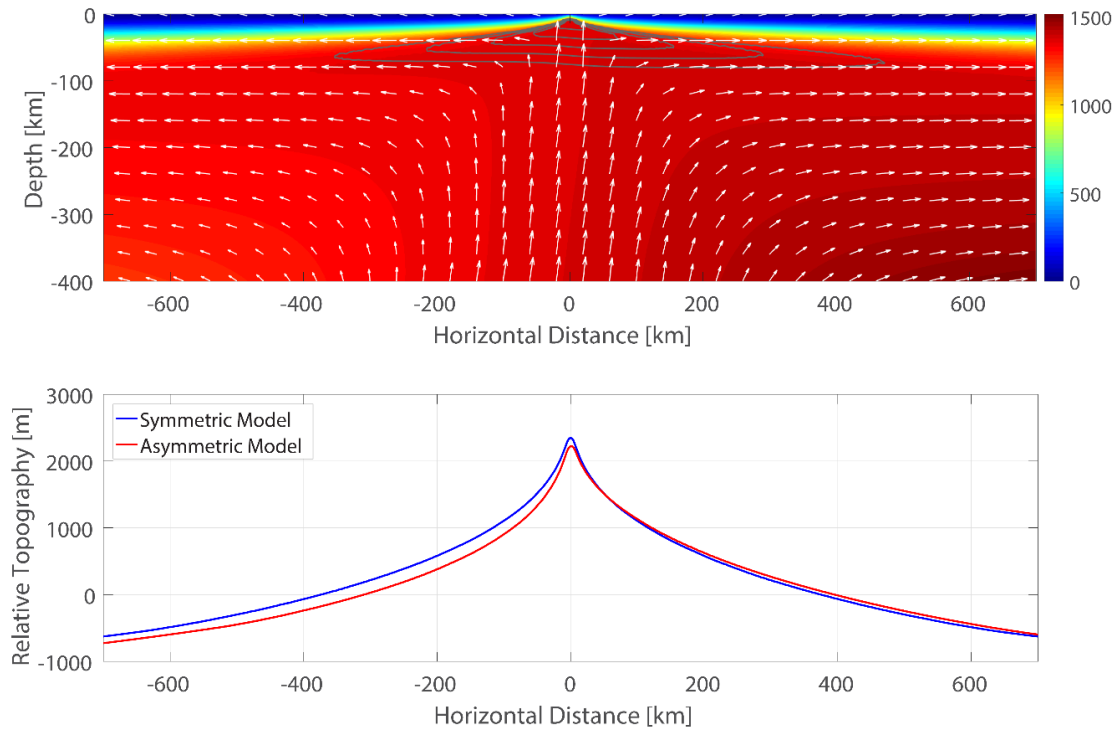
Figure 4.10 Results from an example mantle temperature anomaly model with a full-spreading rate of 6 cm/yr and a temperature gradient of 0.2 K/km. Upper figure shows the mantle temperature (color surface), velocity (white arrows) and melt fraction (gray contours). Lower figure shows the model-predicted seafloor topography (red profile), with topography from a symmetric model for reference (blue profile).

gradient needed to offset the topography asymmetry from high degree of spreading asymmetry is unrealistically large. Therefore, like background mantle flow, mantle thermal anomalies are unlikely to be the origin of the topography asymmetry, although they can contribute to the scatters in the observations.

4.4.4 Ridge Migration

Ridge migration refers to the migration of plate boundaries as a result of the absolute motion of the bounding plates [*Stein et al.*, 1977]. Dynamic [*Katz et al.*, 2004; *Weatherley and Katz*, 2010] and kinematic [*Davis and Karsten*, 1986; *Schouten et al.*, 1987] models predict asymmetric mantle upwelling from ridge migration, leading to asymmetric melting. Ridge migration has been invoked to explain the axial depth difference across offsets at intermediate- and fast-spreading ridges [*Carbotte et al.*, 2004; *Katz et al.*, 2004], and the asymmetric distribution of seamounts at Juan de Fuca Ridge [*Davis and Karsten*, 1986]. Current plate kinematics show that all mid-ocean ridges are migrating in a hotspot-fixed reference frame [*Small and Danyushevsky*, 2003].

To investigate the topographic effect of ridge migration using numerical models, we extend the computational domain of our models to 700 km depth and impose a migration velocity on the bottom boundary. Thus, the model is set in a ridge-fixed reference frame with the deeper mantle migrating with respect to the ridge. The magnitude of ridge migration velocity is defined as a fraction of the full-spreading rate, and we test ridge migration ratio ranging from 5% to 50%. When the ratio is 50%, one of the plate is immobile with respect to the deeper mantle.
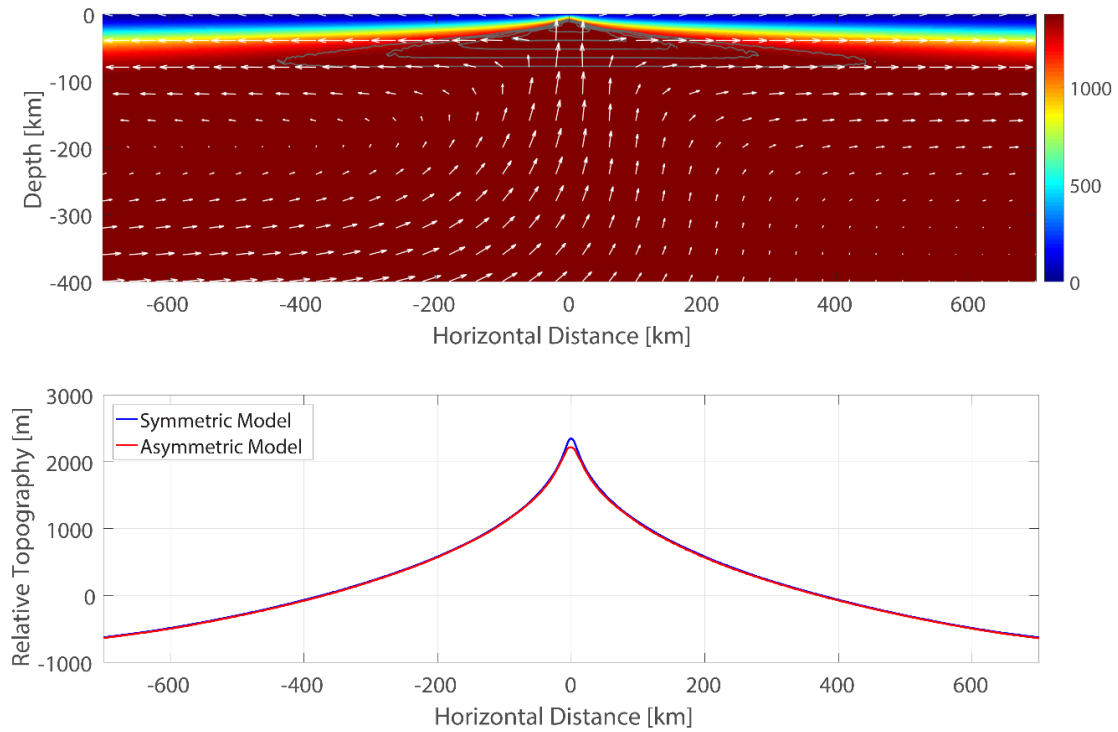
Figure 4.11 Results from an example ridge migration model with a full-spreading rate of 6 cm/yr and a ridge migration rate of 2.4 cm/yr. Upper figure shows the mantle temperature (color surface), velocity (white arrows) and melt fraction (gray contours). Lower figure shows the model-predicted seafloor topography (red profile), with topography from a symmetric model for reference (blue profile).

The imposed ridge migration produces a Couette-like flow in the mantle, but its effects at shallow depth are very limited (Figure 4.11, Appendix Figure B.27). Near the surface, the mantle upwelling is slightly skewed towards the trailing plate, which becomes hotter than the leading plate. However, the temperature anomaly is only about 0.2 °C, barely causing any perturbation in melt fraction. As a result, the topography asymmetry from ridge migration is negligible (Figure 4.9c). The advected heat from the mantle flowing upward at the base of the leading plate and mantle flowing downward at the base of the trailing plate creates the strongest signal in the topography asymmetry, with a maximum amplitude of about 10 m.

As the effect of ridge migration on topography is insignificant, ridge migration is not a plausible explanation for the topography asymmetry.

4.4.5 Flexure

Flexure of the oceanic lithosphere contributes to the topography of mid-ocean ridges [e.g., *Cochran*, 1979; *Buck*, 2001; *Shah and Buck*, 2003]. The elastic oceanic lithosphere deflects in response to negative loads (buoyancy force from mantle upwelling) at ridge axis, or positive loads off-axis (water column deepening, sediment thickening and plate cooling). The amount of deflection depends on the flexural rigidity, which is a function of the elastic thickness of the plate, and on the wavelength of the load. The more rigid a plate is, the less it will deflect. Elastic thickness is determined by the thermal structure of the plate, and can be approximated by the depth of the 600 °C isotherm [*Watts*, 2007].

With asymmetric spreading, the faster-moving side is hotter, and therefore should have a small elastic thickness and is less likely to flexurally support the

negative load from mantle upwelling, resulting in even higher topography. Thus, flexure would further increase Δh_{F-S}, instead of suppressing it.

Flexure might amplify the effects of mantle wind and mantle temperature anomalies. This effect would be small, though, as these processes do not significantly change the thermal structure of the shallow lithosphere, where elastic flexure takes place. The source of buoyancy in these models is also quite deep. Therefore, it is unlikely that plate flexure can counteract the asymmetric spreading and explain the observed topography asymmetry.

4.4.6 Off-Axis Volcanism

Off-axis volcanism punctuates the oceanic lithosphere and creates elevated topographical features like seamounts and volcanic mounds. If a large number of seamounts is present on the slower-moving plate, they may well reverse the pattern of asymmetric topography. However, we do not expect more robust off-axis volcanism on the slower-moving plate, as this side is associated with colder mantle and less melting (Figure 4.6a). Although our compilation does show that at a few locations along the Southern East Pacific Rise, Northeastern Pacific-Antarctic Ridge, Juan de Fuca Ridge and Southern Mid-Atlantic Ridge, seamount distribution is asymmetric and more seamounts are present on the slower-moving plate, these examples are rare and do not contribute much to the global topography asymmetry deviation. The anomalous topography asymmetry persists at segments without the presence of seamounts.

4.4.7 Crustal Thickness

Crustal thickness is an important contributor to the seafloor topography, and it can vary by more than a factor of two at slow- and ultraslow-spreading ridges [*Tolstoy et al.*, 1993; *Hooft et al.*, 2000; *Niu et al.*, 2015], and by more than 2 km at fast-spreading ridges [*Barth and Mutter*, 1996; *Canales* et al., 2003; *Aghaei* et al., 2014]. Assuming isostasy and a constant crustal density, the crustal thickness variations may cause topography variations of:

$$\Delta h = \left(\frac{\rho_m - \rho_c}{\rho_m - \rho_w}\right) \Delta H \approx 0.22 \Delta H \qquad (4.4)$$

where ΔH is the crustal thickness variation, ρ_c is the density of crust. A few kilometers of crustal thickness difference can create topography variations of more than 1000 m. Crustal density variations likely have a smaller effect on topography but cannot be completely ruled out. For example, *Toomey and Hooft* [2008] proposed crustal density variations of 150 kg/m^3 due to magmatic differentiation, which, if uniformly distributed throughout a 6-km thick crust, would generate about 320 m of topography.

When predicting the topography from our models (Equation 4.1), due to the lack of constraints, we assumed a constant crustal thickness and equal accretion of crust on both sides of the ridge. However, the unexplained topography asymmetry forces us to question the validity of this assumption.

In fact, how crust is distributed at asymmetrically spreading ridge segments is not well understood. Few seismic studies have constrained crustal thickness variations significantly off the ridge axis. Crust is accreted in a region that extends only a few kilometers off the axis [*Vera et al.*, 1990; *Bai and Montési*, 2015]. It is

conceivable that the slower-moving plate stays in this accretion zone longer than the faster-moving plate. If the crustal accretion rate is fixed, more crustal materials may accumulate on the slower-moving plate. In this case, the crustal thickness of the slower-moving plate will be larger than that on the faster-moving plate. The thicker crust will result in higher topography on the slower-moving side, and offset the topographic effects of asymmetric spreading.

The amount of crustal thickness difference needed to compensate the topographic effects of asymmetric spreading can be calculated by combining Equation 4.4 with Equation 4.3 (Figure 4.12).

$$\Delta h = -3.45A_{\mathrm{s}}^2 + 290A_{\mathrm{s}} - 5865 \tag{4.5}$$

Based on the calculation, even with a high degree of spreading asymmetry of 75%, a crustal thickness difference of 3 km is sufficient to neutralize the topography asymmetry. It would be interesting to test this hypothesis with crustal thickness determination at some of the segments where we predict the largest Δh_{C}.

4.5 Conclusions

Our compilation of seafloor topography data shows that topography asymmetry is ubiquitous along the ridges and varies segment-to-segment. By creating different rate of plate aging across ridge axis, asymmetric spreading can produce significant topography asymmetry at mid-ocean ridges. Surprisingly, the link between the topography asymmetry and the spreading asymmetry is missing. Whereas asymmetric spreading predicts that the faster-moving plate should be more elevated than the slower-moving plate, by up to 1500 m, and that the asymmetry increases
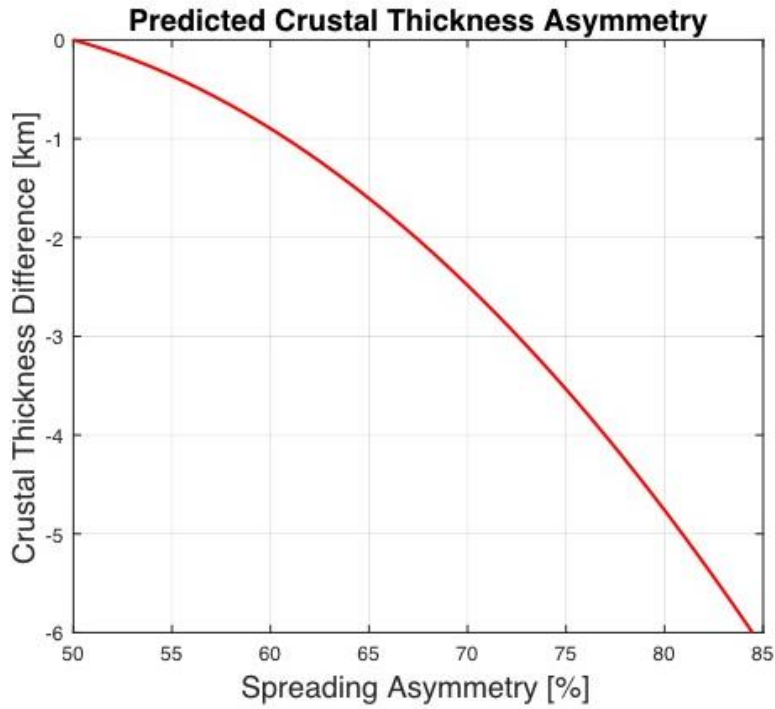
Figure 4.12 Crustal thickness difference between the faster-moving and slower-moving plates needed to explain the trend of corrected topography asymmetry vs. spreading asymmetry: $\Delta H = \frac{\rho_m - \rho_c}{\rho_m - \rho_w}(-0.75A_s^2 + 63A_s - 1275)$.

with increasing degree of spreading asymmetry and decreasing spreading rate, neither trend is visible in the observations. The observed topography asymmetry is consistently smaller than the model predictions, and there are several instances where the faster-moving plate is even at lower elevation than the slower-moving plate. We argue that the topography asymmetry from asymmetric spreading is compensated by the effects of asymmetric crustal thickness. Asymmetric crustal thickness may be an intrinsic feature of asymmetric spreading, with thinner crust on the faster-moving plate, and thicker crust on the slower-moving side, as the slower-moving plate spends more time in the crustal accretion zone at the ridge axis. Background mantle flow and mantle thermal anomalies may contribute to topography asymmetry, but their effects are likely limited.

Chapter 5: Mid-ocean ridges blowing in the mantle wind

Abstract

Mid-ocean ridges are underlain and influenced by mantle wind, the pressure-driven horizontal flow in the low-viscosity asthenosphere. Near the ridge axis, mantle wind follows the lithosphere morphology. Variations in lithospheric thickness result in enhanced or suppressed mantle upwelling, which perturbs melt generation and migration, and leads to variations in crustal thickness and seafloor topography. We construct three-dimensional models of segmented mid-ocean ridge over which the mantle wind is blowing, and demonstrate that the direction of mantle wind relative to ridge axes determines the pattern of perturbations at ridges. Ridge-perpendicular, ridge-parallel, and oblique asthenospheric flows affect the mid-ocean ridges differently, resulting in distinct variations in crustal thickness and topography. Our model provides an explanation alternative to ridge migration for the observed changes in axial depth and geochemistry across ridge offsets. It may also be used to constrain the global mantle wind flow field.

5.1 Introduction

Mid-ocean ridges, where the divergence of tectonic plates occurs, are underlain by the mechanically weak asthenosphere in the upper mantle. Pressure gradients associated with mantle upwellings (plumes) and downwellings (subductions) [e.g., *Phipps Morgan and Smith*, 1992; *Höink and Lenardic*, 2010],

113

mantle density heterogeneities [e.g., *Behn et al*., 2004], continental keels [e.g., *Harig et al*., 2010], and/or asthenospheric thickness variations [e.g., *Buck et al*., 2009] may drive a horizontal asthenospheric flow faster than plate motion by an order of magnitude and with a different direction [e.g., *Vogt*, 1971; *Phipps Morgan et al*., 1995; *Yale and Phipps Morgan*, 1998; *Winterbourne et al*., 2009; *Conrad and Behn*, 2010; *Parnell-Turner et al*., 2014]. This horizontal asthenospheric flow, also known as mantle wind, has been proposed to deflect mantle plumes [*Steinberger and O'Connell*, 1998; *Steinberger*, 2000], induce intraplate volcanism [*Conrad et al.*, 2011; *Ballmer et al.,* 2013], and cause subslab anisotropy at subduction zones [*Paczkowski et al.,* 2014a, b]. Mantle wind also blows at mid-ocean ridges, where it sways the plate-driven mantle upwelling, perturbs mantle melting, and at the surface, impacts ridge segmentation, crustal thickness, seafloor topography, off-axis volcanism, and basalt geochemistry [e.g., *Conder et al*., 2002; *Yamamoto et al*., 2007a; *Buck et al*., 2009; *Ballmer et al*., 2013; *VanderBeek et al*., 2016].

Interactions between the mantle wind and mid-ocean ridges have typically been studied numerically in two-dimension, assuming a mantle wind direction perpendicular to the ridge axis [*Conder et al*., 2002; *Toomey et al*., 2002]. Previous models show that the pressure-driven asthenospheric flow follows the morphology of the overlying lithosphere. As the lithosphere thins towards the ridge axis, the mantle wind develops an upwelling component on the leading (upwind) side, and a downwelling component on the trailing (downwind) side, creating an asymmetric mantle flow pattern. Mantle melting is accordingly affected. The modeled mantle wind successfully explained the across-ridge differences in seismic velocity [*Forsyth*

et al., 1998; *Toomey et al*., 1998] and electrical conductivity [*Evans et al*., 1999] at the MELT region of the East Pacific Rise [*MELT Seismic Team*, 1998]. As it also produces horizontal shear at the base of the plate, ridge migration may cause similar effects on mid-ocean characteristics [*Katz et al.,* 2004; *Weatherley and Katz*, 2010] but probably of a smaller magnitude than mantle wind (Chapter 4).

Although the previous numerical models mentioned above reproduced the observed asymmetries in the target region well, they did not consider the fundamentally three-dimensional nature of the mantle wind. At subduction zones, the orientation of background mantle flow relative to the trench is an important factor for explaining the global variations in subslab seismic anisotropy [*Paczkowski et al*., 2014a, b]. It may have similar significance at mid-ocean ridges. Global mantle flow models [e.g., *Yamamoto et al*., 2007b; *Conrad and Behn*, 2010] show that mantle wind flows obliquely to the axes of most ridges. If the ridge is long and straight, it may be valid to simply ignore the ridge-parallel component of the mantle wind, reducing the total effect to that of an effective mantle wind, akin to the effective spreading rate discussed previously [*Montési and Behn*, 2007]. However, the effect is likely more complex for segmented ridges, where ridge-parallel flow brings materials with contrasting properties across the ridge offset [e.g., *Vogt and Johnson*, 1975; *Katz et al.,* 2004; *Weatherley et al.*, 2010]. A better understanding of the interactions between mid-ocean ridges and mantle wind requires investigating the effects of mantle wind obliquity.

In this paper, we present three-dimensional numerical models of segmented mid-ocean ridges with mantle wind blowing at different angles. We show that the

ridge-perpendicular and ridge-parallel flows affect segmented mid-ocean ridges differently. The mantle wind direction controls the location of enhancement and reduction in mantle upwelling and along-axis variations of crustal thickness and topography.

5.2 Model Setup

Three-dimensional numerical models are constructed to investigate the influence of mantle wind on segmented mid-ocean ridges. The mantle velocity and temperature field are solved using the commercial finite element software COMSOL Multiphysics®, assuming an incompressible mantle with a constant density. A ridge-transform-ridge geometry is applied to divide the top surface of the model into two plates, where half-spreading rates are imposed (Figure 5.1). The mantle wind is simulated as a Poiseuille-like flow, driven by pressure gradients applied on the side and bottom boundaries of the computational domain. Specifically, we impose on the side and bottom boundaries a pressure function that varies as

$$P(x, y) = \frac{\partial P}{\partial x} x + \frac{\partial P}{\partial y} y \qquad (5.1)$$

where $\partial P/\partial x \equiv G_P \sin \theta$ and $\partial P/\partial y \equiv G_P \cos \theta$, with G_P and θ the magnitude and azimuth of the pressure gradient. The temperature on the top and bottom of the model are set to 0 °C and 1375 °C, respectively. To ensure a reasonable temperature for the incoming asthenospheric flow, we impose on the side boundaries the temperature solution from half-space cooling model [*Turcotte and Schubert*, 2002]. A temperature-dependent viscosity with a viscoplastic approximation for brittle weakening is adopted [*Behn et al.*, 2007] and the effects of hydrothermal cooling are

116

approximated as an enhanced thermal conductivity [*Phipps Morgan and Chen*, 1993;

Roland et al., 2010]. A triangular mesh is applied on the top boundary, with

refinement towards the plate boundaries, where the minimum element size is no

larger than 10 km. The mesh is extruded downward to cover the whole computational

domain, with vertical spacing increasing from ~6.5 km near the top boundary to 20

km close to the bottom. In our numerical study, we vary the full-spreading rate (from

2 cm/yr to 12 cm/yr), the length of the transform fault (from 50 km to 200 km), and

the magnitude and azimuth of the mantle pressure gradient (from 0 Pa/m to 2 Pa/m,

and from 0° to 135°, respectively). Model geometry and key boundary conditions are

illustrated in Figure 5.1.

Melt production, migration, crustal thickness and topography are calculated

during postprocessing in MATLAB® using the MeltMigrator software [*Bai et al.*,

2017], based on the mantle flow and temperature structure solved in COMSOL

Multiphysics®. Melt fraction is estimated using a melting parameterization, a linear

function of temperature [*Reid and Jackson*, 1981]. We assume the newly-formed melt

rises vertically through the partial melting region under its buoyancy, and then moves

towards the ridge axis following a low-permeability barrier at the base of thermal

boundary layer [*Sparks and Parmentier*, 1991; *Montési et al.*, 2011]. The location of

permeability barrier is determined using the formula: $T_{\text{barrier}} = 1240 + 1.9z$, where

T_{barrier} is the temperature of the barrier in °C, and z is depth in km [*Montesi and*
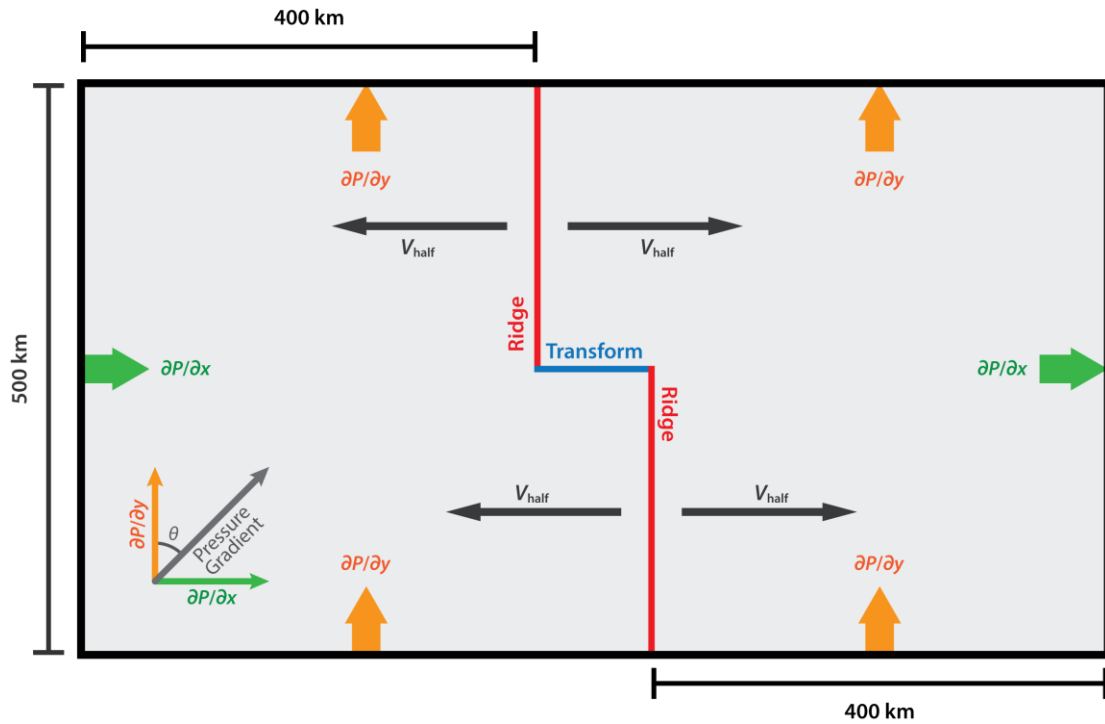
Figure 5.1 Model geometry and key boundary conditions in map view. The computational domain is 500 km wide and 400 km deep (the model is three-dimensional, and the depth dimension is not shown in this figure). The red segments represent ridges and the blue segment represents the transform fault. The length of transform fault is varied in the model. Two plates separated by the ridge-transform-ridge boundaries move perpendicular to the ridges in opposite directions with half-spreading rate of V_{half}. A pressure function (Equation 5.1) is imposed on the side boundaries to drive the mantle wind. The magnitude and azimuth of the mantle wind is controlled by $\partial P / \partial x$ and $\partial P / \partial y$, pressure gradients in x- and y-direction, respectively.

Behn, 2007; *Hebert and Montesi*, 2010]. The permeability barrier morphology controls melt migration pathways. At plate boundaries (ridge and transform segments), we define a melt extraction zone that represents the effects of structural damage, such as diking and fracturing, associated with melt extraction [*Hebert and Montési*, 2011]. The width and depth of the melt extraction zone are set to 4 km and 20 km respectively, as constrained by *Bai and Montési* [2015]. If the melt enters the melt extraction zone, it will be extracted to the surface and contribute to the crustal thickness. By tracking the melt pathways and their destinations on the plate boundaries, we calculate the melt flux and associated crustal thickness along the plate boundaries according to:

$$H = \frac{1}{V_{\text{full}}} \int f \, dl \tag{5.2}$$

$$f = \int p \, dz \tag{5.3}$$

$$p \equiv \max\left(v_z \frac{\partial F}{\partial z}, 0\right) \tag{5.4}$$

where H is the crustal thickness along the axis, V_{full} is the full-spreading rate, f is the melt flux, l is the distance along melt pathways, p is the melt production, v_z is the mantle upwelling velocity and F is the melt fraction. After the crustal thickness profile is obtained, a smoothing algorithm is applied to each plate boundary segment to remove numerical noise. The smoothing can be interpreted as a representation of the crustal-level redistribution of melt. Finally, assuming isostasy and constant crustal density, topography is calculated from crustal thickness using a simple linear relation $\Delta h = 0.23\Delta H$ [*Turcotte and Schubert*, 2002]. A detailed description of our numerical method is documented by *Bai et al.* [2017].

To better illustrate the influence of three-dimensional mantle wind on mid-ocean ridges, we present our mantle wind model results as "perturbations", or differences with models without mantle wind. Specifically, we calculate the perturbations in velocity, temperature, melt fraction, melt production and melt flux. We also focus on the along-axis variations of crustal thickness and topography, and calculate the topography difference between ridge segment ends across the transform fault.

5.3 Model Results

Our numerical experiments reveal how mantle wind impacts mantle flow, which modifies the thermal structure of the ridge, the degree, extent and rate of mantle melting, melt migration pathways, and the crustal thickness and topography at mid-ocean ridges. The influence of mantle wind depends on the angle between the mantle wind and the ridge, the magnitude of the mantle pressure gradient, the spreading rate of the ridge, and the length of the ridge offset.

5.3.1 General Effects of Mantle Wind

The most prominent effect of the mantle wind is that it creates a Poiseuille-like flow in the asthenosphere, superposed on the passively driven mantle corner flow [*Höink and Lenardic*, 2010]. The horizontal velocity of the Poiseuille-like flow decreases with decreasing depth. Near the surface, the asthenospheric flow follows the morphology of lithosphere-asthenosphere interface. As the lithosphere is thinnest at the ridge axis, the mantle wind develops an upward vertical component when

approaching the ridge axis and a downward vertical component when moving away from the ridge axis, resulting in enhancement and reduction in mantle upwelling at the ridge axis (Figure 5.2). This behavior is in accordance with the previous studies [*Conder et al.*, 2002; *Toomey et al.*, 2002; *Katz et al.*, 2004; *Weatherley and Katz*, 2010].

Mantle wind may also carry heat along its path, and perturb the temperature field at mid-ocean ridges. To first order, the thermal structure of an ordinary mid-ocean ridge is controlled by vertical heat conduction, as represented by the half-space cooling model [*Turcotte and Schubert*, 2002]. The further away from its original ridge axis a column of mantle is, the older and colder it gets. With mantle wind, however, a cross-isochron horizontal mobility is enabled. Older, colder materials can be blown toward a younger, warmer region, and *vice versa*. The resulting temperature perturbation may reach up to 20 °C, and lead to up to 2% change in the degree of mantle melting (Figure 5.3). Importantly, it affects the permeability barrier morphology, which is roughly associated with the 1240 °C isotherm [*Kelemen and Aharonov*, 1998; *Hebert and Montési*, 2010]: the barrier gets steeper and shrinks upwind, and gets shallower with milder slope downwind (Figure 5.3). This changes melt migration pathways, the area of melt collection, the rate and distance of melt transport, and potentially the refertilization of depleted mantle.

The melt production rate, calculated as the product of vertical mantle velocity and vertical melt fraction gradient (Equation 5.4), is dominated by the vertical velocity perturbation. As a result, melt flux (Equation 5.3) is enhanced at locations
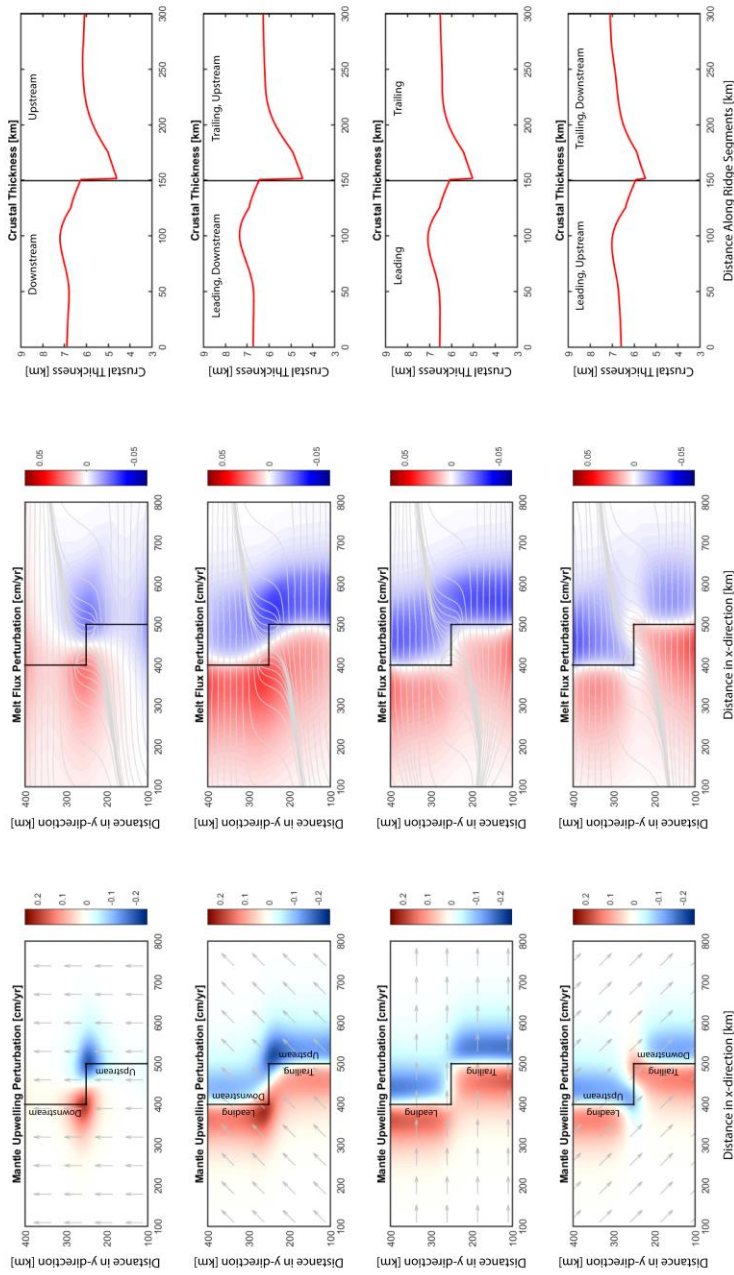
Figure 5.2 Perturbations of mantle upwelling velocity (left column), melt flux (middle column), and profile of on-axis crustal thickness for models with a full-spreading rate of 6 cm/yr, a transform fault length of 100 km, and a mantle pressure gradient of 1 Pa/m. Each row corresponds to a different mantle wind azimuth: from top row to bottom, 0°, 45°, 90° and 135°. The first column illustrates in map view perturbations in vertical mantle velocity at a depth of 40 km. Red color represents enhancement and blue color represents reduction. Pressure gradient directions are shown in the background as gray arrows. The second column demonstrates perturbations in melt flux in map view. Red color represents enhancement and blue color represents reduction. Gray streamlines indicate the melt migration pathways on the permeability barrier. The third column shows crustal thickness profiles along the ridge segments.

122
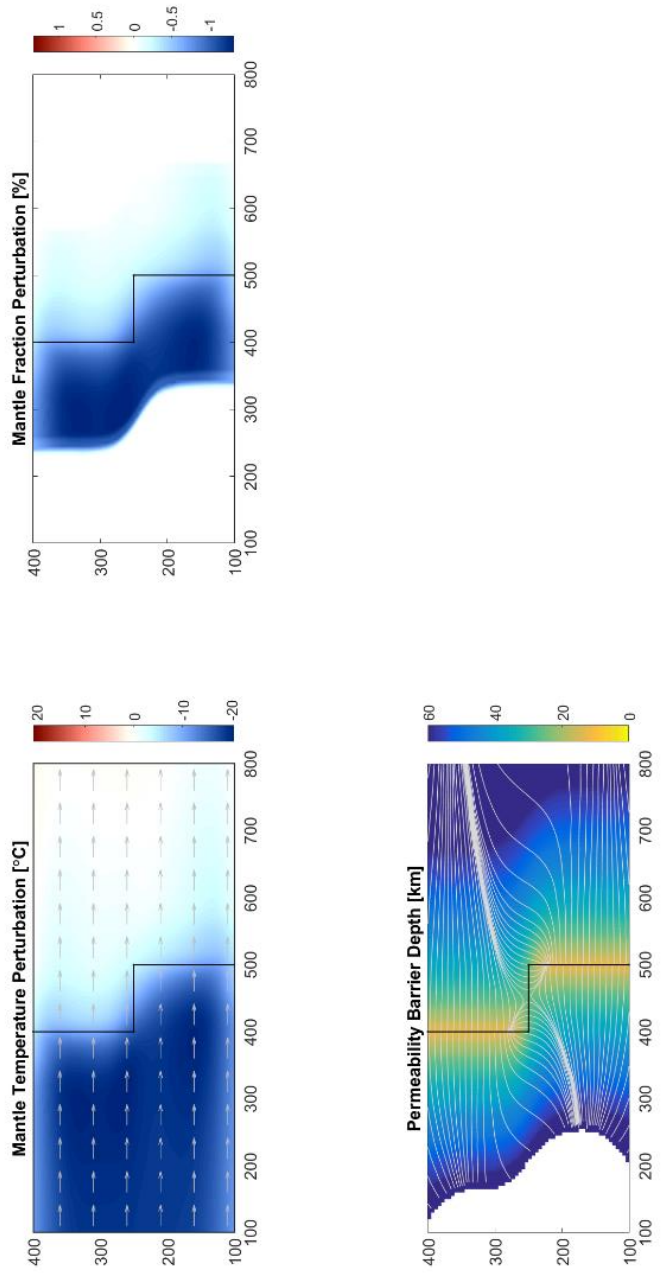
Figure 5.3 Perturbations in mantle temperature (a) and melt fraction (b) at depth of 40 km, and depth of permeability barrier (c) for a model with full-spreading rate of 4 cm/yr, transform fault length of 100 km, mantle pressure gradient of 1 Pa/m and wind angle of 90°. The white lines in panel (c) follow melt migration pathways on the permeability barrier. No permeability barrier is formed in the blank area in panel (c).

with increased mantle upwelling and reduced where mantle upwelling is decreased (Figure 5.2). Melt flux is the dominant control on on-axis crustal thickness. Stronger melt flux leads to thicker crust, while weaker melt flux produces thinner crust. Variations in crustal thickness will further lead to changes in topography. Thus, through its influence on the mantle upwelling and melting, the deep-rooted mantle wind is able to express itself on the surface as along-axis variations in crustal thickness and topography. The ridge segment that stands downwind from the transform fault tends to have thinner crust and lower elevation than the upwind segment (Figure 5.2).

5.3.2 Systematics

5.3.2.1 Effects of the Wind Angle

Our three-dimensional models reveal that the pattern of perturbation caused by mantle wind changes dramatically with wind angle—the angle between the mantle wind direction and the ridge orientation.

When the mantle wind is perpendicular to the ridges (θ=90°), mantle upwelling is enhanced underneath the leading (upwind) plate, increasing melt production and melt flux on that side. This effect is mitigated somewhat by colder off-axis materials blown towards the ridge axis by the mantle wind (Figure 5.3). Underneath the trailing (downwind) plate, the asthenospheric flow moves downslope and away from the ridge axis, suppressing mantle upwelling and reducing melt production and flux (Figure 5.2). Most of the melts collected at the end of the leading ridge segment are from regions of increased melt flux, while the melts collected at the end of the trailing ridge are mostly from regions where the melt flux is reduced. Thus,

124

at the ridge-transform intersection, the leading ridge has a thicker crust and higher topography than the trailing ridge across the transform fault (Figure 5.2).

When mantle wind is parallel to the ridge (θ=0°), the wind moves laterally in the along-axis direction without inducing significant perturbations in mantle upwelling outside of the transform fault region. Close to the oceanic fracture zone, though, the age contrast between the juxtaposed plates creates a step at the base of the lithosphere. As the mantle wind approaches the transform fault along the upstream ridge, it follows the thickening lithosphere and move downward, reducing mantle upwelling at the tip of the ridge. Along the downstream ridge, the mantle wind develops an upward motion at the tip of the ridge, boosting the local mantle upwelling (Figure 5.2). The effects of these upwelling perturbations on melting are partially offset by the anomalous temperature of the material transported across the fracture zone (hot where upwelling is reduced and cold where it is enhanced, Figure 5.4). Dominated by the mantle upwelling perturbation, the melt production perturbation is localized at the end of each ridge segment. The upstream ridge is fed by a region of decreased melt-flux, while the downstream ridge is within the region of increased melt flux. This results in larger overall crustal thickness and higher topography on the downstream ridge than on the upstream ridge (Figure 5.2).

At an oblique wind angle, the mantle wind will have both ridge-perpendicular and ridge-parallel components. Its effects on mid-ocean ridges can be approximated as the superposition of the perturbations from each component. The strengths of the two components depend on the wind directions, as well as the plate boundary geometry. In our model, we use a left-lateral ridge-transform-ridge geometry. At a
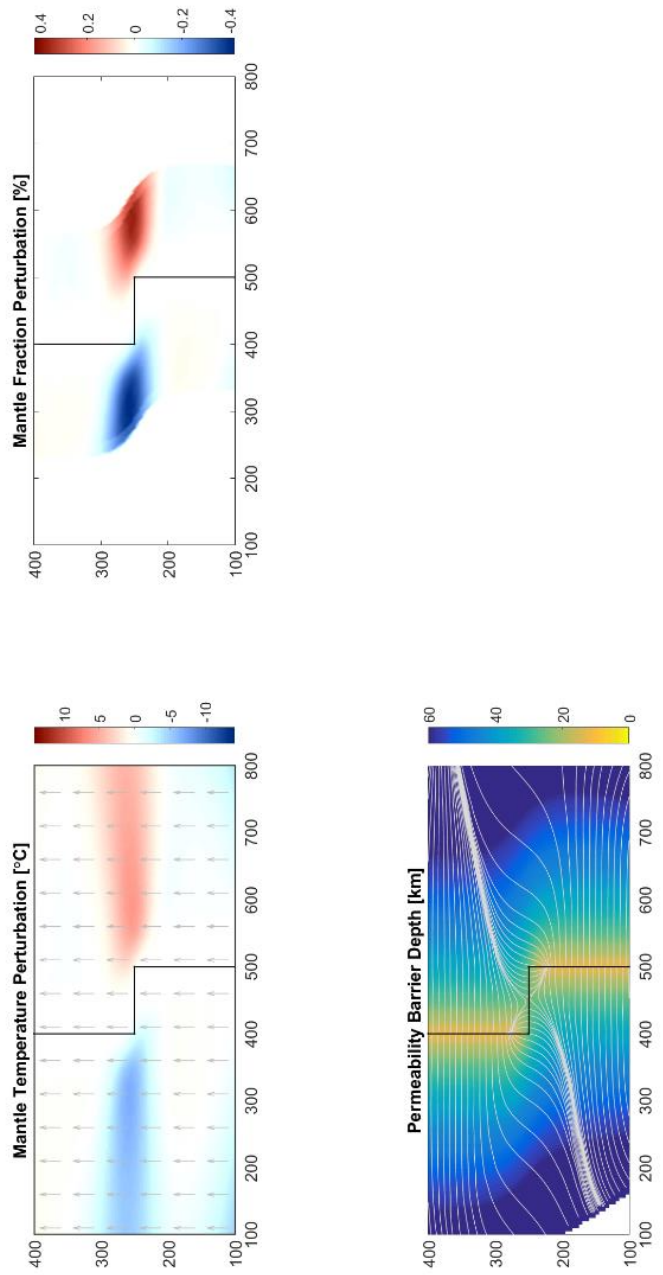
Figure 5.4 Panel representations are same as in Figure 5.3, except that this is for a model with wind angle of 0°.

wind angle of 45°, the leading ridge relative to the ridge-perpendicular flow is also the downstream ridge relative to the ridge-parallel flow. Therefore the perturbations from both components reinforce each other, creating the strongest mantle wind impacts. On the contrary, with a wind angle of 135°, at the ends of the ridge segments, perturbations from the two components have opposite signs. The mantle wind influences are thus tuned down, or even canceled out, resulting in a complex, alternating pattern of upwelling enhancement and reduction, and nearly symmetric crustal thickness profiles across the transform fault and (Figure 5.2).

Theoretically, the possible wind angle may range from 0° to 360°. We only test mantle angle from 0° to 135°, because our simple ridge-transform-ridge plate boundary geometry has a central symmetry. For example, the effect of a wind angle of 225° is identical to that of a wind angle of 45° after a 180° rotation, except that the sign of the perturbation and the topography differences between the two ridge segments is switched. This has been confirmed by our validation models. Thus, we can safely extrapolate our results to cover the full range of wind angle from 0° to 360°.

Compilation of model results reveals that the topography contrast between the ends of two ridge segments separated by the transform fault is a sinusoidal function of the wind angle (Figure 5.5). With our left-lateral plate boundary geometry, the topography contrast increases with wind angle increasing from 0° to 45°, reaching its peak at the 45°, then decreases with increasing wind angle, changing from positive to negative between 135° and 180°, hitting the minimum at 225°, and after the turning point, it starts to rise with the wind angle again.

127

5.3.2.2 Effects of the Wind Magnitude

Increasing the magnitude of the mantle pressure gradient amplifies the perturbations but does not significantly change the perturbation patterns. The amplifying effect also depends on wind angle. At a wind angle of 0°, a mantle pressure gradient of 2 Pa/m may create a topography contrast of ~500 m at ridge system with a full-spreading rate of 6 cm/yr, which is more than 100 m larger than the topography contrast created by a pressure gradient of 1 Pa/m at the same angle. In contrast, increasing the mantle pressure gradient from 1 Pa/m to 2 Pa/m at an angle of 90° only increases the topography contrast by less than 50 m (Figure 5.5b). This indicates that the ridge-parallel asthenospheric flow is more sensitive to the mantle wind magnitude increase than the ridge-perpendicular flow, probably due to a lack of interference with the passively driven mantle flow in this direction.

5.3.2.3 Effects of the Spreading Rate

Ridges with different spreading rates react to mantle wind differently due to the competition between the effects of modifying mantle upwelling and advecting temperature anomalies (Figure 5.5a). At the slowest full-spreading rate (e.g., 2 cm/yr), the temperature reduction dominates the perturbation of melting. The overall melt supply to the ridge is reduced, especially at the ridge-transform intersection (Figure 5.6), leading to a small topography contrast between two ridge segments. With increasing spreading rate, the perturbations in mantle upwelling grow in importance while the temperature perturbation diminishes. The amplified melt flux perturbation creates the largest topography contrast at full-spreading rate between 4 cm/yr and 6 cm/yr. At spreading rates higher than 6 cm/yr, however, the increase in
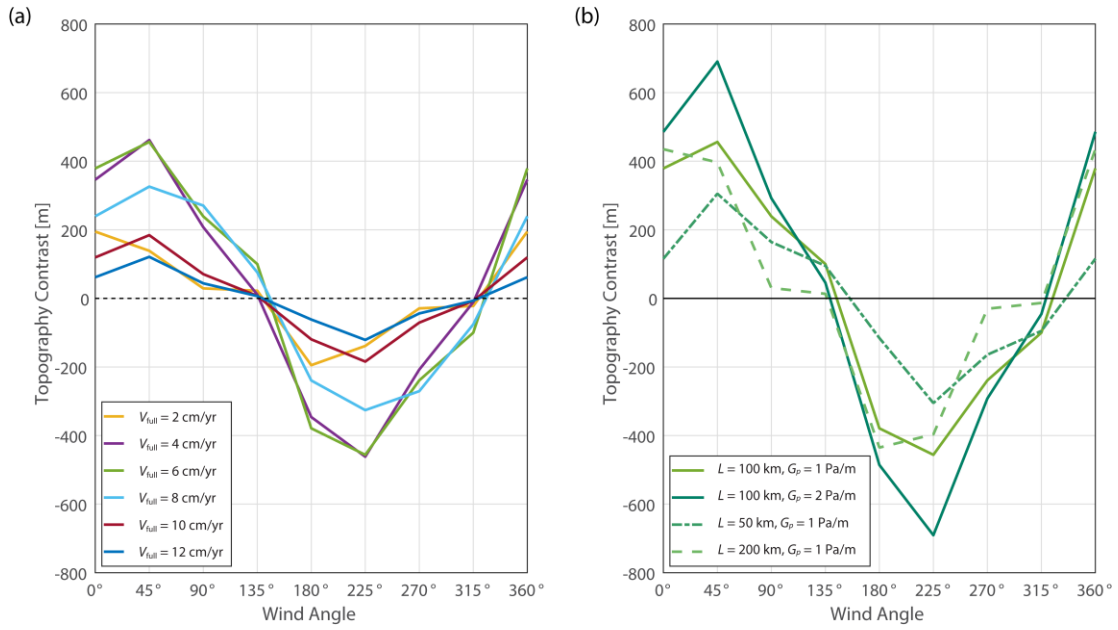
Figure 5.5 (a) Compilation of topography contrast from models with spreading rates ranging from 2 to 12 cm/yr, a transform fault length of 100 km, and a mantle pressure gradient magnitude of 1 Pa/m. (b) Compilation of topography contrast from models with a full spreading rate of 6 cm/yr, and varying transform fault lengths and pressure gradient magnitudes. V_{full} is the full spreading rate, L is the length of transform fault, and G_p is the magnitude of pressure gradient.
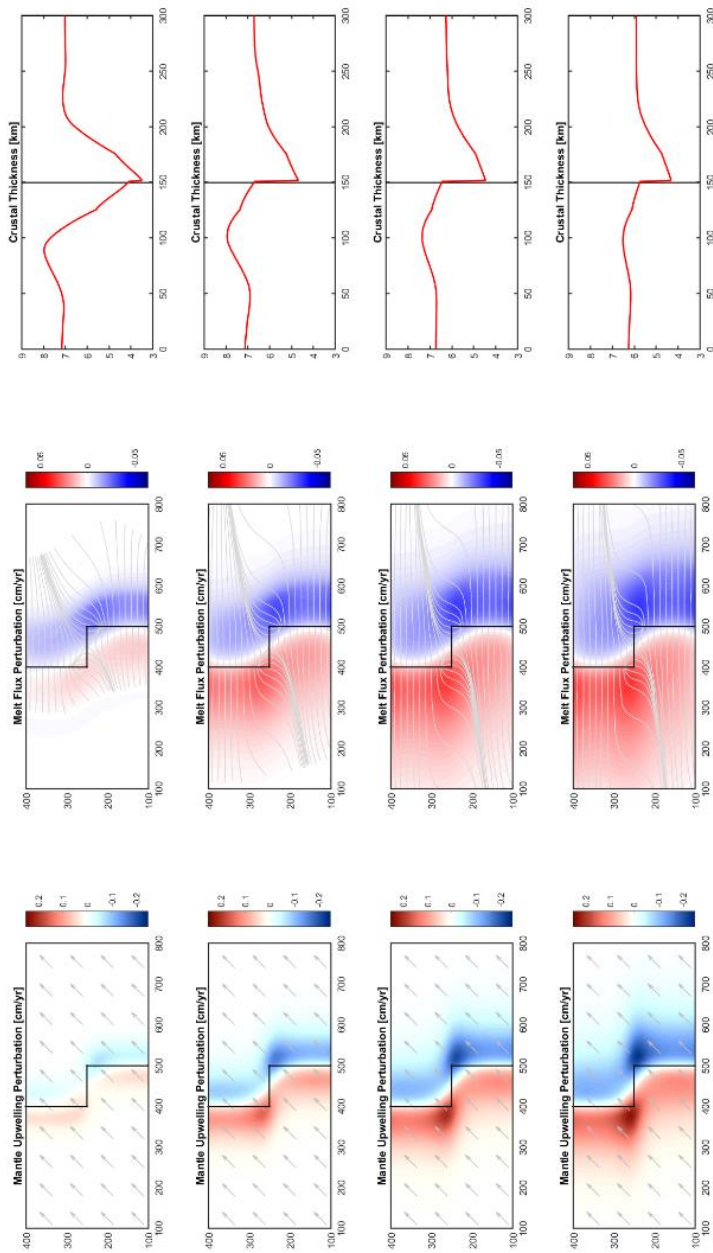
Figure 5.6 Results for models with a transform fault length of 100 km, a mantle pressure gradient of 1 Pa/m and a wind angle of 45°. From top row to bottom row, results from models with full-spreading rates of 2 cm/yr, 4 cm/yr, 6 cm/yr and 8 cm/yr are shown. Column representations are same as in Figure 5.2.

130

the melt flux perturbation amplitude no longer scales with spreading rate. Crustal

thickness is consequently decreased, causing the topography contrast to shrink.

5.3.2.4 Effects of the Transform Fault Length

The perturbations caused by mantle wind vary with transform fault lengths.

Most of the models with transform fault lengths of 50 km and 200 km produce

smaller topography contrast than models with a 100 km transform fault (Figure 5.5b).

The origin of the dependence on transform length is two-fold.

(1) With a ridge-perpendicular mantle wind, the topography contrast is

controlled by source regions of melt supply (Figure 5.7). With a short transform fault,

the leading ridge collects slightly more melts from the melt-flux-increased region

than from the melt-flux-decreased region, while the trailing ridge collects slightly

more melts from the melt-flux-decreased region. As transform fault length increases,

a larger fraction of the melt collected at the leading ridge originates underneath the

leading plate, where melt flux enhancement occurs, and the trailing ridge gets more

and more melt from regions with reduced melt flux. This contrast in melt source

region leads to large topography contrasts. However, increasing the transform fault

length also leads to expansion of unperturbed areas. If a transform fault is too long,

the end of the ridge segment will collect melts from unperturbed regions, and the

topography contrast will decrease.

(2) With a ridge-parallel mantle wind, the lithosphere morphology plays a

more important role. The transform fault length primarily determines the age contrast

between juxtaposing plates along the offset. The longer the transform fault, the larger

the age contrast across the fracture zone is. A larger age contrast deepens the

131
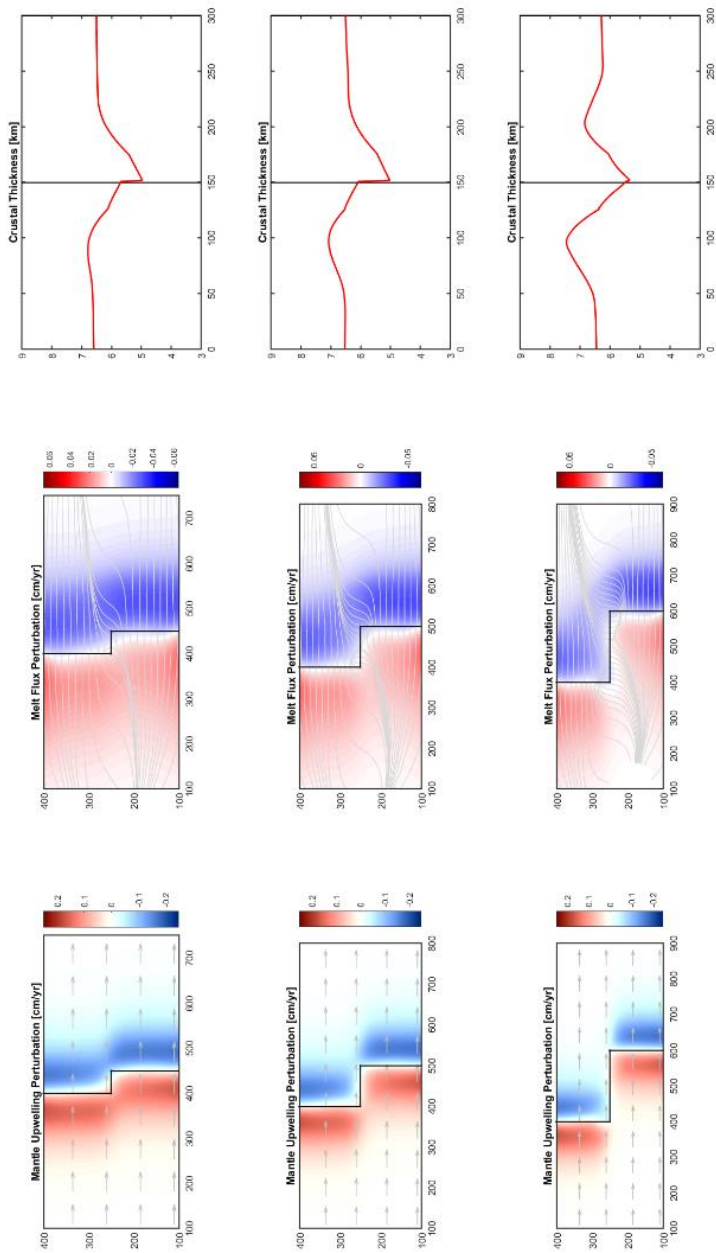
Figure 5.7 Results for models with a full-spreading rate of 6 cm/yr, a mantle pressure gradient of 1 Pa/m and a wind angle of 90°. From top row to bottom row, results from models with transform fault lengths of 50 km, 100 km, and 200 km are shown. Column representations are same as in Figure 5.2.

lithosphere more towards the fracture zone, thus the along-axis asthenospheric flow will have larger perturbation in vertical velocity, resulting in larger melt production and melt flux perturbations, and eventually to a greater topography contrast.

<u>*5.4 Discussions*</u>

5.4.1 Comparisons with Observations

Our three-dimensional numerical models show that the mantle wind perturbs melt generation and migration, and creates along-axis variations in crustal thickness and topography at segmented ridges. This study provides a viable explanation for the observed changes in axial depth across ridge discontinuities: as noted by *Carbotte et al*. [2004], at fast- and intermediate spreading centers, the leading segments (relative to the ridge migration direction) are typically shallower than trailing segments (relative to the ridge migration direction) across first- and second-order discontinuities. A comparison between the model results and observations show that the mantle wind has the potential to account for the majority of observed topography contrasts (Figure 5.8).

To make the comparison, we compile along-axis topography data for major mid-ocean ridge systems, including Juan de Fuca Ridge, East Pacific Rise, Pacific-Antarctic Ridge, Southeast Indian Ridge, Central Indian Ridge, and Mid-Atlantic Ridge, using the ridge segment coordinates from a global spreading center catalog [*Gale et al*., 2013] and the topography from the ETOPO1 dataset [*Amante and Eakins*, 2009]. We calculate the topography contrast as the difference between adjacent ridge segments within 10 km of distance toward the shared discontinuity.

Data for ridge segments shorter than 50 km are removed to avoid interferences from nearby ridge offsets.

Topography contrast averages ~180 m, with a maximum value of ~810 m, and varies from ridge to ridge. It increases with full-spreading rate from 2 to 3 cm/yr, and decreases at spreading rate higher than 7 cm/yr. This is consistent with the trend predicted by our numerical model (Figure 5.8). With a mantle pressure gradient of 1 Pa/m, the predicted topography contrast maxima (occuring at a wind angle between 0° and 45°) encompasses 76.5% of the observed data, and reaches maximum for spreading rates between 4 and 6 cm/yr. The topography contrasts below that model prediction may correspond to mantle wind with a smaller pressure gradient or oriented in a less favorable direction. Data points outside the model prediction envelope can potentially be accounted for by a higher mantle pressure gradient. Besides the spreading rate, the length of discontinuity also affects the amplitude of the observed data. Maximum topography contrasts are associated with a critical transform fault length of ~100 km [*Supak et al.*, 2007], which agrees with the model results as well (Figure 5.5). Thus, the mantle wind models are capable of capturing the amplitude variations of the observed data.

5.4.2 Mantle Wind vs. Ridge Migration

The observed changes in axial depth across ridge offsets were previously attributed to the migration of ridges in a fixed hot-spot reference frame [*Carbotte et al.*, 2004; *Katz et al.*, 2004]. Here we propose an alternative explanation with the three-dimensional mantle wind models. Although mantle wind is a pressure-driven
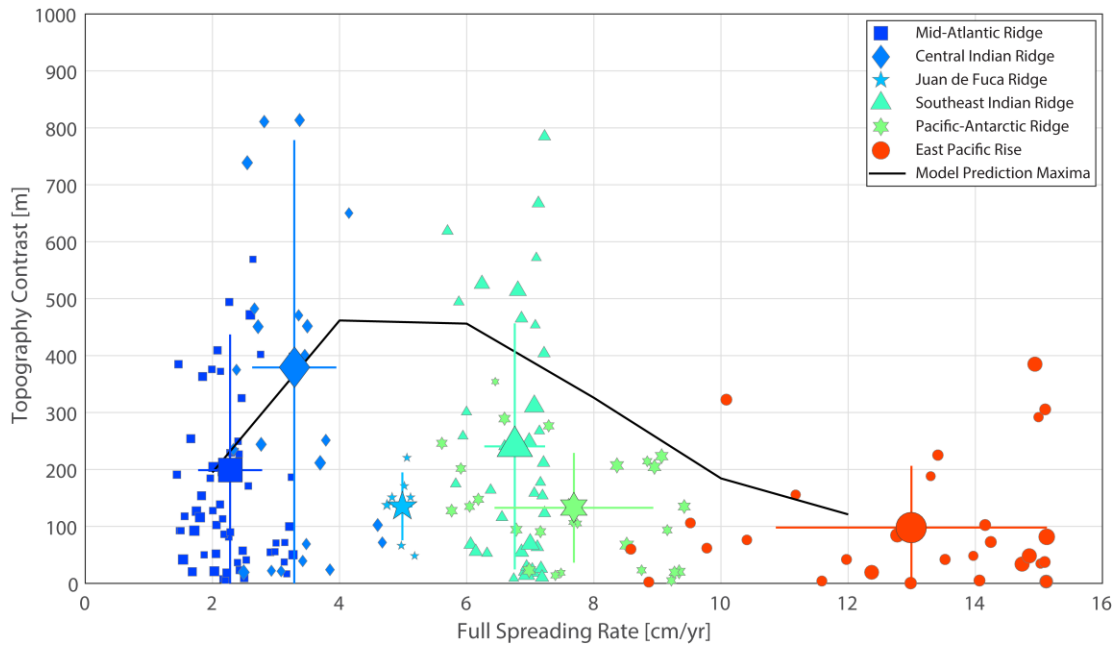
Figure 5.8 Comparison between observed (colored dots) and predicted (black curve) topography contrast. Dots with different colors and makers are data collected at different ridge systems. The mean value for each ridge system is represented as an enlarged symbol with 1-sigma error bars.

Poiseuille flow while ridge migration creates a shear-driven Couette flow, dynamically, mantle wind and ridge migration are similar in that they both induce a horizontal asthenospheric flow superposed on the passively driven corner flow at mid-ocean ridges. In either case, the induced asthenospheric flow follows the morphology of lithosphere and develops a vertical component, which enhances or suppresses the mantle upwelling at the ridge axis. Indeed, our model with a wind angle of 90° shows behaviors consistent with the previous models of both mantle wind [*Conder et al.*, 2002; *Toomey et al.*, 2002] and ridge migration [*Katz et al.*, 2004; *Weatherley and Katz*, 2010]. However, in the mantle wind model, flow is more localized to the base of the lithosphere than in ridge migration models (Chapter 4), making mantle wind a more potent source of perturbations than ridge migration.

What distinguishes our model from the previous ones is that it emphasizes the three-dimensional nature of the asthenospheric flow. Numerical models of ridge migration [*Katz et al.*, 2004; *Weatherley and Katz*, 2010] ignored the obliquity of the ridge migration direction relative to the spreading direction [*Small and Danyushevsky*, 2003]. With oblique ridge migration, the leading ridge in the ridge-perpendicular direction, where upwelling is enhanced, may very well be an upstream ridge (associated with decreased mantle upwelling) in the ridge-parallel direction. This complicates the pattern of mantle flow in a manner similar to the case of an oblique mantle wind. At the obliquely migrating East Pacific Rise, for example, the ridge segment to the south of the Siqueiros Transform is a trailing ridge but also a downstream ridge. If ridge migration is the cause of changes in axial depth, the flow azimuth would be close to 135° and the mantle upwelling at the tip of the segment

would be enhanced rather than reduced as predicted by the previous models (Figure 5.2). The resulting topography contrast would be inconsistent with the observation. Considering background mantle flow may provide a more viable explanation to the observed topography contrast.

Additionally, while the importance of mantle wind on mid-ocean ridges has been widely recognized [e.g., *Phipps Morgan and Smith*, 1992; *Conder et al.*, 2002; *Buck et al.*, 2009; *Ballmer et al.*, 2013; *VanderBeek et al.*, 2016], the effects of ridge migration appears to depend largely on the rheology and numerical techniques of choice, and have not been consistently reported [*Conder et al.*, 2002; *Katz et al.*, 2004; *Katz*, 2010; *Cuffaro and Miglio*, 2012]. *Natarov and Conrad* [2012] investigated the relative importance of Poiseuille and Couette flows in the asthenosphere using the depth-dependence of azimuthal seismic anisotropy, and found that Poiseuille flow dominates the asthenospheric flow at mid-ocean ridges. A recent high-resolution seismic anisotropy study on the oceanic lithosphere-asthenosphere system in the middle of the Pacific plate also indicated that the shear associated with plate motion is weak compared to the pressure-driven asthenospheric flow [*Lin et al.*, 2016], suggesting that the effects of ridge migration are less significant than those of the mantle wind.

5.4.3 Inference on Direction and Strength of Mantle Pressure Gradient

Despite its significant roles on global mid-ocean ridges, the direction and strength of the background mantle flow is not well constrained. Although some global mantle flow models are available [e.g., *Yamamoto et al.*, 2007b; *Conrad et al.*, 2007;

Conrad and Behn, 2010; *Natarov and Conrad*, 2012], they either do not properly represent the mantle wind, or exhibit discrepancy with each other.

Conrad et al. [2007] and *Conrad and Behn* [2010] calculated the global mantle flow driven by mantle density heterogeneities, plate motions and net lithosphere rotation, using the SKS splitting observations as constraints. Their models comprehensively represent mantle convection, a combination of both pressure-driven Poiseuille flow and shear-driven Couette flow [*Höink and Lenardic*, 2010; *Crowley and O'Connell*, 2012], and thus cannot be used to isolate the pressure-driven mantle wind in the thin layer of asthenosphere.

Natarov and Conrad [2012] calculated the Poiseuille flow component from the global mantle flow model by *Conrad and Behn* [2010], but their study required the horizontal pressure gradient to be non-parallel to plate motions and is limited by the uncertainties in the asthenosphere rheological structure. The global asthenospheric flow model by *Yamamoto et al*. [2007b] is calculated with the assumption that the pressure-driven asthenospheric flow is fed by the plumes only, ignoring the pressure gradient from subducting slabs, which has been deemed significant by others [e.g., *Höink and Lenardic*, 2010]. Unsurprisingly, the pressure-driven flow fields by *Natarov and Conrad* [2012] and *Yamamoto et al*. [2007] show a great discrepancy.

As our study has established a link between the topography contrast and the pressure-driven mantle wind, if we assume that the observed topography contrast is produced by mantle wind only, we could infer the direction of mantle wind by matching the amplitude and sign of each observed topography contrast to model predictions. For example, topography contrasts across transform faults at the Southern

138

East Pacific Rise are consistent with a mantle wind angled between 90° and 180° from the ridge azimuth, in rough agreement with the direction of the proposed asthenospheric flow in the region [*Conder et al*., 2002; *Toomey et al*., 2002]. As our method produces non-unique solutions, it can only be used as a reference for the established models. To make more rigorous prediction, detailed regional studies and associated models are necessary.

5.4.4 Implications on Basalt Geochemistry and Mantle Refertilization

The perturbations in melt generation and migration caused by the mantle wind likely affect the chemical characteristics of mid-ocean ridge basalts and mantle. Specifically, our model predicts three geochemical signatures for mantle wind. (1) The ridge segments on either side of a transform fault are supplied by different amounts of melts from source regions with different temperature, melt fraction and melt production rate. This effect may contribute to the observed geochemical segmentation [e.g., *Schilling et al*., 1982; *Machado et al*., 1982; *Langmuir and Bender*, 1984; *Thompson et al*., 1985; *Langmuir et al*., 1986]. (2) Mantle wind, if fed by a plume, may carry the chemical signature from its source and introduce more enriched basalt to the affected ridge segments [e.g., *Niu et al*., 1999]. (3) At slow-spreading ridges, where the mantle wind perturbs the temperature most effectively, the permeability barrier underneath the leading plate shrinks in size leaving a large portion of melts available to refertilize the mantle on that side.

Our three-dimensional numerical models of segmented mid-ocean ridges on which the mantle wind blows demonstrate the crucial role of the wind angle in perturbing mantle upwelling, temperature, permeability barrier depth, melt fraction, melt production, melt flux, crustal thickness and ridge axis depth. Ridge-perpendicular flow enhances upwelling underneath the leading plate, and reduces it underneath the trailing plate. Ridge-parallel flow suppresses mantle upwelling at the tip of the upstream ridge near the ridge offset, and augments mantle upwelling at the tip of the downstream ridge. As oblique mantle wind has both ridge-perpendicular and ridge-parallel components, its effects can be approximated as the superposition of these components. With a left-stepping ridge, a wind angle of 45° creates the largest topography contrast between the ends of ridge segments across transform fault. The topography contrast increases with increasing magnitude of mantle pressure gradient. The topography contrast also varies with spreading rate and transform fault length, reaching maximum values at full-spreading rate of 6 cm/yr and transform fault length of 100 km, respectively. We favor mantle wind over ridge migration as the explanation for the observed changes in axial depth across discontinuities. Our model may be helpful in constraining the global mantle flow field.

Chapter 6: Summary

Crustal thickness at mid-ocean ridges may vary along the axis within individual ridge segment or between adjacent segments, exhibit asymmetry across the axis between conjugate plates, and differ between ridge segments and transform faults. Crustal thickness variations are influenced by plate motion, mantle flow, mantle temperature, melt generation, and melt extraction. Disentangling the contributions of each process has been challenging. This dissertation presents a systematic numerical study of the different origins of crustal thickness variations at segmented mid-ocean ridges, and provides some constraints on mantle and melt dynamics. Specifically, I attribute the spreading-rate dependent crustal thickness difference between ridge and transform faults to slip-rate-dependent melt extraction along the transform faults; I predict asymmetric crustal thickness across ridge axes based on the relation between spreading asymmetry and topography asymmetry; and I propose the presence of mantle wind as an explanation for the observed along-axis crustal thickness variation patterns.

The three-dimensional numerical simulations of mid-ocean ridges with complexities such as transform faults, oblique spreading and mantle wind presented in this dissertation are made possible by the MeltMigrator software workflow: Mantle flow and thermal structures are first solved in finite element models, and then processed through the MeltMigrator software to calculate melt migration trajectories, melt flux along plate boundaries and crustal thickness distribution. The versatility of the MeltMigrator software is demonstrated in this dissertation.

141

This dissertation also highlights the crucial role of permeability barriers in melt migration. The three-dimensional morphology of permeability barriers directly controls the melt pathways and destinations, and potentially affects the rate of melt transport and the degree of mantle refertilization. Melt migration focused toward certain localities on the permeability barrier helps to create the observed along-axis crustal thickening toward the segment center and crustal thinning toward the segment ends. The spatial relation between the permeability barrier and the melt extraction zone determines whether melt eruption may occur along the transform faults.

Modeling shows that mid-ocean ridge dynamics can be significantly perturbed by asymmetric spreading and mantle wind. The fact that these phenomena are ubiquitous in ocean basins worldwide implies that mid-ocean ridges are fundamentally asymmetric. The significance of these symmetry breakers should be considered in future studies of mid-ocean ridges. The unobserved asymmetric topography predicted by asymmetric spreading models poses an enigma that requires more detailed investigations, and may lead to better comprehensions of the crustal and mantle processes. Additionally, in simulations, I catch the mantle wind at mid-ocean ridges, the understanding gained from models may help to constrain the mantle wind in reality.

Appendices

Appendix A: Supporting Information for Chapter 2

Here we provide the MATLAB®-based melt migration software MeltMigrator to calculate melt migration trajectories, estimate melt flux and predict crustal thickness distribution from user-supplied numerical models of mid-ocean ridges.

The MeltMigrator package contains a main script, `meltMain`, and a number of attendant functions, most of which are defined in stand-alone scripts. The scripts contained in the MeltMigrator package are cataloged in Table A.1, which includes an ID, a name and a brief description of each script, and the IDs of the upper-level scripts each script attends. A flowchart of major calculation steps is shown in Figure A.1.

Table A.1 A list of scripts in MeltMigrator package.

Number	Script Name	Description	Script Attended
1	**meltMain**[a]	MeltMigrator main script	-
2	**setParameters**[a]	Set key parameters	1
3	geometryTrim	Trim the edges of computational domain to avoid boundary effects	1
4	meltFunctionRJ1981	Calculate mantle melting using parameterization by *Reid and Jackson* [1981]	2
5	meltFunctionMELTS	Calculate mantle melting using thermodynamic model alphaMELTS	2
6	**lidSample**[a]	Extract the permeability barrier information	1
7	plotLidInfo	Plot the permeability barrier information	1
8	**meltCalibration**[a]	Normalize the crustal thickness to a reference value	1
9	crustalThicknessCalculation2D	Calculate crustal thickness along a vertical cross-section	8
10	**saddlePreparation**[a]	Extract key features of permeability barrier morphology	1
11	alongSlopeSlopeGrad	Describe the horizontal gradient of permeability barrier slope	10
12	inBounds	Determine if a point is within the computational domain	11, 13, 14, 15
13	alongSlopeGrad	Describe the slope of permeability barrier	10, 16
14	**meltTrajectorySeed**[a]	Set up starting points for melt trajectory calculation	1
15	crossToGrad	Describe the contour of permeability barrier	14
16	**meltTrajectory**[a]	Calculate melt trajectories	1
17	lineTruncate	Remove overlapping points on a line	16
18	lineSegmentIntersect[b]	Calculate intersections of line segments	16
19	lineStore	Store current melt trajectory information	16
20	**meltSwath**[a]	Define the space between adjacent melt trajectories as melt swaths	1
21	lineSampleDepth	Truncate and resample melt trajectories	20
22	assignSegment	Assign the nearest plate boundary segment to points on melt trajectories	21, 26
23	clockwiseAreaCalc	Calculate the area of a quadrangle	20
24	**crustCalculation**[a]	Calculate melt flux and crustal thickness	1
25	meltFluxCalculation	Calculate melt flux in melt shoulders and swaths	24
26	**meltExtraction**[a]	Simulate melt extraction and calculate crustal thickness along plate boundaries	24
27	extractionDetermination	Determine if a batch of melt is extracted	26
28	minDistBetweenTwoPolygons[b]	Calculate the minimum distance between two polygons	26, 27, 33
29	curveIntersect[b]	Calculate intersections of curves	28
30	plotCrustalAccretionProfile	Plot crustal thickness profile	24
31	crustalThicknessSmoothing	Smooth crustal thickness profile along plate boundary segments	24
32	fastSmooth[b]	Smooth a vector with a fixed smoothing width	31, 33
33	**crustalHistory**[a]	Advect crustal thickness along spreading direction and generate a map of crustal thickness	24
34	plotCrustalThicknessMapIn3D	Plot crustal thickness map in 3D	33
35	dataOutput	Output selected model results	24

[a]Script names in bold indicate major operations.

[b]Scripts from *MATLAB Central*.
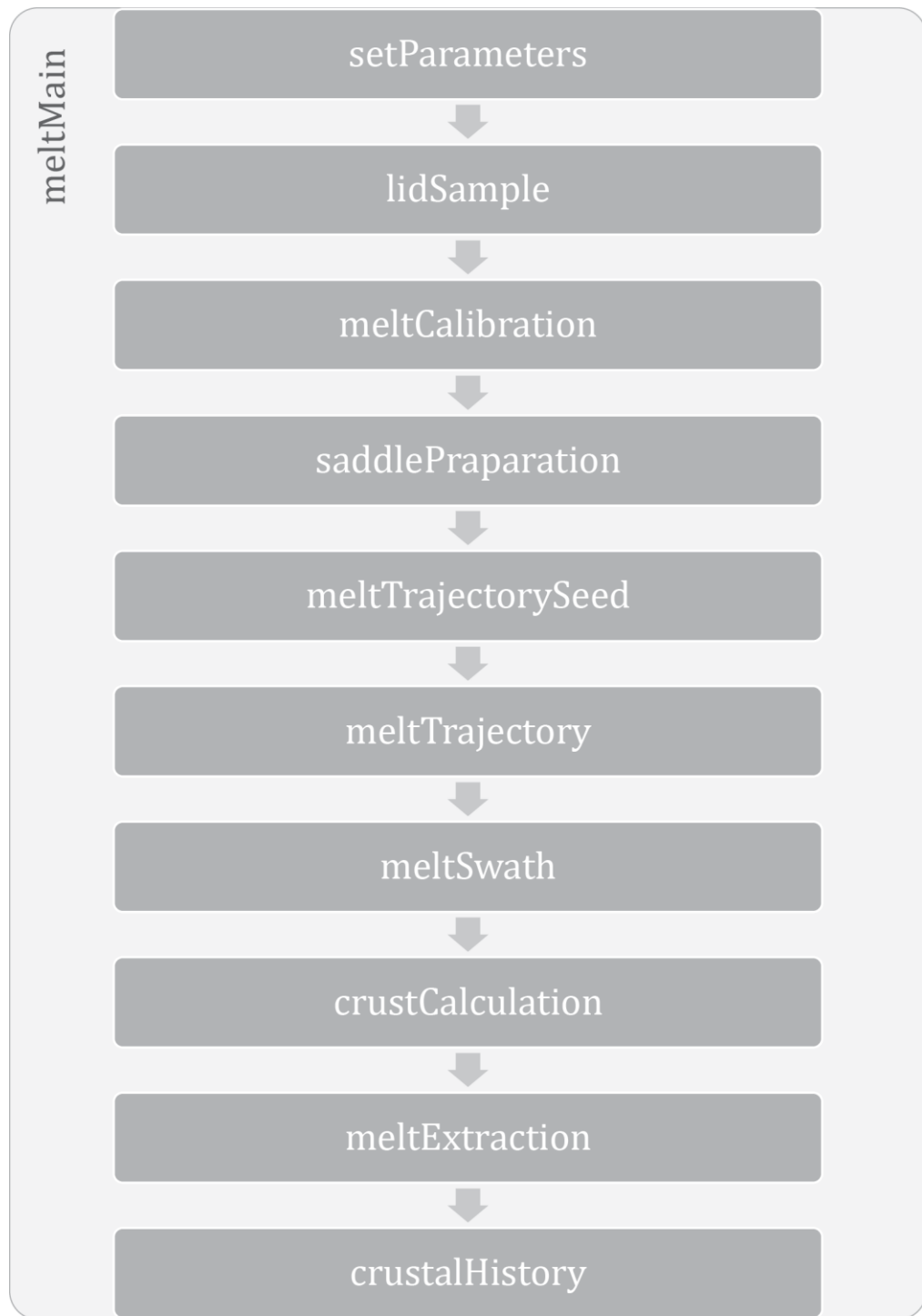
Figure A.1 A flowchart of major MeltMigrator calculation steps.

Appendix B: Supporting Information for Chapter 4

B.1 Numerical Model Setup

　　Mantle flow and the thermal structure of mid-ocean ridge system are solved using the commercial finite element software COMSOL Multiphysics® 4.3. Conservation of mass, momentum and energy are expressed by:

$$\nabla \cdot \mathbf{V} = 0 \tag{B.1}$$

$$\nabla P = \nabla \cdot [\eta(\nabla \mathbf{V} + (\nabla \mathbf{V})^{\mathrm{T}})] \tag{B.2}$$

$$\rho c_p (\mathbf{V} \cdot \nabla)T = \nabla \cdot (k\nabla T) \tag{B.3}$$

where $\mathbf{V}$ is the mantle velocity field, ρ_m is the reference mantle density, η is the mantle viscosity, c_p is the heat capacity, k is the thermal conductivity, P is the pressure and T is the temperature. This set of equations describes the mantle as an incompressible material, and neglects the thermal and mechanical effects of mantle melting.

　　We adopt the temperature-dependent viscosity with a viscoplastic approximation for brittle weakening following *Behn et al.* [2007] and *Roland et al.* [2010]:

$$\eta = min(\eta_T, \eta_Y) \tag{B.4}$$

$$\eta_T = \eta_0 \exp\left[\frac{Q}{R}\left(\frac{1}{T} - \frac{1}{T_m}\right)\right] \tag{B.5}$$

$$\eta_Y = \frac{C_0 - \mu\rho_m g y}{\sqrt{2}\dot{\varepsilon}_{II}} \tag{B.6}$$

where η_T is the temperature-dependent viscosity, η_Y is the effective viscosity associated with brittle failure [*Chen and Morgan*, 1990], η_0 is the reference viscosity, Q is the activation energy, R is the gas constant, T_m is the mantle temperature, C_0 is

the cohesion, μ is the friction coefficient, g is the gravity acceleration, y is the depth, and $\dot{\varepsilon}_{II}$ is the second invariant of the strain rate tensor.

The thermal structure of mid-ocean ridges is influenced by the hydrothermal circulation of seawater in the cold brittle crust [*Sinha and Evans*, 2004]. Here we use the parameterization of *Phipps Morgan and Chen* [1993] where hydrothermal circulation is approximated as enhanced thermal conductivity, and limited to temperatures less than $T_{\text{cut}} = 600\ ^\circ\text{C}$ and depth less than $y_{\text{cut}} = 6$ km:

$$k = k_0 + k_0(\text{Nu} - 1)\exp\left[A\left(1 - \frac{T}{T_{\text{cut}}}\right)\right]\exp\left[A\left(1 - \frac{y}{y_{\text{cut}}}\right)\right]/\exp(2A) \quad \text{(B.7)}$$

where k_0 is the reference thermal conductivity, Nu is the Nusselt number, A is a smoothing factor.

B.2 Compiled Topography Data
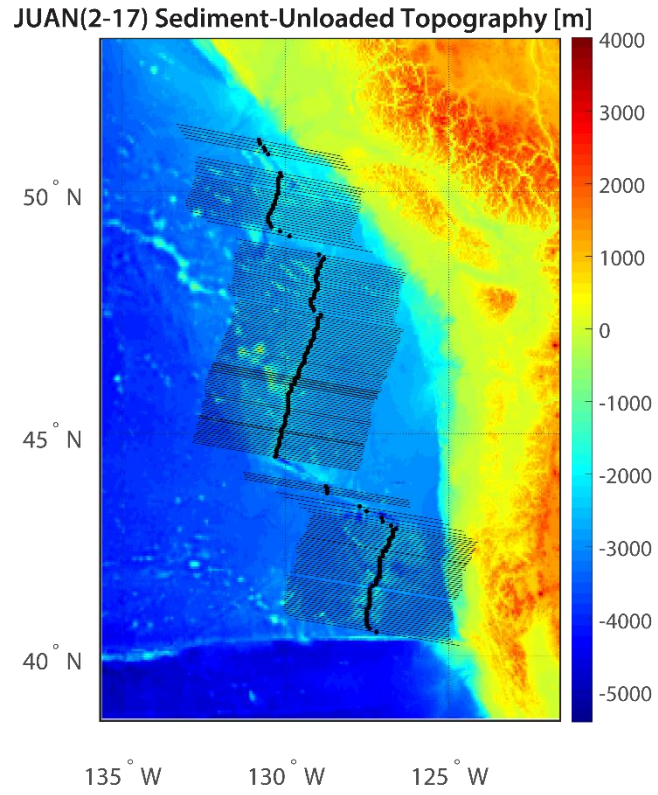
Figure B.1 Sediment-unloaded topography of the Juan de Fuca Ridge. Black dots represent the locations of ridge axes determined from the seafloor age. Thin black lines are the sampling profiles.
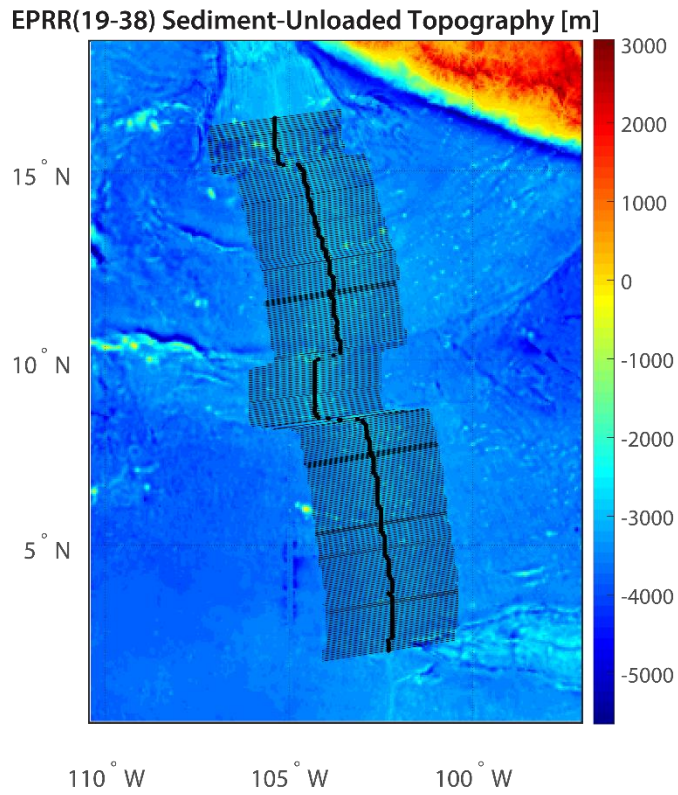
Figure B.2 Sediment-unloaded topography of the East Pacific Rise. Black dots represent the locations of ridge axes determined from the seafloor age. Thin black lines are the sampling profiles.
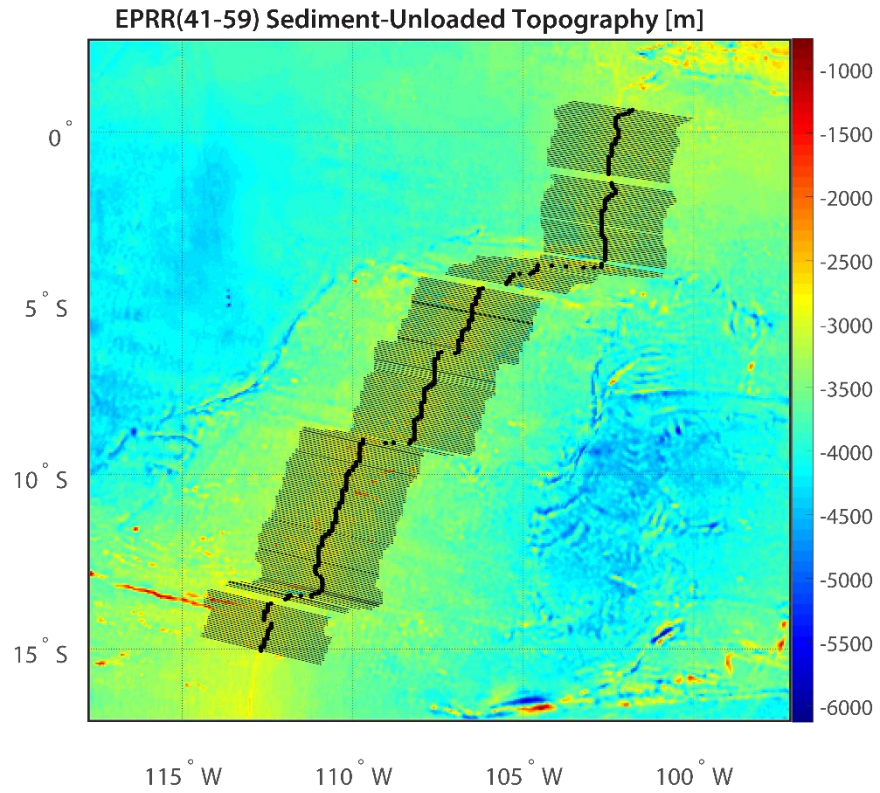
Figure B.3 Sediment-unloaded topography of the East Pacific Rise. Black dots represent the locations of ridge axes determined from the seafloor age. Thin black lines are the sampling profiles.
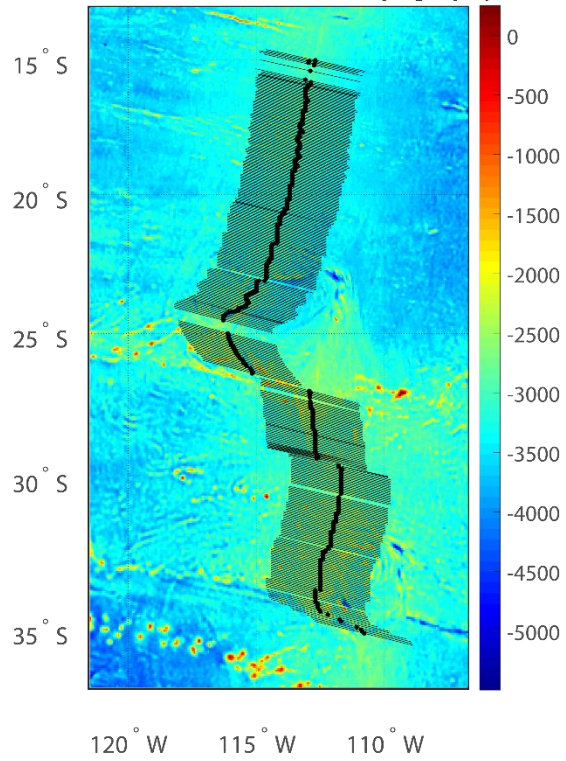
Figure B.4 Sediment-unloaded topography of the East Pacific Rise. Black dots represent the locations of ridge axes determined from the seafloor age. Thin black lines are the sampling profiles.
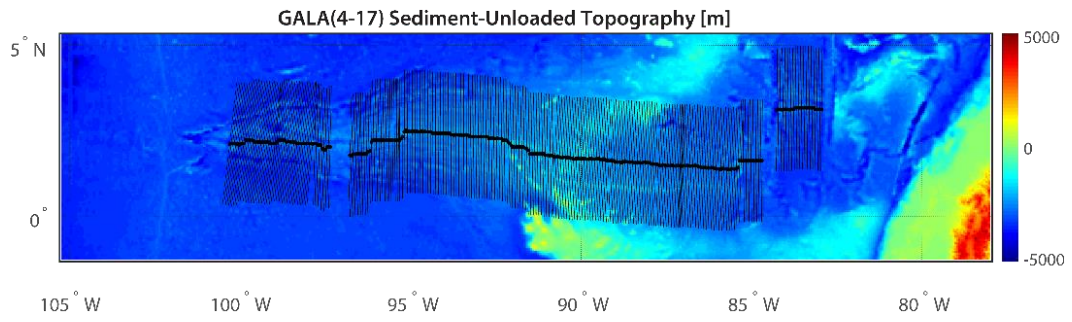
Figure B.5 Sediment-unloaded topography of the Galapagos Ridge. Black dots represent the locations of ridge axes determined from the seafloor age. Thin black lines are the sampling profiles.
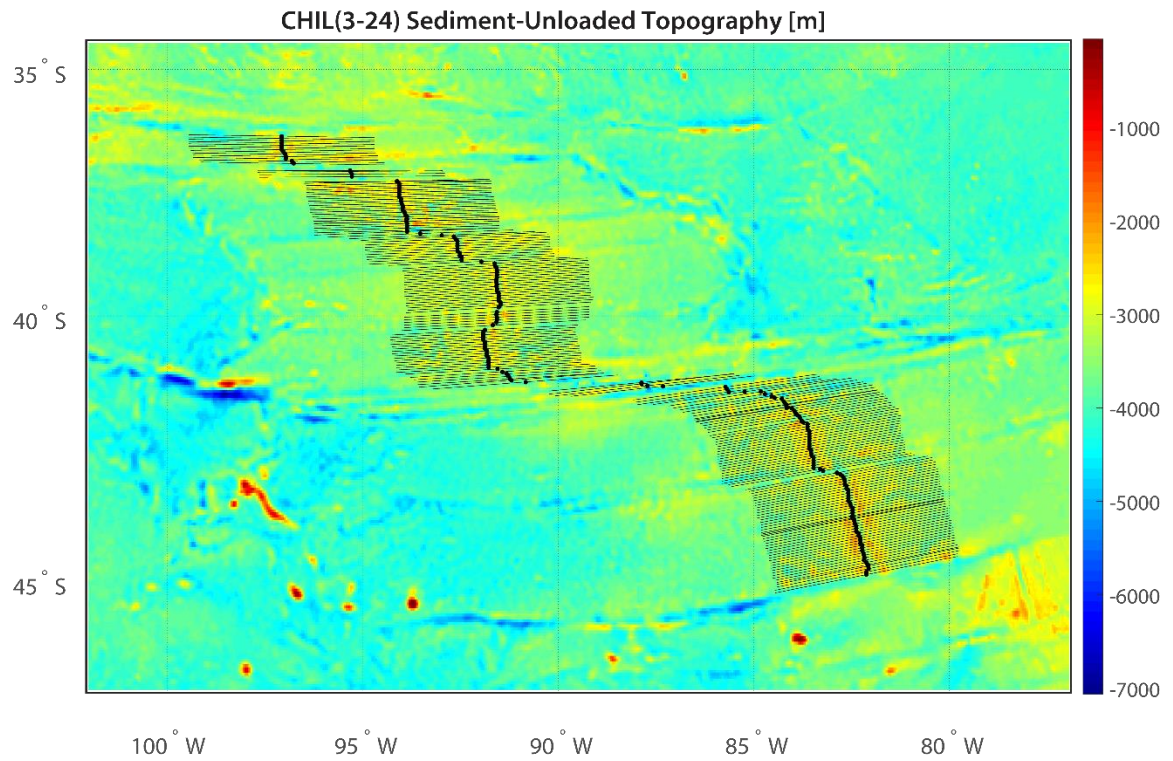
Figure B.6 Sediment-unloaded topography of the Chile Rise. Black dots represent the locations of ridge axes determined from the seafloor age. Thin black lines are the sampling profiles.
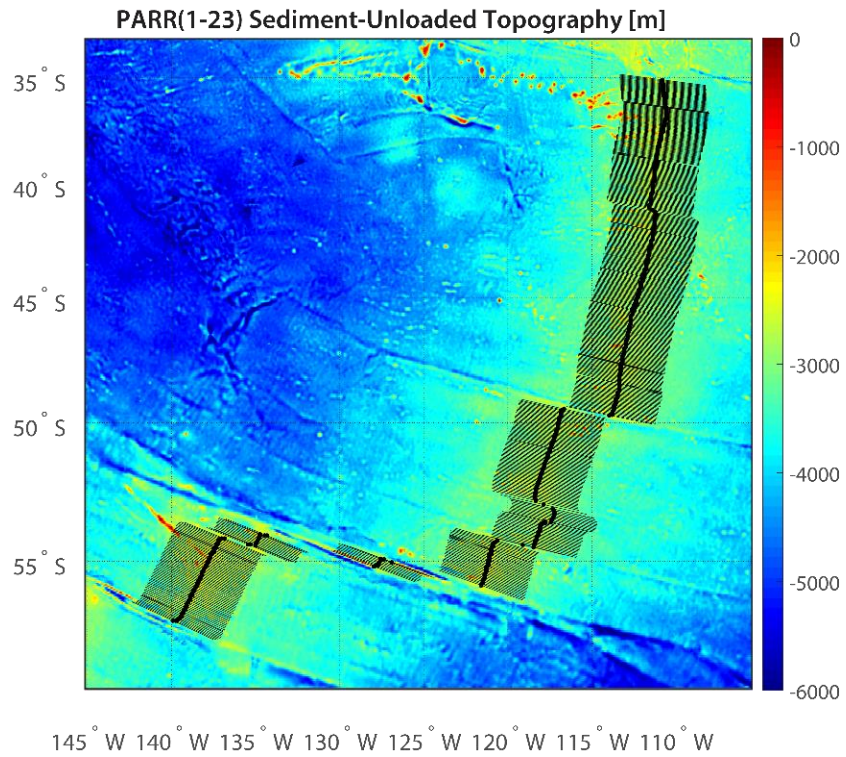
Figure B.7 Sediment-unloaded topography of the Pacific-Antarctic Ridge. Black dots represent the locations of ridge axes determined from the seafloor age. Thin black lines are the sampling profiles.
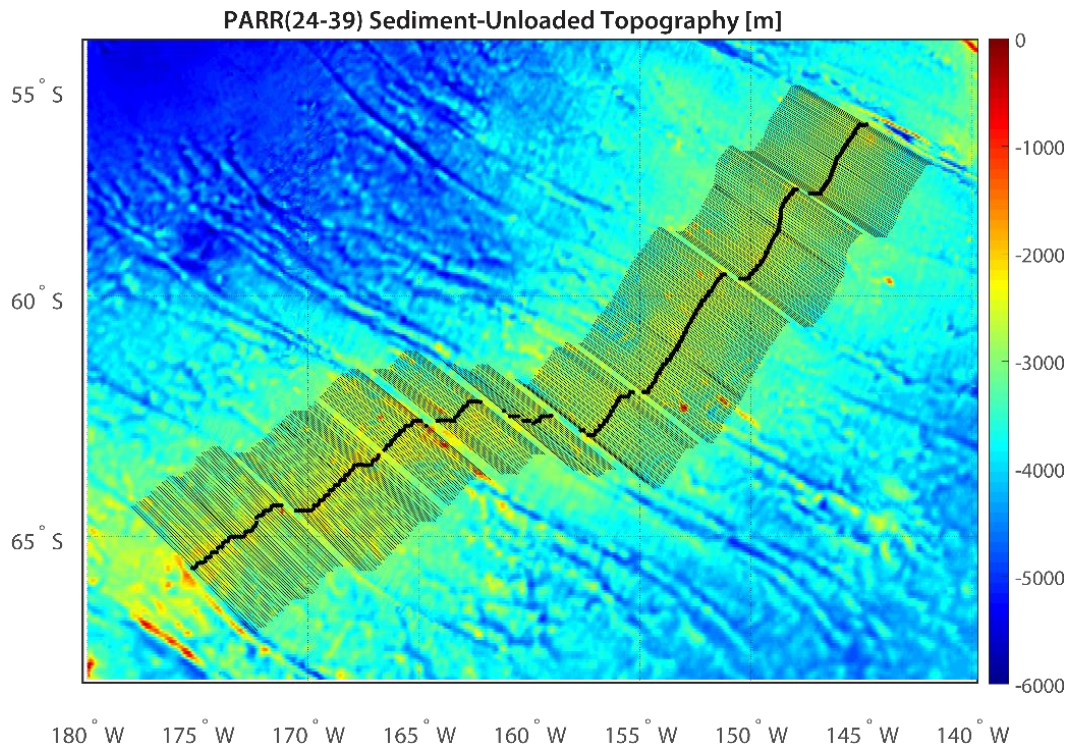
Figure B.8 Sediment-unloaded topography of the Pacific-Antarctic Ridge. Black dots represent the locations of ridge axes determined from the seafloor age. Thin black lines are the sampling profiles.
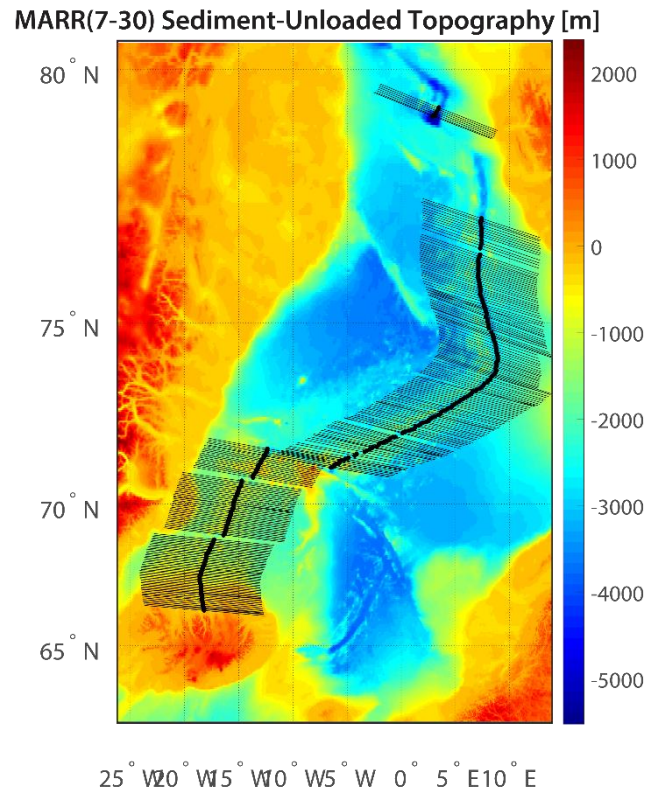
Figure B.9 Sediment-unloaded topography of the Mid-Atlantic Ridge. Black dots represent the locations of ridge axes determined from the seafloor age. Thin black lines are the sampling profiles.
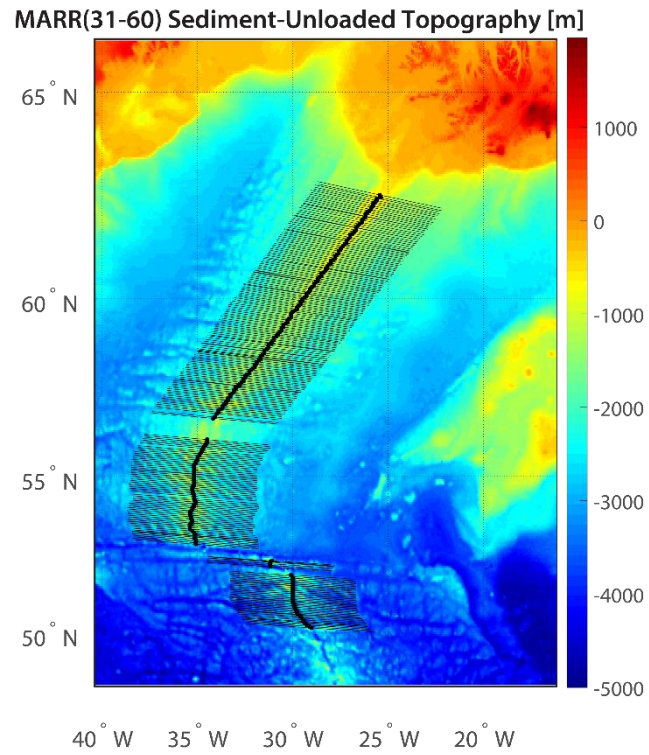
Figure B.10 Sediment-unloaded topography of the Mid-Atlantic Ridge. Black dots represent the locations of ridge axes determined from the seafloor age. Thin black lines are the sampling profiles.
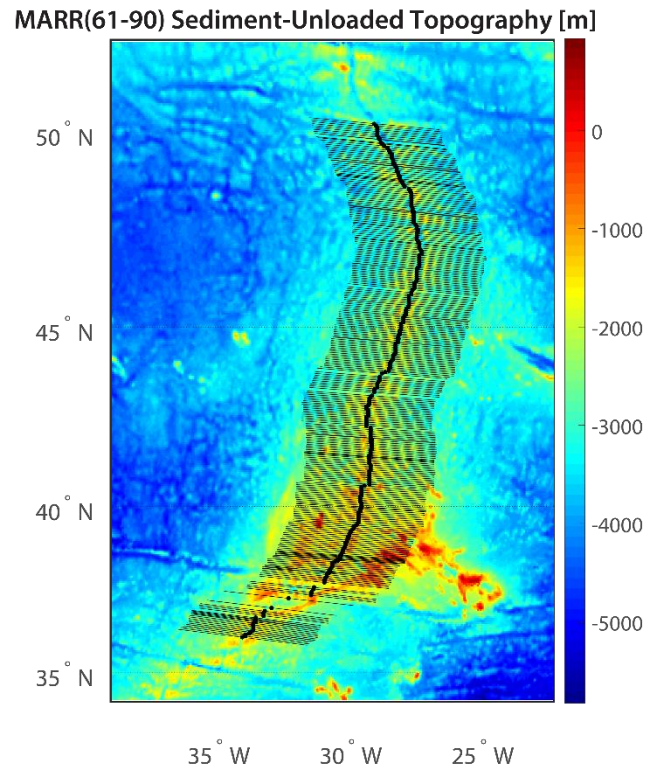
Figure B.11 Sediment-unloaded topography of the Mid-Atlantic Ridge. Black dots represent the locations of ridge axes determined from the seafloor age. Thin black lines are the sampling profiles.
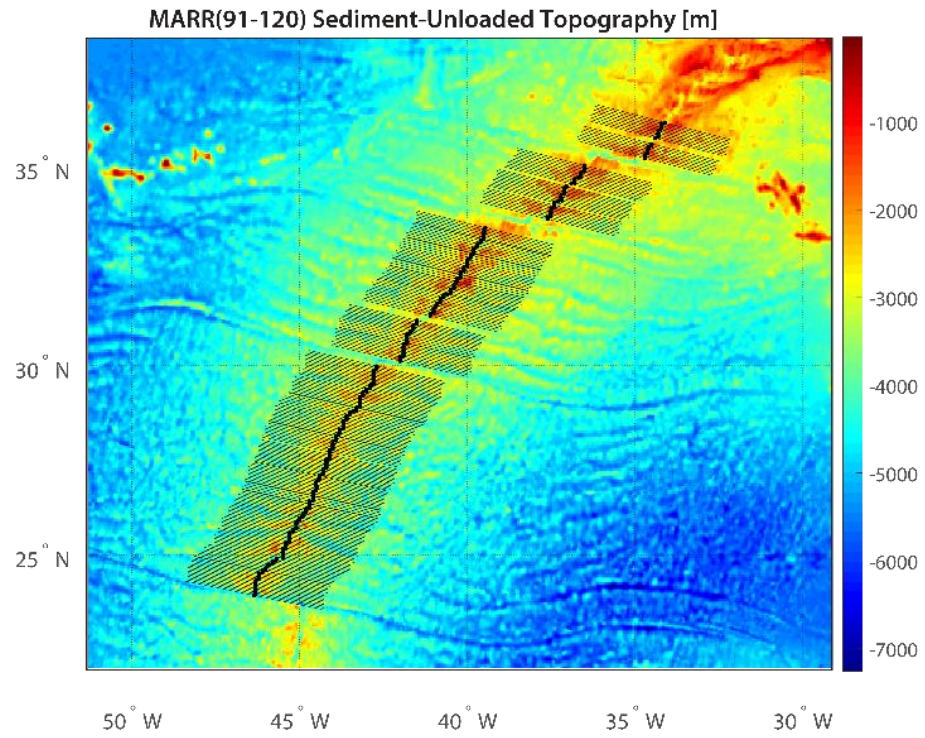
Figure B.12 Sediment-unloaded topography of the Mid-Atlantic Ridge. Black dots represent the locations of ridge axes determined from the seafloor age. Thin black lines are the sampling profiles.
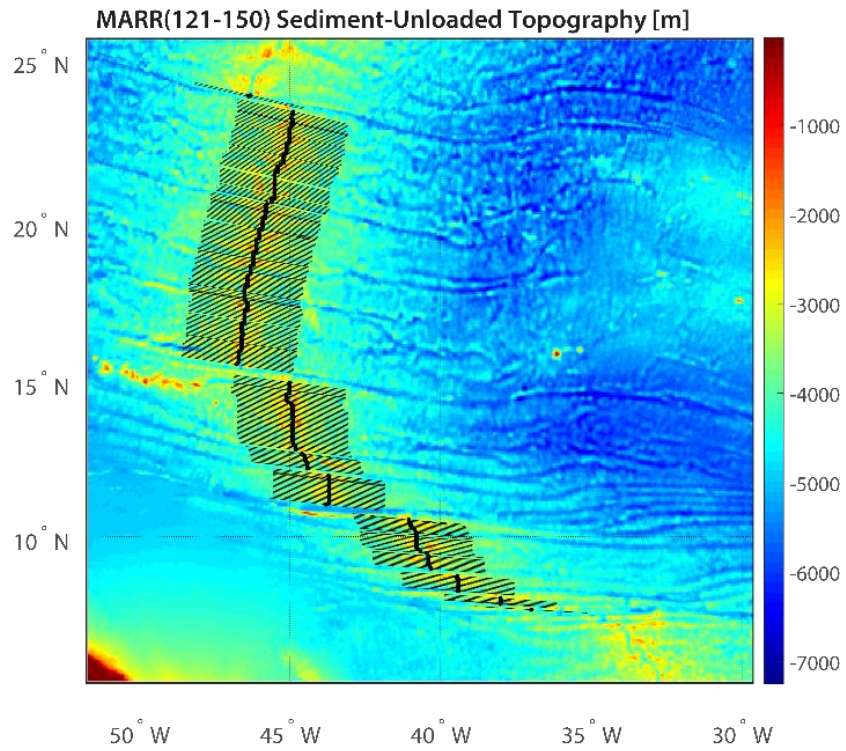
Figure B.13 Sediment-unloaded topography of the Mid-Atlantic Ridge. Black dots represent the locations of ridge axes determined from the seafloor age. Thin black lines are the sampling profiles.
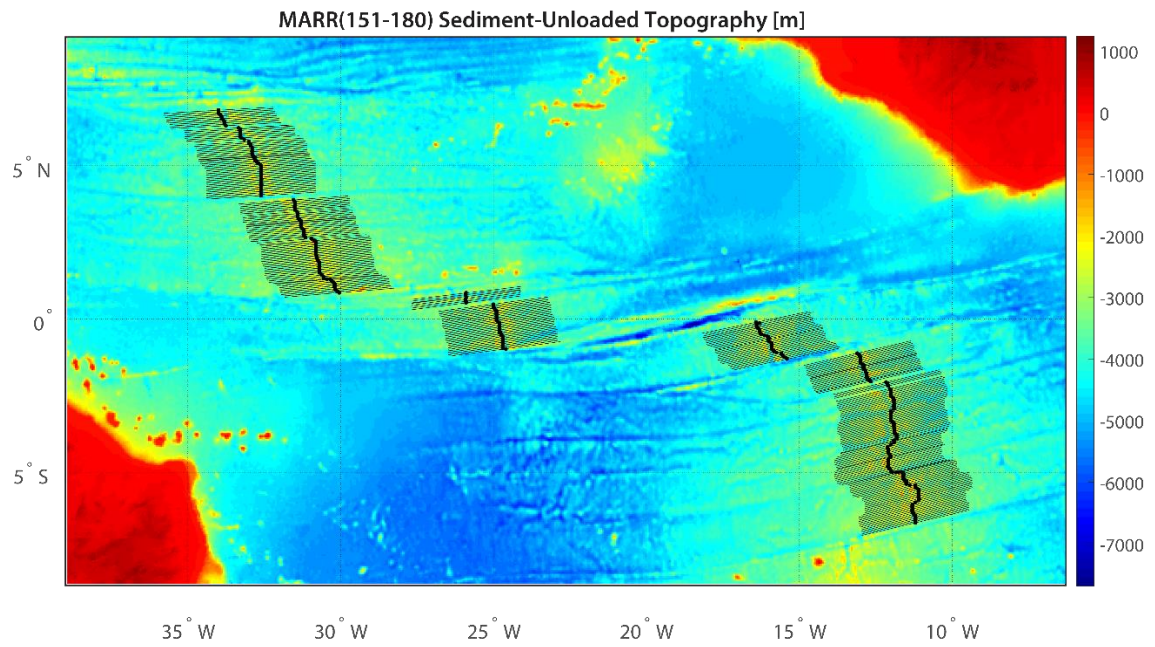
Figure B.14 Sediment-unloaded topography of the Mid-Atlantic Ridge. Black dots represent the locations of ridge axes determined from the seafloor age. Thin black lines are the sampling profiles.
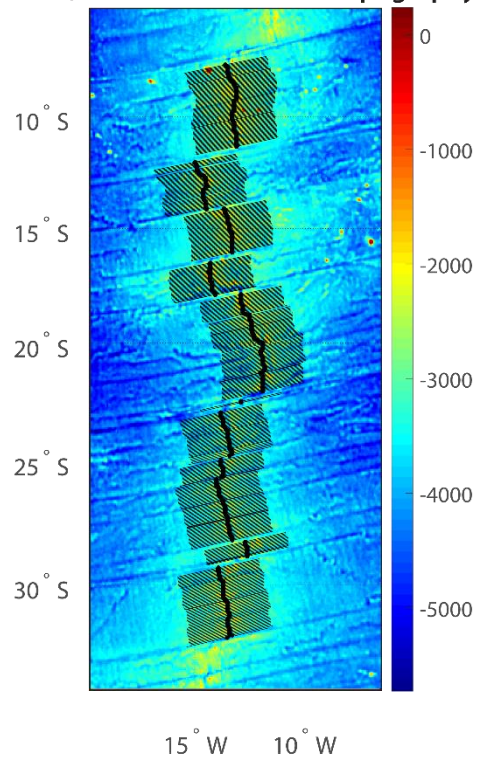
Figure B.15 Sediment-unloaded topography of the Mid-Atlantic Ridge. Black dots represent the locations of ridge axes determined from the seafloor age. Thin black lines are the sampling profiles.
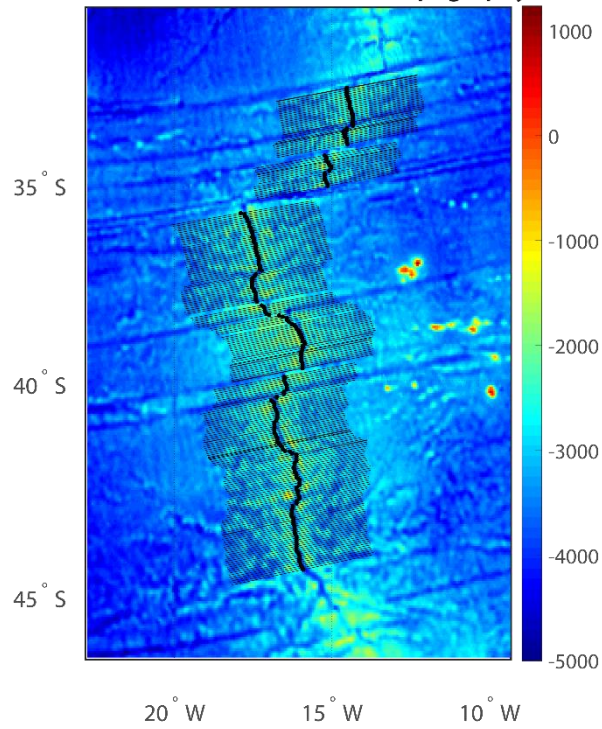
Figure B.16 Sediment-unloaded topography of the Mid-Atlantic Ridge. Black dots represent the locations of ridge axes determined from the seafloor age. Thin black lines are the sampling profiles.
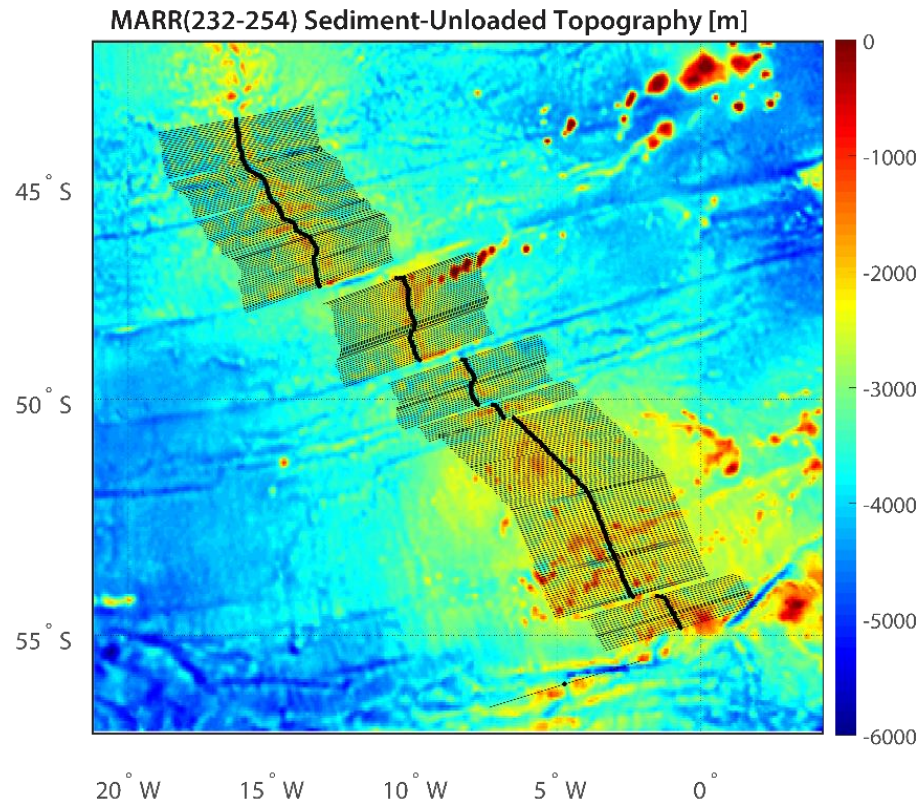
Figure B.17 Sediment-unloaded topography of the Mid-Atlantic Ridge. Black dots represent the locations of ridge axes determined from the seafloor age. Thin black lines are the sampling profiles.
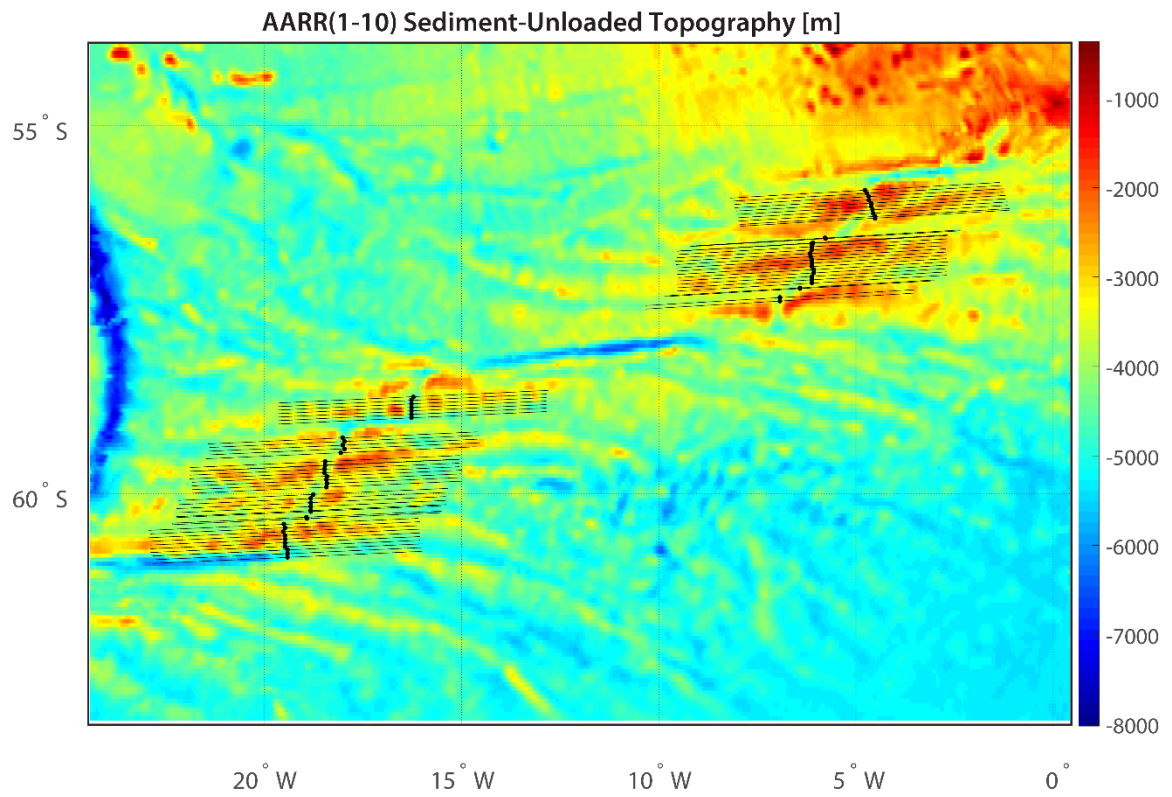
Figure B.18 Sediment-unloaded topography of the American-Antarctic Ridge. Black dots represent the locations of ridge axes determined from the seafloor age. Thin black lines are the sampling profiles.
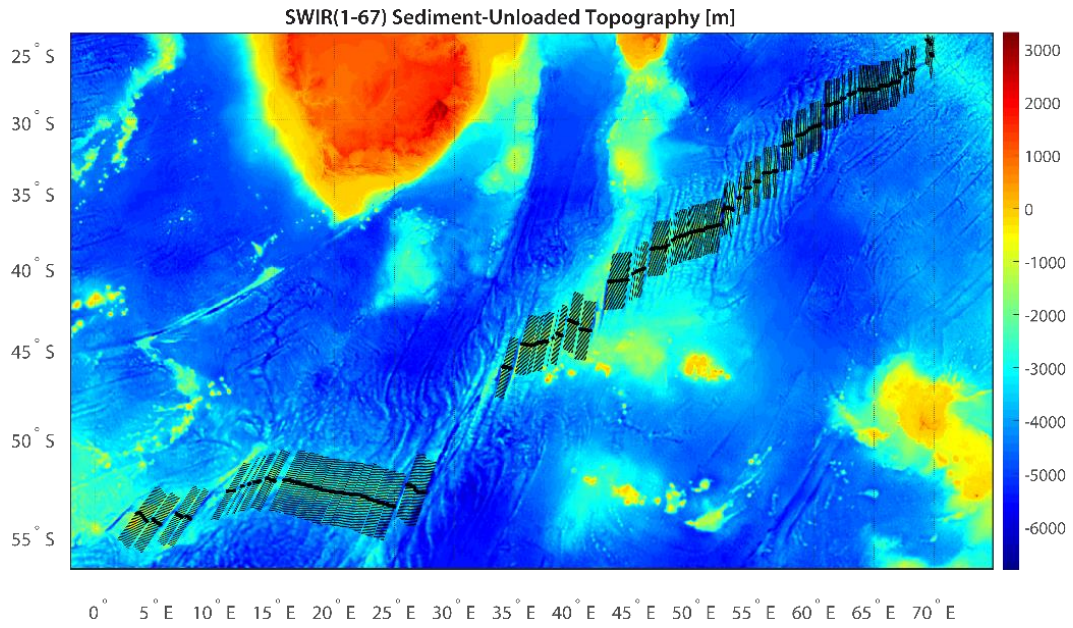
Figure B.19 Sediment-unloaded topography of the Southwest Indian Ridge. Black dots represent the locations of ridge axes determined from the seafloor age. Thin black lines are the sampling profiles.
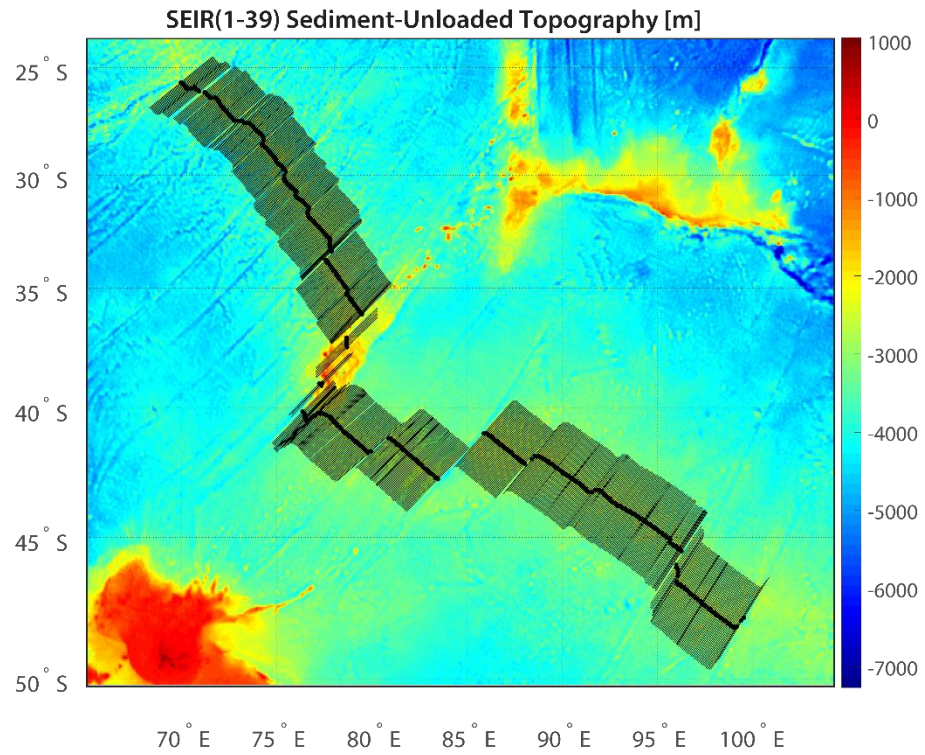
Figure B.20 Sediment-unloaded topography of the Southeast Indian Ridge. Black dots represent the locations of ridge axes determined from the seafloor age. Thin black lines are the sampling profiles.
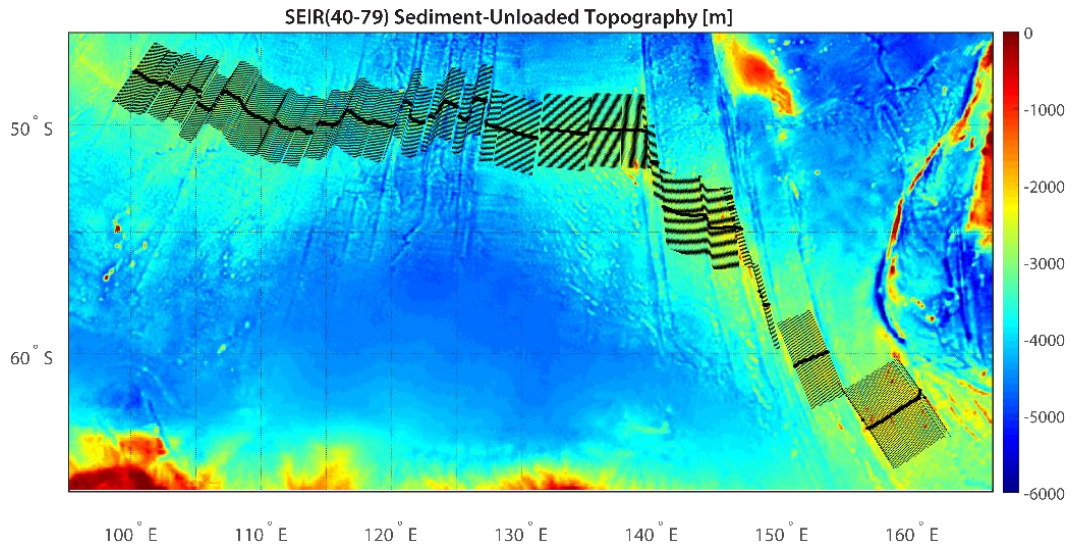
Figure B.21 Sediment-unloaded topography of the Southeast Indian Ridge. Black dots represent the locations of ridge axes determined from the seafloor age. Thin black lines are the sampling profiles.
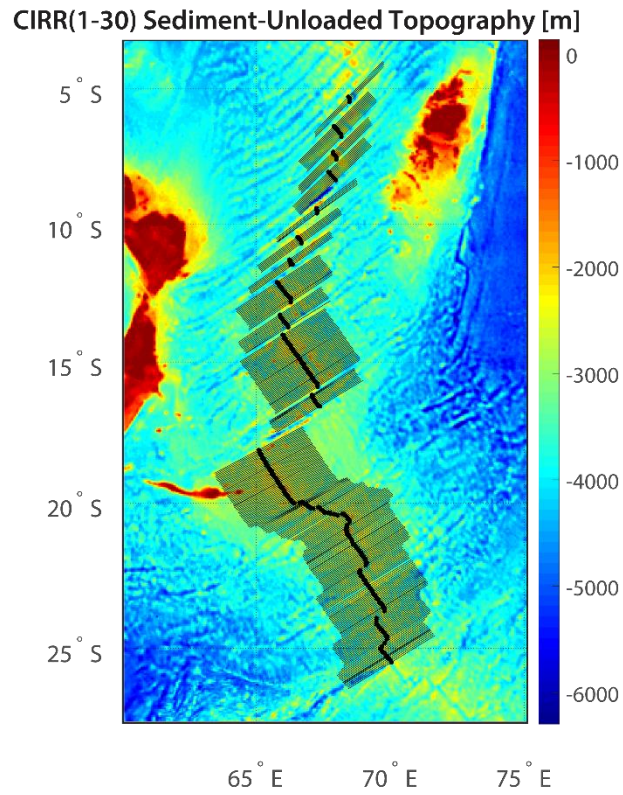
Figure B.22 Sediment-unloaded topography of the Central Indian Ridge. Black dots represent the locations of ridge axes determined from the seafloor age. Thin black lines are the sampling profiles.
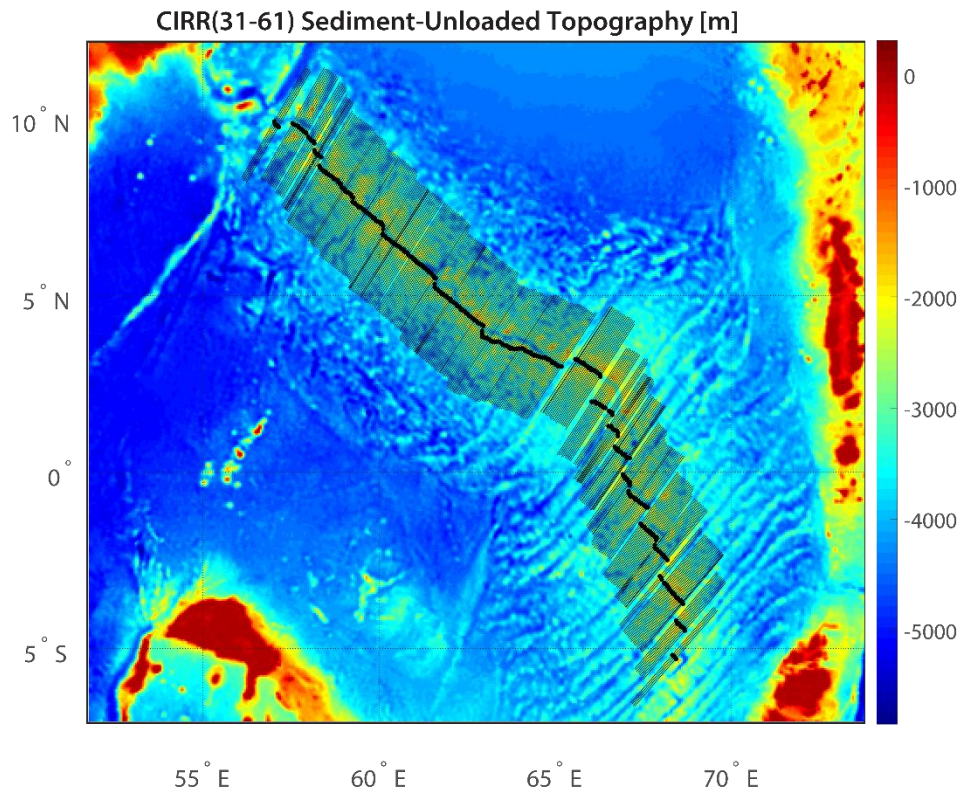
Figure B.23 Sediment-unloaded topography of the Central Indian Ridge. Black dots represent the locations of ridge axes determined from the seafloor age. Thin black lines are the sampling profiles.
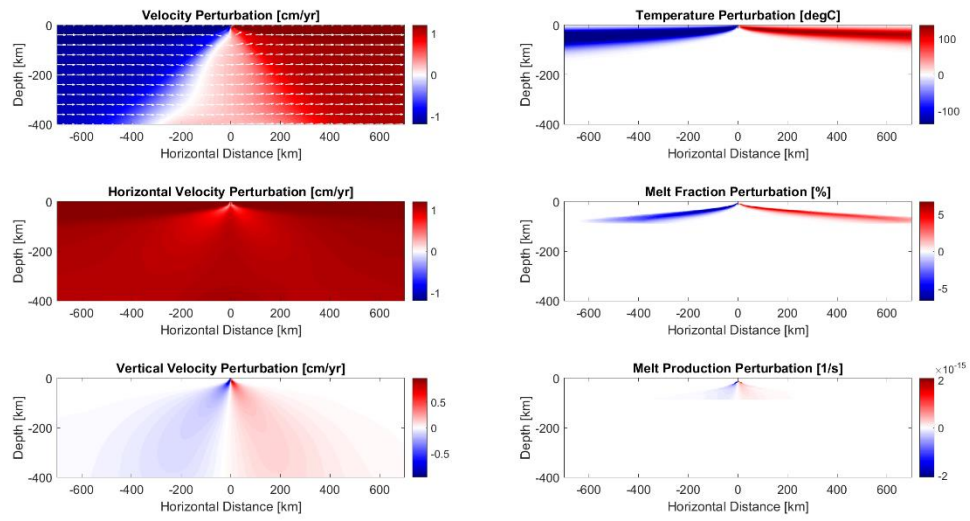
Figure B.24 Perturbation in velocity (upper left), horizontal velocity (middle left), vertical velocity (lower left), temperature (upper right), melt fraction (middle right), and melt production (lower right) for an asymmetric spreading model with a full-spreading rate of 6 cm/yr and a spreading asymmetry of 70%.
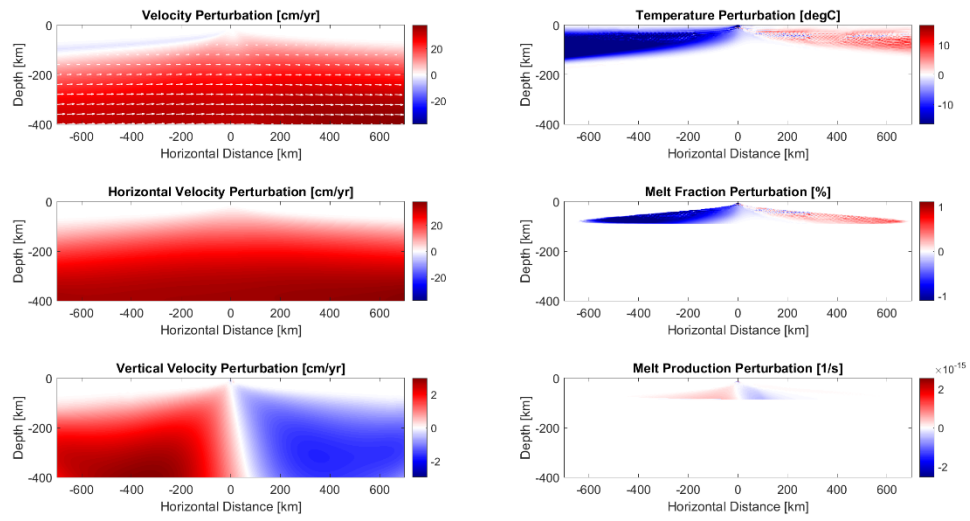
Figure B.25 Perturbation in velocity (upper left), horizontal velocity (middle left), vertical velocity (lower left), temperature (upper right), melt fraction (middle right), and melt production (lower right) for a mantle wind model with a full-spreading rate of 6 cm/yr and a mantle pressure gradient of 2 Pa/m.
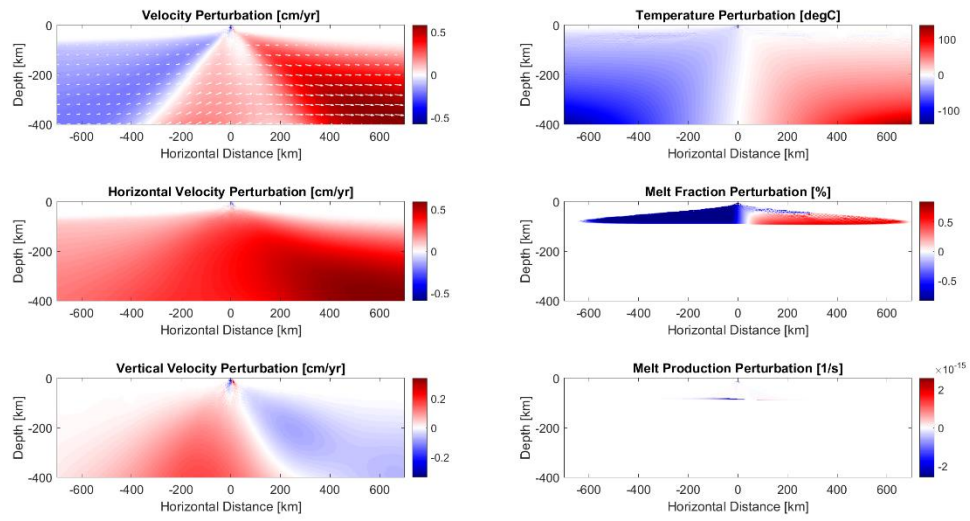
Figure B.26 Perturbation in velocity (upper left), horizontal velocity (middle left), vertical velocity (lower left), temperature (upper right), melt fraction (middle right), and melt production (lower right) for a mantle thermal anomaly model with a full-spreading rate of 6 cm/yr and a mantle temperature gradient of 0.2 K/km.
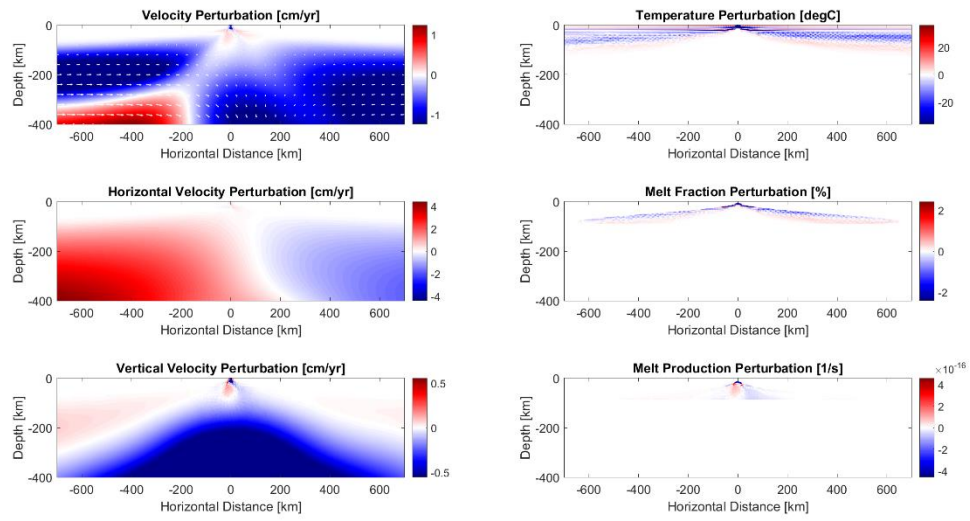
Figure B.27 Perturbation in velocity (upper left), horizontal velocity (middle left), vertical velocity (lower left), temperature (upper right), melt fraction (middle right), and melt production (lower right) for a ridge migration model with a full-spreading rate of 6 cm/yr and a ridge migration rate of 2.4 cm/yr.

Table B.1 Statistics of spreading rate, spreading asymmetry, and topography asymmetry averaged over each ridge. Segment-averaged data was weighted using segment length. Topography asymmetry is defined as the difference between the fast-spreading and slow-spreading plate, Δh_{F-S} and its amplitude as $|\Delta h|$. Ridge abbreviations AARR: America-Antarctica ridge; CHIL: Chile Rise; CIRR: Central Indian Ridge; EPRR: East Pacific Rise; GALA: Galápagos Ridge; JUAN: Juan de Fuca Ridge; MARR: Mid-Atlantic Ridge; PARR: Pacific-Antarctic Ridge; SEIR: Southeast Indian Ridge; SWIR: Southwest Indian Ridge.

Ridge	Spreading rate [mm/yr]	Spreading asymmetry [%]	Topography asymmetry [m]	Topography asymmetry amplitude [m]	Length [km]	Number of segments	Number of profiles
SWIR	17.6±4.1	61±7	81±219	182±147	4376	63	658
AARR	19.9±3.0	59±4	17±372	279±246	514	10	69
MARR	28.8±7.2	56±5	9±162	120±109	15525	235	2822
CIRR	33.6±5.5	56±4	15±166	132±103	3860	61	719
GALA	50.9±8.2	61±5	31±113	104±52	1863	14	366
JUAN	62.1±2.6	62±6	-59±431	329±285	973	16	192
SEIR	62.9±3.9	54±3	49±169	100±145	7268	79	1450
PARR	69.0±12.6	57±4	-18±134	108±82	4838	38	950
CHIL	75.2±3.5	60±5	46±145	92±121	1006	22	199
EPRR	145.3±22.3	56±4	-9±101	85±55	5724	53	1115
Global	54.8±35.1	56±5	18±197	186±156	45947	591	8540

Table B.2 Statistics of spreading rate, spreading asymmetry, and topography asymmetry averaged over each ridge segment. Ridge abbreviations: AARR: America-Antarctica ridge; CHIL: Chile Rise; CIRR: Central Indian Ridge; EPRR: East Pacific Rise; GALA: Galápagos Ridge; JUAN: Juan de Fuca Ridge; MARR: Mid-Atlantic Ridge; PARR: Pacific-Antarctic Ridge; SEIR: Southeast Indian Ridge; SWIR: Southwest Indian Ridge.

Ridge	Segment	Spreading rate [mm/yr]	Spreading asymmetry [%] *	Topography asymmetry [m]	Topography asymmetry amplitude [m]	Length [km]	Number of profiles
AARR	1	19.7±0.2	56±2	164±130	164±130	59	9
AARR	2	18.9±0.5	54±3	151±260	180±232	28	3
AARR	3	20.3±1.6	63±11	333±293	369±243	76	15
AARR	4	20.0±1.1	58±6	-839±450	839±450	72	3
AARR	5	27.0±12.5	58±1	63±431	353±211	68	7
AARR	6	17.8±0.6	66±6	327±380	375±324	64	7
AARR	7	17.7±0.2	58±1	-195±330	328±167	35	7
AARR	8	18.7±1.0	61±4	88±41	88±41	29	5
AARR	9	16.8±0.5	60±4	148±7	148±7	31	2
AARR	10	17.3±0.4	53±1	86±672	549±358	52	11
CHIL	3	79.7±5.7	65±5	426±196	426±196	67	13
CHIL	4	92.7±0.0	52±0	400±0	400±0	11	1
CHIL	5	76.1±10.7	65±10	33±196	157±84	30	4
CHIL	6	74.3±2.1	67±3	-34±210	170±121	90	19
CHIL	7	74.0±1.0	67±0	331±193	331±193	25	6
CHIL	8	75.6±5.0	58±8	-53±159	131±63	12	3
CHIL	9	76.0±2.6	55±3	33±78	70±43	59	12
CHIL	10	73.9±0.9	55±1	-35±55	54±35	97	20
CHIL	11	74.2±0.4	57±0	-78±37	78±37	28	6
CHIL	12	75.5±2.7	62±5	41±71	55±60	86	18
CHIL	13	76.6±4.1	75±3	-19±115	79±73	17	4
CHIL	14	70.2±3.1	70±10	-26±162	114±36	14	2
CHIL	15	89.9±0.0	51±0	483±0	483±0	14	1
CHIL	16	84.1±4.8	58±2	136±277	215±187	17	3
CHIL	17	69.5±5.7	67±6	40±36	40±36	23	4
CHIL	18	80.7±4.4	54±3	-243±99	243±99	13	3
CHIL	19	74.9±0.8	57±0	-152±155	172±126	25	5
CHIL	20	74.4±0.2	56±1	-114±114	130±90	32	7
CHIL	21	74.6±0.6	54±1	44±175	114±139	113	23
CHIL	22	73.9±1.0	59±1	49±112	104±61	99	20
CHIL	23	73.7±0.3	60±0	-25±83	66±54	103	21
CHIL	24	68.9±6.3	61±2	66±359	280±173	31	4
CIRR	1	45.2±1.3	53±3	-293±471	454±278	30	6
CIRR	2	45.0±0.5	52±1	11±208	165±116	54	11
CIRR	3	43.9±0.4	53±2	-100±151	153±94	106	22
CIRR	4	43.2±0.2	55±2	188±190	208±166	72	15
CIRR	5	42.7±0.1	52±1	-208±165	213±158	25	5
CIRR	6	42.2±0.5	52±2	176±309	280±211	64	13
CIRR	7	42.1±0.2	52±0	-31±71	62±43	45	10
CIRR	8	41.7±0.1	51±0	20±49	40±32	43	9
CIRR	9	41.3±0.1	52±0	103±68	103±68	30	6
CIRR	10	41.1±0.1	52±0	112±119	124±105	36	8

176

Ridge	Segment	Spreading rate [mm/yr]	Spreading asymmetry [%] *	Topography asymmetry [m]	Topography asymmetry amplitude [m]	Length [km]	Number of profiles
CIRR	11	41.4±0.7	56±3	123±96	130±86	69	14
CIRR	12	40.8±0.2	55±1	-12±65	51±38	39	8
CIRR	13	40.9±1.0	57±1	37±106	83±71	50	10
CIRR	14	39.4±0.5	53±1	-27±75	69±38	124	25
CIRR	15	38.6±0.1	52±0	-204±111	204±111	35	8
CIRR	16	38.2±0.1	51±0	-208±169	208±169	30	7
CIRR	17	37.2±1.6	51±3	-109±124	131±99	98	16
CIRR	18	35.6±1.9	64±6	206±375	293±305	59	11
CIRR	19	35.4±1.4	53±1	142±208	172±181	61	11
CIRR	20	35.6±0.3	53±0	27±109	82±74	92	19
CIRR	21	34.1±1.6	53±4	67±237	192±149	128	24
CIRR	22	33.9±0.5	63±6	9±167	135±92	79	14
CIRR	23	32.3±1.3	53±3	60±206	128±171	94	17
CIRR	24	31.8±1.2	52±1	399±330	427±286	56	6
CIRR	25	30.8±1.3	57±4	298±331	342±279	75	8
CIRR	26	30.3±0.7	53±0	323±444	419±319	38	4
CIRR	27	30.9±0.7	59±1	238±293	302±217	67	10
CIRR	28	29.6±0.7	58±2	-208±175	209±174	55	7
CIRR	29	35.9±0.8	53±3	138±188	180±143	80	11
CIRR	30	37.1±1.3	58±0	100±180	161±106	27	4
CIRR	31	36.5±0.5	57±0	-278±243	293±219	33	4
CIRR	32	35.8±0.3	56±1	266±321	321±259	74	10
CIRR	33	35.4±0.1	56±0	23±185	134±125	87	18
CIRR	34	35.1±0.2	55±2	-106±182	173±99	32	5
CIRR	35	34.8±0.1	55±1	-14±225	182±120	46	10
CIRR	36	34.5±0.3	57±2	-161±212	194±181	86	17
CIRR	37	33.9±0.1	57±1	157±122	160±118	49	10
CIRR	38	33.9±0.3	56±1	-203±280	294±168	47	10
CIRR	39	33.6±0.1	57±0	-199±182	213±162	21	5
CIRR	40	33.5±0.5	55±2	147±204	196±139	22	4
CIRR	41	33.1±0.1	56±1	-186±275	303±106	44	9
CIRR	42	33.0±0.3	56±1	-476±218	476±218	47	9
CIRR	43	32.9±0.5	57±3	98±654	600±196	52	10
CIRR	44	31.9±0.4	61±1	261±365	287±344	155	28
CIRR	45	30.8±0.0	61±0	388±139	388±139	24	2
CIRR	46	30.8±0.4	58±1	7±269	192±185	145	29
CIRR	47	30.4±0.3	55±2	23±183	154±88	53	10
CIRR	48	29.9±0.1	51±1	-72±183	146±123	39	8
CIRR	49	29.5±0.2	54±3	-14±165	144±71	68	14
CIRR	50	29.0±0.2	56±1	-64±59	69±53	100	20
CIRR	51	28.4±0.3	53±2	-86±202	180±121	83	17
CIRR	52	27.8±0.2	58±1	197±177	203±170	97	20
CIRR	53	27.2±0.1	57±0	-69±58	78±43	59	12
CIRR	54	27.0±0.1	56±1	17±120	103±56	46	10
CIRR	55	26.5±0.2	54±1	-84±173	170±81	86	17
CIRR	56	25.8±0.2	52±1	-148±212	183±180	96	20
CIRR	57	25.2±0.2	57±1	-182±157	191±145	97	20
CIRR	58	24.8±0.4	64±4	25±304	265±94	30	6
CIRR	59	24.9±0.4	71±3	90±95	111±66	53	10
CIRR	60	24.5±0.2	74±1	-170±275	262±179	64	11

Ridge	Segment	Spreading rate [mm/yr]	Spreading asymmetry [%] *	Topography asymmetry [m]	Topography asymmetry amplitude [m]	Length [km]	Number of profiles
CIRR	61	23.6±0.1	55±2	-286±424	414±258	61	5
EPRR	19	87.6±0.5	65±0	-15±38	35±18	43	9
EPRR	20	90.6±2.1	66±1	81±93	89±84	62	13
EPRR	21	93.6±0.6	65±3	207±81	207±81	27	6
EPRR	22	95.4±2.5	55±1	72±43	80±21	90	18
EPRR	23	98.9±1.2	55±1	151±22	151±22	82	17
EPRR	24	100.2±1.0	52±1	188±48	188±48	88	18
EPRR	25	102.4±0.4	51±0	182±56	182±56	28	6
EPRR	26	104.8±1.0	52±1	96±30	96±30	103	21
EPRR	27	106.8±0.9	54±0	70±35	70±35	78	16
EPRR	28	109.1±0.8	53±1	4±70	47±51	94	19
EPRR	29	113.0±1.5	53±2	60±156	95±137	119	24
EPRR	30	118.4±5.1	54±5	-5±40	30±26	75	15
EPRR	31	132.3±3.8	51±1	-184±135	184±135	8	2
EPRR	32	130.4±1.5	52±2	206±123	206±123	7	2
EPRR	33	120.5±3.6	52±1	35±38	42±30	47	10
EPRR	34	120.4±0.7	51±0	79±19	79±19	71	15
EPRR	35	124.5±2.0	51±0	61±31	63±26	218	44
EPRR	36	128.9±0.8	51±0	79±39	81±36	80	16
EPRR	37	132.5±1.7	51±0	84±33	84±33	177	36
EPRR	38	132.4±9.8	52±0	87±92	102±74	148	30
EPRR	41	143.6±0.7	53±1	91±56	101±37	220	44
EPRR	42	145.1±0.7	53±2	48±42	52±37	140	28
EPRR	43	146.2±1.1	53±1	43±142	130±65	104	21
EPRR	44	157.4±10.7	60±4	220±119	220±119	42	9
EPRR	45	151.2±6.0	60±5	143±68	143±68	66	14
EPRR	46	151.2±1.2	57±1	10±82	66±46	86	18
EPRR	47	151.8±0.9	56±1	-72±65	79±55	127	26
EPRR	48	154.2±4.0	59±4	-23±97	71±68	84	17
EPRR	49	153.2±0.2	59±1	-39±6	39±6	29	6
EPRR	50	154.6±1.1	57±2	-60±74	74±59	212	43
EPRR	51	164.9±4.6	53±2	122±243	187±184	20	5
EPRR	52	156.1±0.6	51±0	-68±38	71±31	69	14
EPRR	53	156.3±0.4	52±1	-20±83	71±46	135	27
EPRR	54	156.3±0.5	54±0	-62±52	65±48	95	19
EPRR	55	156.6±1.0	56±1	-49±44	53±38	97	20
EPRR	56	156.9±0.8	55±2	-98±48	98±48	96	20
EPRR	57	158.0±1.0	53±1	-122±131	161±61	26	6
EPRR	58	169.8±5.4	53±1	-17±18	17±18	9	2
EPRR	59	139.5±13.4	55±2	-166±128	176±114	191	35
EPRR	60	124.3±10.7	54±1	-95±91	102±81	64	6
EPRR	61	157.2±9.6	54±1	-107±49	107±49	47	5
EPRR	62	162.8±0.8	54±1	-93±64	98±57	376	75
EPRR	63	163.6±0.8	55±0	-42±23	42±23	155	32
EPRR	64	163.9±1.0	58±1	-92±87	100±79	274	55
EPRR	65	166.0±3.8	63±2	-216±61	216±61	154	30
EPRR	66	168.6±3.3	71±3	-123±63	123±63	71	10
EPRR	67	166.0±3.8	64±5	-198±136	227±74	254	32
EPRR	71	163.6±1.7	64±1	-8±113	84±75	126	25
EPRR	72	163.2±3.1	61±2	130±59	130±59	94	18

Ridge	Segment	Spreading rate [mm/yr]	Spreading asymmetry [%] *	Topography asymmetry [m]	Topography asymmetry amplitude [m]	Length [km]	Number of profiles
EPRR	73	163.0±2.8	52±4	17±102	71±74	128	26
EPRR	74	162.8±0.2	52±1	33±123	88±91	187	38
EPRR	75	162.3±1.2	56±1	-45±153	131±89	189	38
EPRR	76	176.6±35.7	64±10	113±141	131±123	114	14
GALA	4	35.9±7.2	70±2	123±64	123±64	147	30
GALA	5	37.7±1.4	63±1	147±72	147±72	123	25
GALA	6	62.7±14.8	67±7	58±141	122±88	146	18
GALA	7	44.9±2.8	61±3	58±130	106±93	93	19
GALA	8	43.7±0.2	63±1	125±48	125±48	30	6
GALA	9	45.4±1.1	57±3	-17±91	67±63	240	48
GALA	10	48.3±1.0	61±1	-122±41	122±41	120	24
GALA	11	51.3±1.1	67±4	-123±123	144±97	150	30
GALA	12	51.4±0.7	57±4	89±336	265±221	177	36
GALA	13	53.6±1.0	66±3	-212±150	212±150	148	30
GALA	14	56.0±0.3	66±2	61±95	101±47	81	17
GALA	15	57.7±1.2	54±3	102±69	117±38	199	40
GALA	16	60.3±0.8	60±8	177±172	212±123	62	13
GALA	17	62.5±1.4	53±4	135±156	192±72	146	30
JUAN	2	58.0±0.4	66±1	1280±183	1280±183	27	4
JUAN	3	57.4±0.5	61±0	743±164	743±164	35	6
JUAN	4	58.9±0.8	65±3	347±144	347±144	92	18
JUAN	5	59.0±0.3	52±0	-138±81	138±81	49	10
JUAN	6	59.3±0.2	52±0	-154±27	154±27	17	4
JUAN	7	59.6±0.1	53±1	-131±50	131±50	55	11
JUAN	8	60.7±0.4	55±3	-272±94	272±94	119	24
JUAN	9	61.7±0.5	61±2	-323±119	323±119	60	12
JUAN	10	61.8±0.4	65±1	-102±107	117±89	80	16
JUAN	11	62.6±0.5	65±1	125±129	148±99	60	12
JUAN	12	63.2±0.9	67±1	434±120	434±120	66	14
JUAN	13	63.1±0.1	50±0	-8±111	94±23	16	4
JUAN	14	64.2±2.7	61±5	-229±199	229±199	14	3
JUAN	15	65.2±1.5	71±2	-856±102	856±102	69	14
JUAN	16	65.4±0.8	66±2	-539±156	539±156	93	19
JUAN	17	65.7±1.7	61±2	18±169	132±103	121	21
MARR	7	14.3±0.1	54±1	164±74	164±74	175	9
MARR	8	14.2±0.5	53±2	-219±307	330±152	39	7
MARR	9	14.6±1.1	57±5	1±155	133±74	119	23
MARR	10	15.8±0.9	74±6	259±87	259±87	73	12
MARR	11	14.8±1.0	55±8	109±184	186±100	116	23
MARR	12	15.1±0.1	51±1	-23±65	58±33	56	9
MARR	13	15.6±0.3	51±1	50±83	69±68	144	20
MARR	14	14.8±1.2	53±1	202±41	202±41	113	14
MARR	15	14.9±0.6	54±1	301±54	301±54	63	7
MARR	16	16.2±0.1	52±0	306±65	306±65	33	5
MARR	17	16.3±0.1	52±0	217±43	217±43	40	4
MARR	18	16.6±0.2	53±2	300±142	300±142	44	4
MARR	19	17.3±0.5	60±3	625±188	625±188	67	9
MARR	20	18.2±0.9	79±2	-476±495	641±228	128	21
MARR	21	17.3±0.1	57±1	-107±131	117±122	86	17

Ridge	Segment	Spreading rate [mm/yr]	Spreading asymmetry [%] *	Topography asymmetry [m]	Topography asymmetry amplitude [m]	Length [km]	Number of profiles
MARR	22	17.7±0.2	59±2	151±50	151±50	131	23
MARR	23	18.1±0.1	52±1	-46±118	91±86	116	23
MARR	24	18.5±0.3	55±3	-98±84	100±83	96	20
MARR	25	18.8±0.0	61±1	-184±21	184±21	22	5
MARR	26	18.8±0.0	63±0	-125±7	125±7	35	7
MARR	27	18.8±0.1	61±3	-118±10	118±10	110	3
MARR	35	20.1±0.1	51±0	-6±45	38±24	76	13
MARR	36	20.2±0.0	51±0	33±22	33±22	40	7
MARR	37	20.3±0.0	50±0	50±28	50±28	43	8
MARR	38	20.5±0.1	50±0	-54±60	70±39	93	17
MARR	39	20.6±0.0	51±0	-100±35	100±35	45	9
MARR	40	20.7±0.0	51±0	-42±49	50±39	46	9
MARR	41	20.9±0.1	51±0	5±29	25±13	59	11
MARR	42	21.0±0.1	52±1	17±50	44±27	80	14
MARR	43	21.2±0.1	53±0	7±16	13±11	29	6
MARR	44	21.2±0.1	54±0	87±20	87±20	27	5
MARR	45	21.3±0.1	54±1	66±16	66±16	25	5
MARR	46	21.4±0.1	53±0	31±65	60±38	109	19
MARR	47	21.7±0.2	54±3	17±90	79±42	111	19
MARR	48	22.3±0.7	59±1	78±123	123±71	106	9
MARR	49	22.1±0.1	52±2	-16±92	81±43	80	16
MARR	50	22.2±0.1	53±1	132±241	223±153	74	15
MARR	51	22.5±0.1	56±1	15±151	133±64	94	19
MARR	52	22.7±0.1	58±4	38±200	179±66	41	7
MARR	53	23.2±1.7	65±3	-128±194	211±75	57	8
MARR	54	26.1±2.3	73±5	281±541	490±302	44	5
MARR	55	24.4±0.2	53±0	147±294	212±245	53	8
MARR	56	24.4±0.1	53±0	117±137	145±101	35	7
MARR	57	24.3±0.3	53±1	53±219	164±138	26	6
MARR	58	24.8±0.1	52±1	113±311	279±155	48	10
MARR	59	24.9±0.1	57±3	129±282	244±161	27	5
MARR	60	23.2±1.0	58±4	205±153	205±153	31	5
MARR	61	24.6±0.8	65±3	-53±198	172±96	44	9
MARR	62	25.1±0.1	65±1	-310±90	310±90	27	2
MARR	63	25.1±0.3	59±1	44±159	130±94	57	12
MARR	64	25.1±0.1	60±0	-142±72	142±72	60	9
MARR	65	25.1±0.1	56±2	-65±122	112±78	77	15
MARR	66	25.2±0.1	58±0	-258±59	258±59	27	3
MARR	67	25.2±0.1	58±1	127±192	188±124	45	10
MARR	68	25.4±0.2	58±1	125±116	135±103	39	8
MARR	69	25.4±0.1	56±1	155±64	155±64	72	15
MARR	70	25.5±0.1	56±0	84±51	84±51	61	13
MARR	71	25.6±0.1	57±0	202±49	202±49	38	8
MARR	72	25.8±0.1	56±0	27±42	29±41	33	7
MARR	73	25.8±0.1	54±1	8±57	45±33	81	17
MARR	74	24.9±0.7	54±3	-13±72	64±32	99	20
MARR	75	24.5±0.0	52±1	-82±54	85±49	50	10
MARR	76	24.6±0.1	55±1	3±41	34±21	41	9
MARR	77	24.6±0.1	57±1	42±34	46±28	53	11
MARR	78	24.8±0.1	54±1	-83±54	83±54	31	7

Ridge	Segment	Spreading rate [mm/yr]	Spreading asymmetry [%] *	Topography asymmetry [m]	Topography asymmetry amplitude [m]	Length [km]	Number of profiles
MARR	79	24.8±0.0	51±1	-32±173	151±79	60	12
MARR	80	24.9±0.1	51±1	-37±93	77±63	89	18
MARR	81	25.0±0.1	51±1	-79±108	106±79	69	14
MARR	82	25.1±0.0	51±1	-59±66	73±49	53	11
MARR	83	21.6±1.4	56±2	-382±253	386±246	119	24
MARR	84	21.0±0.2	53±2	-448±164	448±164	59	12
MARR	85	21.3±0.2	53±1	-393±384	511±169	65	10
MARR	86	21.1±1.1	53±1	101±394	309±203	58	4
MARR	87	21.4±0.0	54±0	-140±0	140±0	21	1
MARR	88	21.6±0.2	55±4	-1±69	54±37	44	7
MARR	89	21.9±0.2	55±3	-29±117	102±56	48	10
MARR	90	21.9±0.1	52±2	12±101	85±36	31	5
MARR	91	22.2±0.2	57±1	-60±102	108±39	47	10
MARR	92	22.5±1.2	51±2	19±177	139±101	69	9
MARR	93	22.3±0.7	63±3	175±126	176±125	89	12
MARR	94	22.8±0.3	57±2	63±121	117±62	51	11
MARR	95	22.7±0.5	52±2	-109±280	261±124	47	9
MARR	97	23.0±0.0	52±1	-447±157	447±157	65	7
MARR	98	23.3±0.2	53±2	-68±358	315±147	61	9
MARR	99	23.3±0.1	55±0	138±175	155±155	20	4
MARR	100	23.3±0.1	55±0	152±128	154±125	38	8
MARR	101	23.5±0.1	54±0	307±34	307±34	26	4
MARR	102	23.6±0.2	53±0	62±102	82±85	42	9
MARR	103	23.7±0.2	57±2	169±280	262±183	57	9
MARR	104	23.8±0.2	58±0	108±131	149±66	41	5
MARR	105	23.9±0.3	62±1	250±236	255±230	47	9
MARR	106	23.8±0.3	58±3	50±280	218±157	30	6
MARR	107	24.0±0.2	53±2	252±406	381±274	65	11
MARR	108	24.1±0.3	53±3	73±347	296±180	87	15
MARR	109	24.4±0.1	50±0	4±230	162±155	53	11
MARR	110	24.3±0.3	52±2	-73±52	77±44	44	7
MARR	111	24.7±0.1	53±1	-56±41	58±38	60	12
MARR	112	24.8±0.1	51±0	99±76	108±61	49	10
MARR	113	24.9±0.1	51±0	41±129	117±61	66	14
MARR	114	25.1±0.1	52±0	1±106	94±39	59	12
MARR	115	25.1±0.0	51±0	71±85	101±27	24	5
MARR	116	25.3±0.1	52±1	-61±201	183±84	45	9
MARR	117	25.4±0.2	55±1	116±330	298±159	54	10
MARR	118	25.3±0.2	55±2	114±197	193±113	79	16
MARR	119	25.8±0.3	53±2	166±115	166±115	58	9
MARR	120	25.6±0.3	52±1	66±285	234±165	84	16
MARR	121	25.7±0.2	59±3	101±126	115±112	58	10
MARR	122	26.1±0.3	61±0	260±82	260±82	45	9
MARR	123	26.2±0.2	59±1	43±104	75±82	68	14
MARR	124	26.2±0.3	57±3	50±312	247±185	72	15
MARR	125	26.6±0.2	63±2	316±132	316±132	45	10
MARR	126	26.7±0.4	64±1	142±172	180±122	26	6
MARR	127	27.0±0.5	55±4	-136±155	166±116	38	7
MARR	128	26.6±0.1	53±0	77±192	181±91	65	14
MARR	129	26.7±0.1	55±1	48±133	122±67	103	21

Ridge	Segment	Spreading rate [mm/yr]	Spreading asymmetry [%] *	Topography asymmetry [m]	Topography asymmetry amplitude [m]	Length [km]	Number of profiles
MARR	130	26.9±0.2	56±0	80±197	151±143	47	10
MARR	131	27.0±0.1	54±1	3±206	172±103	70	15
MARR	132	27.0±0.0	53±1	-322±95	322±95	45	5
MARR	133	27.1±0.0	50±1	-97±208	190±121	74	15
MARR	134	27.3±0.1	52±1	48±69	64±53	75	15
MARR	135	27.4±0.3	54±1	90±148	147±86	93	16
MARR	136	27.8±0.5	53±4	-1±83	64±46	58	6
MARR	137	27.5±0.2	53±2	124±190	205±91	116	23
MARR	138	28.0±0.2	53±2	46±131	105±87	99	19
MARR	139	28.7±0.5	59±4	1±317	247±180	52	10
MARR	140	28.3±0.4	53±3	264±176	282±139	43	5
MARR	141	28.7±0.3	51±0	20±153	112±103	115	20
MARR	142	29.0±0.2	52±1	151±257	222±192	71	10
MARR	143	29.1±0.2	55±1	-79±132	100±109	27	3
MARR	144	29.3±0.3	52±2	188±262	271±165	55	11
MARR	145	29.2±0.7	58±3	-86±69	86±69	19	2
MARR	146	30.0±0.6	57±2	-29±77	68±41	55	10
MARR	147	29.7±0.6	70±2	-72±304	202±231	63	11
MARR	148	30.7±0.6	55±7	-82±414	259±315	41	6
MARR	149	29.8±0.5	51±1	-109±384	271±154	27	2
MARR	152	33.2±4.5	70±17	205±259	250±212	68	13
MARR	153	31.1±0.4	56±2	93±85	93±85	38	8
MARR	154	31.2±0.2	56±6	-15±90	72±51	62	12
MARR	155	31.4±0.1	54±2	-48±155	109±119	155	29
MARR	156	32.8±1.6	68±5	-128±163	131±160	46	8
MARR	157	32.1±0.8	69±2	-184±72	184±72	15	3
MARR	158	32.2±0.5	68±1	-112±78	112±78	32	7
MARR	159	32.4±0.3	65±2	21±162	118±107	60	12
MARR	160	32.6±0.3	57±4	-123±266	224±135	52	3
MARR	161	32.3±0.2	54±2	-42±162	106±128	111	23
MARR	162	32.9±0.7	68±2	43±50	48±45	30	6
MARR	163	33.5±1.1	59±3	-187±437	379±267	57	11
MARR	165	32.7±0.1	59±0	96±74	96±74	25	3
MARR	166	32.4±0.6	57±3	365±181	365±181	29	5
MARR	167	33.4±0.4	53±1	-195±353	260±307	200	34
MARR	168	33.6±0.2	52±1	8±84	61±48	78	4
MARR	169	33.8±0.1	52±1	69±130	134±50	53	11
MARR	170	34.1±0.4	53±1	-164±210	177±198	98	17
MARR	171	34.4±0.1	53±0	18±184	156±86	77	11
MARR	172	34.5±0.1	53±0	-75±347	303±159	52	11
MARR	173	34.8±0.6	58±5	258±253	328±119	36	6
MARR	174	34.9±0.3	61±1	348±175	355±159	80	16
MARR	175	35.0±0.3	60±1	312±145	315±138	91	19
MARR	176	35.3±0.7	59±1	54±58	54±58	24	3
MARR	177	35.3±0.2	52±2	-59±273	249±102	57	11
MARR	178	35.3±0.2	53±1	-260±147	288±70	60	12
MARR	179	35.5±0.5	60±4	248±230	277±191	103	21
MARR	180	36.0±0.6	59±3	159±152	192±104	92	19
MARR	182	35.8±0.1	55±0	92±207	204±85	84	13
MARR	183	36.1±0.2	59±2	196±177	214±152	123	25

Ridge	Segment	Spreading rate [mm/yr]	Spreading asymmetry [%] *	Topography asymmetry [m]	Topography asymmetry amplitude [m]	Length [km]	Number of profiles
MARR	184	36.2±0.3	59±2	-158±170	179±145	91	19
MARR	185	36.4±0.3	56±0	-101±82	114±63	157	27
MARR	186	36.0±0.6	53±0	-334±212	334±212	38	6
MARR	187	36.8±0.3	57±3	-172±147	175±143	134	27
MARR	188	36.9±0.5	54±1	-245±202	263±176	63	13
MARR	189	36.9±0.6	54±2	0±190	148±117	234	44
MARR	190	36.9±0.9	52±2	66±254	203±163	177	32
MARR	191	37.3±0.4	53±1	208±171	252±87	123	21
MARR	192	37.4±0.1	52±0	-112±110	127±89	59	12
MARR	193	37.5±0.2	53±3	-220±175	253±118	97	20
MARR	194	37.5±0.2	55±2	-125±204	207±116	125	25
MARR	195	37.7±0.4	51±1	-44±289	242±153	97	18
MARR	196	36.4±2.1	57±4	-181±42	181±42	35	2
MARR	197	37.0±1.0	53±5	148±252	230±175	83	17
MARR	198	37.6±0.1	52±0	-97±203	175±138	87	18
MARR	199	38.0±0.6	53±0	77±361	302±167	35	6
MARR	200	37.7±0.4	52±0	131±364	323±198	76	16
MARR	201	37.5±0.3	53±1	-48±229	184±138	103	21
MARR	202	37.5±0.0	51±1	52±138	122±79	86	18
MARR	203	37.6±0.1	52±1	72±187	170±100	111	21
MARR	204	37.6±0.2	51±0	25±135	110±76	71	13
MARR	205	38.6±1.1	51±0	-3±186	131±4	24	2
MARR	206	37.1±0.9	52±3	435±110	435±110	56	11
MARR	207	37.5±0.0	51±1	-3±150	112±96	93	19
MARR	208	37.5±0.1	52±0	20±169	146±78	69	14
MARR	209	37.4±0.0	51±1	33±17	33±17	15	3
MARR	210	37.5±0.4	50±0	-34±254	202±149	83	16
MARR	211	36.3±0.0	58±0	93±0	93±0	16	1
MARR	212	37.2±0.1	52±2	138±198	178±161	99	20
MARR	213	37.0±1.0	58±3	-51±295	230±155	36	5
MARR	214	37.3±0.3	61±1	246±268	286±219	51	9
MARR	215	38.4±1.8	61±2	-255±116	255±116	24	4
MARR	216	37.2±0.2	61±1	268±149	268±149	26	6
MARR	217	37.7±0.5	59±1	174±140	177±134	47	8
MARR	218	36.9±0.5	53±1	80±219	192±121	79	13
MARR	219	36.9±0.1	51±0	37±185	155±103	110	22
MARR	220	37.0±0.3	60±2	-259±164	261±160	72	15
MARR	221	37.8±1.4	66±2	125±22	125±22	32	7
MARR	222	36.6±0.6	60±3	311±38	311±38	27	5
MARR	223	37.0±0.3	62±1	423±89	423±89	67	14
MARR	224	37.1±0.4	61±2	126±95	126±95	29	4
MARR	225	36.6±0.6	58±2	80±119	111±87	45	10
MARR	226	36.6±0.6	53±2	-30±256	205±142	56	11
MARR	227	36.4±0.1	54±1	-102±225	155±191	88	18
MARR	228	36.4±0.0	53±1	-87±85	101±66	45	10
MARR	229	36.7±0.5	59±3	-175±109	181±97	46	8
MARR	230	36.3±0.2	63±1	-9±146	125±68	74	15
MARR	231	36.3±0.4	60±3	-2±257	207±142	88	18
MARR	232	36.0±0.1	58±1	-163±139	168±133	129	52
MARR	233	36.1±0.2	63±3	-179±324	291±210	45	7

Ridge	Segment	Spreading rate [mm/yr]	Spreading asymmetry [%] *	Topography asymmetry [m]	Topography asymmetry amplitude [m]	Length [km]	Number of profiles
MARR	234	36.0±0.3	72±2	-278±194	296±164	73	15
MARR	235	35.2±0.7	60±4	-192±291	305±158	72	15
MARR	236	34.5±0.9	54±1	-122±478	415±200	27	6
MARR	237	36.1±0.2	52±1	8±49	38±25	36	5
MARR	238	35.5±0.3	56±1	98±63	98±63	55	12
MARR	239	35.3±0.1	55±1	-36±70	51±56	23	4
MARR	240	35.3±0.1	55±0	-65±182	166±85	54	11
MARR	241	36.0±0.9	57±2	-668±389	668±389	26	3
MARR	242	35.0±0.2	57±1	-136±412	273±333	151	27
MARR	243	34.5±0.1	54±2	-82±139	129±82	31	5
MARR	244	34.5±0.5	51±1	10±350	207±277	90	16
MARR	245	34.8±0.4	66±1	-323±272	354±226	70	11
MARR	246	34.6±0.3	64±1	-70±60	70±60	24	4
MARR	247	34.8±0.2	66±1	160±195	190±163	63	11
MARR	248	34.9±1.4	57±2	-24±183	160±73	42	9
MARR	249	34.2±0.4	61±3	-80±181	166±102	98	20
MARR	250	33.5±0.2	55±3	95±397	387±106	126	25
MARR	251	33.4±0.3	58±2	57±88	88±55	171	33
MARR	252	33.0±0.2	55±1	-133±146	153±123	101	20
MARR	253	35.2±1.4	64±6	64±97	92±67	78	13
PARR	1	88.3±4.7	57±1	-140±69	140±69	142	29
PARR	2	86.0±0.6	58±1	-285±195	285±195	279	56
PARR	3	84.9±0.4	59±0	-58±58	68±45	144	29
PARR	4	84.2±0.5	59±1	-43±73	73±41	115	23
PARR	5	83.9±0.9	57±0	-254±117	254±117	92	18
PARR	6	82.6±1.0	61±1	-69±113	80±105	225	45
PARR	7	81.1±0.5	61±0	-115±36	115±36	161	33
PARR	8	79.6±0.6	59±1	-52±103	90±72	249	50
PARR	9	78.5±0.2	59±0	1±39	32±21	86	18
PARR	10	76.7±3.1	58±0	-48±105	94±64	148	29
PARR	11	76.1±0.5	52±0	-15±87	73±48	186	36
PARR	12	74.6±0.6	53±1	-86±56	94±43	230	46
PARR	13	73.1±1.4	53±2	151±139	169±116	171	34
PARR	15	71.8±0.4	61±1	149±86	157±70	47	9
PARR	16	70.8±1.0	61±0	33±112	93±69	165	28
PARR	17	69.4±13.3	66±7	251±755	617±465	58	10
PARR	18	69.2±1.1	51±1	49±233	207±105	109	14
PARR	19	68.8±0.8	62±2	22±82	63±54	48	10
PARR	20	67.8±0.6	63±0	-47±150	130±85	150	30
PARR	21	66.5±0.4	62±0	271±60	271±60	70	14
PARR	22	66.0±0.4	62±0	-36±164	139±84	51	10
PARR	23	62.0±4.1	56±5	-69±172	152±95	63	9
PARR	24	65.0±0.9	52±1	141±107	141±107	69	11
PARR	25	64.1±0.3	52±0	-17±51	42±32	83	17
PARR	26	63.4±0.5	52±1	57±64	73±45	117	24
PARR	27	61.9±0.9	55±1	52±85	79±58	111	23
PARR	28	60.2±0.7	52±1	-169±141	182±125	165	33
PARR	29	58.2±1.0	56±1	46±75	70±53	225	45
PARR	30	56.4±0.5	54±0	136±138	163±103	131	27
PARR	31	53.7±2.7	61±1	-158±113	173±88	168	32

Ridge	Segment	Spreading rate [mm/yr]	Spreading asymmetry [%] *	Topography asymmetry [m]	Topography asymmetry amplitude [m]	Length [km]	Number of profiles
PARR	32	51.9±3.6	60±5	-82±48	82±48	53	11
PARR	33	56.8±1.8	58±3	-359±153	359±153	35	7
PARR	34	53.1±0.9	60±2	228±174	261±117	113	23
PARR	35	50.3±1.8	57±7	239±176	239±176	118	24
PARR	36	49.6±0.4	52±1	97±121	121±94	98	20
PARR	37	48.3±0.5	55±1	155±88	155±88	129	26
PARR	38	46.4±0.7	52±2	37±72	58±56	123	25
PARR	39	45.1±0.8	57±2	-58±77	77±57	111	22
SEIR	1	52.1±0.2	52±3	88±186	187±74	77	16
SEIR	2	52.7±0.1	52±0	-229±22	229±22	22	5
SEIR	3	52.9±0.1	51±0	-98±232	218±106	46	9
SEIR	4	53.5±0.3	52±1	-99±123	135±79	95	19
SEIR	5	54.0±0.1	51±0	-94±174	161±109	68	14
SEIR	6	54.3±0.0	51±0	109±13	109±13	21	5
SEIR	7	54.5±0.2	52±1	12±186	158±89	67	14
SEIR	8	55.1±0.3	53±0	-62±103	91±77	62	13
SEIR	9	55.6±0.5	53±1	-4±179	146±99	121	25
SEIR	10	56.1±0.2	52±0	-13±255	229±90	58	12
SEIR	11	56.8±0.7	55±1	16±113	86±73	126	26
SEIR	12	57.1±0.4	53±2	36±175	154±85	97	20
SEIR	13	58.0±1.0	54±2	-44±138	106±98	221	44
SEIR	14	58.8±2.1	58±3	57±214	168±142	130	26
SEIR	15	59.4±0.2	56±1	133±91	133±91	65	13
SEIR	16	59.7±1.2	57±0	99±237	168±139	8	2
SEIR	17	59.6±1.0	54±2	403±155	408±141	116	24
SEIR	18	57.6±1.2	57±5	485±90	485±90	30	5
SEIR	19	60.8±3.6	61±10	790±1006	1174±464	101	19
SEIR	20	61.4±2.4	58±5	1080±106	1080±106	44	9
SEIR	21	61.3±1.8	53±3	265±536	466±364	99	20
SEIR	22	61.3±0.1	52±0	67±37	67±37	75	15
SEIR	23	61.8±0.4	53±0	-93±52	97±44	151	31
SEIR	24	62.3±0.5	51±1	-158±120	158±120	33	6
SEIR	25	62.3±0.1	52±0	-84±42	84±42	47	10
SEIR	26	62.5±0.1	52±0	-99±54	99±54	40	8
SEIR	27	62.6±0.1	53±0	-200±34	200±34	54	11
SEIR	28	62.8±0.6	54±3	-77±140	138±76	113	23
SEIR	29	63.9±1.0	54±1	9±108	70±82	234	45
SEIR	30	64.4±0.7	51±0	-14±58	52±28	112	23
SEIR	31	64.4±0.1	52±0	38±26	39±23	80	16
SEIR	32	64.8±0.2	53±1	-21±42	38±25	135	27
SEIR	33	65.1±0.2	53±1	37±66	63±41	224	45
SEIR	34	65.5±0.1	54±1	-65±75	79±61	135	27
SEIR	35	66.3±1.8	57±1	-23±115	78±84	66	13
SEIR	36	66.5±2.8	57±5	-59±147	124±92	54	11
SEIR	37	66.0±0.2	51±1	-35±105	78±76	96	20
SEIR	38	66.1±0.1	52±0	22±23	27±16	47	10
SEIR	39	66.4±0.7	55±1	74±97	96±75	174	35
SEIR	40	66.6±0.4	51±0	-3±61	55±23	96	20
SEIR	41	66.4±0.2	51±0	-1±47	38±27	97	20
SEIR	42	66.7±0.4	51±1	85±72	102±42	115	23

Ridge	Segment	Spreading rate [mm/yr]	Spreading asymmetry [%] *	Topography asymmetry [m]	Topography asymmetry amplitude [m]	Length [km]	Number of profiles
SEIR	43	66.2±0.3	54±0	173±90	174±89	70	14
SEIR	44	67.0±1.0	53±1	204±105	204±105	21	5
SEIR	45	65.6±1.0	57±2	-12±166	129±100	82	17
SEIR	46	67.2±1.1	52±0	-99±121	99±121	9	2
SEIR	47	67.5±0.4	56±1	120±96	134±74	119	24
SEIR	48	67.7±0.1	52±1	128±135	150±103	22	5
SEIR	49	67.3±0.2	53±1	-123±111	153±62	177	36
SEIR	50	67.0±0.4	53±0	-246±54	246±54	40	9
SEIR	51	67.1±0.4	56±1	41±55	57±38	99	20
SEIR	52	66.9±0.5	55±1	21±129	108±69	81	17
SEIR	53	66.8±0.3	56±1	-135±114	155±82	87	18
SEIR	54	66.6±0.4	54±1	190±53	190±53	18	4
SEIR	55	67.2±0.3	52±1	230±252	279±176	19	4
SEIR	56	67.3±0.5	53±1	-80±111	107±82	41	9
SEIR	57	66.8±0.1	55±1	103±71	104±69	26	6
SEIR	58	66.8±0.3	56±1	6±38	31±21	86	18
SEIR	59	66.7±0.3	57±1	-4±120	90±78	100	21
SEIR	60	66.4±1.5	56±2	152±216	154±213	23	3
SEIR	61	67.1±1.0	51±1	398±336	409±322	45	10
SEIR	62	66.4±0.3	55±1	-16±134	114±66	83	17
SEIR	63	66.2±0.2	52±0	15±300	259±97	28	6
SEIR	64	65.8±0.3	53±1	-271±153	271±153	21	5
SEIR	65	66.0±0.1	51±1	17±259	223±123	87	18
SEIR	66	65.9±0.6	55±2	-10±143	113±82	59	12
SEIR	67	65.8±1.4	52±1	66±167	125±126	89	17
SEIR	68	65.7±0.7	52±0	128±116	154±76	86	15
SEIR	69	65.3±0.2	52±1	6±136	114±72	212	43
SEIR	70	64.6±0.2	51±1	87±157	162±75	255	51
SEIR	71	64.0±0.2	52±1	242±79	248±58	179	36
SEIR	72	63.4±0.4	51±0	316±252	345±210	144	28
SEIR	73	63.9±2.4	60±6	257±280	310±216	85	15
SEIR	74	62.9±1.0	58±5	-21±118	93±74	202	39
SEIR	75	62.3±0.7	53±2	-30±178	144±105	158	32
SEIR	76	61.7±0.4	54±1	-247±89	247±89	44	7
SEIR	77	62.0±2.1	57±4	78±192	160±120	64	7
SEIR	78	62.1±1.3	68±1	70±150	144±78	161	30
SEIR	79	59.8±2.0	52±1	28±160	123±104	295	51
SWIR	1	16.5±0.1	59±3	474±565	602±415	123	15
SWIR	2	16.4±0.4	63±6	413±464	461±412	64	11
SWIR	3	16.8±0.2	63±5	11±364	295±197	97	14
SWIR	5	19.3±1.3	83±4	-232±190	232±190	53	7
SWIR	6	18.8±0.5	72±0	147±110	147±110	72	2
SWIR	7	17.0±0.4	68±1	689±51	689±51	13	2
SWIR	8	16.7±0.1	57±5	14±386	307±202	101	8
SWIR	9	16.6±0.1	55±1	209±229	238±193	36	7
SWIR	10	16.7±0.1	52±1	-51±25	51±25	49	3
SWIR	11	16.7±0.1	70±2	-53±45	60±33	47	7
SWIR	12	16.6±0.1	65±1	19±46	38±27	24	5
SWIR	13	16.7±0.1	60±2	206±213	222±195	72	14
SWIR	14	16.7±0.0	52±2	18±90	75±49	62	13

Ridge	Segment	Spreading rate [mm/yr]	Spreading asymmetry [%] *	Topography asymmetry [m]	Topography asymmetry amplitude [m]	Length [km]	Number of profiles
SWIR	15	16.8±0.0	53±1	-219±99	219±99	77	15
SWIR	16	16.9±0.1	56±1	228±212	259±168	43	9
SWIR	17	16.9±0.2	59±1	127±220	208±135	50	10
SWIR	18	17.0±0.1	63±1	275±160	275±160	46	9
SWIR	19	16.9±0.1	60±3	170±310	252±242	63	13
SWIR	20	16.9±0.0	54±1	88±152	131±114	61	13
SWIR	21	16.9±0.2	51±1	92±775	676±329	52	11
SWIR	22	18.4±1.3	74±9	-264±844	658±577	121	23
SWIR	25	16.8±0.1	51±0	122±893	770±402	79	11
SWIR	26	16.8±0.1	53±2	335±639	372±617	125	19
SWIR	27	16.9±0.1	52±2	305±241	305±241	70	11
SWIR	28	17.0±0.2	56±5	200±472	437±229	70	9
SWIR	29	16.8±0.1	56±1	-82±235	174±174	87	15
SWIR	30	16.8±0.5	63±10	299±197	299±197	86	14
SWIR	32	16.9±0.2	62±7	9±584	423±393	124	25
SWIR	33	17.0±0.3	73±1	349±77	349±77	35	3
SWIR	34	16.7±0.0	59±2	-277±108	277±108	26	2
SWIR	35	16.6±0.1	56±1	136±481	400±272	82	10
SWIR	36	16.8±0.2	61±4	132±384	285±284	120	21
SWIR	37	16.4±0.2	59±3	40±216	175±103	81	5
SWIR	38	16.7±0.1	62±1	335±126	335±126	52	9
SWIR	39	16.7±0.2	57±5	-132±275	221±198	43	8
SWIR	40	16.4±0.0	51±1	-133±546	513±64	30	6
SWIR	41	16.4±0.1	51±1	211±231	230±212	89	17
SWIR	42	16.5±0.1	59±1	527±155	527±155	66	13
SWIR	43	16.8±0.8	63±8	-313±716	601±475	70	12
SWIR	44	19.2±0.8	84±4	236±666	589±355	96	12
SWIR	45	17.3±1.6	54±4	202±247	231±212	64	5
SWIR	46	16.6±0.2	60±6	462±637	665±390	66	10
SWIR	47	16.1±0.0	56±2	-2±796	694±302	57	9
SWIR	48	16.1±0.1	55±3	-66±528	448±266	120	18
SWIR	49	16.5±0.2	68±2	288±720	560±491	52	6
SWIR	50	16.1±0.1	60±3	179±691	602±341	74	12
SWIR	51	15.9±0.1	57±0	529±712	704±515	53	9
SWIR	52	15.8±0.2	57±5	-42±199	156±117	70	8
SWIR	53	16.0±0.3	62±5	-144±658	535±386	118	16
SWIR	54	17.3±0.4	79±2	769±223	769±223	35	3
SWIR	55	16.1±0.4	68±6	148±321	289±190	66	12
SWIR	56	15.7±0.2	54±3	-176±173	188±157	35	7
SWIR	57	15.6±0.1	56±4	70±191	169±102	96	10
SWIR	58	15.6±0.0	58±1	25±125	96±73	57	6
SWIR	59	15.5±0.0	63±1	-47±67	67±45	70	14
SWIR	60	15.4±0.1	58±3	-258±189	268±174	97	19
SWIR	61	15.5±0.2	66±5	-65±71	79±51	35	7
SWIR	62	15.4±0.2	62±3	-79±133	94±122	74	13
SWIR	63	15.6±0.2	63±5	-313±90	313±90	59	11
SWIR	64	15.0±0.8	56±2	16±310	209±175	26	3
SWIR	65	15.2±0.1	61±2	10±53	37±14	33	2
SWIR	66	17.4±3.8	66±6	-47±52	53±45	57	8
SWIR	67	35.7±10.1	66±15	-82±252	216±145	207	17

* A standard deviation of 0 means that it is less than 0.5

Table B.3 Parameters and variables used in this study

Name	Symbol	Value	Unit	Equation
Coordinates	x, y		km	
Topography difference between right-hand-side plate and left-hand-side plate	Δh_{R-L}		m	
Topography difference between faster-moving plate and slower-moving plate	Δh_{F-S}		m	
Degree of spreading asymmetry	A_S	55 – 85	%	(4.3)
Full spreading rate	V_{full}	2 – 18	cm·yr^{-1}	
Relative topography	h		m	(4.1)
Compensation depth	y_c	125	Km	(4.1)
Mantle density	ρ		kg·m^{-3}	(4.1)(4.2)
Reference mantle density	ρ_m	3300	kg·m^{-3}	(4.1)(4.2)(4.4)(B.3) (B.6)
Crustal density	ρ_c	2800	kg·m^{-3}	(4.4)
Water density	ρ_w	1000	kg·m^{-3}	(4.1)(4.4)
Thermal expansion	α	3^{-5}	K^{-1}	(4.2)
Compressibility	β	10^{-11}	Pa^{-1}	(4.2)
Depletion coefficient	γ	0.1	No dimension	(4.2)
Melt fraction	F		%	(4.2)
Temperature	T		°C	(4.2)(B.3) (B.5) (B.7)
Reference temperature	T_{ref}	20	°C	(4.2)
Pressure	P		Pa	(4.2)(B.2)
Reference pressure	P_{ref}	10^5	Pa	(4.2)
Topography variation	Δh		m	(4.4)
Crustal thickness variation	ΔH		km	(4.4)
Mantle velocity	$\mathbf{V}$		cm·yr^{-1}	(B.1) (B.2) (B.3)
Gravity	g	9.8	m·s^{-2}	(B.6)
Effective viscosity	η		Pa·s	(B.2) (B.4)
Viscosity (ductile process)	η_T		Pa·s	(B.4) (B.5)
Viscosity (brittle process)	η_Y		Pa·s	(B.4) (B.6)
Reference viscosity	η_0	10^{19}	Pa·s	(B.5)
Activation energy	Q	250	kJ·mol^{-1}	(B.5)
Gas constant	R	8.314	J·mol^{-1}·K^{-1}	(B.5)
Mantle potential temperature	T_m	1375	°C	(B.5)
Cohesion	C_0	10	MPa	(B.6)
Friction coefficient	μ	0.6	No dimension	(B.6)
Second invariant of the strain rate tensor	$\dot{\varepsilon}_{II}$		s^{-1}	(B.6)
Specific heat capacity	c_p	1250	J·kg^{-1}·K^{-1}	(B.3)
Effective thermal conductivity	K		W·m^{-1}·K^{-1}	(B.3) (B.7)
Reference thermal conductivity	k_0	3	W·m^{-1}·K^{-1}	(B.7)
Nusselt number	Nu	8	No dimension	(B.7)
Smoothing factor	A	0.75	No dimension	(B.7)
Maximum temperature of hydrothermal circulation	T_{cut}	600	°C	(B.7)
Maximum depth of hydrothermal circulation	y_{cut}	6	km	(B.7)

References

Abercrombie, R. E., and G. Ekström (2001), Earthquake slip on oceanic transform
    faults, *Nature*, 410, 74–77, doi:10.1038/35065064.

Aghaei, O., M. R. Nedimović, H. Carton, S. M. Carbotte, J. P. Canales, and J. C.
    Mutter (2014), Crustal thickness and Moho character of the fast-spreading
    East Pacific Rise from 9°42′N to 9°57′N from poststack-migrated 3-D MCS
    data, *Geochem. Geophys. Geosyst.*, 15, 634–657,
    doi:10.1002/2013GC005069.

Aharonov, E., J. A. Whitehead, P. B. Kelemen, and M. Spiegelman (1995),
    Channeling instability of upwelling melt in the mantle, *J. Geophys. Res.*, 100,
    20433–20450, doi:10.1029/95JB01307.

Allerton, S., J. Escartín, and R. C. Searle (2000), Extremely asymmetric magmatic
    accretion of oceanic crust at the ends of slow-spreading ridge segments,
    Geology, 28, 179–182, doi:10.1130/0091-7613(2000)28<179:EAMAOO>
    2.0.CO;2.

Amante, C. and B.W. Eakins (2009), ETOPO1 1 Arc-Minute Global Relief Model:
    Procedures, Data Sources and Analysis, NOAA Technical Memorandum
    NESDIS NGDC-24, National Geophysical Data Center, NOAA,
    doi:10.7289/V5C8276M.

Arnoux, G. M., and D. R. Toomey (2013), Observations of anomalous subcrustal
    reflections along the East Pacific Rise: Possible detection of a melt

permeability barrier, Abstract OS43A-1883 presented at 2013 Fall Meeting, AGU, San Francisco, Calif., 9–13 Dec.

Asimow, P. D., and E. M. Stolper (1999), Steady-state mantle-melt interactions in one dimension: I. Equilibrium transport and melt focusing, *J. Petrol.*, 40, 475–494, doi:10.1093/petroj/40.3.475.

Auzende, J.-M., D. Bideau, E. Bonatti, M. Cannat, J. Honnorez, Y. Lagabrielle, J. Malavieille, V. Mamaloukas-Frangoulis, and C. Mevel (1989), Direct observation of a section through slow-spreading oceanic crust, *Nature*, 337, 726–729, doi:10.1038/337726a0.

Bai, H., and L. G. J. Montési (2015), Slip-rate-dependent melt extraction at oceanic transform faults, *Geochem. Geophys. Geosyst.*, 16, 401–419, doi:10.1002/2014GC005579.

Bai, H., L. G. J. Montési, and M. D. Behn (2017), MeltMigrator: A MATLAB-based software for modeling three-dimensional melt migration and crustal thickness variations at mid-ocean ridges following a rules-based approach, *Geochem. Geophys. Geosyst.*, 18, 445–456, doi:10.1002/2016GC006686.

Ballmer, M. D., C. P. Conrad, E. I. Smith, and N. Harmon (2013), Non-hotspot volcano chains produced by migration of shear-driven upwelling toward the East Pacific Rise, *Geology*, 41, 479–482, doi:10.1130/G33804.1.

Ballu, V., J. Dubois, C. Deplus, M. Diament, and S. Bonvalot (1998), Crustal structure of the Mid-Atlantic Ridge south of the Kane Fracture Zone from seafloor and sea surface gravity data, *J. Geophys. Res.*, 103, 2615–2631, doi:10.1029/97JB02542.

Barth, G. A., and J. C. Mutter (1996), Variability in oceanic crustal thickness and structure: Multichannel seismic reflection results from the northern East Pacific Rise, *J. Geophys. Res.*, 101, 17951–17975, doi:10.1029/96JB00814.

Batiza, R., W. G. Melson, and T. O'Hearn (1988), Simple magma supply geometry inferred beneath a segment of the Mid-Atlantic Ridge, *Nature*, 335, 428–431, doi:10.1038/335428a0.

Becken, M., O. Ritter, P. A. Bedrosian, and U. Weckmann (2011), Correlation between deep fluids, tremor and creep along the central San Andreas fault, *Nature*, 480, 87–90, doi:10.1038/nature10609.

Behn, M. D., C. P. Conrad, and P. G. Silver (2004), Detection of upper mantle flow associated with the African Superplume, *Earth Planet. Sci. Lett.*, 224, 259–274, doi:10.1016/j.epsl.2004.05.026.

Behn, M. D., M. S. Boettcher, and G. Hirth (2007), Thermal structure of oceanic transform faults, *Geology*, 35, 307–310, doi:10.1130/G23112A.1.

Behn, M. D., and T. L. Grove (2015), Melting systematics in mid-ocean ridge basalts: Application of a plagioclase-spinel melting model to global variations in major element chemistry and crustal thickness, *J. Geophys. Res.*, 120, 4863–4886, doi:10.1002/2015JB011885.

Bergman, E. A., and S. C. Solomon (1988), Transform fault earthquakes in the North Atlantic: Source mechanisms and depth of faulting, *J. Geophys. Res.*, 93, 9027–9057, doi:10.1029/JB093iB08p09027.

Beroza, G. C., and T. H. Jordan (1990), Searching for slow and silent earthquakes
using free oscillations, *J. Geophys. Res.*, 95, 2485–2510,
doi:10.1029/JB095iB03p02485.

Blackman, D. K., and D. W. Forsyth (1991), Isostatic compensation of tectonic
features of the Mid-Atlantic Ridge: 25–27°30′S, *J. Geophys. Res.*, 96, 11741–
11758, doi:10.1029/91JB00602.

Bodmer, M., D. R. Toomey, E. E. Hooft, J. Nábělek, and J. Braunmiller (2015),
Seismic anisotropy beneath the Juan de Fuca plate system: Evidence for
heterogeneous mantle flow, *Geology*, 43, 1095–1098, doi:10.1130/G37181.1.

Boettcher, M. S., and T. H. Jordan (2004), Earthquake scaling relations for mid-ocean
ridge transform faults, *J. Geophys. Res.*, 109, B12302,
doi:10.1029/2004JB003110.

Boettcher, M. S., G. Hirth, and B. Evans (2007), Olivine friction at the base of
oceanic seismogenic zones, *J. Geophys. Res.*, 112, B01205,
doi:10.1029/2006JB004301.

Boettcher, M. S., and J. J. McGuire (2009), Scaling relations for seismic cycles on
mid-ocean ridge transform faults, *Geophys. Res. Lett.*, 36, L21301,
doi:10.1029/2009GL040115.

Bonatti, E., M. Ligi, D. Brunelli, A. Cipriani, P. Fabretti, V. Ferrante, L. Gasperini,
and L. Ottolini (2003), Mantle thermal pulses below the Mid-Atlantic Ridge
and temporal variations in the formation of oceanic
lithosphere, *Nature*, 423, 499–505, doi:10.1038/nature01594.

Bottinga, Y., C. J. Allegre, and R. N. Thompson (1978), Partial melting under

    spreading ridges [and discussion], *Philos. Trans. R. Soc. London A*, 288, 501–

    525, doi:10.1098/rsta.1978.0031.

Boudier, F., A. Nicolas, and B. Ildefonse (1996), Magma chambers in the Oman

    ophiolite: Fed from the top and the bottom, *Earth Planet. Sci. Lett.*, 144, 239–

    250, doi:10.1016/0012-821X(96)00167-7.

Bown, J. W., and R. S. White (1994), Variation with spreading rate of oceanic crustal

    thickness and geochemistry, *Earth Planet. Sci. Lett.*, 121, 435–449,

    doi:10.1016/0012-821X(94)90082-5.

Braun, M. G., and P. B. Kelemen (2002), Dunite distribution in the Oman Ophiolite:

    Implications for melt flux through porous dunite conduits, *Geochem.*

    Geophys. Geosyst., 3, 8603, doi:10.1029/2001GC000289.

Bryan, W. B., G. Thompson, and J. N. Ludden (1981), Compositional variation in

    normal MORB from 22°–25°N: Mid-Atlantic ridge and Kane fracture zone, *J.*

    Geophys. Res., 86, 11,815–11,836, doi:10.1029/JB086iB12p11815.

Buck, W. R. (2001), Accretional curvature of lithosphere at magmatic spreading

    centers and the flexural support of axial highs, *J. Geophys. Res.*, 106, 3953–

    3960, doi:10.1029/2000JB900360.

Buck, W. R. and W. Su (1989), Focused mantle upwelling below mid-ocean ridges

    due to feedback between viscosity and melting, *Geophys. Res. Lett.*, 16, 641–

    644, doi:10.1029/GL016i007p00641.

Buck, W. R., C. Small, and W. B. F. Ryan (2009), Constraints on asthenospheric flow

    from the depths of oceanic spreading centers: The East Pacific Rise and the

Australian-Antarctic Discordance, *Geochem. Geophys. Geosyst.,* 10, Q09007, doi:10.1029/2009GC002373.

Calcagno, P., and A. Cazenave (1994), Subsidence of the seafloor in the Atlantic and Pacific Oceans: Regional and large-scale variations, *Earth Planet. Sci. Lett.*, 126, 473–492, doi:10.1016/0012-821X(94)90125-2.

Canales, J. P., R. S. Detrick, J. Lin, J. A. Collins, and D. R. Toomey (2000a), Crustal and upper mantle seismic structure beneath the rift mountains and across a nontransform offset at the Mid-Atlantic Ridge (35°N), *J. Geophys. Res.*, 105, 2699–2719, doi:10.1029/1999JB900379.

Canales, J. P., J. A. Collins, J. Escartín, and R. S. Detrick (2000b), Seismic structure across the rift valley of the Mid-Atlantic Ridge at 23°20′ (MARK area): Implications for crustal accretion processes at slow spreading ridges, *J. Geophys. Res.*, 105, 28411–28425, doi:10.1029/2000JB900301.

Canales, J. P., R. S. Detrick, D. R. Toomey, and W. S. D. Wilcock (2003), Segment-scale variations in the crustal structure of 150–300 kyr old fast spreading oceanic crust (East Pacific Rise, 8°15′N–10°5′N) from wide-angle seismic refraction profiles, *Geophys. J. Int.*, 152, 766–794, doi:10.1046/j.1365-246X.2003.01885.x.

Cann, J. R. (1974), A model for ocean crust structure developed, *Geophys. J. R. Astron. Soc.*, 39, 169–187, doi:10.1111/j.1365-246X.1974.tb05446.x.

Cann, J. R., D. K. Blackman, D. K. Smith, E. McAllister, B. Janssen, S. Mello, E. Avgerinos, A. R. Pascoe, and J. Escartín (1997), Corrugated slip surfaces

formed at ridge-transform intersections on the Mid-Atlantic Ridge, *Nature*, 385, 329–332, doi:10.1038/385329a0.

Carbotte, S. M., C. Small, and K. Donnelly (2004), The influence of ridge migration on the magmatic segmentation of mid-ocean ridges, *Nature*, 429, 743–746, doi:10.1038/nature02652.

Carbotte, S. M., M. R. Nedimović, J. P. Canales, G. M. Kent, A. J. Harding, and M. Marjanović (2008), Variable crustal structure along the Juan de Fuca Ridge: Influence of on-axis hot spots and absolute plate motions, *Geochem. Geophys. Geosyst.*, 9, Q08001, doi:10.1029/2007GC001922.

Carbotte, S. M., D. Smith, M. Cannat, and E. Klein (2015), Tectonic and magmatic segmentation of the Global Ocean Ridge System: A synthesis of observations, *Geol. Soc. Spec. Publ.*, 420, doi:10.1144/SP420.5.

Castillo, P. R., J. H. Natland, Y. Niu, and P. F. Lonsdale (1998), Sr, Nd and Pb isotopic variation along the Pacific–Antarctic risecrest, 53–57°S: Implications for the composition and dynamics of the South Pacific upper mantle, *Earth Planet. Sci. Lett.*, 154, 109–125, doi:10.1016/S0012-821X(97)00172-6.

Cazenave, A., and B. Lago (1991), Long wavelength topography, seafloor subsidence and flattening, *Geophys. Res. Lett.,* 18, 1257–1260, doi:10.1029/91GL01605.

Cessaro, R. K., and D. M. Hussong (1986), Transform seismicity at the intersection of the oceanographer fracture zone and the Mid-Atlantic Ridge, *J. Geophys. Res.*, 91, 4839–4853, doi:10.1029/JB091iB05p04839.

Chadwick, W. W., Jr., and R. W. Embley (1994), Lava flows from a mid-1980s

submarine eruption on the Cleft segment, Juan de Fuca Ridge, *J. Geophys. Res.*, 99, 4761–4776, doi:10.1029/93JB02041.

Chen, Y. J. (1992), Oceanic crustal thickness versus spreading rate, *Geophys. Res. Lett.*, 19, 753–756, doi:10.1029/92GL00161.

Chen, Y. J. (2000), Dependence of crustal accretion and ridge axis topography on

spreading rate, mantle temperature, and hydrothermal cooling, in *Ophiolites and Oceanic Crust: New Insights from Field Studies and the Ocean Drilling Program, Geol. Soc. Am. Spec. Pap., vol. 349*, edited by Y. Dilek et al., pp. 161–179, Geol. Soc. of Am., Boulder, Colo.

Chen, Y. J., and W. J. Morgan (1990), A nonlinear rheology model for mid-ocean

ridge axis topography, *J. Geophys. Res.*, 95, 17,583–17,604, doi:10.1029/JB095iB11p17583.

Cochran, J. R. (1979), An analysis of isostasy in the world's oceans: 2. Mid-ocean

ridge crests, *J. Geophys. Res.*, 84, 4713–4729, doi:10.1029/JB084iB09p04713.

Cochran, J. R. (1986), Variations in subsidence rates along intermediate and fast

spreading mid-ocean ridges, *Geophys. J. Int.*, 1986; 87, 421–454, doi:10.1111/j.1365-246X.1986.tb06631.x.

Conder, J. A., D. W. Forsyth, and E. M. Parmentier (2002), Asthenospheric flow and

the asymmetry of the East Pacific Rise, MELT area, *J. Geophys. Res.*, 107, 2344, doi:10.1029/2001JB000807,2002.

Conrad, C. P., and C. Lithgow-Bertelloni (2002), How mantle slabs drive plate
tectonics, *Science*, 298, 207–209, doi:10.1126/science.1074161.

Conrad, C. P., and L. Husson (2009), Influence of dynamic topography on sea level
and its rate of change, *Lithosphere*, 1, 110–120, doi:10.1130/L32.1.

Conrad, C. P., and M. D. Behn (2010), Constraints on lithosphere net rotation and
asthenospheric viscosity from global mantle flow models and seismic
anisotropy, *Geochem. Geophys. Geosyst.*, 11, Q05W05,
doi:10.1029/2009GC002970.

Conrad, C. P., T. A. Bianco, E. I, Smith, and P. Wessel (2011), Patterns of intraplate
volcanism controlled by asthenospheric shear, *Nat. Geosci.*, 4, 317–321,
doi:10.1038/ngeo1111.

Constantin, M., R. Hékinian, D. Bideau, and R. Hébert (1996), Construction of the
oceanic lithosphere by magmatic intrusions: Petrological evidence from
plutonic rocks formed along the fast-spreading East Pacific
Rise, *Geology*, 24, 731–734, doi:10.1130/0091-
7613(1996)024<0731:COTOLB>2.3.CO;2.

Cormier, M.-H., and K. C. MacDonald (1994), East Pacific Rise 18°–19°S:
Asymmetric spreading and ridge reorientation by ultrafast migration of axial
discontinuities, *J. Geophys. Res.*, 99, 543–564, doi:10.1029/93JB02382.

Crosby, A. G., and D. McKenzie (2009), An analysis of young ocean depth, gravity
and global residual topography, *Geophys. J. Int.*, 178, 1198–1219,
doi:10.1111/j.1365-246X.2009.04224.x.

Crough, S. T. (1983), The correction for sediment loading on the seafloor, *J. Geophys. Res.*, 88, 6449–6454, doi:10.1029/JB088iB08p06449.

Crowley, J., and R. J. O'Connell (2012), An analytic model of convection in a system with layered viscosity and plates, *Geophys. J. Int.*, 188, 61–78, doi:10.1111/j.1365-246X.2011.05254.x.

Cuffaro, M., and E. Miglio (2012), Asymmetry of thermal structure at slow-spreading ridges: geodynamics and numerical modeling, *Comput. Fluids*, 68, 29-37, doi:10.1016/j.compfluid.2012.07.028.

Dalton, C. A., C. H. Langmuir, and A. Gale (2014), Geophysical and geochemical evidence for deep temperature variations beneath mid-ocean ridges, *Science*, 344, 80–83, doi:10.1126/science.1249466.

Davis, E. E., and J. L. Karsten (1986), On the cause of the asymmetric distribution of seamounts about the Juan de Fuca Ridge: Ridge-crest migration over a heterogeneous asthenosphere, *Earth Planet. Sci. Lett.*, 79, 385–396, doi:10.1016/0012-821X(86)90194-9.

Detrick, R. S., R. S. White, and G. M. Purdy (1993), Crustal Structure of North-Atlantic Fracture-Zones, *Rev. Geophys.*, 31, 439–458, doi:10.1029/93RG01952.

Detrick, R. S., H. D. Needham, and V. Renard (1995), Gravity anomalies and crustal thickness variations along the Mid-Atlantic Ridge between 33°N and 40°N, *J. Geophys. Res.*, 100, 3767–3787, doi:10.1029/94JB02649.

Dick, H. J. B., L. Lin, and H. Schouten (2003), An ultraslow-spreading class of ocean ridge, *Nature*, 426, 405–412, doi:10.1038/nature02128.

Dickson, G. O., W. C. Pitman, and J. R. Heirtzler (1968), Magnetic anomalies in the

    South Atlantic and ocean floor spreading, *J. Geophys. Res.*, 73, 2087–2100,

    doi:10.1029/JB073i006p02087.

Dunn, R. A., V. Lekić, R. S. Detrick, and D. R. Toomey (2005), Three-dimensional

    seismic structure of the Mid-Atlantic Ridge (35°N): Evidence for focused melt

    supply and lower crustal dike injection, *J. Geophys. Res.*, 110, B09101,

    doi:10.1029/2004JB003473.

Dziak, R. P., C. G. Fox, and A. E. Schreiner (1995), The June–July 1993 seismo-

    acoustic event at CoAxial segment, Juan de Fuca Ridge: Evidence for a lateral

    dike injection, *Geophys. Res. Lett.*, 22, 135–138, doi:10.1029/94GL01857.

Dziak, R. P., C. G. Fox, R. W. Embley, J. E. Lupton, G. C. Johnson, W. W.

    Chadwick, and R. A. Koshi (1996), Detection of and response to a probable

    volcanogenic T-wave event swarm on the Western Blanco Transform Fault

    Zone, *Geophys. Res. Lett.*, 23, 873–876, doi:10.1029/96GL00240.

Dziak, R. P., D. R. Bohnenstiehl, H. Matsumoto, M. J. Fowler, J. H. Haxel, M.

    Tolstoy, and F. Waldhauser (2009), January 2006 seafloor-spreading event at

    9°50′ N, East Pacific Rise: Ridge dike intrusion and transform fault

    interactions from regional hydroacoustic data. *Geochem. Geophys.*

    Geosyst., 10, Q06T06, doi:10.1029/2009GC002388.

Einarsson, P., and B. Brandsdottir (1978), Seismological evidence for lateral magma

    intrusion during the July 1978 deflation of the Krafla volcano in NE-

    Iceland, *J. Geophys.*, 47, 160–165, doi:10.2172/890964.

Elvers, D., S. P. Srivastava, K. Potter, J. Morley, and D. Sdidel (1973), Asymmetric
spreading across the Juan de Fuca and Gorda rises as obtained from a detailed
magnetic survey, *Earth Planet. Sci. Lett.*, 20, 211–219, doi:10.1016/0012-
821X(73)90160-X.

Erdem, U. M. (2010), Fast line segment intersection, in *MATLAB Central*,
MathWorks, Natick, Mass. [Available
at https://www.mathworks.com/matlabcentral/fileexchange/27205-fast-line-
segment-intersection.]

Escartín, J., D. K. Smith, J. Cann, H. Schouten, C. H. Langmuir, and S. Escrig (2008),
Central role of detachment faults in accretion of slow-spreading oceanic
lithosphere, *Nature*, 455, 790–795, doi:10.1038/nature07333.

Evans, R. L., P. Tarits, A. D. Chave, A. White, G. Heinson, J. H. Filloux, H. Toh, N.
Seama, H. Utada, J. R. Booker, and M. J. Unsworth (1999), Asymmetric
electrical structure in the mantle beneath the East Pacific Rise at 17°S,
Science, 286, 752–756, doi:10.1126/science.286.5440.752.

Fialko, Y. A., and A. M. Rubin (1998), Thermodynamics of lateral dike propagation:
Implications for crustal accretion at slow spreading mid-ocean ridges, *J.
Geophys. Res.*, 103, 2501–2514, doi:10.1029/97JB03105.

Fontaine, F. J., and W. S. D. Wilcock (2007), Two-dimensional numerical models of
open-top hydrothermal convection at high Rayleigh and Nusselt numbers:
Implications for mid-ocean ridge hydrothermal circulation, *Geochem.
Geophys. Geosyst.*, 8, Q07010, doi:10.1029/2007GC001601.

Fornari, D. J., D. G. Gallo, M. H. Edwards, J. A. Madsen, M. R. Perfit, and A. N. Shor (1989), Structure and topography of the Siqueiros transform fault system: Evidence for the development of intra-transform spreading centers, *Mar. Geophys. Res.*, 11, 263–299, doi:10.1007/BF00282579.

Forsyth, D. W. (1992), Geophysical constraints on mantle flow and melt generation beneath mid-ocean ridges, in *Mantle Flow and Melt Generation at Mid-Ocean Ridges*, *Geophys. Monogr. Ser.*, vol. 71, edited by J. Phipps Morgan, D. K. Blackman, and J. M. Sinton, pp. 1–65, AGU, Washington, D. C.

Forsyth, D., S. Webb, L. Dorman, and Y. Shen (1998), Phase velocities of Rayleigh waves in the MELT experiment on the East Pacific Rise, *Science*, 280, 1235–1238, doi:10.1126/science.280.5367.1235.

Fox, P. J., and D. G. Gallo (1984), A tectonic model for ridge-transform-ridge plate boundaries: Implications for the structure of oceanic lithosphere, *Tectonophysics*, 104, 205–242, doi:10.1016/0040-1951(84)90124-0.

Fox, C. G., W. E. Radford, R. P. Dziak, T. K. Lau, H. Matsumoto, and A. E. Schreiner (1995), Acoustic detection of a seafloor spreading episode on the Juan de Fuca Ridge using military hydrophone arrays, *Geophys. Res. Lett.*, 22, 131–134, doi:10.1029/94GL02059.

Fujiwara, T., J. Lin, T. Matsumoto, P. B. Kelemen, B. E. Tucholke, and J. F. Casey (2003), Crustal Evolution of the Mid-Atlantic Ridge near the Fifteen-Twenty Fracture Zone in the last 5 Ma, *Geochem. Geophys. Geosyst.*, 4, 1024, doi:10.1029/2002GC000364.

Gaetani, G. A., S. E. DeLong, and D. A. Wark (1995), Petrogenesis of basalts from the Blanco Trough, northeast Pacific: Inferences for off-axis melt generation, *J. Geophys. Res.*, 100, 4197–4214, doi:10.1029/94JB02774.

Gale A., C. A. Dalton, C. H. Langmuir, Y. Su, and J.-G. Schilling (2013), The mean composition of ocean ridge basalts, *Geochem. Geophys. Geosyst.*, 14, 489–518, doi:10.1029/2012GC004334.

Gale, A., C. H. Langmuir, and C. A. Dalton (2014), The global systematics of ocean ridge basalts and their origin, *J. Petrol.*, 55, 1051–1082, doi:10.1093/petrology/egu017.

Gerya, T. (2010), Dynamical instability produces transform faults at mid-ocean ridges, *Science*, 329, 1047–1050, doi:10.1126/science.1191349.

Ghiorso, M. S. (1994), Algorithms for the estimation of phase stability in heterogeneous thermodynamic systems, *Geochim. Cosmochim. Acta*, 58, 5489–5501, doi:10.1016/0016-7037(94)90245-3.

Ghiorso, M. S., and R. O. Sack (1995), Chemical mass transfer in magmatic processes IV. A revised and internally consistent thermodynamic model for the interpolation and extrapolation of liquid-solid equilibria in magmatic systems at elevated temperatures and pressures, *Contrib. Mineral. Petrol.*, 119, 197–212, doi:10.1007/BF00307281.

Ghiorso, M. S., M. M. Hirschmann, P. W. Reiners, and V. C. Kress (2002), The pMELTS: A revision of MELTS for improved calculation of phase relations and major element partitioning related to partial melting of the mantle to 3 GPa, *Geochem. Geophys. Geosyst.*, 3(5), doi:10.1029/2001GC000217.

Ghods, A., and J. Arkani-Hamed (2000), Melt migration beneath mid-ocean ridges, *Geophys. J. Int.*, 140, 687–697, doi:10.1046/j.1365-246X.2000.00032.x.

Gregg, P. M., J. Lin, M. D. Behn, and L. G. J. Montési (2007), Spreading rate dependence of gravity anomalies along oceanic transform faults, *Nature*, 448, 183–187, doi:10.1038/nature05962.

Gregg, P. M., M. D. Behn, J. Lin, and T. L. Grove (2009), Melt generation, crystallization, and extraction beneath segmented oceanic transform faults, *J. Geophys. Res.*, 114, B11102, doi:10.1029/2008JB006100.

Gregg, P. M., L. B. Hebert, L. G. J. Montési, and R. F. Katz (2012), Geodynamic models of melt generation and extraction at mid-ocean ridges, Oceanography, 25, 8–88, doi:10.5670/oceanog.2012.05.

Grove, T. L., R. J. Kinzler, and W. B. Bryan (1992), Fractionation of mid-ocean ridge basalt (MORB), in *Mantle Flow and Melt Generation at Mid-Ocean Ridges, Geophys. Monogr. Ser., vol. 71*, edited by J. Phipps Morgan, D. K. Blackman, and J. M. Sinton, pp. 281–310, AGU, Washington, D. C.

Hager, B. H., and M. A. Richards (1989), Long-wavelength variations in Earth's geoid: physical models and dynamical implications, *Philos. Trans. R. Soc. London A*, 328, 309–327, doi:10.1098/rsta.1989.0038.

Harig, C., S. Zhong, and F. J. Simons (2010), Constraints on upper mantle viscosity from the flow-induced pressure gradient across the Australian continental keel, *Geochem. Geophys. Geosyst.*, 11, Q06004, doi:10.1029/2010GC003038.

Hart, S. R. (1993), Equilibration during mantle melting: A fractal tree model, *Proc. Natl. Acad. Sci.*, 90, 11,914–11,918.

Hayes, D. E. (1976), Nature and implications of asymmetric sea-floor spreading — "Different rates for different plates", *Geol. Soc. Am. Bull.*, 87, 994–1002, doi:10.1130/0016-7606(1976)87<994:NAIOAS>2.0.CO;2.

Hebert, L. B., and L. G. J. Montési (2010), Generation of permeability barriers during melt extraction at mid-ocean ridges, *Geochem. Geophys. Geosyst.*, 11, Q12008, doi:10.1029/2010GC003270.

Hebert, L. B., and L. G. J. Montési (2011), Melt extraction pathways at segmented oceanic ridges: Application to the East Pacific Rise at the Siqueiros transform, *Geophys. Res. Lett.*, 38, L11306, doi:10.1029/2011GL047206.

Heezen, B. C. (1960), The rift in the ocean floor, *Sci. Am.*, 203, 99–110.

Hékinian, R., D. Bideau, M. Cannat, J. Francheteau, and R. Hébert (1992), Volcanic activity and crust-mantle exposure in the ultrafast Garrett transform fault near 13°28′S in the Pacific, *Earth Planet. Sci. Lett.*, 108, 259–275, doi:10.1016/0012-821X(92)90027-S.

Hékinian, R., D. Bideau, R. Hébert, and Y. Niu (1995), Magmatism in the Garrett transform fault (East Pacific Rise near 13°27′S), *J. Geophys. Res.*, 100, 10,163–10,185, doi:10.1029/94JB02125.

Henstock, T. J., A. W. Woods, and R. S. White (1993), The accretion of oceanic crust by episodic sill intrusion, *J. Geophys. Res.*, 98, 4143–4161, doi:10.1029/92JB02661.

Hess, H. H. (1962), History of ocean basins, in *Petrologic Studies*, edited by E. F. Buddington, pp. 599–620, Geol. Soc. Am. Mem., Boulder, Colo.

Hey, R., G. L. Johnson, and A. Lowrie (1977), Recent plate motions in the Galapagos
area, *Geol. Soc. Am. Bull.*, 88, 1385–1403, doi:10.1130/0016-
7606(1977)88<1385:RPMITG>2.0.CO;2.

Hirschmann, M. M. (2000), Mantle solidus: Experimental constraints and the effects
of peridotite composition, *Geochem. Geophys. Geosyst.*, 1, 1042–26.
doi:10.1029/2000GC000070.

Höink, T., and A. Lenardic (2010), Wavelength convection, Poiseuille-Couette flow
in the low viscosity asthenosphere and the strength of plate margins, *Geophys.
J. Int.,* 180, 23–33, doi:10.1111/j.1365-246X.2009.04404.x.

Hooft, E. E. E., R. S. Detrick, D. R. Toomey, J. A. Collins, and J. Lin (2000), Crustal
thickness and structure along three contrasting spreading segments of the Mid-
Atlantic Ridge, 33.5°–35°N, *J. Geophys. Res.*, 105, 8205–8226,
doi:10.1029/1999JB900442.

Iwamori, H. (1994), ^{238}U-^{230}Th-^{226}Ra and ^{235}U-^{231}Pa disequilibria produced by mantle
melting with porous and channel flows, *Earth Planet. Sci. Lett.*, 125, 1–16,
doi:10.1016/0012-821X(94)90203-8.

Johnson, K. T. M., H. J. B. Dick, and N. Shimizu (1990), Melting in the oceanic
upper mantle: An ion microprobe study of diopsides in abyssal peridotites, *J.
Geophys. Res.*, 95, 2661–2678, doi:10.1029/JB095iB03p02661.

Kaczmarek, M.-A., and O. Müntener (2008), Juxtaposition of melt impregnation and
high-temperature shear zones in the upper mantle; Field and petrological
constraints from the Lanzo Peridotite (Norther Italy), *J. Petrol.*, 49, 2187–
2220, doi:10.1093/petrology/egn065.

Kaczmarek, M.-A., and A. Tommasi (2011), Anatomy of an extensional shear zone in the mantle, Lanzo massif, Italy, *Geochem. Geophys. Geosyst.*, 12, Q0AG06, doi:10.1029/2011GC003627.

Karson, J. A., M. A. Tivey, and J. R. Delaney (2002), Internal structure of uppermost oceanic crust along the Western Blanco Transform Scarp: Implications for subaxial accretion and deformation at the Juan de Fuca Ridge, *J. Geophys. Res.*, 107(B9), 2181, doi:10.1029/2000JB000051.

Kastens, K. A., W. B. F. Ryan, and P. J. Fox (1986), Structural and volcanic expression of a fast slipping ridge-transform-ridge-plate boundary: Sea MARC I and photographic surveys at the Clipperton Transform Fault, *J. Geophys. Res.*, 91, 3469–3488, doi:10.1029/JB091iB03p03469.

Katz, R. F. (2008), Magma dynamics with the enthalpy method: Benchmark solutions and magmatic focusing at mid-ocean ridges, *J. Petrol.*, 49, 2099–2121, doi:10.1093/petrology/egn058.

Katz, R. (2010), Porosity-driven convection and asymmetry beneath mid-ocean ridges, *Geochem. Geophys. Geosyst.*, 11, Q0AC07, doi:10.1029/2010GC003282.

Katz, R. F., M. Spiegelman, and C. H. Langmuir (2003), A new parameterization of hydrous mantle melting, *Geochem. Geophys. Geosyst.*, 4(9), 1073, doi:10.1029/2002GC000433.

Katz, R. F., M. Spiegelman, and S. M. Carbotte (2004), Ridge migration, asthenospheric flow and the origin of magmatic segmentation in the global

mid-ocean ridge system, *Geophys. Res. Lett.*, 31, L15605, doi:10.1029/2004GL020388.

Katz, R. F., M. Spiegelman, and B. K. Holtzman (2006), The dynamics of melt and shear localization in partially molten aggregates, *Nature*, 442, doi:10.1038/nature05039.

Katz, R. F., and S. M. Weatherley (2012), Consequences of mantle heterogeneity for melt extraction at mid-ocean ridges, *Earth Planet. Sci. Lett.*, 335, 226–237, doi:10.1016/j.epsl.2012.04.042.

Kawasaki, I., Y. Kawahara, I. Takata, and N. Kosugi (1985), Mode of seismic moment release at transform faults, *Tectonophysics*, 118, 313–327, doi:10.1016/0040-1951(85)90131-3.

Kelemen, P. B., H. J. B. Dick, and J. E. Quick (1992), Formation of harzburgite by pervasive melt/rock reaction in the upper mantle, *Nature*, 358, 635–641, doi:10.1038/358635a0.

Kelemen, P. B., N. Shimizu, and V. J. M. Salters (1995a), Extraction of mid-ocean-ridge basalt from the upwelling mantle by focused flow of melt in dunite channels, *Nature*, 375, 747–753, doi:10.1038/375747a0.

Kelemen, P. B., J. A. Whitehead, E. Aharonov, and K. A. Jordahl (1995b), Experiments on flow focusing in soluble porous media, with applications to melt extraction from the mantle, *J. Geophys. Res.*, 100, 475–496, doi:10.1029/94JB02544.

Kelemen, P. B., and H. J. B. Dick (1995), Focused melt flow and localized deformation in the upper mantle: Juxtaposition of replacive dunite and ductile

shear zones in the Josephine peridotite, SW Oregon, *J. Geophys. Res.*, 100, 423–438, doi:10.1029/94JB02063.

Kelemen, P. B., G. Hirth, N. Shimizu, M. Spiegelman, and H. J. B. Dick (1997a), A review of melt migration processes in the adiabatically upwelling mantle beneath oceanic spreading ridges, *Philos. Trans. Math. Phys. Eng. Sci.*, 355, 283–318, doi:10.1098/rsta.1997.0010.

Kelemen, P. B., K. Koga, and N. Shimizu (1997b), Geochemistry of gabbro sills in the crust-mantle transition zone of the Oman ophiolite: Implications for the origin of the oceanic lower crust, *Earth Planet. Sci. Lett.*, 146, 475–488, doi:10.1016/S0012-821X(96)00235-X.

Kelemen, P. B., and E. Aharonov (1998), Periodic formation of magma fractures and generation of layered gabbros in the lower crust beneath oceanic spreading ridges, in *Faulting and Magmatism at Mid-Ocean Ridges*, *Geophys. Monogr. Ser.*, vol. 106, edited by W. R. Buck, P. T. Delaney, J. A. Karson, and Y. Lagabrielle, pp. 267–289, AGU, Washington, D. C.

Key, K., S. Constable, L. Liu, and A. Pommier (2013), Electrical image of passive mantle upwelling beneath the northern East Pacific Rise, *Nature*, 495, 499–502, doi:10.1038/nature11932.

Kinzler, R. J., and T. L. Grove (1992), Primary magmas of mid-ocean ridge basalts 1. Experiments and methods, *J. Geophys. Res.*, 97, 6885–6906, doi:10.1029/91JB02840.

Kinzler, R. J. (1997), Melting of mantle peridotite at pressures approaching the spinel to garnet transition: Application to mid-ocean ridge basalt petrogenesis, *J. Geophys. Res.*, 102, 853–874, doi:10.1029/96JB00988.

Klein, E. M., and C. H. Langmuir (1987), Global correlations of ocean ridge basalt chemistry with axial depth and crustal thickness, *J. Geophys. Res.*, 92, 8089–8115, doi:10.1029/JB092iB08p08089.

Klein, F., R. Y. Koyanagi, J. S. Nakata, and W. R. Tanigawa (1987), The seismicity of Kilauea's magma system, in *Volcanism in Hawaii, U.S. Geol. Surv. Prof. Pap. 1350*, edited by R. W. Decker, T. L. Wright, and P. H. Stauffer, pp. 1019–1186. [Available at http://pubs.usgs.gov/pp/1987/1350/.]

Kodaira, S., T. Iidaka, A. Kato, J. O. Park, T. Iwasaki, and Y. Kaneda (2004), High pore fluid pressure may cause silent slip in the Nankai Trough, *Science*, 304, 1295–1298, doi:10.1126/science.1096535.

Kohlstedt, D. L. (1992), Structure, rheology and permeability of partially molten rocks at low melt fractions, in *Mantle Flow and Melt Generation at Mid-Ocean Ridges*, *Geophys. Monogr. Ser.*, vol. 71, edited by J. Phipps Morgan, D. K. Blackman, and J. M. Sinton, pp. 103–121, AGU, Washington, D. C.

Kohlstedt, D. L., and B. K. Holtzman (2009), Shearing melt out of the Earth: An experimentalist's perspective on the influence of deformation on melt extraction, *Annu. Rev. Earth Planet. Sci.*, 37, 561–93, doi:10.1146/annurev.earth.031208.100104.

Korenaga, J., and P. B. Kelemen (1997), Origin of gabbro sills in the Moho transition zone of the Oman ophiolite: Implications for magma transport in the oceanic lower crust, *J. Geophys. Res.*, 102, 27,729–27,749, doi:10.1029/97JB02604.

Kuo, B. Y., and D. W. Forysth (1988), Gravity anomalies of the ridge-transform system in the South Atlantic between 31 and 31°S: Upwelling centers and variations in crustal thickness, *Mar. Geophys. Res.*, 10, 205–232, doi:10.1007/BF00310065.

Kustowski, B., G. Ekström, and A. M. Dziewoński (2008), Anisotropic shear-wave velocity structure of the Earth's mantle: A global model, *J. Geophys. Res.,* 113, B06306, doi:10.1029/2007JB005169.

Langmuir, C. H., and J. F. Bender (1984), The geochemistry of oceanic basalts in the vicinity of transform faults: Observations and implications, *Earth Planet. Sci. Lett.*, 69, 107–127, doi:10.1016/0012-821X(84)90077-3.

Langmuir, C. H., J. F. Bender, and R. Batiza (1986), Petrological and tectonic segmentation of the East Pacific Rise, 5°30′–14°30′ N, *Nature*, 322, 422–429, doi:10.1038/322422a0.

Langmuir, C. H., E. M. Klein, and T. Plank (1992), Petrological systematics of mid-ocean ridge basalts: Constraints on melt generation beneath ocean ridges, in *Mantle Flow and Melt Generation at Mid-Ocean Ridges, Geophys. Monogr. Ser.*, 71, edited by J. Phipps Morgan, D. K. Blackman, and J. M. Sinton, pp. 183–280, AGU, Washington, D. C.

Langmuir, C. H., C. Hamelin, Z. Chen, J. Escartin, M. Laubier, O. E. Jagoutz, and J. Looney (2013), Do ridge segments with asymmetric and symmetric spreading

have distinctive geochemical signatures? Abstract T21F-01 presented at 2013 Fall Meeting, AGU, San Francisco, Calif., 9–13 Dec.

Lawson, K., R. C. Searle, J. A. Pearce, P. Browning, and P. Kempton (1996), Detailed volcanic geology of the MARNOK area, Mid-Atlantic Ridge north of Kane transform, *Geol. Soc. London Spec. Publ.*, 118, 61–102, doi:10.1144/GSL.SP.1996.118.01.05.

Le Pichon, X., R. E. Houtz, C. L. Drake, and J. E. Nafe (1965), Crustal structure of the mid-ocean ridges: 1. Seismic refraction measurements, *J. Geophys. Res.*, 70, 319–339, doi:10.1029/JZ070i002p00319.

Lin, J., G. M. Purdy, H. Schouten, J. C. Sempere, and C. Zervas (1990), Evidence from gravity data for focused magmatic accretion along the Mid-Atlantic Ridge, *Nature*, 344, 627–632, doi:10.1038/344627a0.

Lin, J., and J. Phipps Morgan (1992), The spreading rate dependence of 3-dimensional mid-ocean ridge gravity structure, *Geophys. Res. Lett.*, 19, 13–16, doi:10.1029/91GL03041.

Liu, Y., J. J. McGuire, and M. D. Behn (2012), Frictional behavior of oceanic transform faults and its influence on earthquake characteristics, *J. Geophys. Res.*, 117, B04315, doi:10.1029/2011JB009025.

Lin, P.-Y. P., J. B. Gaherty, G. Jin, J. A. Collins, D. Lizarralde, R. L. Evans, and G. Hirth (2016), High-resolution seismic constraints on flow dynamics in the oceanic asthenosphere, *Nature*, 535, 538–541, doi:10.1038/nature18012.

Long, M. D., and T. W. Becker (2010), Mantle dynamics and seismic anisotropy, *Earth Planet. Sci. Lett.*, 297, 341–354, doi:10.1016/j.epsl.2010.06.036.

Macdonald, K. C. (1982), Mid-ocean ridges: Fine scale tectonic, volcanic and

hydrothermal processes within the plate boundary zone, *Annu. Rev. Earth

Planet. Sci.*, 10, 155–190, doi:10.1146/annurev.ea.10.050182.001103.

Macdonald, K. C., P. J. Fox, R. T. Alexander, R. Pockalny, and P.

Gente (1996), Volcanic growth faults and the origin of Pacific abyssal

hills, *Nature*, 380, 125–129, doi:10.1038/380125a0.

Machado, N., J. N. Ludden, and C. Brooks (1982), Fine-scale isotopic heterogeneity

in the sub-Atlantic mantle, *Nature*, 295, 226–228, doi:10.1038/295226a0.

Magde, L. S., and D. W. Sparks (1997), Three-dimensional mantle upwelling, melt

generation, and melt migration beneath segment slow spreading ridges, *J.

Geophys. Res.*, 102, 20,571–20,583, doi:10.1029/97JB01278.

Matthews, K. J., R. D. Müller, P. Wessel, and J. M. Whittaker (2011), The tectonic

fabric of the ocean basins, *J. Geophys*. *Res*., 116, B12109,

doi:10.1029/2011JB008413.

McCaig, A. M., R. A. Cliff, J. Escartin, A. E. Fallick, and C. J. MacLeod (2007),

Oceanic detachment faults focus very large volumes of black smoker fluids,

Geology, 35, 935–938, doi:10.1130/G23657A.1.

McKenzie, D. P. (1969), Speculations on the consequences and causes of plate

motions, *Geophys. J. R. Astron. Soc.*, 18, 1–32, doi:10.1111/j.1365-

246X.1969.tb00259.x.

McKenzie, D. (1984), The generation and compaction of partial melts, *J. Petrol.*, 25,

713–765, doi:10.1093/petrology/25.3.713.

McKenzie, D. P. (1985), ^{230}Th-^{238}U disequilibrium and the melting processes beneath ridge axes, *Earth Planet. Sci. Lett.*, 72, 149–157, doi:10.1016/0012-821X(85)90001-9.

McKenzie, D., and M. J. Bickle (1988), The volume and composition of melt generated by extension of the lithosphere, *J. Petrology*, 29, 625–679. doi:10.1093/petrology/25.3.713.

McKenzie, D. P., and R. K. O'Nions (1991), Partial melt distributions from inversion of rare earth element concentrations, *J. Petrol.*, 32, 1021–1091, doi:10.1093/petrology/32.5.1021.

Melt Seismic Team (1998), Imaging the deep seismic structure beneath a mid-ocean ridge: The MELT experiment, *Science*, 280, 1215–1218, doi:10.1126/science.280.5367.1215.

Menard, H. W., and T. Atwater (1969), Origin of fracture zone topography, *Nature*, 222, 1037–1040, doi:10.1038/2221037a0.

Miller, M. M., T. Melbourne, D. J. Johnson, and W. Q. Sumner (2002), Periodic slow earthquakes from the Cascadia subduction zone, *Science*, 295, 2423–2423, doi:10.1126/science.1071193.

Miller, K. J., W. L. Zhu, L. G. J. Montési, and G. A. Gaetani (2014), Experimental quantification of permeability of partially molten mantle rock, *Earth Planet. Sci. Lett.*, 388, 273–282, doi:10.1016/j.epsl.2013.12.003.

Montési, L. G. J., and M. D. Behn (2007), Mantle flow and melting underneath oblique and ultraslow mid-ocean ridges, *Geophys. Res. Lett.*, 34, L24307, doi:10.1029/2007GL031067.

Montési, L. G. J., M. D. Behn, L. B. Hebert, J. Lin, and J. L. Barry (2011), Controls on melt migration and extraction at the ultraslow Southwest Indian Ridge 10–16°E, *J. Geophys. Res.*, 116, B10102, doi:10.1029/2011JB008259.

Morgan, W. J. (1971), Convection plumes in the lower mantle, *Nature*, 230, 42–43, doi:10.1038/230042a0.

Moulik, P. and G. Ekstrom (2014), An anisotropic shear velocity model of the Earth's mantle using normal modes, body waves, surface waves and long-period waveforms, *Geophys. J. Int.*, 199, 1713–1738, doi: 10.1093/gji/ggu356.

Müller, R. D., W. R. Roest, J.-Y. Royer, L. M. Gahagan, and J. G. Sclater (1997), Digital isochrons of the world's ocean floor, *J. Geophys. Res.*, 102, 3211–3214, doi:10.1029/96JB01781.

Müller, R. D., W. R. Roest, and J. Y. Royer (1998), Asymmetric sea-floor spreading caused by ridge–plume interactions, *Nature*, 396, 455–459, doi:10.1038/24850.

Müller, R. D., M. Sdrolias, C. Gaina, and W. R. Roest (2008), Age, spreading rates, and spreading asymmetry of the world's ocean crust, *Geochem. Geophys. Geosyst.*, 9, Q04006, doi:10.1029/2007GC001743.

Murton, B. J., and I. G. Gass (1986), Western Limassol Forest complex, Cyprus: Part of an upper Cretaceous leaky transform fault, *Geology*, 14, 255–258, doi:10.1130/0091-7613(1986)14<255:WLFCCP>2.0.CO;2.

Natarov, S. I. and C. P. Conrad (2012), The role of Poiseuille flow in creating depth-variation of asthenospheric shear, *Geophys. J. Int.*, 190, 1297–1310, doi:10.1111/j.1365-246X.2012.05562.x.

Nicolas, A. (1986), A melt extraction model based on structural studies in mantle peridotites, *J. Petrol.*, 27, 999–1022, doi:10.1093/petrology/27.4.999.

Nicolas, A. (1990), Melt extraction from mantle peridotites: Hydrofracturing and porous flow, with consequences for oceanic ridge activity, in *Magma Transport and Storage*, edited by M. P. Ryan, pp. 159–174, Wiley, New York.

Nicolas, A., and I. Reuber (1988), A new magma chamber model based on structural studies in the Oman ophiolite, *Tectonophysics*, 151, 87–105, doi:10.1016/0040-1951(88)90242-9.

Nicolas, A., F. Boudier, and B. Ildefonse (1996), Variable crustal thickness in the Oman ophiolite: Implication for oceanic crust, *J. Geophys. Res.*, 101, 17941–17950, doi:10.1029/96JB00195.

Niu, Y., K. D. Collerson, R. Batiza, J. I. Wendt, and M. Regelous (1999), Origin of enriched-type mid-ocean ridge basalt at ridges far from mantle plumes: The East Pacific Rise at 11°20′N, *J. Geophys. Res.*, 104(B4), 7067–7087, doi:10.1029/1998JB900037.

Niu, X., A. Ruan, J. Li, T. A. Minshull, D. Sauter, Z. Wu, X. Qiu, M. Zhao, Y. J. Chen, and S. Singh (2015), Along-axis variation in crustal thickness at the ultraslow spreading Southwest Indian Ridge (50°E) from a wide-angle seismic experiment, *Geochem. Geophys. Geosyst.,* 16, 468–485, doi:10.1002/2014GC005645.

Obara, K., H. Hirose, F. Yamamizu, and K. Kasahara (2004), Episodic slow slip events accompanied by non-volcanic tremors in southwest Japan subduction zone, *Geophys. Res. Lett.*, 31, L23602, doi:10.1029/2004GL020848.

O'Haver, T. (2008), Fast smoothing function, in *MATLAB Central*, MathWorks, Natick, Mass. [Available at https://www.mathworks.com/matlabcentral/fileexchange/19998-fast-smoothing-function.]

Oxburgh, E. R., and E. M. Parmentier (1977), Compositional and density stratification in oceanic lithosphere-causes and consequences, *J. Geol. Soc.*, 133, 343–355, doi:10.1144/gsjgs.133.4.0343.

Pacheco, J. F., L. R. Sykes, and C. H. Scholz (1993), Nature of seismic coupling along simple plate boundaries of the subduction type, *J. Geophys. Res.*, 98, 14,133–14,159, doi:10.1029/93JB00349.

Paczkowski, K., C. J. Thissen, M. D. Long, and L. G. J. Montési (2014a), Deflection of mantle flow beneath subducting slabs and the origin of subslab anisotropy, *Geophys. Res. Lett.*, 41, 6734–6742, doi:10.1002/2014GL060914.

Paczkowski, K., L. G. J. Montési, M. D. Long, and C. J. Thissen (2014b), Three-dimensional flow in the subslab mantle, *Geochem. Geophys. Geosyst.,* 15, 3989–4008, doi: 10.1002/2014GC005441.

Parmentier, E. M., and D. W. Forsyth (1985), Three-dimensional flow beneath a slow spreading ridge axis: A dynamic contribution to the deepening of the Median Valley toward fracture zones, *J. Geophys. Res.*, 90, 678–684, doi:10.1029/JB090iB01p00678.

Parmentier, E. M., and J. Phipps Morgan (1990), Spreading rate dependence of three-dimensional structure in oceanic spreading centres, *Nature*, 348, 325–328, doi:10.1038/348325a0.

Parnell-Turner, R., N. White, T. Henstock, B. Murton, J. Maclennan, and S. M. Jones (2014), A continuous 55 million year record of transient mantle plume activity beneath Iceland, *Nat. Geosci.*, 7, 914–919, doi:10.1038/ngeo2281.

Parnell-Turner, R., H. Schouten, and D. K. Smith (2016), Tectonic structure of the Mid-Atlantic Ridge near 16°30'N, *Geochem. Geophys. Geosyst.*, 17, doi:10.1002/2016GC006514.

Parsons, B., and J. G. Sclater (1977), An analysis of the variation of ocean floor bathymetry and heat flow with age, *J. Geophys. Res.*, 82, 803–827, doi:10.1029/JB082i005p00803.

Perfit, M. R., et al. (1996), Recent volcanism in the Siqueiros transform fault: Picritic basalts and implications for MORB magma genesis, *Earth Planet. Sci. Lett.*, 141, 91–108, doi:10.1016/0012-821X(96)00052-0.

Phipps Morgan, J. (1987), Melt migration beneath mid-ocean spreading centers, *Geophys. Res. Lett.*, 14, 1238–1241, doi:10.1029/GL014i012p01238.

Phipps Morgan, J., E. M. Parmentier, and J. Lin (1987), Mechanisms for the origin of mid-ocean ridge axial topography: Implications for the thermal and mechanical structure of accreting plate boundaries, *J. Geophys. Res.*, 92, 12,823–12,836, doi:10.1029/JB092iB12p12823.

Phipps Morgan, J., and D. W. Forsyth (1988), Three-dimensional flow and temperature perturbations due to a transform offset: Effects on oceanic crustal and upper mantle structure, *J. Geophys. Res.*, 93, 2955–2966, doi:10.1029/JB093iB04p02955.

Phipps Morgan, J., and W. H. Smith (1992), Flattening of the sea-floor depth-age curve as a response to asthenospheric flow, *Nature*, 359, 524–527, doi:10.1038/359524a0.

Phipps Morgan, J., and Y. J. Chen (1993), The genesis of oceanic crust: Magma injection, hydrothermal circulation, and crustal flow, *J. Geophys. Res.*, 98, 6283–6297, doi:10.1029/92JB02650.

Phipps Morgan, J., W. J. Morgan, Y.-S. Zhang, and W. H. F. Smith (1995), Observational hints for a plume-fed, suboceanic asthenosphere and its role in mantle convection, *J. Geophys. Res.*, 100(B7), 12753–12767, doi:10.1029/95JB00041.

Pockalny, R. A. (1997), Evidence of transpression along the Clipperton Transform: Implications for processes of plate boundary reorganization, *Earth Planet. Sci. Lett.*, 146, 449–464, doi:10.1016/S0012-821X(96)00253-1.

Press, W. H., B. P. Flannery, S. A. Teukolsky, and W. T. Vetterling (2007), *Numerical Recipes: The Art of Scientific Computing*, 3rd ed., pp. 778–780, Cambridge Univ. Press, N. Y.

Püthe, C., and T. Gerya (2014), Dependence of mid-ocean ridge morphology on spreading rate in numerical 3-D models, *Gondwana Res.*, 25, 270–283, doi:10.1016/j.gr.2013.04.005.

Rabinowicz, M., A. Nicolas, and J. Vigneresse (1984), A rolling mill effect in the asthenosphere beneath oceanic spreading centers, *Earth Planet. Sci. Lett.*, 67, 97–108, doi:10.1016/0012-821X(84)90042-6.

Rea, D. K. (1976), Analysis of a fast-spreading rise crest: the East Pacific Rise, 9° to
12° South, *Mar. Geophys. Res.*, 2, 291–313, doi:10.1007/BF00426250.

Reid, I., and H. R. Jackson (1981), Oceanic spreading rate and crustal thickness, *Mar. Geophys. Res.*, 5, 165–172. doi:10.1007/BF00163477.

Reynolds, J. R., and C. H. Langmuir (1997), Petrological systematics of the Mid-Atlantic ridge south of Kane: Implications for ocean crust formation, *J. Geophys. Res.*, 102, 14,915–14,946, doi:10.1029/97JB00391.

Ribe, N. M. (1988), On the dynamics of mid-ocean ridges, *J. Geophys. Res.*, 93, 429–436, doi:10.1029/JB093iB01p00429.

Richards, M. A., W. Yang, J. R. Baumgardner, and H. Bunge (2001), Role of a low-viscosity zone in stabilizing plate tectonics: implications for comparative terrestrial planetology, *Geochem. Geophys. Geosyst.,* 2, 1026, doi:10.1029/2000GC000115.

Rohr, K. M. M., B. Milkereit, and C. J. Yorath (1988), Asymmetric deep crustal structure across the Juan de Fuca Ridge, *Geology*, 16, 533–537, doi:10.1130/0091-7613(1988)016<0533:ADCSAT>2.3.CO;2.

Roland, E., M. D. Behn, and G. Hirth (2010), Thermal-mechanical behavior of oceanic transform faults: Implications for the spatial distribution of seismicity, *Geochem. Geophys. Geosyst.*, 11, Q07001, doi:10.1029/2010GC003034.

Royer, J. Y., R. D. Müller, L. M. Gahagan, L. A. Lawver, C. L. Mayes, D. Nürnberg, and J. G. Sclater (1992), A global isochron chart, *Tech. Rep.*, 117, Austin, Univ. of Tex. Inst. for Geophys.

Rundquist, D. V., and P. O. Sobolev (2002), Seismicity of mid-oceanic ridges and its

    geodynamic implications: A review, *Earth Sci. Rev.*, 58, 143–161,

    doi:10.1016/S0012-8252(01)00086-1.

Sandwell, D. T., and W. H. Smith (1997), Marine gravity anomaly from Geosat and

    ERS 1 satellite altimetry, *J. Geophys. Res.*, 102, 10,039–10,054,

    doi:10.1029/96JB03223.

Sandwell, D. T., and W. H. F. Smith (2009), Global marine gravity from retracked

    Geosat and ERS-1 altimetry: Ridge segmentation versus spreading rate, *J.*

    Geophys. Res., 114, B01411, doi:10.1029/2008JB006008.

Scheirer, D. S., D. W. Forsyth, M. H. Cormier, and K. C. Macdonald (1998),

    Shipboard geophysical indications of asymmetry and melt production beneath

    the East Pacific Rise near the MELT experiment, *Science*, 280, 1221–1224,

    doi:10.1126/science.280.5367.1221.

Schilling, J. G., R. H. Kingsley, and J. D. Devine (1982), Galápagos hot spot-

    spreading center system: 1. Spatial petrological and geochemical variations

    (83°W–101°W), *J. Geophys. Res.*, 87, 5593–5610,

    doi:10.1029/JB087iB07p05593.

Schlindwein, V., A. Demuth, W. H. Geissler, and W. Jokat (2013), Seismic gap

    beneath Logachev Seamount: Indicator for melt focusing at an ultraslow mid-

    ocean ridge?, *Geophys. Res. Lett.*, 40, 1703–1707, doi:10.1002/grl.50329.

Scott, D. R., and D. J. Stevenson (1989), A self-consistent model of melting, magma

    migration and buoyancy-driven circulation beneath mid-ocean ridges, *J.*

    Geophys. Res., 94, 2973–2988, doi:10.1029/JB094iB03p02973.

Schouten, H., H. J. Dick, and K. D. Klitgord (1987), Migration of mid-ocean-ridge

    volcanic segments, *Nature*, 326, 835–839, doi:10.1038/326835a0.

Shah, A. K., and W. R. Buck (2003), Plate bending stresses at axial highs, and

    implications for faulting behavior, *Earth Planet. Sci. Lett.*, 211, 343–356,

    doi:10.1016/S0012-821X(03)00187-0.

Shen, Y., and D. W. Forsyth (1992), The effects of temperature- and pressure-

    dependent viscosity on three-dimensional passive flow of the mantle beneath a

    ridge-transform system, *J. Geophys. Res.*, 97, 19,717–19,728,

    doi:10.1029/92JB01467.

Shiels, C., and S. L. Butler (2015), Couette and Poiseuille flows in a low viscosity

    asthenosphere: Effects of internal heating rate, Rayleigh number, and plate

    representation, *Phys. Earth Planet. Int.*, 246, 31–40,

    doi:10.1016/j.pepi.2015.07.002.

Sinha, M. C., and R. L. Evans (2004), Geophysical constraints upon the thermal

    regime of the ocean crust, in *Mid-Ocean Ridges: Hydrothermal Interactions*

    Between the Lithosphere and Oceans, Geophys. Monogr. Ser., vol. 148, edited

    by C. R. German, J. Lin, and L. M. Parson, pp. 19–62, AGU, Washington D.

    C.

Sinton, J., E. Bergmanis, K. Rubin, R. Batiza, T. K. P. Gregg, K. Grönvold, K. C.

    Macdonald, and S. M. White (2002), Volcanic eruptions on mid-ocean ridges:

    New evidence from the superfast spreading East Pacific Rise, 17°–19°S, *J.*

    Geophys. Res., 107(B6), doi:10.1029/2000JB000090.

Sleep, N. H. (1988), Tapping of melt by veins and dikes, *J. Geophys. Res.*, 93(B9),

> 10255–10272, doi:10.1029/JB093iB09p10255.

Small, C., and L. V. Danyushevsky (2003), Plate-kinematic explanation for mid-

> oceanic-ridge depth discontinuities, *Geology*, 31, 399–402, doi:10.1130/0091-

> 7613(2003)031<0399:PEFMDD>2.0.CO;2.

Smith, C. S. (1948), Grains, phases, and interfaces: An interpretation of

> microstructure, *Trans. Am. Inst. Min. Metall. Eng.*, 175, 15–51,

> doi:10.1007/s11661-010-0215-5.

Smith, C. S. (1964), Some elementary principles of polycrystalline microstructure,

> *Metall. Rev.*, 9(33), 1–48, doi:10.1179/mtlr.1964.9.1.1.

Smith, D. K., and J. R. Cann (1999), Constructing the upper crust of the Mid-Atlantic

> Ridge: A reinterpretation based on the Puna Ridge, Kilauea Volcano, *J.*

> *Geophys. Res.*, 104, 25,379–25,399, doi:10.1029/1999JB900177.

Smith, D. K., M. Tolstoy, C. G. Fox, D. R. Bohnenstiehl, H. Matsumoto, and M. J.

> Fowler (2002), Hydroacoustic monitoring of seismicity at the slow-spreading

> Mid-Atlantic ridge, *Geophys. Res. Lett.*, 29(11), doi:10.1029/2001GL013912.

Smith, D. K., J. Escartin, M. Cannat, M. Tolstoy, C. G. Fox, D. R. Bohnenstiehl,

> and S. Bazin (2003), Spatial and temporal distribution of seismicity along the

> northern Mid-Atlantic ridge (15°–35° N), *J. Geophys. Res.*, 108(B3), 2167,

> doi:10.1029/2002JB001964.

Smith, D. K., J. R. Cann, and J. Escartín (2006), Widespread active detachment

> faulting and core complex formation near 13°N on the Mid-Atlantic Ridge,

> *Nature*, 442, 440–443, doi:10.1038/nature04950.

Smith, D. K., et al. (2014), Development and evolution of detachment faulting along

  50 km of the Mid-Atlantic Ridge near 16.5°N, *Geochem. Geophys. Geosyst.*,

  15, 4692–4711, doi:10.1002/2014GC005563.

Smith, P. M., and P. D. Asimow (2005), Adiabat_1ph: A new public front-end to the

  MELTS, pMELTS, and pHMELTS models, *Geochem. Geophys.*

  Geosyst., 6, Q02004, doi:10.1029/2004GC000816.

Sparks, D. W., and E. M. Parmentier (1991), Melt extraction from the mantle beneath

  spreading centers, *Earth Planet. Sci. Lett.*, 105, 368–377, doi:10.1016/0012-

  821X(91)90178-K.

Spiegelman, M. (1993), Physics of melt extraction: Theory, implications, and

  applications, *Philos. Trans. R. Soc. London A*, 342, 23–41,

  doi:10.1098/rsta.1993.0002.

Spiegelman, M. (2003), Linear analysis of melt band formation by simple shear,

  Geochem. Geophys. Geosyst., 4, 8615, doi:10.1029/2002GC000499.

Spiegelman, M., and D. McKenzie (1987), Simple 2-D models for melt extraction at

  mid-ocean ridges and island arcs, *Earth Planet. Sci. Lett.*, 83, 137–152,

  doi:10.1016/0012-821X(87)90057-4.

Spiegelman, M., and J. R. Reynolds (1999), Combined dynamic and geochemical

  evidence for convergent melt flow beneath the East Pacific Rise, *Nature*, 402,

  282–285, doi:10.1038/46260.

Spiegelman, M., P. B. Kelemen, and E. Aharonov (2001), Causes and consequences

  of flow organization during melt transport: The reaction infiltration instability

in compactible media, *J. Geophys. Res.*, 106, 2061–2077,
doi:10.1029/2000JB900240.

Standish, J. J., and K. W. W. Sims (2010), Young off-axis volcanism along the
ultraslow-spreading Southwest Indian Ridge, *Nat. Geosci.*, 3, 286–292,
doi:10.1038/ngeo824.

Stein, S., H. J. Melosh, and J. B. Minster (1977), Ridge migration and asymmetric
sea-floor spreading, *Earth Planet. Sci. Lett.*, 36, 51–62, doi:10.1016/0012-
821X(77)90187-X.

Steinberger, B. (2000), Plumes in a convecting mantle: Models and observations for
individual hotspots, *J. Geophys. Res.*, 105, 11,127–11,152,
doi:10.1029/1999JB900398.

Steinberger, B., and R. J. O'Connell (1998), Advection of plumes in mantle flow:
Implications on hotspot motion, mantle viscosity and plume
distribution, *Geophys. J. Int.*, 132, 412–434, doi:10.1046/j.1365-
246x.1998.00447.x.

Stevenson, D. J. (1989), Spontaneous small-scale melt segregation in partial melts
undergoing deformation, *Geophys. Res. Lett.*, 16, 1067–1070,
doi:10.1029/GL016i009p01067.

Su, W., and W. R. Buck (1993), Buoyancy effects on mantle flow under Mid-Ocean
Ridges, *J. Geophys. Res.*, 98, 12191–12205, doi:10.1029/93JB00994.

Supak, S., S. M. Carbotte, and K. C. Macdonald (2007), Influence of ridge migration
and proximity to hot spots on the morphology of slow- and intermediate-

spreading centers, *Geochem. Geophys. Geosyst.*, 8, Q01010, doi:10.1029/2006GC001387.

Talwani, M., X. Le Pichon, and M. Ewing (1965), Crustal structure of the mid-ocean ridges: 2. Computed model from gravity and seismic refraction data, *J. Geophys. Res.*, 70, 341–352, doi:10.1029/JZ070i002p00341.

Talwani, M., C. C. Windisch, and M. G. Langseth (1971), Reykjanes ridge crest: A detailed geophysical study, *J. Geophys. Res.*, 76, 473–517, doi:10.1029/JB076i002p00473.

Tepley, F. J., III, C. C. Lundstrom, K. W. W. Sims, and R. Hékinian (2004), U-series disequilibria in MORB from the Garrett Transform and implications for mantle melting, *Earth Planet. Sci. Lett.*, 223, 79–97, doi:10.1016/j.epsl.2004.04.010.

Thompson, G., and W. G. Melson (1972), The petrology of oceanic crust across fracture zones in the Atlantic Ocean: Evidence of a new kind of sea-floor spreading, *J. Geol.*, 80, 526–538.

Thompson, G., W. B. Bryan, R. Ballard, K. Hamuro, and W. G. Melson (1985), Axial processes along a segment of the East Pacific Rise. 10°-12°N, *Nature*, 318, 429–433, doi:10.1038/318429a0.

Till, C. B., T. L. Grove, and M. J. Krawczynski (2012), A melting model for variably depleted and enriched lherzolite in the plagioclase and spinel stability fields, *J. Geophys. Res.*, 117, B06206, doi:10.1029/2011JB009044.

226

Tolstoy, M., A. Harding, and J. Orcutt (1993), Crustal thickness on the Mid-Atlantic Ridge: Bull's-eye gravity anomalies and focused accretion, *Science*, 262, 726–729, doi:10.1126/science.262.5134.726.

Toomey, D. R., S. C. Solomon, and G. M. Purdy (1994), Tomographic imaging of the shallow crustal structure of the East Pacific Rise at 9°30′N, *J. Geophys. Res.*, 99, 24135–24157, doi:10.1029/94JB01942.

Toomey, D. R., W. S. Wilcock, S. C. Solomon, W. C. Hammond, and J. A. Orcutt (1998), Mantle seismic structure beneath the MELT region of the East Pacific Rise from P and S wave tomography, *Science*, 280, 1224–1227, doi:10.1126/science.280.5367.1224.

Toomey, D. R., W. S. D. Wilcock, J. A. Conder, D. W. Forsyth, J. D. Blundy, E. M. Parmentier, and W. C. Hammond (2002), Asymmetric mantle dynamics in the MELT region of the East Pacific Rise, *Earth Planet. Sci. Lett.*, 200, 287–295, doi:10.1016/S0012-821X(02)00655-6.

Tucholke, B. E., and J. Lin (1994), A geological model for the structure of ridge segments in slow-spreading ocean crust, *J. Geophys. Res.*, 99, 11,937–11,958, doi:10.1029/94JB00338.

Turcotte, D. L., and E. R. Oxburgh (1967), Finite amplitude convective cells and continental drift, *J. Fluid Mech.*, 28, 29–42, doi:10.1017/S0022112067001880.

Turcotte, D., and G. Schubert (2002), *Geodynamics*, 456 pp., Cambridge Univ. Press, N. Y.

van Keken, P. E., et al. (2008), A community benchmark for subduction zone modeling, *Phys. Earth Planet. Inter.*, 171, 187–197, doi:10.1016/j.pepi.2008.04.015.

VanderBeek, B., D. R. Toomey, E. E. E. Hooft, and W. S. D. Wilcock (2016), Segmentation of mid-ocean ridges caused by oblique mantle divergence, *Nature Geosci.*, 9, 636–642, doi:10.1038/NGEO2745.

Vera, E. E., J. C. Mutter, P. Buhl, J. A. Orcutt, A. J. Harding, M. E. Kappus, R. S. Detrick, and T. M. Brocher (1990), The structure of 0- to 0.2-m.y.-old oceanic crust at 9N on the East Pacific Rise from expanded spread profiles, *J. Geophys. Res.*, 95, 15,529–15,556, doi:10.1029/JB095iB10p15529.

Vidale, J. E., and P. M. Shearer (2006), A survey of 71 earthquake bursts across southern California: Exploring the role of pore fluid pressure fluctuations and aseismic slip as drivers, *J. Geophys. Res.*, 111, B05312, doi:10.1029/2005JB004034.

Vogt, P. R. (1971), Asthenosphere motion recorded by the ocean floor south of Iceland, *Earth Planet. Sci. Lett.*, 13, 153–160, doi:10.1016/0012-821X(71)90118-X.

Waff, H. S., and J. R. Bulau (1982), Experimental determination of near-equilibrium textures in partially molten silicates at high pressures, *Adv. Earth Planet. Sci.*, 12, 229-236.

Waff, H. S., and U. H. Faul (1992), Effects of crystalline anisotropy on fluid distribution in ultramafic partial melts, *J. Geophys. Res.*, 97, 9003–9014, doi:10.1029/92JB00066.

Wang, X., J. R. Cochran, and G. A. Barth (1996), Gravity anomalies, crustal

thickness, and the pattern of mantle flow at the fast spreading East Pacific

Rise, 9°–10°N: Evidence for three-dimensional upwelling, *J. Geophys. Res.*,

101, 17927–17940, doi:10.1029/96JB00194.

Wang, Y., D. W. Forsyth, and B. Savage (2009), Convective upwelling in the mantle

beneath the Gulf of California., *Nature*, 462, 499–501,

doi:10.1038/nature08552.

Wang, T., J. Lin, B. Tucholke, and Y. J. Chen (2011), Crustal thickness anomalies in

the North Atlantic Ocean basin from gravity analysis, *Geochem. Geophys.*

Geosyst., 12, Q0AE02, doi:10.1029/2010GC003402.

Wang, T., B. E. Tucholke, and J. Lin (2015), Spatial and temporal variations in

crustal production at the Mid-Atlantic Ridge, 25°N–27°30′N and 0–27 Ma, *J.*

Geophys. Res., 120, 2119–2142. doi: 10.1002/2014JB011501.

Watkins, C.E., (2016), Constraints on dynamic topography from asymmetric

subsidence across the mid-ocean ridges, M.S. Thesis, University of Hawai'i at

Manoa,

Watts, A. B. (2007), An overview, in *Treatise on Geophysics*, vol. 6, *Crustal and*

Lithosphere Dynamics, edited by G. Schubert, pp. 1–48, Elsevier, Amsterdam.

Weatherley, S. M., and R. F. Katz (2010), Plate-driven mantle dynamics and global

patterns of mid-ocean ridge bathymetry, *Geochem. Geophys. Geosyst.*, 11,

Q10003, doi:10.1029/2010GC003192.

Weissel, J. K., and D. E. Hayes (1971), Asymmetric seafloor spreading south of

Australia, *Nature*, 231, 518–522, doi:10.1038/231518a0.

Wendt, J. I., M. Regelous, Y. Niu, R. Hékinian, and K. D.

    Collerson (1999), Geochemistry of lavas from the Garrett Transform Fault:

    Insights into mantle heterogeneity beneath the eastern Pacific, *Earth Planet.*

    Sci. Lett., 173, 271–284, doi:10.1016/S0012-821X(99)00236-8.

Wessel, P., K. J. Matthews, R. D. Müller, A. Mazzoni, J. M. Whittaker, R. Myhill,

    and M. T. Chandler (2015), Semiautomatic fracture zone tracking, *Geochem.*

    Geophys. Geosyst., 16, 2462–2472, doi:10.1002/2015GC005853.

Wesson, R. L. (1988), Dynamics of fault creep, *J. Geophys. Res.*, 93, 8929–8951,

    doi:10.1029/JB093iB08p08929.

White, R. S. (1997), Rift-plume interaction in the North Atlantic, *Philos. Trans. R.*

    Soc. London A, 355, 319–339, doi:10.1098/rsta.1997.0011.

White, R. S., D. McKenzie, and R. K. O'Nions (1992), Oceanic crustal thickness from

    seismic measurements and rare earth element inversions, *J. Geophys. Res.*, 97,

    19683–19715, doi:10.1029/92JB01749.

White, R. S., T. A. Minshull, M. J. Bickle, and C. J. Robinson (2001), Melt

    generation at very slow-spreading oceanic ridges: Constraints from

    geochemical and geophysical data, *J. Petrol.*, 42, 1171–1196,

    doi:10.1093/petrology/42.6.1171.

Whitmarsh, R. B., and A. J. Calvert (1986), Crustal structure of Atlantic fracture

    zones, I, The Charlie Gibbs fracture zone, *Geophys. J. R. Astron. Soc.*, 85,

    107–138, doi:10.1111/j.1365-246X.1986.tb05174.x.

Whittaker, J., A. Goncharov, S. Williams, R. D. Müller, and G. Leitchenkov (2013),

    Global sediment thickness data set updated for the Australian-Antarctic

Southern Ocean, *Geochem. Geophys. Geosyst.*, 14, 3297–3305, doi:10.1002/ggge.20181.

Wilcock, W. S., G. M. Purdy, and S. C. Solomon (1990), Microearthquake evidence for extension across the Kane transform fault, *J. Geophys. Res.*, 95, 15,439–15,462, doi:10.1029/JB095iB10p15439.

Wilson, J. T. (1965), A new class of faults and their bearing on continental drift, *Nature*, 207, 343–347, doi:1038/207343a0.

Wilson, C. R., M. Spiegelman, P. E. van Keken, and B. R. Hacker (2014), Fluid flow in subduction zones: The role of solid rheology and compaction pressure, *Earth Planet. Sci. Lett.*, 401, 261–274, doi:10.1016/j.epsl.2014.05.052.

Winterbourne, J., A. Crosby, and N. White (2009), Depth, age and dynamic topography of oceanic lithosphere beneath heavily sedimented atlantic margins, *Earth Planet. Sci. Lett.*, 287, 137–151, doi:10.1016/j.epsl.2009.08.019.

Workman, R. K., and S. R. Hart (2005), Major and trace element composition of the depleted MORB mantle (DMM), *Earth Planet. Sci. Lett.*, 231, 53–72, doi:10.1016/j.epsl.2004.12.005.

Yale, M. M., and J. Phipps Morgan (1998), Asthenosphere flow model of hotspot-ridge interactions: a comparison of Iceland and Kerguelen, *Earth Planet. Sci. Lett.*, 161, 45–56, doi:10.1016/S0012-821X(98)00136-8.

Yamamoto, M., J. P. Morgan, and W. J. Morgan (2007a), Global plume-fed asthenosphere flow II: Application to the geochemical segmentation of mid-

ocean ridges, in *Plates, Plumes and Planetary Processes*, edited by G. R. Foulger and D. M. Jurdy, *Geol. Soc. Spec. Pap.*, 430, 189–208, doi:10.1130/2007.2430(10).

Yamamoto, M., J. Phipps Morgan, and W. J. Morgan (2007b), Global plume-fed asthenosphere flow—I: Motivation and model development, in *Plates, Plumes and Planetary Processes*, edited by G. R. Foulger and D. M. Jurdy, *Geol. Soc. Spec. Pap.*, 430, p. 165–188, doi:10.1130/2007.2430(09).

Yang, H. J., R. J. Kinzler, and T. L. Grove (1996), Experiments and models of anhydrous, basaltic olivine-plagioclase-augite saturated melts from 0.001 to 10 kbar, *Contrib. Mineral. Petrol.*, 124, 1–18, doi:10.1007/s004100050169.

Zhu, W., and G. Hirth (2003), A network model for permeability in partially molten rocks, *Earth Planet. Sci. Lett.*, 212, 407–416, doi:10.1016/S0012-821X(03)00264-4.

Zhu, W., G. A. Gaetani, F. Fusseis, L. G. J. Montési, and F. De Carlo (2011), Microtomography of partially molten rocks: Three-dimensional melt distribution in mantle peridotite, *Science*, 332, 88–91, doi:10.1126/science.1202221.

Zou, H., A. Zindler, and Y. Niu (2002), Constraints on melt movement beneath the East Pacific Rise from ^{230}Th-^{238}U disequilibrium, *Science*, 295, 107–110, doi:10.1126/science.1064295.